Modeling and simulation of disordered light management structures in optoelectronic devices

Zur Erlangung des akademischen Grades eines

DOKTOR-INGENIEURS
(Dr.-Ing.)

von der KIT-Fakultät für
Elektrotechnik und Informationstechnik
des Karlsruher Instituts für Technologie (KIT)

genehmigte

DISSERTATION

von

M.Sc. Dominik Theobald
geb. in Hadamar

Tag der mündlichen Prüfung:	30.11.2021
Hauptreferent:	Prof. Dr. Ulrich Lemmer
Korreferent:	Prof. Dr. Carsten Rockstuhl

Kurzfassung

Um die Lichtausbreitung innerhalb optoelektronischer Bauelemente gezielt zu manipulieren greift Lichtmanagement zunehmend auf ungeordnete Strukturen und Materialien zurück. Die quantitative Beschreibung dieser ungeordneten Teilchensysteme wird jedoch maßgeblich durch das Fehlen von Symmetrien erschwert. Hierdurch verlangt insbesondere die Diskrepanz der einzelnen Größenordnungen innerhalb eines Systems Modellierungswerkzeuge mit einem breiten Anwendungsbereich. Um die Streuprobleme in den typischen Dünnschichtsystemen optoelektronischer Bauelemente abzubilden, wird in dieser Arbeit eine Simulationsmethode genutzt, welche die gestreuten elektromagnetischen Felder in Kugelwellen abbildet und mit einem Formalismus für ebene Wellen kombiniert. Im Vergleich zu den etablierten differentiellen Methoden und Integralansätzen profitiert der gewählte Reihenansatz maßgeblich von einer stark reduzierten Anzahl an Unbekannten, erweist sich allerdings im Falle komplexer Streugeometrien bisher als nicht ausreichend flexibel. Bei Streuanordnungen aus nichtkugelförmigen Partikeln erfordert die T-Matrix-Methode beispielsweise einen Mindestabstand zwischen benachbarten Partikeln, um die Mehrfachstreuung richtig auflösen zu können und erweist sich daher ungeeignet für das Modellieren von dichten Partikelanhäufungen. In der Praxis kann die Methode zur optischen Modellierung somit nicht immer ihrem Ziel der Optimierung und Unterstützung der Bauelementeherstellung gerecht werden.

In dieser Arbeit wird ein alternatives Verfahren zur Berücksichtigung direkter Wechselwirkungen zwischen nichtkugelförmigen Teilchen vorgestellt. Der Formalismus basiert auf einer zwischenzeitlichen Umwandlung des Translationsoperators für Kugelwellen in ein System ebener Wellen. Hierdurch können die sich ausbreitenden Felder vom evaneszenten Feld getrennt und die direkten Wechselwirkungen zwischen nichtsphärischen, konvexen Partikeln für beliebige Abstände ermittelt werden.
Um den Rechenaufwand weiter zu reduzieren, werden periodische Randbedingungen für die T-matrix-Methode auf Basis von Ewald-Summen in das bestehende Modell integriert. Neben der Modellierung streng periodische Systeme kann der Reihenansatz somit ebenfalls auf die Untersuchung großer, periodischer Einheitszellen erweitert werden. Es wird untersucht, inwieweit sich eine weitreichende Periodizität auf die lokale Unordnung innerhalb der Einheitszellen auswirkt und unter welchen Bedingungen solch eine Periodizität geeignet ist um ungeordnete Partikelsysteme zu beschreiben.

Die numerischen Herausforderungen der vorgestellten Techniken zur optischen Modellierung ungeordneter Partikelsysteme werden erörtert und anschließend anhand zweier praxisrelevanter Fallbeispiele illustriert. Zunächst wird ein Vergleich zwischen planarisierten Extraktionsschichten mit niedrigem und hohen Brechungsindex zur Auskopplung von Licht aus einer organischen Leuchtdiode für unterschiedliche Dichten der Streutextur gezogen. Anschließend werden poröse Polymere in eine Perowskit-Solarzelle integriert um eine diffuse und breitbandige Reflexion zu ermöglichen, wie sie für die Gebäudeintegration von Photovoltaikanlagen wünschenswert sein kann.

Abstract

Light management in optoelectronics increasingly relies on disordered textures and materials to manipulate the propagation of light to one's desires. The lack of symmetry in such disordered particle arrangements renders their quantitative description highly challenging. In particular, the discrepancy of the involved length scales demands for simulation tools with a wide range of applicability.
The presented work builds on a simulation framework that combines the spherical wave representation of a particle's scattered electromagnetic field with a plane wave formalism to account for light propagation in thin-film environments of optoelectronic devices. The series approach thrives from a severe reduction of unknowns compared to the more established differential or integral approaches, but so far lacks in flexibility when it comes to complex scattering geometries. In particle arrangements consisting of nonspherical scatterers for example, the superposition T-matrix method requires a minimal particle separation to account for the multiple scattering response and hereby prohibits the aggregation of nonspherical scatterers. In practice, such restrictions do not satisfy the incentive of optical modeling to optimize and support the device fabrication.

In this thesis, an alternative procedure to account for direct particle interactions between nonspherical scatterers in close vicinity is presented. The formalism is based on an intermediate plane wave expansion of the translation operator for spherical vector wave functions that allows to separate the propagating and evanescent field contributions from each other. Hereby, the direct interactions between nonspherical, convex scatterers can be obtained for arbitrary particle separations.
To further lower the computation cost and time necessary to derive information from the optical models, periodic boundary conditions are formulated, based on Ewald lattice sums. Besides opening up the series approach to strictly periodic systems, the boundary conditions allow to investigate light scattering in large, periodic super cells. It is discussed, to which extent a long range periodicity influences the short range disorder within one unit cell and under which conditions disorder can be mimicked.

Numerical challenges of the developed modeling techniques are discussed and finally two light management applications are presented. First, a comparison is drawn between low and high index planarized extraction layers in an organic light emitting diode for various texture densities. Secondly, porous polymer networks are integrated in a Perovskite solar cell to tailor a diffuse and broadband reflectance that facilitates the photovoltaics' building integration.

Table of Contents

1 Modeling of disordered light management structures

This chapter familiarizes the reader with the challenge of optical modeling of disordered light management structures. After a comparison of the various numerical techniques available to address these challenges, the state-of-the-art of a superposition T-matrix framework and the therewith arising open questions are summarized. At the end of this chapter the outline of this work is given.

In optoelectronics *light management* comprises all efforts possibly made to manipulate the propagation of light in order to serve a certain goal. Ultimately, most of these goals can be narrowed down to efficiency optimization of a specific device, but can also revolve around safety concerns or more subjective desires like visual appearance.
With optical components in a size range similar to the wavelength of radiation, light management tools often have to bridge a scale-discrepancy between the macroscopic device and optical effects that take place on a microscopic level. Considering the example of organic light emitting diodes (OLEDs) that constitute surface emitters with a size of multiple square centimeters, light extraction can be significantly enhanced by incorporating nanophotonic grids [18] that break the transverse translation symmetry of the otherwise planar, layered device architecture.[1]
It is the objective of a quantitative description of such a device to derive design rules that support its experimental optimization and herewith save material and time. However, the described multi-scale nature of optical components and optoelectronic devices complicates a proper choice of simulation techniques as any available method is somewhat limited in its applicability to a specific range of dimensions. In the example above, the periodicity of the nanophotonic grid fortunately lowers the computational cost as tools can come into play that explicitly exploit the periodicity in their solution strategy. With the emergence of disordered light management structures, periodic constraints have gone missing, rendering their optical modeling even more complex.

[1] The trapped light problem in thin-film light emitting devices and possible extraction strategies will be reviewed in chapter 5.

1.1 Structural disorder

Compared to their periodic counterparts, disordered textures and materials gain in popularity as they are perceived to provide outstanding spectral- and angular-independent performance characteristics [19]. More robust against fabrication defects, the large scale processing of disordered nanostructures becomes especially interesting for light harvesting [20, 21] and other applications that operate over a broad spectral or angular range, like white light emission [22] or biosensing [23].
Inspired by the disorder of natural, photonic structures found in animal [24, 25] or plant epidermal cells [26], a lot of research has been driven by the question of how to replicate such natural structures [27, 28] and whether disorder can even be tailored to overcome the properties found in nature [29, 30].

Before one dives into the optical modeling of disordered particle arrangements, it is worth to further specify the here considered degrees of *structural disorder* that denote different types of positional uncertainty of the individual scatterers. Being enclose by the two extremes of perfect periodicity and absolute randomness, structural disorder can be more inclined to one or the other, promoting various optical properties and hereby enable different applications.
The different degrees of structural disorder are illustrated in figure 1.1 by means of two-dimensional point patterns of constant filling fraction. Originating from a strict periodicity, a random, local distortion of the periodic pattern creates a *short range disorder*, but maintains the periodicity on a large scale. Applied, e.g., to photonic crystals, the local distortion can significantly increase the number of modes that couple to the quasi-crystal structure, which enables the design of highly efficient and angular robust broadband absorber materials for photovoltaics [19, 31].
In the opposing case, enforcing a short range correlation between neighboring particles of an otherwise random pattern creates materials with a *long range disorder*. Such structures can be obtained from highly controlled techniques like electron beam lithography, but also from fast and scalable self-assembly techniques like the deposition of charged nanoparticles [32] or polymer blend

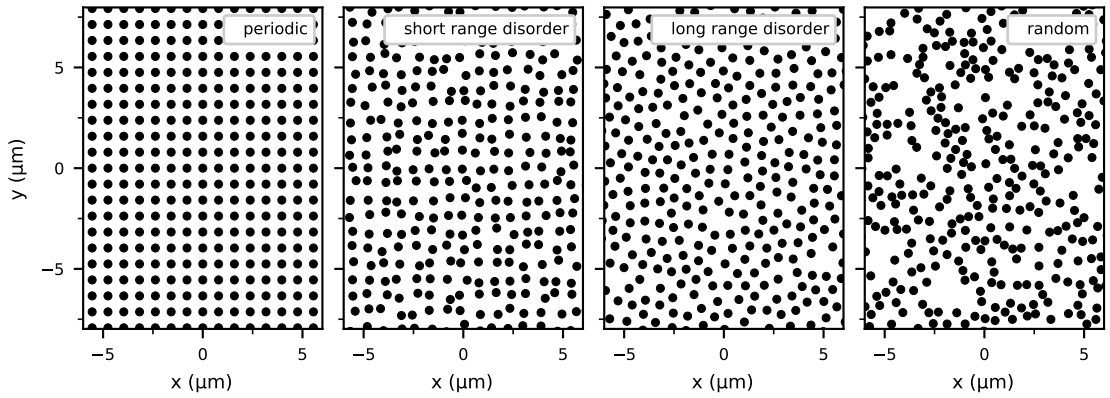

Figure 1.1: Two-dimensional point patterns with varying degrees of structural disorder, but constant filling fraction.

lithography [33]. The resulting structures can promote, e.g., the localization of light in surface enhanced Raman spectroscopy textures [34] or facilitate new optical properties of metasurfaces [35]. When the disordered structures do not exhibit any density fluctuations on a large scale, a state of *hyperuniform disorder* is reached that allows further control of the scattering response [36].
Finally, the largest degree of disorder is observed in fully random structures. Obtained, e.g., from a solution-processed particle dispersion, arbitrary scattering events allow the suppression of waveguide modes [37] or enable broadband diffuse reflection [38].

1.2 Optical modeling of disordered materials

The different degrees of disorder in mind, flexible simulation tools are required that provide insights into the different aspects of disorder and their effect on the optical properties of scattering materials. Whether or not a simulation method is suitable for a specific question initially depends on the central quantity of interest. Therefore, one must ask oneself whether it is the electromagnetic field distribution or the intensity distribution that is primarily of interest. The former case demands for a wave optics approach as a coherent description of scattering events becomes necessary. In the latter case however, an incoherent ray optics scheme may be sufficient to derive the statistical properties that map the probabilistic nature of a scattering arrangement.

1.2.1 Ray optics approach

With a focus on material characteristics of volumetric scattering media, Monte-Carlo ray optics schemes allow to estimate quantities like the scattering mean free path, the scattering asymmetry or the effective refractive index that can fully describe the transport of radiation in such media. Hereby, the ray optics scheme provides a stochastic solution of the *radiative transfer equation* (RTE) [39] for which closed-form solutions only exist in simple cases. Originally postulated on the basis of heuristic observations like energy balance and geometric trajectories of light rays, its derivation based on Maxwell's equations has been realized in recent years [40, 41].
To describe scattering by individual nanoparticles, the ray optics scheme allows to assign a probability distribution to each particle that resembles the angular dependence of a scattering event [42] and thus is not only applicable to micro-sized textures or particles. Independent of the considered geometry, ray-tracing can be deployed to almost any optoelectronic design.

Considering very dense particle arrangements however, coherent multiple scattering effects are expected to become significant, leading to a deviating prediction of transmittance and reflectance by the RTE compared to a full wave analysis [43].

1.2.2 Wave optics approach

The electromagnetic field distribution, which is expressed within a distinct arrangement of particles as the direct result of an explicit source of excitation, is a unique solution to the scattering problem and can only be obtained from a full wave analysis.
In literature, a variety of different optical modeling approaches have been suggested to approximate such a unique solution. An average of different random particle arrangements and possibly of different excitation sources[2] is then necessary to obtain statistically reliable quantities of observation. The different wave optics methods can be classified as the *differential approach*, the *integral approach* and the *series approach* [44]. With a specific problem in mind, a proper choice of the simulation technique can be crucial, as it is determined by the problem's complexity, the involved geometries, the targeted accuracy and the availability and usability of a specific computer program.

Differential approach

Targeting a direct, numerical solution of Maxwell's equations, differential equation methods are based on a discretization of the entire domain of simulation. The most common techniques are:

- The *Finite-Difference Time-Domain* (FDTD) Method [45] that is based on an interlocked cubic grid of electric and magnetic field points. Each magnetic grid point is characterized by the unknown surrounding edges of electric field and vice versa. Applying a time marching scheme that evaluates the time and space derivatives of the electric and magnetic fields between each neighboring nodes and time steps, allows to obtain a steady-state-solution [46].
- The *Finite Element Method* (FEM) that allows to split the global task into smaller, accessible problems. This is achieved by a spatial discretization of the simulation domain into grids of various shapes, e.g., tetrahedral or triangular prisms, that are best suited to approximate the given geometries. Now, basis functions are formulated to approximate the solution of the vector wave equation at each node of the finite elements [47]. From this, a linear set of equations is formulated to obtain the solution of the entire simulation domain.

With the ability to assign arbitrary material properties to each node of the discretization, differential approaches are well suited to model highly inhomogeneous materials and arbitrary geometries. To limit the simulation domain, and herewith the total number of unknowns, boundary conditions are needed that shield the domain of interest from reflections at the outer interfaces. Limited simulation domains imply that only the near-field can be directly obtained. Hence, transformation procedures are required that also provide far-field properties [48]. Although the set of equations is highly

[2] In case of statistically isotropic dipole excitation, the explicit dipole moment of an individual source contributes to the stochastic uncertainty.

sparse allowing an efficient memory usage, the overall effort to obtain results of certain accuracy can be magnitudes larger than those of the integral or series approaches [44].
A significant number of different commercial and freely accessible solvers is available.

Integral approach

In contrast to the differential approach, integral equation methods rely on an integral formulation of Maxwell's equations. Based on an analytic Green's function representation of the electric field that arises from a given distribution of point current sources, integral approaches only need to discretize the scatterer but not the surrounding homogeneous media. In general, one can distinguish between two classes of integral approaches:

- The *Volume Integral Equation* (VIE) Methods. The most common volume-based approach is the *Discrete Dipole Approximation* (DDA), which relies on a discretization of each scatterer into a three-dimensional cubic grid. By assigning a complex polarizability to each cell, the scatterer is replaced by local point dipole sources [49]. Accounting for the initial incoming field and the interactions between each pair of dipoles, the localized sources in sum radiate each particle's scattered field.
- The *Surface Integral Equation* (SIE) Methods. If a Green's function representation of the electric field is also feasible within a scatterer, the complexity of the integral approach can be reduced to its surface currents, significantly lowering the number of unknowns [50].

In contrast to the differential approaches, the integral equation methods rely on a much smaller number of unknowns. However, the resulting matrix equations are fully-populated, leading to an expensive evaluation. In combination with a spectral acceleration technique like the fast Fourier transform, the efficient evaluation allows to study the optical response of large, disordered and densely packed particle arrangements [51, 52]. Similar to the previous methods, the particle discretization allows to deal with particle's of arbitrary shape, providing good flexibility in use cases.
A number of DDA codes is freely available, one of which (ADDA, reference [53]) will be used in chapter 5 as a reference for dense, cylindrical particles located directly on a substrate.

Series approach

In the series approach, the entire simulation domain is divided into domains of constant refractive index. This segmentation allows to define the electric field in each domain as a series of basis functions that solve the homogeneous Helmholtz equation (cf. section 2.2). The solution in each domain is then obtained via a linear set of equations that relies on the continuity of the solution across each domain boundary. Hence, the total number of unknowns depends on the domain

count and the number of basis functions necessary to construct the field to a demanded accuracy. Depending on the choice of basis functions, the different series approaches thrive in the description of varying geometries and can be distinguished into:

- Techniques that expand the scattered field in plane waves. Often denoted as the *Rigorous Coupled Wave Analysis* (RCWA) [54], these methods allow an effective description of rectangular and often periodic geometries.
- Methods based on a spherical wave expansion. With the commonly applied assumption of spherical scatterers and particles of near-spherical shape, the *T-matrix method* [55, 56] provides a commonly applied framework for single and multiple particle scattering.
- Methods relying on cylindrical [33] or spheroidal wave expansions [57]. Less common, these two basis sets provide a specialized framework for geometries of cylindrical and spheroidal shape, for which they can draw severe advantages over the more frequently applied techniques.

Bypassing the discretization of space, methods following the series approach can build up the electromagnetic field distribution in complex scattering geometries with a much lower number of unknowns. Hereby, the series approach becomes especially interesting for large, random particle arrangements that cannot be reproduced by the differential approach. However, relying on a certain set of basis functions can be insufficient to describe highly nonspherical particles or anisotropic media.

1.3 State-of-the-art of a T-matrix framework

The T-matrix method is one of the most powerful tools to describe electromagnetic scattering by single particles and discrete, random particle arrangements, comprising up to tens of thousands of individual scatterers [58, 59]. Although available for a long time, and in many applications surpassing other frequently applied techniques in terms of efficiency, the T-matrix method has seen relatively little use in the nanophotonics community. This however has changed considerably in the most recent years.
In a previous work[3] [60], the superposition T-matrix method to account for multiple particle scattering in conjunction with a plane-wave-based description of light propagation in planar, layered environments has been identified as a suitable simulation framework for the accurate and time-efficient description of light extraction from thin-film organic light emitting diodes.
For this specific application, the approach draws a major advantage over the more established differential and integral equation methods from a severe reduction of unknowns that are necessary to describe the involved scattering arrangements. Instead of a rapidly growing number of unknowns

[3] Work that was done by Amos Egel, partly in parallel with my work.

that arises from a discretization of space, the linear set of equations in a series approach only grows linearly with the particle count[4], but independent of the populated volume. Due to the available transformation properties between spherical and plane wave expansions, the suggested framework allows to embed the particle arrangements within a planar, layered environment, making use of the geometrical accordance between basis wave functions and space. In addition, the series approach does not require boundary conditions to limit the domain of simulation and hence allows the direct evaluation of far-field quantities.
With the described properties in mind, the framework is well suited not only for the description of light extraction from thin-film OLEDs, but for many scenarios that include particle-based light scattering in planar layer-environments.

Despite these advantages, the series approach also suffers from a clear disadvantage compared to the differential or integral approaches. The latter both rely on a discretization of a particle's volume, which allows to consider arbitrary and inhomogeneous scatterers in the same way perfectly regular-shaped particles are. The T-matrix approach however can struggle with particles of arbitrary shape. While it is in principle possible to construct the T-matrix of any scatterer, a series expansion of spherical wave functions is not always able to resemble such a particle's near-field correctly at every point in space. This invalidity of the so-called *Rayleigh hypothesis* (cf. section 4.1) requires a minimal separation between nonspherical particles in the superposition T-matrix scheme. Enforcing a minimal inter-particle distance in the optical model does not cope well with the fabrication of most commonly solution-processed scattering layers in optoelectronic devices.
Another drawback of the monochromatic series approach, compared to time-domain methods, is the large number of simulations that are necessary to evaluate wavelength dependencies, which can be critical for many applications like photovoltaics or white light emission.
In addition, a lack of simulation domain boundaries in the series approach implies that light can escape the domain of interest and therefore cannot be correctly attributed to the observed quantities. This becomes especially critical in thick, volumetric scattering samples for which a sufficiently wide lateral extent of the particle arrangement cannot be easily ensured.

With these disadvantages in mind, a number of questions can be posed, the answer to which can be decisive for the further application of the T-matrix approach:

> *Can the superposition T-matrix framework be suitable for dense, nonspherical particle systems and particle aggregates?*
>
> *Is it possible to reduce the computational cost of a single simulation to a level that allows for efficient wavelength or angular sweeps?*
>
> *How does one impose periodic boundary conditions to the T-matrix framework?*

[4] This naive scaling relation is in fact also affected by the number of multipoles necessary to accurately describe each individual scatterer.

It is the main objective of this work to address these questions and thereby extend the applicability of the superposition T-matrix framework for the optical modeling of light management structures in optoelectronic devices.

1.4 Outline

With the focus set on the numerical challenges in optical modeling that arise from different light management tools and their integration in various device architectures, I forgo the typical upfront introduction of one or more specific devices and their respective working principles. Instead, the reader can directly familiarize themselves with the mathematical and physical foundations applied in the T-matrix simulation framework in chapters 2 and 3. With this foundation set, this work's main theoretical contributions and their numerical implications are presented in chapters 4 and 6. Readers from the OLED or solar cell community that might not be too concerned with the numerical details can directly dive into chapters 5 and 7, where the respective devices and working principles emphasize the application of the developed simulation tools.

To this end, I have organized this thesis as follows:
Chapter 2 introduces some concepts of electromagnetic theory, including two basis sets of solutions to Maxwell's equations in homogeneous space. With these wave functions available, namely the plane and spherical vector waves, the basis for the simulation framework is set, which is described in detail in chapter 3.
Chapter 4 deals with the separation restriction for nonspherical particles that prevents the use of the superposition T-matrix method for dense particle arrangements of nonspherical scatterers. An alternative formulation of the translation addition operator for spherical vector wave functions is presented that allows to model light scattering in such systems. Equipped with this tool, the trapped light problem in organic light emitting diodes is reviewed in chapter 5 and the effect of different filling fractions of internal outcoupling structures on the extraction efficiency is investigated.
In chapter 6, periodic boundary conditions on the basis of Ewald lattice sums are incorporated into the existing simulation framework that prevent edge effects from the otherwise finite particle arrangements. The effect of an artificial long-range periodicity on disordered particle arrangements is investigated and conditions are formulated that prevent the excitation of artificial lattice resonances. Provided with the necessary tools to efficiently derive the spectral and angular dependence of thick volumetric scattering layers, the integration of porous polymer films in Perovskite solar cells is studied in chapter 7 that can provide a diffuse, broadband reflectance and facilitate building integration of solar cells.
In chapter 8, I draw conclusions from this work and give an outlook of possible developments and extensions of the current simulation framework.

2 Description of electromagnetic waves

This chapter will briefly introduce the Helmholtz wave equation, describing electromagnetic wave propagation in piecewise homogeneous media, as we will later deal with light scattering in planar, layered environments. Depending on the geometry at hand, a proper choice of the coordinate system and therewith the set of basis solutions to the wave equation will strongly benefit the description of fields. To freely switch between one another, translation, rotation and transformation properties of plane and spherical vector wave functions are summarized.
As this work revolves around a simulation framework (see chapter 3) originally published by Amos Egel, the here found notations of basis functions and quantities largely match the notations in reference [60], which should simplify the comparability and readability of the different available sources.

2.1 Maxwell equations

The response of electric and magnetic fields $\mathbf{E}$ and $\mathbf{H}$ on the presence of electric currents and electric charges can be described by the macroscopic Maxwell equations. Their spectral representation reads [61]

$$\nabla \times \mathbf{E}(\mathbf{r},\omega) = \mathrm{i}\omega\mathbf{B}(\mathbf{r},\omega), \tag{2.1}$$
$$\nabla \times \mathbf{H}(\mathbf{r},\omega) = -\mathrm{i}\omega\mathbf{D}(\mathbf{r},\omega) + \mathbf{j}(\mathbf{r},\omega), \tag{2.2}$$
$$\nabla \cdot \mathbf{D}(\mathbf{r},\omega) = \rho(\mathbf{r},\omega), \tag{2.3}$$
$$\nabla \cdot \mathbf{B}(\mathbf{r},\omega) = 0, \tag{2.4}$$

with the electric displacement $\mathbf{D}$, the magnetic induction $\mathbf{B}$, the current density $\mathbf{j}$ and the charge density ρ being functions of the position vector $\mathbf{r}$ and the angular frequency ω.
In combination with the *constitutive relations*, defining the material response to the respective fields

$$\mathbf{D}(\mathbf{r},\omega) = \epsilon_0\epsilon_r\mathbf{E}(\mathbf{r},\omega), \tag{2.5}$$
$$\mathbf{B}(\mathbf{r},\omega) = \mu_0\mu_r\mathbf{H}(\mathbf{r},\omega), \tag{2.6}$$

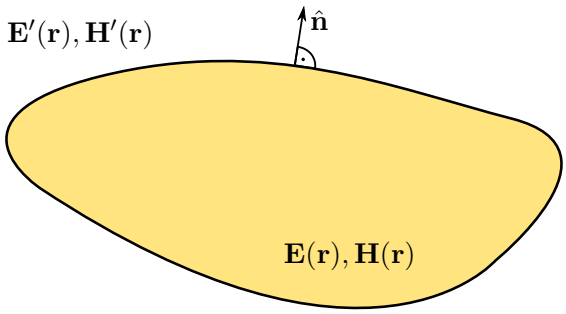

Figure 2.1: A particle embedded in an homogeneous ambient medium. Each solution of the wave equation is valid in its respective sub-domain. At the domain boundaries, the fields' tangential components are continuous.

a self-consistent set of equations is formed. ϵ_0 denotes the vacuum permittivity, μ_0 the vacuum permeability, ϵ_r the relative permittivity and μ_r the relative permeability.
The time-dependent electric field can be obtained from its spectral components via the inverse Fourier transform

$$\mathbf{E}(\mathbf{r}, t) = \int_{-\infty}^{\infty} \mathbf{E}(\mathbf{r}, \omega) \mathrm{e}^{-\mathrm{i}\omega t} d\omega. \tag{2.7}$$

This implies, that the Maxwell equations can be solved for each spectral component individually. Hence, time-harmonic electric and magnetic fields can be obtained from the monochromatic fields

$$\mathbf{E}(\mathbf{r}, t) = \mathbf{E}(\mathbf{r}, \omega) \mathrm{e}^{-\mathrm{i}\omega t}, \tag{2.8}$$

$$\mathbf{H}(\mathbf{r}, t) = \mathbf{H}(\mathbf{r}, \omega) \mathrm{e}^{-\mathrm{i}\omega t}. \tag{2.9}$$

In the following, I will neglect the frequency dependence of the electric $\mathbf{E}(\mathbf{r}) = \mathbf{E}(\mathbf{r}, \omega)$ and magnetic fields $\mathbf{H}(\mathbf{r}) = \mathbf{H}(\mathbf{r}, \omega)$ to allow for a more condensed notation. The opportunity arises, as we will only consider time-harmonic fields. But keep in mind that almost all quantities show wavelength dependence.

2.2 The Helmholtz equation

Inserting equation (2.6) into (2.1) and making use of (2.2) and (2.5) one obtains the system of inhomogeneous Helmholtz equations [61]

$$\nabla \times \nabla \times \mathbf{E}(\mathbf{r}) - k^2 \mathbf{E}(\mathbf{r}) = \mathrm{i}\omega\mu_0\mu_r \mathbf{j}(\mathbf{r}) \tag{2.10}$$

$$\nabla \cdot \mathbf{E}(\mathbf{r}) = \frac{\rho(\mathbf{r})}{\epsilon_r \epsilon_0} \tag{2.11}$$

and

$$\mathbf{H}(\mathbf{r}) = \frac{1}{\mathrm{i}\omega\mu_0\mu_r} \nabla \times \mathbf{E}(\mathbf{r}). \tag{2.12}$$

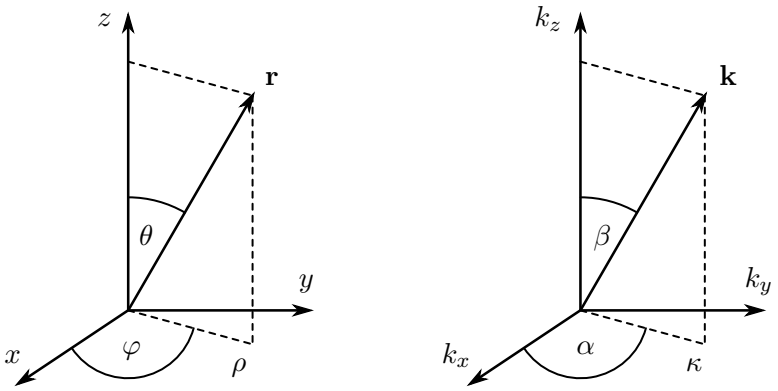

Figure 2.2: Cartesian, cylindrical and spherical coordinate systems of the real-space position vector $\mathbf{r}$: (x, y, z), (ρ, φ, z), (r, θ, φ) and of the reciprocal-space wave vector $\mathbf{k}$: (k_x, k_y, k_z), (κ, α, k_z), (k, β, α).

The wavenumber k

$$k = \frac{\omega}{c_0} n, \tag{2.13}$$

is a function of the complex refractive index n

$$n(\omega) = \sqrt{\epsilon_r + \frac{\mathrm{i}\sigma}{\omega \epsilon_0}}. \tag{2.14}$$

c_0 denotes the vacuum speed of light and $\sigma(\omega)$ a medium's conductivity.
All problems considered throughout this work revolve around particles embedded in non-magnetic, linear, isotropic and locally homogeneous media. Such piecewise homogeneous environments allow to solve the wave equations in each homogeneous domain separately. However, as the material properties are discontinuous along the domain boundaries, boundary conditions need to be met. In the absence of surface current densities, the fields' tangential components have to satisfy

$$\begin{aligned} \hat{\mathbf{n}} \times (\mathbf{E}(\mathbf{r}) - \mathbf{E}'(\mathbf{r})) &= \mathbf{0}, \\ \hat{\mathbf{n}} \times (\mathbf{H}(\mathbf{r}) - \mathbf{H}'(\mathbf{r})) &= \mathbf{0}, \end{aligned} \tag{2.15}$$

with $\mathbf{E}(\mathbf{r})$, $\mathbf{H}(\mathbf{r})$, $\mathbf{E}'(\mathbf{r})$ and $\mathbf{H}'(\mathbf{r})$ denoting the electric and magnetic fields on either side of a boundary (cf. figure 2.1).
In a source-free domain, the wave equations simplify to the homogeneous Helmholtz equations

$$\begin{aligned} (\nabla^2 + k^2)\mathbf{E}(\mathbf{r}) &= \mathbf{0}, \\ \nabla \cdot \mathbf{E}(\mathbf{r}) &= \mathbf{0}. \end{aligned} \tag{2.16}$$

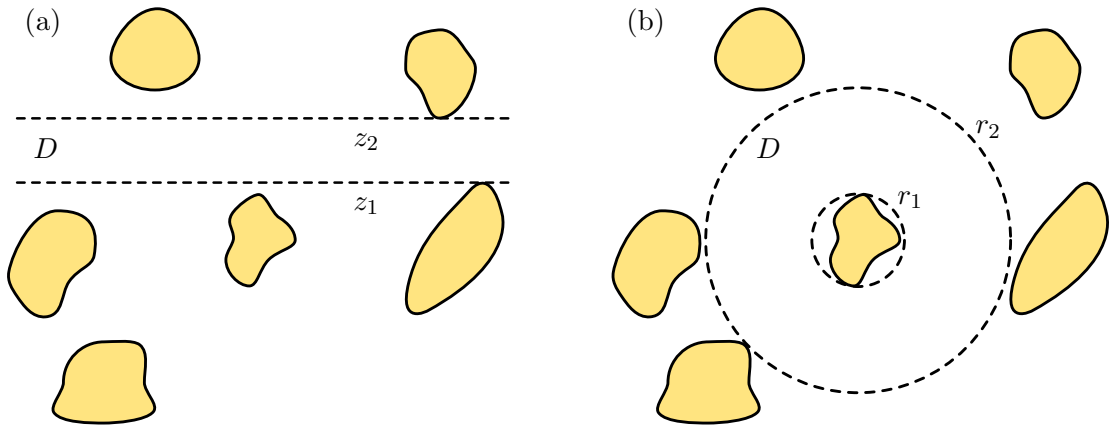

Figure 2.3: In a homogeneous domain D that is: (a) bounded in z direction by two planes, any electromagnetic field can be expanded in plane waves. (b) bounded by two spherical surfaces, any electromagnetic field can be expanded in spherical waves.

2.3 Vector wave functions

To construct the electric and magnetic field in a domain of constant refractive index, I will apply two basis sets of solutions that solve the homogeneous Helmholtz equation. Those are the *plane vector wave functions* and the *spherical vector wave functions*, which can be derived from a separation of variables in their respective coordinate system.

2.3.1 Plane vector wave functions

In cylindrical coordinates $(\kappa, \alpha, \pm k_z)$ of wave vector $\mathbf{k}^{\pm}$, the plane vector wave functions (PVWFs) are defined as

$$\mathbf{\Phi}_j^{\pm}(\kappa, \alpha; \mathbf{r}) = \mathrm{e}^{\mathrm{i}\mathbf{k}^{\pm}\mathbf{r}} \hat{\mathbf{e}}_j^{\pm}. \tag{2.17}$$

Denoting the orientation of propagation, the plus and minus sign correspond to waves oriented along the positive $(+)$ and negative $(-)$ z-direction. Index j distinguishes between a wave's transversal electric (TE: $j = 1$) and transversal magnetic (TM: $j = 2$) polarizations that are defined by the unit vectors $\hat{\mathbf{e}}_1 = \hat{\mathbf{e}}_\alpha$ of the azimuthal and $\hat{\mathbf{e}}_2 = \hat{\mathbf{e}}_\beta$ of the polar angle of $\mathbf{k}^{\pm}$

$$\hat{\mathbf{e}}_1^{\pm} = \hat{\mathbf{e}}_\alpha^{\pm} = \begin{pmatrix} -\sin\alpha \\ \cos\alpha \\ 0 \end{pmatrix}, \qquad \hat{\mathbf{e}}_2^{\pm} = \hat{\mathbf{e}}_\beta^{\pm} = \frac{1}{k} \begin{pmatrix} \pm k_z \cos\alpha \\ \pm k_z \sin\alpha \\ \kappa \end{pmatrix}. \tag{2.18}$$

To ensure that $|\mathbf{k}| = k$ the z-component k_z of wave vector $\mathbf{k}$ is a function of it's in-plane component $\kappa = |\mathbf{k}_\parallel|$

$$k_z = \sqrt{k^2 - \kappa^2}, \tag{2.19}$$

with positive square root convention.
In a medium of a real-valued refractive index ($\operatorname{Im} n = 0$) PVWFs of $\kappa \leq k$ do not undergo any damping and are called *propagating waves*. In contrast, for $\kappa > k$ the complex k_z results in an oscillation of decaying amplitude along the z-direction. In the latter case, one refers to *evanescent waves*.
Let us assume a homogeneous, source-free domain $D \subset \mathbb{R}^3$ that is bounded in z-direction by two planes $z = z_1$ and $z = z_2$, $D = \{\mathbf{r}| -\infty \leq z_1 \leq z \leq z_2 \leq \infty\}$. In such a domain (illustrated in figure 2.3 (a)), the PVWFs form a complete set of equations that fulfill the homogeneous Helmholtz equation (2.16) in a sense, that there exist functions $g_j^+(\kappa, \alpha)$ and $g_j^-(\kappa, \alpha)$ that allow to construct any divergence-free field

$$\mathbf{E}(\mathbf{r}) = \sum_{j=1}^{2} \int_{\mathbb{R}^2} d^2\mathbf{k}_\parallel \left(g_j^+(\kappa,\alpha)\mathbf{\Phi}_j^+(\kappa,\alpha;\mathbf{r}) + g_j^-(\kappa,\alpha)\mathbf{\Phi}_j^-(\kappa,\alpha;\mathbf{r}) \right), \tag{2.20}$$

with $d^2\mathbf{k}_\parallel = dxdy = d\kappa\kappa d\alpha$ denoting integration over all in-plane wave vectors $\mathbf{k}_\parallel = (\kappa, \alpha)$. A proof of the completeness of PVWFs can be found, e.g., in reference [62].

In analogy to the electric field, the magnetic field can be constructed via

$$\begin{aligned} \mathbf{H}(\mathbf{r}) &= \frac{1}{\mathrm{i}\omega\mu_0} \nabla \times \mathbf{E}(\mathbf{r}) \qquad (2.21) \\ &= \frac{1}{\omega\mu_0} \sum_{j=1}^{2} \int_{\mathbb{R}^2} d^2\mathbf{k}_\parallel \left(g_j^+(\kappa,\alpha)\mathbf{k}^+ \times \mathbf{\Phi}_j^+(\kappa,\alpha;\mathbf{r}) + g_j^-(\kappa,\alpha)\mathbf{k}^- \times \mathbf{\Phi}_j^-(\kappa,\alpha;\mathbf{r}) \right). \end{aligned}$$

With

$$\mathbf{k}^\pm \times \hat{\mathbf{e}}_1^\pm = -k\hat{\mathbf{e}}_2^\pm \tag{2.22}$$

and

$$\mathbf{k}^\pm \times \hat{\mathbf{e}}_2^\pm = k\hat{\mathbf{e}}_1^\pm, \tag{2.23}$$

the magnetic field takes the form

$$\begin{aligned} \mathbf{H}(\mathbf{r}) = \frac{1}{\omega\mu_0} \int_{\mathbb{R}^2} d^2\mathbf{k}_\parallel \big(k \big(& g_2^+(\kappa,\alpha)\mathbf{\Phi}_1^+(\kappa,\alpha;\mathbf{r}) - g_1^+(\kappa,\alpha)\mathbf{\Phi}_2^+(\kappa,\alpha;\mathbf{r}) \\ & + g_2^-(\kappa,\alpha)\mathbf{\Phi}_1^-(\kappa,\alpha;\mathbf{r}) - g_1^-(\kappa,\alpha)\mathbf{\Phi}_2^-(\kappa,\alpha;\mathbf{r}) \big) \big). \end{aligned} \tag{2.24}$$

2.3.2 Spherical vector wave functions

In a spherical domain $D \subset \mathbb{R}^3$ that is bound by two spherical surfaces $r = r_1$ and $r = r_2$, $D = \{\mathbf{r}|0 \leq r_1 \leq r \leq r_2 \leq \infty\}$, the spherical vector wave functions (SVWFs) $\mathbf{M}_{lm\tau}^{(\nu)}$ form a characteristic set of solutions of the homogeneous Helmholtz equation. A graphical illustration of

D can be found in figure 2.3(b).
In the spherical coordinates θ, φ, r of position vector $\mathbf{r}$, the SVWFs read [63]

$$\mathbf{M}_{lm1}^{(\nu)}(\mathbf{r}) = \frac{1}{\sqrt{2l(l+1)}} \nabla \times \left[\mathbf{r} z_l^{(\nu)}(kr) Y_{lm}(\theta, \varphi) \right], \tag{2.25}$$

$$\mathbf{M}_{lm2}^{(\nu)}(\mathbf{r}) = \frac{1}{k} \nabla \times \mathbf{M}_{lm1}^{(\nu)}(\mathbf{r}). \tag{2.26}$$

Denoted by indices l, m and τ, one distinguishes between a spherical wave's multipole degree l, multipole order m and polarization τ. $\tau = 1$ refers to spherically transverse electric and $\tau = 2$ to spherically transverse magnetic polarized waves. Which means, that in the spherical wave's coordinate system, either the electric or magnetic field is perpendicular to any position vector $\mathbf{r}$.
Similar to the upgoing and downgoing plane waves, the SVWFs exist in two kinds. Spherical waves of regular kind ($\nu = 1$) involve the spherical Bessel function $z_l^{(1)} = j_l$, while outgoing SVWFs ($\nu = 3$) make use of the spherical Hankel function of first kind $z_l^{(1)} = h_l^{(1)}$.
The spherical harmonics

$$Y_{lm}(\theta, \varphi) = P_l^{|m|}(\cos\theta) \mathrm{e}^{\mathrm{i}m\varphi}, \tag{2.27}$$

involve the normalized associated Legendre functions

$$P_l^m(x) = \sqrt{\frac{2l+1}{2} \frac{(l-m)!}{(l+m)!}} \tilde{P}_l^m(x), \tag{2.28}$$

based on the associate Legendre functions $\tilde{P}_l^m(x)$ and the Legendre polynomials $P_l(x)$

$$\tilde{P}_l^m(x) = \left(1 - x^2\right)^{m/2} \frac{d^m P_l(x)}{dx^m}. \tag{2.29}$$

Given that the electric field in the homogeneous domain D is divergence-free, any field can be expanded in spherical waves

$$\mathbf{E}(\mathbf{r}) = \sum_{\tau=1}^{2} \sum_{l=1}^{\infty} \sum_{m=-l}^{l} a_{lm\tau} \mathbf{M}_{lm\tau}^{(1)}(\mathbf{r}) + b_{lm\tau} \mathbf{M}_{lm\tau}^{(3)}(\mathbf{r}). \tag{2.30}$$

The magnetic field takes the form [56, 63]

$$\mathbf{H}(\mathbf{r}) = \frac{k}{\mathrm{i}\omega\mu_0} \sum_{\tau=1}^{2} \sum_{l=1}^{\infty} \sum_{m=-l}^{l} b_{lm\tau} \mathbf{M}_{lm\tau}^{(1)}(\mathbf{r}) + a_{lm\tau} \mathbf{M}_{lm\tau}^{(3)}(\mathbf{r}). \tag{2.31}$$

2.3.3 Translations, rotations and transformations

To provide the reader with the necessary tools, I will summarize some translation, rotation and transformation properties of plane and spherical vector wave functions that will be utilized throughout this work.

Translations

The translation of PVWFs by a displacement vector $\mathbf{d}$ can be expressed by a simple phase shift

$$\mathbf{\Phi}_j^{\pm}(\mathbf{r}+\mathbf{d}) = \mathrm{e}^{\mathrm{i}\mathbf{k}^{\pm}\mathbf{d}}\mathbf{\Phi}_j^{\pm}(\mathbf{r}). \tag{2.32}$$

For a translation of SVWFs one can make use of the *translation addition theorem* [64]

$$\mathbf{M}_n^{(3)}(\mathbf{r}+\mathbf{d}) = \sum_{n'} A_{nn'}(\mathbf{d})\mathbf{M}_{n'}^{(1)}(\mathbf{r}), \qquad |\mathbf{r}| < |\mathbf{d}|, \tag{2.33}$$

with

$$A_{nn'}(\mathbf{d}) = \delta_{\tau\tau'}A_{lml'm'}(\mathbf{d}) + (1-\delta_{\tau\tau'})B_{lml'm'}(\mathbf{d}). \tag{2.34}$$

To allow for a more condensed notation, I have introduced the multi-index n, which subsumes the spherical waves multipole degree l, multipole order m and polarization τ, $(l,m,\tau) \to n$.
The translation operator $\mathbf{A}(\mathbf{d})$ can be build by recurrence formulas presented in references [63, 65] or by making use of the Wigner-3j symbols [56, 63, 66]. In the latter case, the Kronecker delta $\delta_{\tau\tau'}$ indicates whether the translation operator reads [56]

$$A_{lml'm'}(\mathbf{d}) = \mathrm{e}^{\mathrm{i}(m-m')\varphi_d} \sum_{\lambda=|l-l'|}^{|l+l'|} a_5(l,m|l',m'|\lambda)h_\lambda^{(1)}(kd)P_\lambda^{|m-m'|}(\cos\theta_d), \tag{2.35}$$

or

$$B_{lml'm'}(\mathbf{d}) = \mathrm{e}^{\mathrm{i}(m-m')\varphi_d} \sum_{\lambda=|l-l'|}^{|l+l'|} b_5(l,m|l',m'|\lambda)h_\lambda^{(1)}(kd)P_\lambda^{|m-m'|}(\cos\theta_d). \tag{2.36}$$

At this point, I omit the lengthy derivation of a_5 and b_5 that contain the Wigner-3j symbols. Explicit formulas that apply to the here used normalization conventions can be found, e.g., in reference [58].

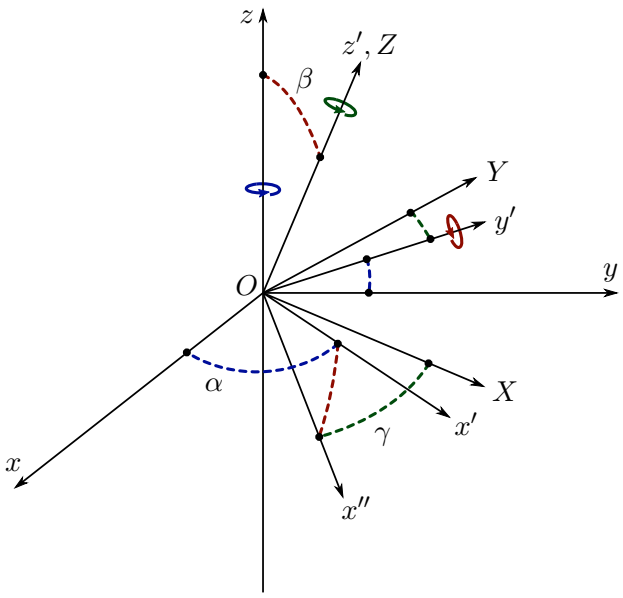

Figure 2.4: With Euler angles α, β and γ, the laboratory coordinate system $(Oxyz)$ can be rotated into coordinate system $(OXYZ)$. This is achieved by successive rotations around the z-, y'- and z'-axis. The figure has been adapted from reference [63].

Rotations

To display the SVWFs in a rotated coordinate system, one can make use of the *rotation addition theorem* [66].
I define the laboratory coordinate system (L) with the Cartesian coordinates $(Oxyz)$ and a rotated coordinate system (R) with Cartesian coordinates $(OXYZ)$. Now a series of three successive rotations by Euler angles α, β and γ allow to rotate the laboratory coordinate system into the rotated coordinate system. The here applied rotations follow the z, y', z'-convention:

- rotation of α around the z-axis: $Oxyz \rightarrow Ox'y'z$ with $\alpha \in [0, 2\pi)$,
- rotation of β around the y'-axis: $Ox'y'z \rightarrow Ox''y'z'$ with $\beta \in [0, \pi]$,
- rotation of γ around the z'-axis: $Ox''y'z' \rightarrow OXYZ$ with $\gamma \in [0, 2\pi)$.

A graphical illustration of the different coordinate systems can be found in figure 2.4.
With the above rotation convention, SVWFs $\tilde{\mathbf{M}}_n^{(1,3)}(\mathbf{r})$ in coordinate system (R) can be displayed as a sum of SVWFs $\mathbf{M}_{n'}^{(1,3)}(\mathbf{r})$ in coordinate system (L)

$$\tilde{\mathbf{M}}_n^{(1,3)}(\mathbf{r}) = \sum_{m'=-l}^{l} D_{mm'}^{l}(\alpha, \beta, \gamma) \mathbf{M}_{n'}^{(1,3)}(\mathbf{r}), \tag{2.37}$$

and vice versa

$$\mathbf{M}_n^{(1,3)}(\mathbf{r}) = \sum_{m'=-l}^{l} D^l_{mm'}(-\gamma,-\beta,-\alpha)\tilde{\mathbf{M}}_{n'}^{(1,3)}(\mathbf{r}), \tag{2.38}$$

where $D(\alpha,\beta,\gamma)$ denotes the Wigner D-functions. A recurrence formula for evaluation of Wigner D-functions can be found in Appendix A.

Transformations

Depending on the configuration at hand, it can be advantageous to express PVWFs in terms of SVWFs and vice versa. A comprehensive description of transformation properties of plane and spherical vector wave functions can be found in reference [67].
In this work, I will make use of plane waves expanded in terms of regular spherical waves

$$\mathbf{\Phi}_j^{\pm}(\kappa,\alpha;\mathbf{r}) = 4\sum_n \mathrm{e}^{-\mathrm{i}m\alpha} B^{\dagger}_{nj}\left(\pm\frac{k_z}{k}\right)\mathbf{M}_n^{(1)}(\mathbf{r}), \tag{2.39}$$

and outgoing spherical waves expressed in plane waves

$$\mathbf{M}_n^{(3)}(\mathbf{r}) = \frac{1}{2\pi}\sum_{j=1}^{2}\int_{\mathbb{R}^2}\frac{d^2\mathbf{k}_\parallel}{k_z k}\mathrm{e}^{\mathrm{i}m\alpha}B_{nj}\left(\pm\frac{k_z}{k}\right)\mathbf{\Phi}_j^{\pm}(\kappa,\alpha;\mathbf{r}), \qquad \text{for } z \gtrless 0. \tag{2.40}$$

The transformation operator B reads [63]

$$B_{nj}(x) = -\frac{1}{\mathrm{i}^{l+1}}\frac{1}{\sqrt{2l(l+1)}}\left(\mathrm{i}\delta_{j1}+\delta_{j2}\right)\left(\delta_{\tau j}\tau_l^{|m|}(x) + (1-\delta_{\tau j})m\pi_l^{|m|}(x)\right) \tag{2.41}$$

with the angular functions

$$\tau_l^m(\cos\theta) = \partial_\theta P_l^m(\cos\theta), \tag{2.42}$$

$$\pi_l^m(\cos\theta) = \frac{P_l^m(\cos\theta)}{\sin\theta}. \tag{2.43}$$

For $B^{\dagger}$ all explicit i in equation (2.41) have to be set to $-\mathrm{i}$.

3 Simulation framework

In the previous work of Amos Egel [60], a simulation framework to describe multiple scattering in a planar, layered environment has been presented. At the beginning of my work, a Matlab based prototype of this framework already existed and later the free Python package SMUTHI was published [3]. SMUTHI stands for "scattering by multiple particles in thin-film systems". From its launch on, SMUTHI allowed the user to investigate the scattering of light by spherical particles, distributed in a layer environment that are excited by either an external plane wave, a Gaussian beam or an internal point dipole distribution.
Throughout this thesis, I have worked on the development of the Matlab prototype and later on the continuous extension of functionality provided by SMUTHI. Since its publication in 2018, a number of different researchers joined this project and contributed to its growth.
To provide the reader with the necessary insights and notations, I will describe the simulation framework in detail. Even though many of these aspects have been published elsewhere, I consider them necessary to follow the here presented work. However, I will omit a comprehensive description of aspects that are not strictly necessary, but rather refer to the original publications.

To approach the optical modeling of light scattering in disordered particle arrangements that are embedded in planar, layered media, one has to specify the individual scattering events, their influence on each other, and how these interactions are affected by the presence of the layered medium.

3.1 Planar, layered media

A planar, layered medium consists of $N+1$ homogeneous layers $\Lambda_i \subset \mathbb{R}^3$, $i = 0 \dots N$. Each layer is fully characterized by a refractive index n_i, a thickness d_i and its bounding planes z_i and z_{i+1} that are parallel to the xy-plane, with $z_i < z_{i+1}$. The outer layers Λ_0 and Λ_N are semi-infinite, i.e., $d_0 = d_N = \infty$ and therefore only have a single bounding plane.

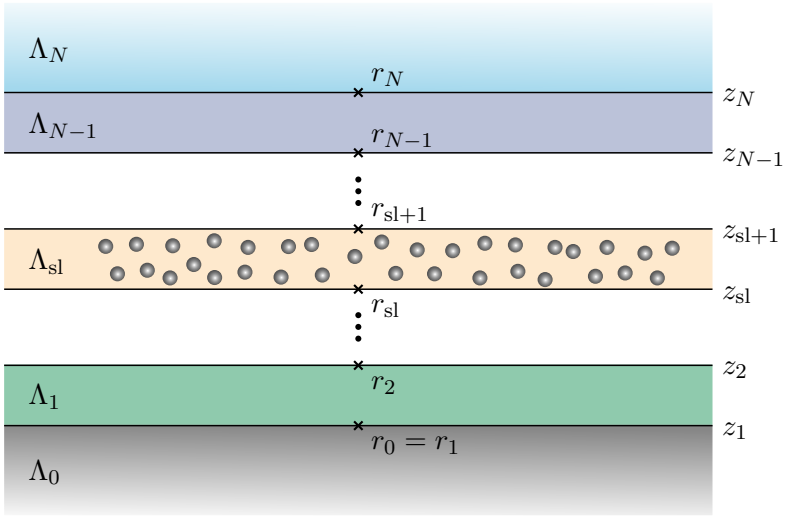

Figure 3.1: A scattering layer in a planar, layered environment.

In each layer that is free of sources, the electric field can be expanded in terms of plane waves according to equation (2.20). In a vector notation, the field expansion reads

$$\mathbf{E}(\mathbf{r}) = \sum_{j=1}^{2} \int_{\mathbb{R}^2} d^2\mathbf{k}_{\parallel} \left[\mathbf{\Phi}_j^+(\kappa, \alpha; \mathbf{r} - \mathbf{r}_i), \mathbf{\Phi}_j^-(\kappa, \alpha; \mathbf{r} - \mathbf{r}_i) \right] \begin{bmatrix} g_{i,j}^+(\kappa, \alpha) \\ g_{i,j}^-(\kappa, \alpha) \end{bmatrix} \tag{3.1}$$

for $\mathbf{r} \in \Lambda_i$.
As index i denotes the layer number, the amplitudes $g_{i,j}^{\pm}(\kappa, \alpha)$ of upwards and downwards oriented PVWFs are defined at anchor point $r_i = (0, 0, z_i)$. Only layer Λ_0 has no lower bound (cf. figure 3.1). Its anchor point is set to $r_0 = r_1$.

3.1.1 Transfer matrix method

Plane waves propagating in a layered environment are partially transmitted and reflected at each interface. The electromagnetic fields formed on each side of an interface have to meet the boundary

conditions (2.15). Describing the amplitudes of partially transmitted and reflected plane waves at interface i, the Fresnel coefficients read

$$t_{i,i+1,1}(\kappa) = \frac{2k_{z,i}}{k_{z,i} + k_{z,i+1}}, \tag{3.2}$$

$$r_{i,i+1,1}(\kappa) = \frac{k_{z,i} - k_{z,i+1}}{k_{z,i} + k_{z,i+1}}, \tag{3.3}$$

$$t_{i,i+1,2}(\kappa) = \frac{2n_i n_{i+1} k_{z,i}}{n_{i+1}^2 k_{z,i} + n_i^2 k_{z,i+1}}, \tag{3.4}$$

$$r_{i,i+1,2}(\kappa) = \frac{n_{i+1}^2 k_{z,i} - n_i^2 k_{z,i+1}}{n_{i+1}^2 k_{z,i} + n_i^2 k_{z,i+1}}, \tag{3.5}$$

with the non-negative, complex $k_{z,i} = \sqrt{k_i^2 - \kappa^2}$ denoting the z-component of wavenumber $k_i = n_i\omega/c_0$ in layer Λ_i.

As the transmission and reflection only couples to plane waves of identical polarization and incident angle, the boundary conditions can be met for each component of the plane-wave spectrum individually. The transfer matrix [68, 69]

$$I_j^{i,i+1}(\kappa) = \begin{cases} D_j^{i,i+1}(\kappa) & \text{for } i = 0 \\ P^i(\kappa) D_j^{i,i+1}(\kappa) & \text{else} \end{cases} \tag{3.6}$$

connects the plane wave amplitudes in layers Λ_i and Λ_{i+1}

$$\begin{bmatrix} g_{i,j}^+(\kappa,\alpha) \\ g_{i,j}^-(\kappa,\alpha) \end{bmatrix} = I_j^{i,i+1}(\kappa) \begin{bmatrix} g_{i+1,j}^+(\kappa,\alpha) \\ g_{i+1,j}^-(\kappa,\alpha) \end{bmatrix}. \tag{3.7}$$

Where the interface matrix

$$D_j^{i,i+1}(\kappa) = \frac{1}{t_{i,i+1,j}(\kappa)} \begin{bmatrix} 1 & r_{i,i+1,j}(\kappa) \\ r_{i,i+1,j}(\kappa) & 1 \end{bmatrix} \tag{3.8}$$

accounts for the partial transmission and reflection and the propagation matrix

$$P^i(\kappa) = \begin{bmatrix} \mathrm{e}^{-\mathrm{i}k_{z,i}d_i} & 0 \\ 0 & \mathrm{e}^{\mathrm{i}k_{z,i}d_i} \end{bmatrix} \tag{3.9}$$

for the phase shift each plane wave accumulates by passing through layer Λ_i.
In case of multiple interfaces, the upwards and downwards propagating wave amplitudes of any layers Λ_{i_1} and Λ_{i_2}, with $i_1 < i_2$, can be connected via

$$\begin{bmatrix} g^+_{i_1,j}(\kappa,\alpha) \\ g^-_{i_1,j}(\kappa,\alpha) \end{bmatrix} = I_j^{i_1,i_2}(\kappa) \begin{bmatrix} g^+_{i_2,j}(\kappa,\alpha) \\ g^-_{i_2,j}(\kappa,\alpha) \end{bmatrix} \tag{3.10}$$

with

$$I_j^{i_1,i_2}(\kappa) = I_j^{i_1,i_1+1}(\kappa) I_j^{i_1+1,i_1+2}(\kappa) \dots I_j^{i_2-2,i_2-1}(\kappa) I_j^{i_2-1,i_2}(\kappa). \tag{3.11}$$

3.1.2 Scattering matrix method

The transfer matrix allows to connect the upwards and downwards propagating plane-wave spectra of two layers. However, in case of evanescent waves with strongly decaying field amplitudes, the transfer matrix scheme is known to be unstable [70]. In our case of light scattering in planar, layered environments, these evanescent wave spectra play a crucial role, since most plane-wave expansions arise from a transformation of scattered spherical waves (cf. equation (2.40)). To achieve a better stability for evanescent waves, one can make use of the scattering matrix scheme.
In contrast to the transfer matrix, the scattering matrix connects the incoming field amplitudes of layers Λ_{i_1} and Λ_{i_2}, i.e. of waves oriented towards the interfaces, with the amplitudes of outgoing waves

$$\begin{bmatrix} g^+_{i_2,j}(\kappa,\alpha) \\ g^-_{i_1,j}(\kappa,\alpha) \end{bmatrix} = S_j^{i_1,i_2}(\kappa) \begin{bmatrix} g^+_{i_1,j}(\kappa,\alpha) \\ g^-_{i_2,j}(\kappa,\alpha) \end{bmatrix}. \tag{3.12}$$

The scattering matrix can be constructed iteratively [70] from one layer to another. Starting with

$$S_j^{i_1,i_1}(\kappa) = \begin{bmatrix} 1 & 0 \\ 0 & 1 \end{bmatrix}, \tag{3.13}$$

the scattering matrix $S' = S_j^{i_1,i+1}(\kappa)$ is constructed form the scattering matrix $S = S_j^{i_1,i}(\kappa)$ of the previous layer and the transfer matrix $I = I^{i,i+1}(\kappa)$ into the next layer

$$S' = \begin{bmatrix} S'_{11} & S'_{12} \\ S'_{21} & S'_{22} \end{bmatrix}, \qquad I = \begin{bmatrix} I_{11} & I_{12} \\ I_{21} & I_{22} \end{bmatrix}, \tag{3.14}$$

with

$$S'_{11} = \frac{S_{11}}{I_{11} - S_{12}I_{21}}, \tag{3.15}$$

$$S'_{12} = \frac{S_{12}I_{22} - I_{12}}{I_{11} - S_{12}I_{21}}, \tag{3.16}$$

$$S'_{21} = S_{22}I_{21}S'_{11} + S_{21}, \tag{3.17}$$

$$S'_{22} = S_{22}I_{21}S'_{12} + S_{22}I_{22}. \tag{3.18}$$

3.1.3 The layer system response

The goal of the simulation framework is to investigate light scattering by particles that are distributed in a layered environment (see figure 3.1). In that sense, a plane wave impinging onto a layer stack from one side, as can be described by the transfer matrix or the scattering matrix, is only a special case. More commonly we face the question of how the electric field of an internal source distributes throughout the layered medium. The source of such an electric field can be a point dipole, radiating power into its environment, but also a particle emitting a scattered field.
In the excitation layer Λ_{exc} the "source-free" condition for the completeness of PVWFs is not fulfilled. Hence, no plane-wave expansion of the electric field exists that holds everywhere in Λ_{exc}. However, to make use of the transfer matrix or the scattering matrix, a plane-wave representation

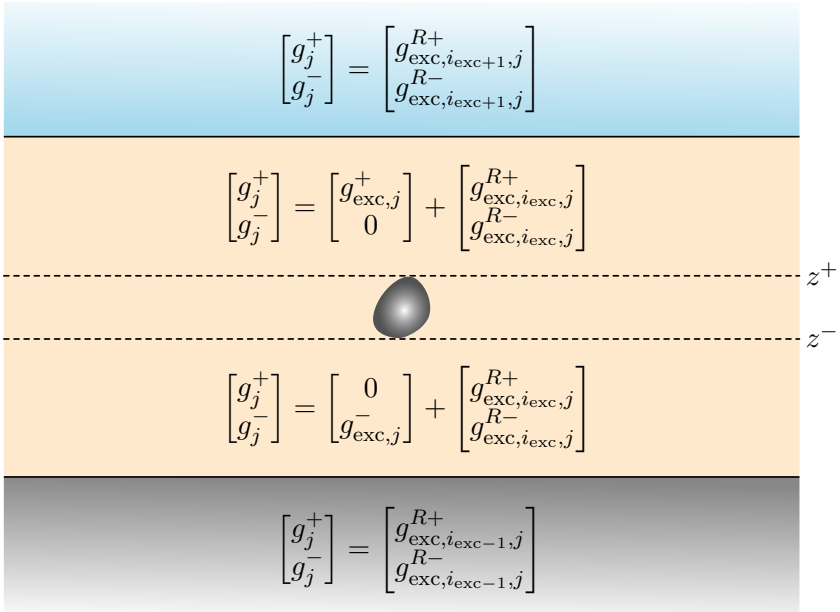

Figure 3.2: An electric field emitted from an excitation source within a planar, layered medium, causes a layer system response. Illustration of the domains of validity of the respective field expansions. The figure is adapted from reference [60].

of the field is only necessary at the interfaces. Egel *et al.* suggest to split the electric field into an *excitation field* $\mathbf{E}_{\mathrm{exc}}$ and its *layer system response* $\mathbf{E}^{\mathrm{R}}_{\mathrm{exc}}$ [60, 71] on top and below of the excitation source

$$\mathbf{E}(\mathbf{r}) = \delta_{ii_{\mathrm{exc}}}\mathbf{E}_{\mathrm{exc}}(\mathbf{r}) + \mathbf{E}^{\mathrm{R}}_{\mathrm{exc}}(\mathbf{r}). \tag{3.19}$$

The excitation field, only valid within the layer of excitation and specified by amplitudes $g^{\pm}_{\mathrm{exc},j}(\kappa,\alpha)$, then reads

$$\mathbf{E}_{\mathrm{exc}}(\mathbf{r}) = \sum_{j=1}^{2}\int_{\mathbb{R}^2} d^2\mathbf{k}_{\parallel} \begin{cases} \mathbf{\Phi}^{+}_{j}(\kappa,\alpha;\mathbf{r}-\mathbf{r}_{i_{\mathrm{exc}}})g^{+}_{\mathrm{exc},j}(\kappa,\alpha) & \text{for } z \geq z^{+} \\ \mathbf{\Phi}^{-}_{j}(\kappa,\alpha;\mathbf{r}-\mathbf{r}_{i_{\mathrm{exc}}})g^{-}_{\mathrm{exc},j}(\kappa,\alpha) & \text{for } z \leq z^{-}, \end{cases} \tag{3.20}$$

with $\mathbf{r} \in \Lambda_{\mathrm{exc}}$ and $z^{\pm}$ bounding the excitation source from atop and from below. The layer system response, piecewise valid throughout the layer system, is specified by amplitudes $g^{\mathrm{R}\pm}_{\mathrm{exc},i,j}(\kappa,\alpha)$ via

$$\mathbf{E}^{\mathrm{R}}_{\mathrm{exc}}(\mathbf{r}) = \sum_{j=1}^{2}\int_{\mathbb{R}^2} d^2\mathbf{k}_{\parallel} \left[\mathbf{\Phi}^{+}_{j}(\kappa,\alpha;\mathbf{r}-\mathbf{r}_i), \mathbf{\Phi}^{-}_{j}(\kappa,\alpha;\mathbf{r}-\mathbf{r}_i)\right] \begin{bmatrix} g^{\mathrm{R}+}_{\mathrm{exc},i,j}(\kappa,\alpha) \\ g^{\mathrm{R}-}_{\mathrm{exc},i,j}(\kappa,\alpha) \end{bmatrix}, \tag{3.21}$$

with $\mathbf{r} \in \Lambda_i$.
To get an overview of the different domains of validity, the composition of fields is illustrated in figure 3.2.
Finally, the layer system response matrix $L^{i,i_{\mathrm{exc}}}_{j}(\kappa)$ connects the layer system response in layer Λ_i with its excitation in layer $\Lambda_{i_{\mathrm{exc}}}$

$$\begin{bmatrix} g^{\mathrm{R}+}_{\mathrm{exc},i,j}(\kappa,\alpha) \\ g^{\mathrm{R}-}_{\mathrm{exc},i,j}(\kappa,\alpha) \end{bmatrix} = L^{i,i_{\mathrm{exc}}}_{j}(\kappa) \begin{bmatrix} g^{+}_{\mathrm{exc},j}(\kappa,\alpha) \\ g^{-}_{\mathrm{exc},j}(\kappa,\alpha) \end{bmatrix}. \tag{3.22}$$

Hereby, it becomes possible to observe how the source of an electric field acts onto another source, e.g., another particle or another point dipole, but also how it effects itself by means of layer interface reflections and interference. A comprehensive derivation of the layer system response matrix and its explicit formulation can be found in references [60, 71].

3.2 The scattering problem

The task of the here presented simulation framework is to determine the electromagnetic field distribution in a planar, layered environment, populated with a distinct distribution of N_S particles that are excited by an initial field.
Within layer Λ_{i_S}, particle S of refractive index n_S occupies the domain $D_S \subset \mathbb{R}^3$, centered around position $\mathbf{r}_S$. D_S is fully bound by the particle's circumscribing sphere of radius $r_{\mathrm{circ},S}$. For now, I assume that no other particle S' nor its circumscribing sphere intersects with one another,

$|\mathbf{d}_{SS'}| > r_{\mathrm{circ},S} + r_{\mathrm{circ},S'}$.
With the definition of the planar, layered environment (cf. section 3.1) and the relation between a field's excitation and its layer response (equation (3.19)), the total electric field can be split into four constituents

$$\mathbf{E}(\mathbf{r}) = \delta_{ii_{\mathrm{init}}}\mathbf{E}_{\mathrm{init}}(\mathbf{r}) + \mathbf{E}^{\mathrm{R}}_{\mathrm{init}}(\mathbf{r}) + \sum_S \left(\delta_{ii_S}\mathbf{E}^S_{\mathrm{sca}}(\mathbf{r}) + \mathbf{E}^{\mathrm{R},S}_{\mathrm{sca}}(\mathbf{r})\right), \qquad \text{for } \mathbf{r} \in \Lambda_i. \tag{3.23}$$

The initial field $\mathbf{E}_{\mathrm{init}}(\mathbf{r})$ represents the field that the initial excitation source would radiate into an infinite homogeneous environment of refractive index $n_{i_{\mathrm{init}}}$. From the four constituents it is the only quantity that is known a priori. Specified by the layer system response matrix, $\mathbf{E}^{\mathrm{R}}_{\mathrm{init}}(\mathbf{r})$ is the initial field's layer system response. In analogy, $\mathbf{E}^S_{\mathrm{sca}}(\mathbf{r})$ denotes the scattered field that particle S emits in layer Λ_{i_S} and $\mathbf{E}^{\mathrm{R},S}_{\mathrm{sca}}(\mathbf{r})$ its respective layer system response.

3.3 Single particle scattering

Outside a particle's circumscribing sphere, the electric field can be expanded in terms of SVWFs (2.30)

$$\mathbf{E}(\mathbf{r}) = \sum_n a^S_n \mathbf{M}^{(1)}_n(\mathbf{r}) + b^S_n \mathbf{M}^{(3)}_n(\mathbf{r}), \tag{3.24}$$

at any position $\mathbf{r} \in \tilde{D}_S$ that fulfills the requirements for the completeness of SVWFs (cf. section 2.3.2 or figure 2.3(b)). The total field consists of the incoming field at particle S,

$$\mathbf{E}^S_{\mathrm{inc}}(\mathbf{r}) = \sum_n a^S_n \mathbf{M}^{(1)}_n(\mathbf{r}) \tag{3.25}$$

and the particle's direct scattered field

$$\mathbf{E}^S_{\mathrm{sca}}(\mathbf{r}) = \sum_n b^S_n \mathbf{M}^{(3)}_n(\mathbf{r}). \tag{3.26}$$

Now the question arises, how a single particle's outgoing field coefficients b^S_n are related to the incoming field coefficients a^S_n.

3.3.1 Transition matrix

Introduced by Peter C. Waterman [55] for a single, perfectly-conducting particle of arbitrary shape, embedded in a homogeneous background medium, the transition matrix (*T-matrix*) denotes the linear operator that connects a particle's incoming field amplitudes to its scattered field

$$b_n^S = \sum_{n'}^{\infty} T_{nn'}^S a_{n'}^S. \tag{3.27}$$

Due to the convergence of the electric field expanded in spherical waves (cf. equation (2.30)), the T-matrix represents a complete description of the single scattering event. For practical reasons, the infinite sum in (2.30) has to be limited to a finite number of contributions. Hence, one has to truncate the T-matrix at a sufficiently large index $n_{\max}$ that contains the multipole degrees $l = 1 \dots l_{\max}$, the multipole orders $m = -m_{\max} \dots m_{\max}$ and the polarizations $\tau = 1, 2$.

In this work, I will consider particles of regular shape only and assume that each particle's T-matrix is precisely known. However, fostered by the wide range of possible particle geometries and materials, the computation of the T-matrix can be a challenging task on its own. Various techniques have been applied for its construction and I will here outline some of them. A comprehensive and continuously updated collection of publications about the T-matrix method can be found in references [72–80].

Extended boundary condition method

Known as the *Extended boundary condition method* (EBCM), Waterman [55] formulated a set of linear relations that exploit the boundary conditions (2.15) to connect a particle's internal field with its incoming and scattered field. The central assumption of the approach is, that the surface currents induced on a particle by an external field must result in an internal field that cancels itself at a position within the scatterer by interference. From here, the boundary conditions can be formulated and it can be shown that the field vanishes everywhere inside the particle [81]. Due to these vanishing fields, the method is also refereed to as the *Null field method* (NFM).
Initially introduced for perfectly-conduction particles, Waterman and others continuously applied the approach to different types of scatterers [81, 82] like dielectric particles or scatterers of cylindrical shape. For spherical particles, the T-matrix reduces to its principle diagonal, for which the elements are identical with the Mie coefficients [83].

Null field method with discrete sources

Based on the expansion in SVWFs, the EBCM faces poor convergence for particles that strongly deviate from a spherical shape. To improve its stability, the *Null field method with discrete sources*

(NFMDS) [63] utilizes a finite set of equivalent sources for the field construction. Especially helpful for flat or strongly elongated particles, the multipole sources can be distributed along a particle's axis of symmetry and can even be positioned on the axis' extend in the complex plane [84].
For the here presented work, the NFMDS is especially important as it provides the T-matrix for all nonspherical particles. Doicu *et al.* have published a *Fortran* code for different homogeneous, axis-symmetric, dielectric and metallic particles but also for inhomogeneous and layered particles [63]. A copy of which is directly distributed within SMUTHI.
Please note that the order of variation of the here applied multi-index n follows a different logic compared to the index arrangement of the T-matrix provided by Doicu's *Fortran* code. In general, the T-matrix' element arrangement is not unique. A careful rearrangement between different notations can be necessary.

Further techniques

Besides the null field methods, a variety of different numerical techniques have been applied to construct the T-matrix of different particle geometries. In fact, the linear operator can be constructed from any numerical method that is applied to solve the Maxwell equations. Examples span from the discrete dipole approximation [85] to the FEM [86] and volume integral equation methods [59]. For more complex scattering geometries it can even be desirable to combine different methods like the FEM and the surface integral equation method [87].

3.3.2 T-matrix of nonspherical particles

With the introduction of nonspherical particles, a scatterer's T-matrix becomes dependent on its orientation in space with respect to the laboratory coordinate system. Hence, one has to take the particle's orientation into account when computing its T-matrix. For particle arrangements consisting of a multitude of identical particles but different orientations, it is beneficial to construct each particle's T-matrix from one specified orientation, making use of the rotation addition theorem for SVWFs (cf. section 2.3.3), rather than a construction for each individual particle orientation.
In a matrix-vector notation, the T-matrix $\mathbf{T}$ provides the linear relation between the incoming field amplitudes $\mathbf{a}$ and the particle's scattered field coefficients $\mathbf{b}$,

$$\mathbf{b} = \mathbf{T}\mathbf{a}. \tag{3.28}$$

This relation remains true in any rotated coordinate system

$$\tilde{\mathbf{b}} = \tilde{\mathbf{T}}\tilde{\mathbf{a}}, \tag{3.29}$$

with tilded symbols denoting the respective quantities in that coordinate system. With the rotation addition theorem (2.37) and (2.38) relating the SVWFs between both, the laboratory coordinate system and the rotated coordinate system, one finds

$$\begin{aligned} \mathbf{a} &= \mathbf{D}^{\mathrm{T}}(\alpha,\beta,\gamma)\tilde{\mathbf{a}}, \\ \tilde{\mathbf{b}} &= \mathbf{D}^{\mathrm{T}}(-\gamma,-\beta,-\alpha)\mathbf{b}. \end{aligned} \tag{3.30}$$

The elements of rotation matrix $\mathbf{D}(\alpha,\beta,\gamma)$ are specified by the Wigner D-functions (cf. equation (A.1))

$$D_{nn'}(\alpha,\beta,\gamma) = D^{l}_{mm'}(\alpha,\beta,\gamma)\delta_{ll'}. \tag{3.31}$$

Inserting (3.30) into (3.28) yields

$$\tilde{\mathbf{T}}(\alpha,\beta,\gamma) = \mathbf{D}^{\mathrm{T}}(-\gamma,-\beta,-\alpha)\mathbf{T}\mathbf{D}^{\mathrm{T}}(\alpha,\beta,\gamma) \tag{3.32}$$

and for the single elements of the rotated particle's T-matrix one obtains [63]

$$\tilde{T}_{lm\tau l'm'\tau'}(\alpha,\beta,\gamma) = \sum_{m_1=-l}^{l}\sum_{m_1'=-l'}^{l'} D^{l}_{m_1 m}(-\gamma,-\beta,-\alpha)T_{lm_1\tau l'm_1'\tau'}D^{l'}_{m'm_1'}(\alpha,\beta,\gamma). \tag{3.33}$$

3.4 The incoming field

The T-matrix equation (3.27) allows to describe the scattered field of a single particle, given that its incoming field is known in terms of SVWFs. However, in a system containing multiple particles, this incoming field does not only depend on the initial field and its layer system response, but also on the scattered field of any other particle S' and their respective layer system responses.
In analogy to equation (3.23), the incoming field of particle S can be split into four constituents

$$\mathbf{E}^{S}_{\mathrm{inc}}(\mathbf{r}) = \delta_{i_S i_{\mathrm{init}}}\mathbf{E}_{\mathrm{init}}(\mathbf{r}) + \mathbf{E}^{\mathrm{R}}_{\mathrm{init}}(\mathbf{r}) + \sum_{S'\neq S}\delta_{i_S i_{S'}}\mathbf{E}^{S'}_{\mathrm{sca}}(\mathbf{r}) + \sum_{S'}\mathbf{E}^{\mathrm{R},S'}_{\mathrm{sca}}(\mathbf{r}) \tag{3.34}$$

with field coefficients

$$a^{S}_{n} = a^{S,\mathrm{init}}_{n} + a^{S,\mathrm{R},\mathrm{init}}_{n} + \sum_{S'}\left(a^{S,S'}_{n} + a^{S,\mathrm{R},S'}_{n}\right). \tag{3.35}$$

In this notation, the superscript has to be read from left to right in a sense that it specifies the receiver of an incoming field and its respective source. Hence, $a^{S,\mathrm{init}}_{n}$ denotes the incoming field amplitudes at particle S directly originating from the initial field source, $a^{S,\mathrm{R},\mathrm{init}}_{n}$ the initial field's layer system response at particle S, $a^{S,S'}_{n}$ the direct field stemming from particle S' and $a^{S,\mathrm{R},S'}_{n}$ the field coefficients at particle S that have been transferred through the layer system and indirectly originate from particle S'.

Please note that the sum over particles S' includes the particle S itself. Although $a_n^{S,S} = 0$, the particles scattered field can contribute to its incoming field via the layer system response.

3.4.1 The initial field

Within the SMUTHI simulation framework, currently three different types of excitation sources are available:

- a propagating plane wave,
- a focused beam,
- a finite number of dipole sources.

In case of the former two source types, the *initial field* originates from afar in terms of a plane-wave expansion that is impinging onto the layered environment from one side of the layer stack. In the latter case, the excitation is given by a set of spherical-wave expansions that originate from within the layered environment.
In the present work, I have not applied any changes to the initial field sources that are available in this simulation framework. Explicit formulas for the computation of the initial field coefficients $a_n^{S,\mathrm{init}}$ and its layer system response $a_n^{S,\mathrm{R,init}}$ exciting particle S for the different types of excitation can be found in reference [60].

3.4.2 Particle coupling

Besides the initial field, any particle can be excited by the scattered field of other particles or by the layer system response of its own scattered field. To yield a particle's incoming field coefficients

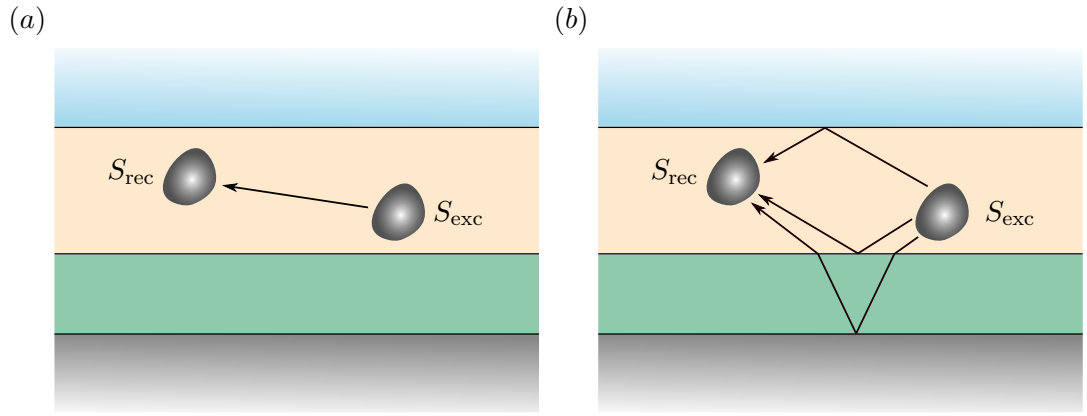

Figure 3.3: Two particles in a layered environment. The scattered field of particle S_{exc} affects the incoming field of particle S_{rec} (a) directly and (b) indirectly by means of a layer system response.

that originate from such a scattered (outgoing) spherical-wave expansion, we distinguish between the direct coupling matrix $W_{nn'}$ and the indirect coupling matrix $W^{\mathrm{R}}_{nn'}$ that accounts for the layer system response

$$a_n^{\mathrm{rec,exc}} + a_n^{\mathrm{rec,R,exc}} = \sum_{n'} \left(W_{nn'}(\mathbf{r}_{\mathrm{rec}}, \mathbf{r}_{\mathrm{exc}}) + W^{\mathrm{R}}_{nn'}(\mathbf{r}_{\mathrm{rec}}, \mathbf{r}_{\mathrm{exc}}) \right) b_{n'}^{\mathrm{exc}}. \tag{3.36}$$

An illustration of two different contributions can be found in figure 3.3.

3.4.2.1 Direct particle coupling

According to equation (3.34), the direct coupling between two particles is only defined for particles within the same layer. In this layer, a spherical-wave expansion originating from a position $\mathbf{r}_{\mathrm{exc}}$ reads (cf. equation (3.26))

$$\mathbf{E}_{\mathrm{exc}}(\mathbf{r}) = \sum_{n'} b_{n'}^{\mathrm{exc}} \mathbf{M}^{(3)}_{n'}(\mathbf{r} - \mathbf{r}_{\mathrm{exc}}). \tag{3.37}$$

Utilizing the translation addition theorem (2.33), the same electric field can be expanded in terms of an incoming field expansion centered at position $\mathbf{r}_{\mathrm{rec}}$

$$\begin{aligned} \mathbf{E}_{\mathrm{exc}}(\mathbf{r}) &= \sum_{n'} b_{n'}^{\mathrm{exc}} \sum_{n} A_{n'n}(\mathbf{r}_{\mathrm{rec}} - \mathbf{r}_{\mathrm{exc}}) \mathbf{M}^{(1)}_{n}(\mathbf{r} - \mathbf{r}_{\mathrm{rec}}) \\ &= \sum_{n} a_n^{\mathrm{rec,exc}} \mathbf{M}^{(1)}_{n}(\mathbf{r} - \mathbf{r}_{\mathrm{rec}}), \end{aligned} \tag{3.38}$$

for $|\mathbf{r} - \mathbf{r}_{\mathrm{rec}}| < |\mathbf{r}_{\mathrm{exc}} - \mathbf{r}_{\mathrm{rec}}|$.
Hereby, one obtains the field coefficients $a_n^{\mathrm{rec,exc}}$ that directly originate from an outgoing excitation field

$$a_n^{\mathrm{rec,exc}} = \sum_{n'} A_{n'n}(\mathbf{r}_{\mathrm{rec}} - \mathbf{r}_{\mathrm{exc}}) b_{n'}^{\mathrm{exc}}, \tag{3.39}$$

and the direct coupling matrix elements

$$W_{nn'}(\mathbf{r}_{\mathrm{rec}}, \mathbf{r}_{\mathrm{exc}}) = A_{n'n}(\mathbf{r}_{\mathrm{rec}} - \mathbf{r}_{\mathrm{exc}}). \tag{3.40}$$

3.4.2.2 Indirect particle coupling

To find the layer system response at a position $\mathbf{r}_{\mathrm{rec}}$ that originates from an outgoing spherical-wave expansion centered around $\mathbf{r}_{\mathrm{exc}}$, we again start with equation (3.37). With a transformation into PVWFs (2.40) and a translation to the layer anchor point $\mathbf{r}_{i_{\mathrm{exc}}}$, the electric field takes the form

$$\begin{aligned}\mathbf{E}_{\mathrm{exc}}(\mathbf{r}) &= \sum_{n'} b_{n'}^{\mathrm{exc}} \mathbf{M}_{n'}^{(3)}(\mathbf{r}-\mathbf{r}_{\mathrm{exc}}) \\ &= \frac{1}{2\pi}\sum_{j=1}^{2}\sum_{n'} b_{n'}^{\mathrm{exc}} \int_{\mathbb{R}^2} \frac{d^2\mathbf{k}_\parallel}{k_{z,i_{\mathrm{exc}}} k_{i_{\mathrm{exc}}}} \mathrm{e}^{\mathrm{i}m'\alpha} B_{n'j}\left(\pm\frac{k_{z,i_{\mathrm{exc}}}}{k_{i_{\mathrm{exc}}}}\right) \\ &\qquad \times \mathrm{e}^{-\mathrm{i}\mathbf{k}_{i_{\mathrm{exc}}}^{\pm}(\mathbf{r}_{\mathrm{exc}}-\mathbf{r}_{i_{\mathrm{exc}}})} \mathbf{\Phi}_j^{\pm}(\kappa,\alpha;\mathbf{r}-\mathbf{r}_{i_{\mathrm{exc}}}) \qquad \text{for } z \gtrless z_{\mathrm{exc}}.\end{aligned} \tag{3.41}$$

Introducing

$$\beta_{\mathrm{exc},n,j}^{\pm}(\kappa) = \mathrm{e}^{\mp k_{z,i_{\mathrm{exc}}}(z_{\mathrm{exc}}-z_{i_{\mathrm{exc}}})} B_{nj}\left(\pm\frac{k_{z,i_{\mathrm{exc}}}}{k_{i_{\mathrm{exc}}}}\right) \tag{3.42}$$

to split the translation into its vertical and horizontal components, yields

$$\begin{aligned}\mathbf{E}_{\mathrm{exc}}(\mathbf{r}) = \frac{1}{2\pi}\sum_{j=1}^{2}\sum_{n'} b_{n'}^{\mathrm{exc}} \int_{\mathbb{R}^2} \frac{d^2\mathbf{k}_\parallel}{k_{z,i_{\mathrm{exc}}} k_{i_{\mathrm{exc}}}} \mathrm{e}^{\mathrm{i}m'\alpha} \mathrm{e}^{-\mathrm{i}\mathbf{k}_\parallel(\mathbf{r}_{\mathrm{exc},\parallel}-\mathbf{r}_{i_{\mathrm{exc}},\parallel})} \\ \times \beta_{\mathrm{exc},n',j}^{\pm}(\kappa)\mathbf{\Phi}_j^{\pm}(\kappa,\alpha;\mathbf{r}-\mathbf{r}_{i_{\mathrm{exc}}}).\end{aligned} \tag{3.43}$$

Now, equation (3.43) has the form of (3.20) with the plane wave amplitudes

$$g_{\mathrm{exc},j}^{\pm}(\kappa,\alpha) = \frac{1}{2\pi}\frac{\mathrm{e}^{-\mathrm{i}\mathbf{k}_\parallel\mathbf{r}_{\mathrm{exc},\parallel}}}{k_{z,i_{\mathrm{exc}}}k_{i_{\mathrm{exc}}}} \sum_{n'} b_{n'}^{\mathrm{exc}} \mathrm{e}^{\mathrm{i}m'\alpha} \beta_{\mathrm{exc},n',j}^{\pm}(\kappa). \tag{3.44}$$

With the definition of the layer system response (equations (3.21) and (3.22)), one finds the electric field in layer $\Lambda_{i_{\mathrm{rec}}}$ that results from the layer system response of the outgoing spherical-wave expansion in layer $\Lambda_{i_{\mathrm{exc}}}$

$$\mathbf{E}_{\mathrm{exc}}^{\mathrm{R}}(\mathbf{r}) = \sum_{j=1}^{2}\int_{\mathbb{R}^2} d^2\mathbf{k}_\parallel \left[\mathbf{\Phi}_j^{+}(\kappa,\alpha;\mathbf{r}-\mathbf{r}_{i_{\mathrm{rec}}}), \mathbf{\Phi}_j^{-}(\kappa,\alpha;\mathbf{r}-\mathbf{r}_{i_{\mathrm{rec}}})\right] \begin{bmatrix} g_{\mathrm{exc},i_{\mathrm{rec}},j}^{\mathrm{R}+}(\kappa,\alpha) \\ g_{\mathrm{exc},i_{\mathrm{rec}},j}^{\mathrm{R}-}(\kappa,\alpha)\end{bmatrix} \tag{3.45}$$

with

$$\begin{bmatrix} g_{\mathrm{exc},i_{\mathrm{rec}},j}^{\mathrm{R}+}(\kappa,\alpha) \\ g_{\mathrm{exc},i_{\mathrm{rec}},j}^{\mathrm{R}-}(\kappa,\alpha)\end{bmatrix} = \frac{1}{2\pi}\frac{\mathrm{e}^{-\mathrm{i}\mathbf{k}_\parallel\mathbf{r}_{\mathrm{exc},\parallel}}}{k_{z,i_{\mathrm{exc}}}k_{i_{\mathrm{exc}}}} \sum_{n'} b_{n'}^{\mathrm{exc}} \mathrm{e}^{\mathrm{i}m'\alpha} L_j^{i_{\mathrm{rec}},i_{\mathrm{exc}}}(\kappa) \begin{bmatrix} \beta_{\mathrm{exc},n',j}^{+}(\kappa) \\ \beta_{\mathrm{exc},n',j}^{-}(\kappa)\end{bmatrix}. \tag{3.46}$$

Next, the layer system response is translated to the desired position $\mathbf{r}_{\mathrm{rec}}$

$$\mathbf{E}^{\mathrm{R}}_{\mathrm{exc}}(\mathbf{r}) = \sum_{j=1}^{2} \int_{\mathbb{R}^2} d^2\mathbf{k}_{\parallel} \Big[\mathrm{e}^{\mathrm{i}\mathbf{k}^{+}_{i_{\mathrm{rec}}}(\mathbf{r}_{\mathrm{rec}}-\mathbf{r}_{i_{\mathrm{rec}}})} \mathbf{\Phi}^{+}_{j}(\kappa,\alpha;\mathbf{r}-\mathbf{r}_{i_{\mathrm{rec}}}), \\ \mathrm{e}^{\mathrm{i}\mathbf{k}^{-}_{i_{\mathrm{rec}}}(\mathbf{r}_{\mathrm{rec}}-\mathbf{r}_{i_{\mathrm{rec}}})} \mathbf{\Phi}^{-}_{j}(\kappa,\alpha;\mathbf{r}-\mathbf{r}_{i_{\mathrm{rec}}}) \Big] \begin{bmatrix} g^{\mathrm{R}+}_{\mathrm{exc},i_{\mathrm{rec}},j}(\kappa,\alpha) \\ g^{\mathrm{R}-}_{\mathrm{exc},i_{\mathrm{rec}},j}(\kappa,\alpha) \end{bmatrix}. \tag{3.47}$$

Utilizing equation (2.39) to retransform the PVWFs into SVWFs and introducing

$$\beta^{\pm,\dagger}_{\mathrm{rec},n,j}(\kappa) = \mathrm{e}^{\pm k_{z,i_{\mathrm{rec}}}(z_{\mathrm{rec}}-z_{i_{\mathrm{rec}}})} B^{\dagger}_{nj}\left(\pm\frac{k_{z,i_{\mathrm{rec}}}}{k_{i_{\mathrm{rec}}}}\right) \tag{3.48}$$

yields

$$\begin{aligned} \mathbf{E}^{\mathrm{R}}_{\mathrm{exc}}(\mathbf{r}) &= 4\sum_{j=1}^{2}\sum_{n}\int_{\mathbb{R}^2} d^2\mathbf{k}_{\parallel}\mathrm{e}^{-\mathrm{i}m\alpha}\mathrm{e}^{\mathrm{i}\mathbf{k}_{\parallel}\mathbf{r}_{\mathrm{rec},\parallel}} \\ &\quad\times\left[\beta^{+,\dagger}_{\mathrm{rec},n,j}(\kappa),\beta^{-,\dagger}_{\mathrm{rec},n,j}(\kappa)\right]\begin{bmatrix} g^{\mathrm{R}+}_{\mathrm{exc},i_{\mathrm{rec}},j}(\kappa,\alpha) \\ g^{\mathrm{R}-}_{\mathrm{exc},i_{\mathrm{rec}},j}(\kappa,\alpha)\end{bmatrix}\mathbf{M}^{(1)}_{n'}(\mathbf{r}-\mathbf{r}_{\mathrm{rec}}) \\ &= \sum_{n} a^{\mathrm{rec,R,exc}}_{n}\mathbf{M}^{(1)}_{n}(\mathbf{r}-\mathbf{r}_{\mathrm{rec}}). \end{aligned} \tag{3.49}$$

Inserting (3.46), one finally obtains the incoming field coefficients at a position $\mathbf{r}_{\mathrm{rec}}$ that result from the layer system response of an outgoing spherical-wave expansion centered around $\mathbf{r}_{\mathrm{exc}}$ (cf. figure 3.3(b))

$$\begin{aligned} a^{\mathrm{rec,R,exc}}_{n} &= \frac{2}{\pi}\sum_{j=1}^{2}\sum_{n'} b^{\mathrm{exc}}_{n'}\int_{\mathbb{R}^2}\frac{d^2\mathbf{k}_{\parallel}}{k_{z,i_{\mathrm{exc}}}k_{i_{\mathrm{exc}}}}\mathrm{e}^{\mathrm{i}(m'-m)\alpha}\mathrm{e}^{\mathrm{i}\mathbf{k}_{\parallel}(\mathbf{r}_{\mathrm{rec},\parallel}-\mathbf{r}_{\mathrm{exc},\parallel})} \\ &\quad\times\left[\beta^{+,\dagger}_{\mathrm{rec},n,j}(\kappa),\beta^{-,\dagger}_{\mathrm{rec},n,j}(\kappa)\right]L^{i_{\mathrm{rec}},i_{\mathrm{exc}}}_{j}(\kappa)\begin{bmatrix}\beta^{+}_{\mathrm{exc},n',j}(\kappa) \\ \beta^{-}_{\mathrm{exc},n',j}(\kappa)\end{bmatrix} \\ &= \sum_{n'} W^{\mathrm{R}}_{nn'}(\mathbf{r}_{\mathrm{rec}},\mathbf{r}_{\mathrm{exc}})b^{\mathrm{exc}}_{n'}, \end{aligned} \tag{3.50}$$

and the elements of the response coupling matrix

$$\begin{aligned} W^{\mathrm{R}}_{nn'}(\mathbf{r}_{\mathrm{rec}},\mathbf{r}_{\mathrm{exc}}) &= \frac{2}{\pi}\sum_{j=1}^{2}\int_{\mathbb{R}^2}\frac{d^2\mathbf{k}_{\parallel}}{k_{z,i_{\mathrm{exc}}}k_{i_{\mathrm{exc}}}}\mathrm{e}^{\mathrm{i}(m'-m)\alpha}\mathrm{e}^{\mathrm{i}\mathbf{k}_{\parallel}(\mathbf{r}_{\mathrm{rec},\parallel}-\mathbf{r}_{\mathrm{exc},\parallel})} \\ &\quad\times\left[\beta^{+,\dagger}_{\mathrm{rec},n,j}(\kappa),\beta^{-,\dagger}_{\mathrm{rec},n,j}(\kappa)\right]L^{i_{\mathrm{rec}},i_{\mathrm{exc}}}_{j}(\kappa)\begin{bmatrix}\beta^{+}_{\mathrm{exc},n',j}(\kappa) \\ \beta^{-}_{\mathrm{exc},n',j}(\kappa)\end{bmatrix}. \end{aligned} \tag{3.51}$$

3.5 Multiple scattering

With the incoming field amplitudes a_n^S and the scattered field amplitudes b_n^S of the series expansion (2.30) an infinite number of coefficients are unknown that describe the electric field in the vicinity of each individual particle. However, as noted in section 3.3.1, the series expansion converges, rendering a truncation at a maximal multipole degree $l_{\max}$ sufficient to describe the electric field up to a desired accuracy

$$\sum_{l=1}^{\infty} \rightarrow \sum_{l=1}^{l_{\max}}. \tag{3.52}$$

As a result, each particle can be described by the coefficients $a_1^S \dots a_{n_{\max}}^S$ and $b_1^S \dots b_{n_{\max}}^S$, with $n_{\max} = 2l_{\max}(l_{\max}+2)$. Assuming an identical number of multipoles necessary to construct each particle's incoming and scattered fields, one seeks a total of $4N_S l_{\max}(l_{\max}+2)$ unknowns. In some cases, one can obtain results of identical accuracy also if the maximal multipole order is already truncated at $m_{\max} < l_{\max}$. Doing so, the number of unknowns per particle reduce to $n_{\max} = 2\left(m_{\max}(m_{\max}+2) + (l_{\max}-m_{\max})(2m_{\max}+1)\right)$.
Combining the T-matrix equation (3.27)

$$b_n^S = \sum_{n'}^{\infty} T_{nn'}^S a_{n'}^S$$

and the incoming field equation (3.35)

$$a_n^S = a_n^{S,\mathrm{init}} + a_n^{S,\mathrm{R,init}} + \sum_{S'}\sum_{n'} \left(W_{nn'}(\mathbf{r}_S, \mathbf{r}_{S'}) + W_{nn'}^{\mathrm{R}}(\mathbf{r}_S, \mathbf{r}_{S'})\right) b_{n'}^{S'}$$

removes the incoming field coefficients that depend on the scattered field of other particles and yields a self-consistent set of linear equations for the scattered field coefficients

$$\sum_{S'}\sum_{n'} M_{nn'}^{SS'} b_{n'}^{S'} = \sum_{n'} T_{nn'}^S \left(a_{n'}^{S,\mathrm{init}} + a_{n'}^{S,\mathrm{R,init}}\right), \tag{3.53}$$

with

$$M_{nn'}^{SS'} = \delta_{SS'}\delta_{nn'} - \sum_{n''} T_{nn''}^S \left(W_{n''n'}(\mathbf{r}_S, \mathbf{r}_{S'}) + W_{n''n'}^{\mathrm{R}}(\mathbf{r}_S, \mathbf{r}_{S'})\right). \tag{3.54}$$

Solving the linear set of equations (3.53) constitutes the core task of the presented simulation framework. Its solution provides the scattered field coefficients of each individual particle that fully describe the particle system and render it possible to derive a variety of near- and far-field properties that can be used to characterize the light transport in large particle arrangements in a planar, layered environment.

3.6 Automated multipole selection

Prior to any simulation, each particle requires the selection of an appropriate maximal multipole degree $l_{\max}$ and multipole order $m_{\max}$, that allows to obtained scattered fields of a desired accuracy. To simplify the selection, an automatic selection procedure is desired, which becomes especially useful in the case of arbitrary particle size distributions.
In the past, a number of such automated criterions have been used to decide at which point the series expansion of spherical waves (2.30), describing the incoming and scattered fields of each particle, can be safely truncated without endangering the respective accuracy constraints. Performing Mie calculations of large, absorbing spheres, Jitendra V. Dave e.g. decided to stop the summation, once the sum of squared Mie coefficients undergoes a value 10^{-14} [88]. Another popular example is Wiscombe's criterion [89] based on an empirical formula to predict the number of necessary summands a prioir, without the need to actually compute those. A convergence test based on Wiscombe's criterion is also provided by the Fortan code [63] that is used in this work for the evaluation of T-matrices of nonspherical particles. Seeking even higher accuracy, an extension of this criterion can be found in reference [90]. Finally, specialized criterions for specific particle shapes like spheroids have been developed [91]. All of these examples have in common that they are mostly concerned with single particle scattering of highest precision with a residual in the range of 10^{-10} to 10^{-100}. However, the multipole degree necessary to achieve such precision, and herewith the number of unknowns allocated to a single particle, are way beyond the quantities that can be practically used in multiple particle scattering and are therefore not applicable.

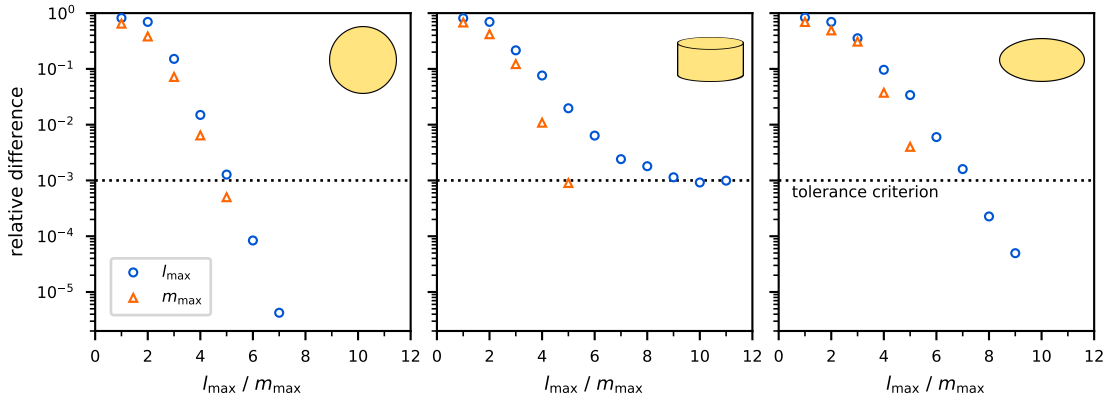

Figure 3.4: Automated selection of the maximal multipole degree $l_{\max}$ and multipole order $m_{\max}$ of a dielectric sphere, cylinder and spheroid of constant volume.

In this work, I have set up an iterative scheme that successively compares the entries of a particle's T-matrix $\mathbf{T}(l_{\max}-1, m_{\max}-1)$ with a pendant of higher accuracy $\mathbf{T}(l_{\max}, m_{\max})$. Once a desired relative difference of matrix norm

$$\epsilon(l_{\max}, m_{\max}) = \frac{\|\mathbf{T}(l_{\max}, m_{\max}) - \mathbf{T}(l_{\max}-1, m_{\max}-1)\|}{\|\mathbf{T}(l_{\max}, m_{\max})\|} \tag{3.55}$$

is obtained, the maximal multipole order and degree is selected. Since SMUTHI allows to choose multipole orders smaller than the multipole degree ($m_{\max} \leq l_{\max}$), first the maximal multipole degree is determined, setting $m_{\max} = l_{\max}$. Once $l_{\max}$ is selected, the multipole order is varied until a further increase does not contribute to a better precision.
Figure 3.4 exemplarily shows the convergence of a particle's T-matrix as a function of the maximal multipole degree and order for a dielectric sphere, cylinder and spheroid of identical volume. Unless stated otherwise, I have used the described automated selection procedure for any involved scatterer, demanding a relative precision of 10^{-3}.

4 Plane-wave coupling

This chapter introduces an alternative formulation of the translation addition theorem for spherical vector wave functions based on an intermediate transformation into plane waves. After briefly describing the Rayleigh hypothesis and the therewith arising difficulty to describe the near-field of nonspherical particles within a single set of vector wave functions, in section 4.2 the plane-wave coupling (PWC) formalism is introduced for arbitrary constellations of nonspherical, convex scatterers. To apply the PWC formalism to large particle clusters, a lookup table approach is formulated for volumetric and planar scattering layers of nonspherical particles (section 4.4). In sections 4.5 and 4.6 a validation of the approach is presented for near- and far-field quantities of light scattering by nonspherical particles. To close the chapter, an overview of competing modeling approaches is given.

The presented formalism has been developed in collaboration with Amos Egel. In part, it has been published in the peer-reviewed journal article ***Phys. Rev. A 96, 033822 (2017)*** *[6] and the preceding articles* ***J. Quant. Spectrosc. Radiat. Transf. 202, 279 (2017)*** *[7] and* ***Opt. Express 24, 25154 (2016)*** *[8].*

The vast majority of analytic and semi-analytic optical models considers nanoparticles to be of perfect spherical shape, although such rarely exist in reality. One could argue that this is simply done due to simplicity, but is often required by a lack of efficient alternatives.
To strengthen the applicability and flexibility of our simulation framework for various light management designs, its extension to nonspherical particles like spheroids and cylinders is inevitable. In principle, the integration of these regular particle shapes is straight forward as a variety of computer codes are publicly available that derive the respective T-matrices (section 3.3.1). However, for multiple scattering scenarios, i.e., two or more particles that couple with each other, the superposition T-matrix scheme is perceived to be limited to spherical particle ensembles or sparse, nonspherical particle distributions. True in general, this perception comes from the limited validity of a long-standing problem known as the *Rayleigh hypothesis*.

4.1 The Rayleigh hypothesis

In essence, the Rayleigh hypothesis [92] states that there exists a series expansion of a particle's scattered field (3.26) that does not only converge beyond the scatterer's circumscribing sphere, but everywhere outside the particle itself. The validity of this hypothesis has been subject of debate for a long time and is still not fully resolved [56, 93]. Following the discussion of Burrows [94], Bates [95] and Millar [96], the Rayleigh hypothesis is found to be valid without restriction, only if all singularities of the interior analytic continuation of the exterior scattered field are located within the largest sphere that is fully located within the particle. Millar finds this sufficient condition of validity by considering an arbitrary nonspherical particle as illustrated in figure 4.1. Assuming the validity of the Rayleigh hypothesis, the scattered field expansion does not only converge outside the particle's circumscribing sphere of radius r_{circ} but everywhere among the particle's surface. If so, this is also the case where the inner sphere of radius r_0 touches the particle surface and as a direct result, everywhere on the inner sphere. However, the particle's interior field converges to the analytic continuation of the exterior scattered field, which is in fact different to the scattered field's series expansion, unless all singularities are located within the inner sphere.
As a result, the applicability of the T-matrix approach has been in question whenever a point of interest is located within the circumscribing sphere of a particle. This can be the case in multiple scattering configurations [97], but also for nonspherical particles close to a surface [98] or near a dipole emitter.

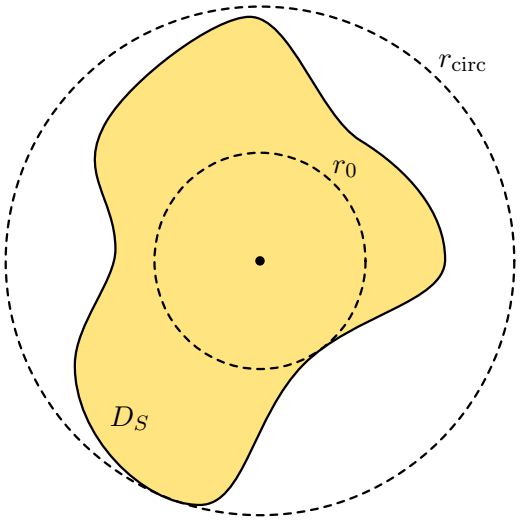

Figure 4.1: A nonspherical particle occupying domain D_S is located completely within the circumscribing sphere of radius r_{circ}. Revolving around the particle center, the largest sphere fully inside the particle has the radius r_0.

4.2 The plane-wave coupling formalism

In this section, I will present an alternative formulation of the translation addition operator for SVWFs to account for particle-particle coupling between nonspherical scatterers in close vicinity. The formulation is based on an intermediate plane-wave expansion of a particle's scattered spherical waves that becomes necessary, whenever the conventional translation addition operator (2.34) cannot resolve the particle coupling correctly. This is the case, if a particle intersects the domain in which the spherical-wave expansion of another particle's scattered field is not valid. As discussed in the previous section, this critical domain is determined by a sphere that revolves around the particle's center and encloses all singularities of the analytic continuation of the particle's exterior scattered field. Determining the locations of these singularities can be difficult. Therefore, I will restrict the discussion to particles that intersect with another particle's circumscribing sphere. Yet, the reader should keep in mind that non-overlapping circumscribing spheres of two scatterers are a sufficient but not a necessary condition to account for the correct particle coupling via the translation addition theorem.

For now I will consider a simple two particle scenario, as illustrated in figure 4.2. Particle S is located in close proximity to particle S' and intersects with its circumscribing sphere of radius r_{circ}. As a result, the translation addition operator for SVWFs is not expected to account for the particle coupling correctly. However, particle S is located entirely below the lower bounding plane ($z = z^-$) of S' and therefore in a domain, in which a plane-wave expansion exists that can resemble any scattered field of particle S'.

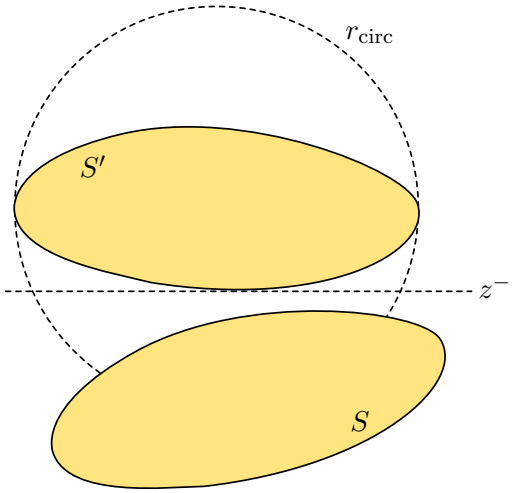

Figure 4.2: Two elongated particles in close vicinity. Particle S intersects the circumscribing sphere of particle S' but is located entirely below its lower bounding plane $z = z^-$. The image has been adopted from reference [12].

To find the coupling operator between the two particles in a close distance, I start with the outgoing SVWF $\mathbf{M}_n^{(3)}(\mathbf{r}-\mathbf{r}_{S'})$ originating from particle S' and expanded in downgoing plane waves (2.40)

$$\mathbf{M}_n^{(3)}(\mathbf{r}-\mathbf{r}_{S'}) = \frac{1}{2\pi}\sum_{j=1}^{2}\int_{\mathbb{R}^2}\frac{d^2\mathbf{k}_\parallel}{k_z k}\mathrm{e}^{\mathrm{i}m\alpha}B_{nj}\left(-\frac{k_z}{k}\right)\mathbf{\Phi}_j^-(\kappa,\alpha;\mathbf{r}-\mathbf{r}_{S'}), \qquad \text{for } z<z^-. \tag{4.1}$$

Now, a translation to the center of particle S

$$\mathbf{M}_n^{(3)}(\mathbf{r}-\mathbf{r}_{S'}) = \frac{1}{2\pi}\sum_{j=1}^{2}\int_{\mathbb{R}^2}\frac{d^2\mathbf{k}_\parallel}{k_z k}\mathrm{e}^{\mathrm{i}m\alpha}B_{nj}\left(-\frac{k_z}{k}\right)\mathrm{e}^{\mathrm{i}\mathbf{k}^-(\mathbf{r}_S-\mathbf{r}_{S'})}\mathbf{\Phi}_j^-(\kappa,\alpha;\mathbf{r}-\mathbf{r}_S) \tag{4.2}$$

and a retransformation into regular spherical waves (2.39) yields

$$\begin{aligned}\mathbf{M}_n^{(3)}(\mathbf{r}-\mathbf{r}_{S'}) = \frac{2}{\pi}\sum_{j=1}^{2}\int_{\mathbb{R}^2}\frac{d^2\mathbf{k}_\parallel}{k_z k}\mathrm{e}^{\mathrm{i}m\alpha}B_{nj}\left(-\frac{k_z}{k}\right)\mathrm{e}^{\mathrm{i}\mathbf{k}^-(\mathbf{r}_S-\mathbf{r}_{S'})} \\ \times\sum_{n'}\mathrm{e}^{-\mathrm{i}m'\alpha}B^\dagger_{n'j}\left(-\frac{k_z}{k}\right)\mathbf{M}_{n'}^{(1)}(\mathbf{r}-\mathbf{r}_S).\end{aligned} \tag{4.3}$$

Assuming that one can interchange the order of summation and integration, equation (4.3) has the form of the translation addition theorem (2.33) with $A(\mathbf{r}_S-\mathbf{r}_{S'})$. By comparison, I find

$$A_{nn'}(\mathbf{r}_S-\mathbf{r}_{S'}) = \frac{2}{\pi}\sum_{j=1}^{2}\int_{\mathbb{R}^2}\frac{d^2\mathbf{k}_\parallel}{k_z k}\mathrm{e}^{\mathrm{i}(m-m')\alpha}B_{nj}\left(-\frac{k_z}{k}\right)B^\dagger_{n'j}\left(-\frac{k_z}{k}\right)\mathrm{e}^{\mathrm{i}\mathbf{k}^-(\mathbf{r}_S-\mathbf{r}_{S'})}. \tag{4.4}$$

To allow for an efficient numerical evaluation, one can carry out $\mathbf{k}^-(\mathbf{r}_S-\mathbf{r}_{S'}) = \kappa\rho_{SS'}\cos(\alpha-\varphi_{SS'}) - k_z z_{SS'}$ with $(\rho_{SS'},\varphi_{SS'},z_{SS'})$ being the cylindrical coordinates of $(\mathbf{r}_S-\mathbf{r}_{S'})$

$$\begin{aligned}A_{nn'}(\mathbf{r}_S-\mathbf{r}_{S'}) = \frac{2}{\pi}\sum_{j=1}^{2}\int_0^\infty d\kappa\,\frac{\kappa}{k_z k}B_{nj}\left(-\frac{k_z}{k}\right)B^\dagger_{n'j}\left(-\frac{k_z}{k}\right)\mathrm{e}^{-\mathrm{i}k_z z_{SS'}} \\ \times\int_0^{2\pi}d\alpha\,\mathrm{e}^{\mathrm{i}\kappa\rho_{SS'}\cos(\alpha-\varphi_{SS'})}\mathrm{e}^{\mathrm{i}(m-m')\alpha}\end{aligned} \tag{4.5}$$

and compare with the integral representation of the Bessel function $J_a(x)$ [99]

$$J_{|a|}(x) = \frac{\mathrm{i}^{-|a|}}{2\pi}\int_0^{2\pi}\mathrm{e}^{\mathrm{i}x\cos\phi}\mathrm{e}^{\mathrm{i}a\phi}d\phi \tag{4.6}$$

to find

$$A_{nn'}(\mathbf{r}_S - \mathbf{r}_{S'}) = 4\mathrm{i}^{|m-m'|} \sum_{j=1}^{2} \int_0^\infty d\kappa \, \frac{\kappa}{k_z k} B_{nj}\left(\pm\frac{k_z}{k}\right) B^{\dagger}_{n'j}\left(\pm\frac{k_z}{k}\right) \times \mathrm{e}^{\pm\mathrm{i}k_z z_{SS'}} \mathrm{e}^{\mathrm{i}\varphi_{SS'}(m-m')} J_{|m-m'|}(\kappa\rho_{SS'}), \qquad z_{SS'} \gtrless z^{\pm} - z_{S'}. \tag{4.7}$$

With the analytic evaluation of the azimuthal integral in form of the Bessel function, the coupling operator $W^{SS'}_{nn'} = A_{n'n}(\mathbf{r}_S - \mathbf{r}_{S'})$ reduces to an integration over all propagating and evanescent waves of in-plane wave number κ.
Please note that at the start of this section I have assumed that particle S is located entirely below the lower bounding plane of S'. To also cover the opposite case, I have inserted $\pm$ signs in equation (4.7).

4.2.1 Arbitrary orientations

So far, I have only considered two nonspherical particles in close vicinity that can be separated by a plane that is parallel to the xy-plane. In a more general case it is not to be expected that such a horizontal plane of separation can be found (illustrated in figure 4.3). Since the transformation between spherical waves and plane waves is in principle possible along any plane, a horizontal plane of separation is not strictly necessary. However, a horizontal plane drastically simplifies the transformation procedure due to an integration over in-plane wave vectors that is independent of the wave vector's z-component.

To ensure a plane of separation that is parallel to the xy-plane, the PWC formalism can be performed in a rotated coordinate system (R). Hence, I seek the direct coupling matrix $\mathbf{W}^{SS'}$ in the laboratory coordinate system as a function of the direct coupling matrix $\tilde{\mathbf{W}}^{SS'}$ in a rotated coordinate system and start with the matrix-vector notation

$$\tilde{\mathbf{a}}^S = \tilde{\mathbf{W}}^{SS'} \tilde{\mathbf{b}}^{S'}. \tag{4.8}$$

Utilizing the rotation addition theorem (cf. equations (2.37) and (2.38))

$$\begin{aligned} \mathbf{a} &= \mathbf{D}^{\mathrm{T}}(\alpha,\beta,\gamma)\tilde{\mathbf{a}}, \\ \tilde{\mathbf{b}} &= \mathbf{D}^{\mathrm{T}}(-\gamma,-\beta,-\alpha)\mathbf{b}. \end{aligned} \tag{4.9}$$

with the rotation matrix elements specified by the Wigner D-functions (cf. equation (A.1))

$$D_{nn'}(\alpha,\beta,\gamma) = D^l_{mm'}(\alpha,\beta,\gamma)\delta_{ll'}, \tag{4.10}$$

one inserts equation (4.9) into (4.8) to find

$$\mathbf{a}^S = \mathbf{D}^{\mathrm{T}}(\alpha,\beta,\gamma)\tilde{\mathbf{W}}^{SS'}\mathbf{D}^{\mathrm{T}}(-\gamma,-\beta,-\alpha)\mathbf{b}^{S'}. \tag{4.11}$$

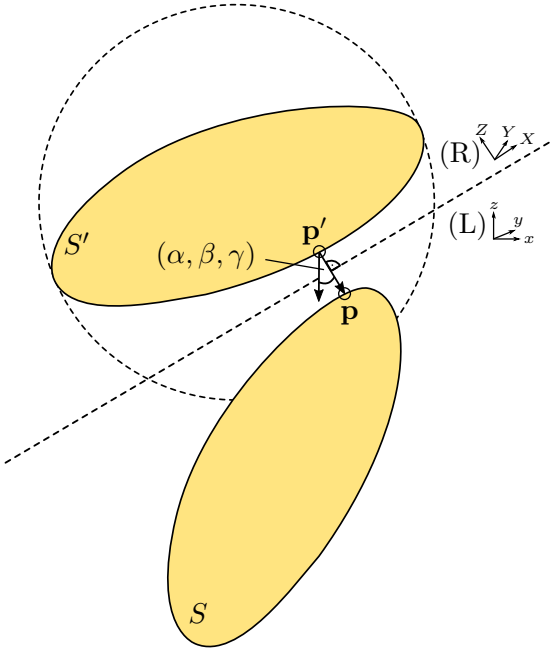

Figure 4.3: Two particles in close vicinity are separated by a plane that is perpendicular to the vector $\overline{\mathbf{p}'\mathbf{p}}$, connecting the two closest points $\mathbf{p}$ and $\mathbf{p}'$ on the particles' surfaces. Rotating $\overline{\mathbf{p}'\mathbf{p}}$ by Euler angles (α, β, γ) into $\pm|\overline{\mathbf{p}'\mathbf{p}}|\hat{\mathbf{e}}_z$ of the laboratory coordinate system (L) ensures a plane of separation that is parallel to the XY-plane of the rotated coordinate system (R). The image has been adopted from reference [12].

Finally, I compare equation (4.11) with

$$\mathbf{a}^S = \mathbf{W}^{SS'}\mathbf{b}^{S'}, \tag{4.12}$$

to obtain

$$\mathbf{W}^{SS'} = \mathbf{D}^{\mathrm{T}}(\alpha, \beta, \gamma)\tilde{\mathbf{W}}^{SS'}\mathbf{D}^{\mathrm{T}}(-\gamma, -\beta, -\alpha). \tag{4.13}$$

As a result, one can perform the PWC formalism for any pair of particles that can be separated by a plane. One strategy to find such a plane of separation is to determine the two locations $\mathbf{p}$ and $\mathbf{p}'$ on the surfaces of particles S and S' that are located closest to each other. For scatterers with a convex surface hull it is ensured that a plane of separation exists to which $\overline{\mathbf{p}'\mathbf{p}}$ is perpendicular. Now, the Euler angles (α, β, γ) rotate $\overline{\mathbf{p}'\mathbf{p}}$ into $\pm|\overline{\mathbf{p}'\mathbf{p}}|\hat{\mathbf{e}}_z$ and (L) into (R). At first glance, finding the positions $\mathbf{p}$ and $\mathbf{p}'$ appears simple. But for arbitrarily oriented, three-dimensional particles, this task can be more challenging than expected. Therefore, I provide the reader with one possible strategy for pairs of spheroidal particles in Appendix B.

4.3 Truncation of the plane-wave spectrum

Although spherical-wave expansions and plane-wave expansions do not exhibit identical domains of validity, the PWC operator for nonspherical scatterers in close vicinity (introduced in section 4.2) and the conventional translation addition operator for SVWFs in fact yield identical results. This comes as no surprise, since the applied transformations (2.39) and (2.40) guarantee the equality of the spherical- and plane-wave expansions, where applicable, i.e., at any point outside the circumscribing sphere that is beyond a scatterer's bounding plane.
In such a domain, the integration over in-plane wave numbers $\int d\kappa$ as well as the summation over multipoles $\sum_{n'}$ both yield finite values and hence the interchange of summation and integration

$$\sum_{n'} \int d\kappa \to \int d\kappa \sum_{n'} \tag{4.14}$$

between equations (2.33) and (4.3) is in general credible.
Here however, I am interested in the scattered field expansion within the circumscribing sphere of a scatterer, where the spherical-wave expansion diverges and the interchange of integration and summation is in general not allowed. To justify the change in integration and summation, one has to ensure that the sum of multipoles has converged for each value of the angular spectrum, rather than a converging angular spectrum for each multipole [8]. In practice, this means that one has to chose the maximal multipole degree $l_{\max}$ large enough that for each $|\mathbf{k}_{\parallel}| < \kappa_{\max}$ the angular spectrum has converged.
In other words, by choosing a small rather than a large cut-off in-plane wave number, one can obtain a converged plane-wave expansion in a domain, where the original outgoing spherical-wave expansion diverges.
At first glance, this seems contradictory. But the benefit of the plane-wave representation of the coupling operator lies in the inherent separation of propagating and evanescent waves.
To clarify this, let us consider an outgoing, scattered spherical-wave expansion. By definition, this expansion converges everywhere outside the scatterers circumscribing sphere, and hence contains the correct information of the scattered far-field. From this, one can conclude that no erroneous propagating field contributions are contained in the spherical-wave expansion. The same field expansion, however, is in general not valid everywhere in the particles near-field, which implies that any error terms must be contained in the evanescent field contributions. The plane-wave expansion allows to cut off these erroneous terms, which can be beneficial, compared to a sum over all in-plane wave numbers.

To illustrate the above, let us consider two oblate silver (Ag) spheroids in close vicinity that are excited by a y-polarized plane wave propagating in negative z-direction at a vacuum wavelength of $\lambda_0 = 500\,\mathrm{nm}$. The spheroids' semimajor axes measure $a = b = 200\,\mathrm{nm}$ and their semiminor axes $c = 50\,\mathrm{nm}$. Embedded in a homogeneous air ambient ($n_{\mathrm{amb}} = 1$), the particles' size corresponds to the dimensionless size parameters of $ka = kb = 2.51$ and $kc = 0.63$ and have a refractive

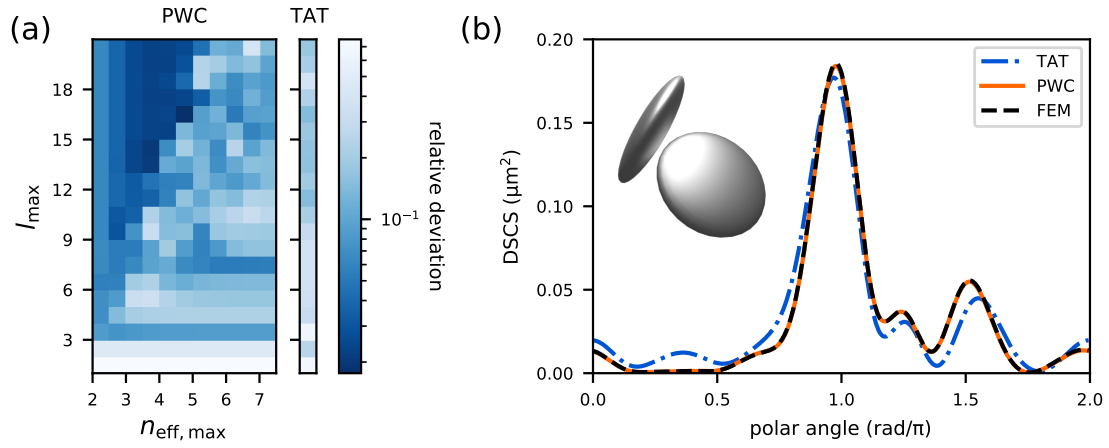

Figure 4.4: (a) Relative deviation of the differential scattering cross section of two oblate Ag spheroids between T-matrix and FEM simulations for different maximal multipole degrees $l_{\max}$: (left) T-matrix simulations based on the plane-wave coupling (PWC) procedure for different truncation of the plane-wave spectrum; (right) based on the conventional translation addition theorem (TAT). (b) Comparison of the differential scattering cross sections along the xz-plane.

index of $n_{\mathrm{p}} = 0.13 + 2.918\mathrm{i}$ [100]. The particles are centered at $c_1 = (-80, 25, 120\,\mathrm{nm})$ and $c_2 = (120, -20, -60\,\mathrm{nm})$ and rotated by Euler angles $(\alpha_1 = 8/9\,\pi, \beta_1 = 1/3\,\pi, \gamma_1 = 0)$ and $(\alpha_2 = 14/9\,\pi, \beta_2 = 5/18\,\pi, \gamma_1 = 0)$ with respect to a spheroid with its semiminor axis aligned along the z-axis. The depicted configuration (inset of figure 4.4(b)) is identical to the example presented in reference [6].

Figure 4.4(a) shows the relative deviation in the differential scattering cross section (DSCS) of the two Ag spheroids between a reference FEM simulation, commercially available in the COMSOL MULTIPHYSICS software [101], and STMM simulations based on both, the PWC procedure (left) and the conventional translation addition theorem (right). T-matrix simulations are shown for maximal multipole degrees $l_{\max} \leq 20$, and in case of PWC for different maximal effective refractive indices

$$n_{\mathrm{eff,max}} = \frac{\kappa_{\max}}{k} \tag{4.15}$$

at which the plane-wave spectrum is truncated.

The depicted results support the previous statements. Given a maximal multipole degree, it is beneficial to truncate the plane-wave spectrum at a lower in-plane wave number, rather than integrating up to stronger decaying evanescent modes. Increasing $l_{\max}$ shifts the erroneous field contributions of the particles' scattered spherical-wave expansions into these stronger decaying evanescent waves and hence allows the integration to a larger in-plane wave number, which is in line with what has been observed for spheroids directly located on a substrate [8]. In contrast, results from the conventional coupling scheme do not fully resemble the reference solution. In this specific example, the relative deviation between the FEM and the conventional scheme does not drop below $10\,\%$, which is one magnitude larger than what is achieved by the PWC procedure.

To highlight the exceptional agreement between T-matrix simulations based on the PWC formalism

(orange, $l_{\max} = 15, n_{\text{eff},\max} = 4$) and FEM results (black, dashed), a cut through the DSCS along the xz-plane is shown in figure 4.4(b), as well as results stemming from the translation addition theorem (blue, dash-dotted, $l_{\max} = 15$).

4.4 Numerical considerations

The alternative formulation of the translation addition operator for SVWFs, introduced in section 4.2, relies on an intermediate transformation into plane waves and vice versa. Computation-wise this might seem unfavorable due to the numerical integration of the angular plane-wave spectrum that becomes necessary. Nevertheless, the PWC scheme does not need to shy away from a performance comparison with the conventional scheme.

To support this claim, figure 4.5(a) compares the computation time of the particle coupling matrix $\mathbf{W}^{SS'}$ between two spheres, located in a clear distance of $|\mathbf{r}_S - \mathbf{r}_{S'}| = 5r_{\text{sphere}}$ to each other, for both coupling schemes and maximal multipole degrees $l_{\max} \leq 20$. Although both spheres are located within one vertical plane ($z_{SS'} = 0$), and hence a coordinate system rotation becomes necessary for PWC, the evaluation of the transformation operators B and $B^\dagger$ (cf. equation (2.41)) only relies on Legendre polynomials, rather than Wigner-3j symbols that are requested for the evaluation of the conventional translation addition operator. Especially in case of large multipole degrees, the PWC formalism surpasses the performance of the conventional scheme, which remains valid for different truncation values of the effective refractive index at $n_{\text{eff},\max} = 3$, 5 and 7.

Due to a clear particle separation in this exemplary configuration, one can expect both coupling schemes to yield identical results. However, to account for high order multipoles one has to ensure that the truncation of the *Sommerfeld integral* is not carried out at too low values of the effective refractive index (see figure 4.5(b)) .

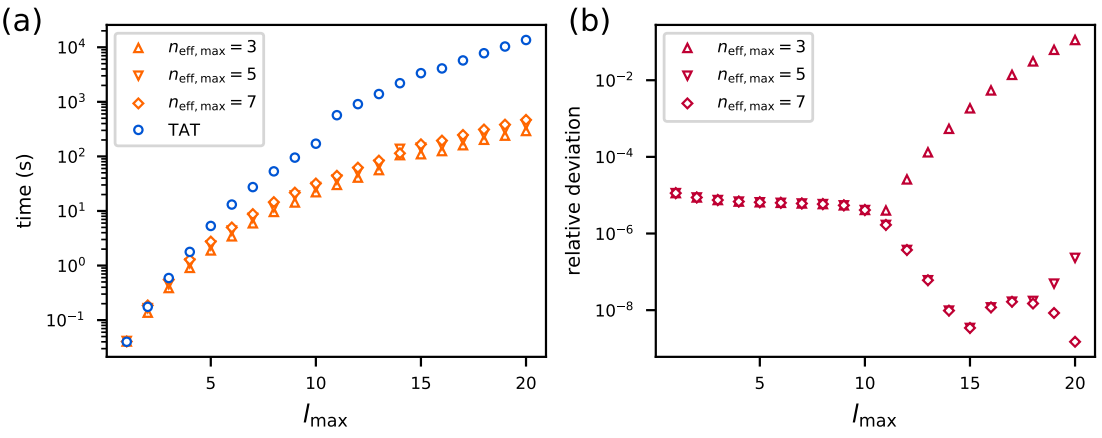

Figure 4.5: (a) Time comparison of the evaluation of direct coupling operators for the plane-wave coupling (PWC) formalism and the conventional translation addition theorem (TAT) based on the Wigner-3j symbols. (b) Relative deviation of coupling matrices evaluated with both schemes.

I would like to note that the here presented time comparison only considers a two-particle system. However, the simulation framework described throughout this work is not built for single particle or low particle-count simulations of highest precision, where large multipole degrees have to be considered. It is likely that more efficient simulation frameworks exist that excel in the direct evaluation of the translation addition operator for SVWFs, and hence outperform the shown computation times. Furthermore, one has to keep in mind that both, result and computation time of the numeric evaluation of the Sommerfeld integral rely on its discretization and upper limit.
Nonetheless, these results emphasize that it can be beneficial to choose the indirect route via plane waves, rather than the conventional translation addition operator for SVWFs, to account for particle coupling between nonspherical but also spherical particles in a clear distance.

4.4.1 Large particle arrangements

To model light propagation in optoelectronic devices, it is necessary to assess the collective scattering response of large disordered particle collections. From a practical point of view, this task comes with two main challenges regarding time and memory. Quadratically scaling with the particle count (or more precisely with the number of multipoles necessary to describe one particle), the evaluation of an immense number of multipole-multipole interactions has to be handled, involving the numerical evaluation of Sommerfeld integrals. In addition, the direct evaluation of the linear set of equations at hand (namely equation (3.53)) rapidly allocates large amounts of the main memory. To cope with both challenges, SMUTHI utilizes a lookup table approach that on one hand allows the interpolation of particle coupling from a discretized set of particle displacements. And on the other hand enables iterative solver schemes for the linear set of equations.
The lookup table approach applied in SMUTHI is based on the idea that the indirect particle coupling (3.51) can be written as

$$W_{nn'}^{S,\mathrm{R},S'} = 4\mathrm{i}^{|m'-m|}\mathrm{e}^{\mathrm{i}\varphi_{SS'}(m'-m)}\sum_{j=1}^{2} I_{jnn'}\left(\rho_{SS'}, z_S, z_{S'}\right), \tag{4.16}$$

with the Sommerfeld integral

$$\begin{aligned} I_{jnn'}\left(\rho_{SS'}, z_S, z_{S'}\right) = \int_0^\infty d\kappa \frac{\kappa}{k_{z,i_S} k_{i_{S'}}} J_{|m'-m|}(\kappa\rho_{SS'}) \\ \times \left[\beta^{+,\dagger}_{S,n,j}(\kappa), \beta^{-,\dagger}_{S,n,j}(\kappa)\right] L_j^{i_S,i_{S'}}(\kappa) \begin{bmatrix} \beta^{+}_{S',n',j}(\kappa) \\ \beta^{-}_{S',n',j}(\kappa) \end{bmatrix}. \end{aligned} \tag{4.17}$$

In the above, the azimuthal integral is expressed in terms of Bessel functions (cf. equation (4.6)). Assuming that all particles are located within the same layer $i_S = i_{S'}$, the Sommerfeld integral can be split into two contributions, one depending on $z_S + z_{S'}$ and the other on $z_S - z_{S'}$ [60]

$$I_{jnn'}\left(\rho_{SS'}, z_S, z_{S'}\right) = I^{+}_{jnn'}\left(\rho_{SS'}, z_S + z_{S'}\right) + I^{-}_{jnn'}\left(\rho_{SS'}, z_S - z_{S'}\right) \tag{4.18}$$

with

$$I^{\pm}_{jnn'}\left(\rho, z\right) = \int_0^\infty d\kappa \frac{\kappa}{k_z k} J_{|m'-m|}(\kappa\rho) f^{\pm}_{jnn'}(z). \tag{4.19}$$

4.4.2 Volumetric lookup for plane-wave coupling

Conceptually, the PWC formalism, based on a transformation-translation-transformation scheme, does not differ too much from the translation-transformation-layer mediated translation-transformation scheme that is applied for indirect particle coupling. Comparing the PWC operator

$$\begin{aligned} W^{SS'}_{nn'} &= 4\mathrm{i}^{|m'-m|}\mathrm{e}^{\mathrm{i}\varphi_{SS'}(m'-m)} \sum_{j=1}^{2} \int_0^\infty d\kappa \, \frac{\kappa}{k_z k} J_{|m'-m|}(\kappa\rho_{SS'}) \\ &\qquad \times \mathrm{e}^{\pm\mathrm{i}k_z z_{SS'}} B_{n'j}\left(\pm\frac{k_z}{k}\right) B^{\dagger}_{nj}\left(\pm\frac{k_z}{k}\right) \\ &= 4\mathrm{i}^{|m'-m|}\mathrm{e}^{\mathrm{i}\varphi_{SS'}(m'-m)} \sum_{j=1}^{2} \tilde{I}_{jnn'}\left(\rho_{SS'}, z_S, z_{S'}\right) \end{aligned} \tag{4.20}$$

with equation (4.16), it comes with no surprise that both have the same form, but this time with

$$\tilde{I}_{jnn'}\left(\rho_{SS'}, z_S, z_{S'}\right) = \tilde{I}^{\pm}_{jnn'}\left(\rho_{SS'}, z_S - z_{S'}\right) = \int_0^\infty d\kappa \frac{\kappa}{k_z k} J_{|m'-m|}(\kappa\rho_{SS'}) \tilde{f}^{\pm}_{jnn'}(z_S - z_{S'}) \tag{4.21}$$

and

$$\tilde{f}^{\pm}_{jnn'}(z) = \mathrm{e}^{\pm\mathrm{i}k_z z} B_{n'j}\left(\pm\frac{k_z}{k}\right) B^{\dagger}_{nj}\left(\pm\frac{k_z}{k}\right). \tag{4.22}$$

In comparison to the indirect coupling operator, the direct PWC only requires a single Sommerfeld integral of either upwards or downwards oriented plane waves for $z_S - z_{S'}$.

To assess the additional cost that comes with a lookup table for direct PWC, let us consider two copies of the largest nonspherical particle within a particle arrangement (see figure 4.6). Assuming intersecting circumscribing spheres as the necessary condition for PWC, one can possibly draw an advantage from the alternative coupling formalism only, if the two particle centers are located within a displacement of $|\mathbf{r}_S - \mathbf{r}_{S'}| \leq 2r_{\mathrm{circ,max}}$. Independent of the exact direction of lateral displacement ρ, the Sommerfeld integrals (4.21) stored in a lookup table, in general only need to cover a point pattern of $(\rho_i, \Delta z_i)$ that discretizes a half circle of radius $2r_{\mathrm{circ,max}}$. By always applying a coordinate system rotation, one can enforce that for all possible configurations particle S

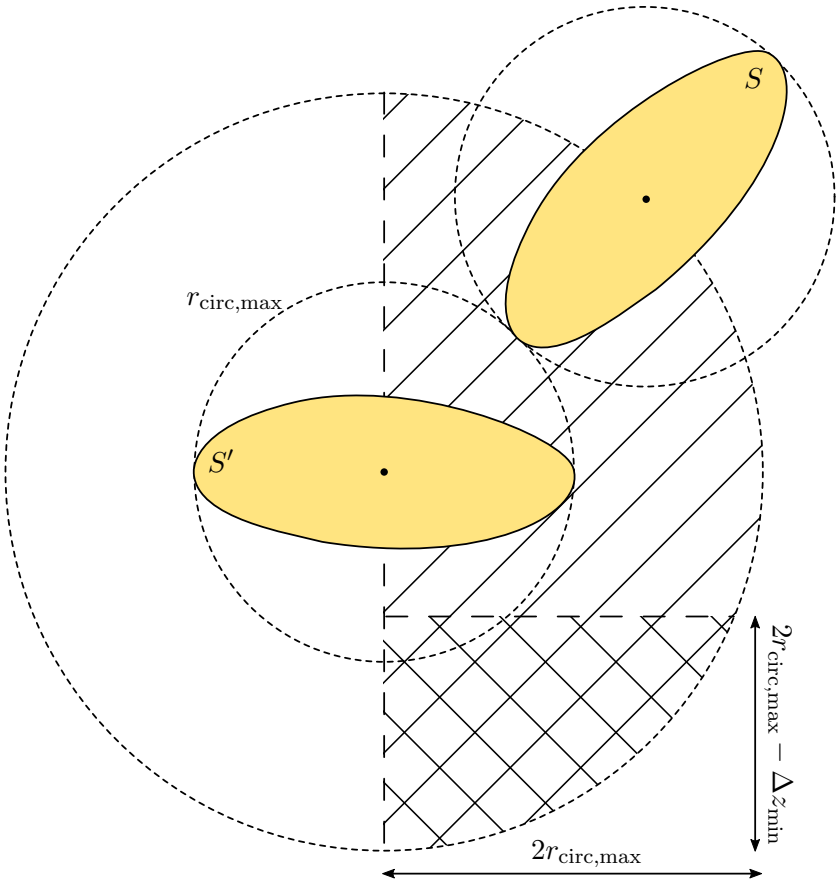

Figure 4.6: The plane-wave coupling formalism is beneficial for particles in close vicinity. Depending on the choice of rotations, the particle coupling is precalculated and stored in a lookup table only for a point patter $(\rho_i, \Delta z_i)$ in a small fraction of the scatterers surrounding.

is located below S' in the rotated coordinate system [1]. Finally, particles are not allowed to overlap, which reduces possible vertical displacement by a minimal vertical separation of Δz_{min}.

In comparison to the lookup tables of direct and indirect particle coupling, covering particle displacements of the maximal lateral and maximal vertical distances ρ_{max} and Δz_{max} within a particle arrangement, the additional lookup table only needs to discretize an area of $2r_{\mathrm{circ,max}}(2r_{\mathrm{circ,max}} - \Delta z_{\mathrm{min}})$ [2]. This area constitutes only a negligible fraction of what is necessary for the generally applied lookup tables.

From here, I conclude that from a preparation and storage point of view, a lookup table to account for particle coupling between nonspherical particles in close vicinity leads to comparably small additional cost. However, such a lookup table can only cover the particle interaction in each particle-particle-specific, rotated coordinate system. Once the interaction is interpolated from the lookup table, the coordinate transformation (4.13) still needs to be applied.

[1] Equally well, one could enforce S to be located above S'.

[2] From a practical point of view one allocates a matrix of rectangular shape.

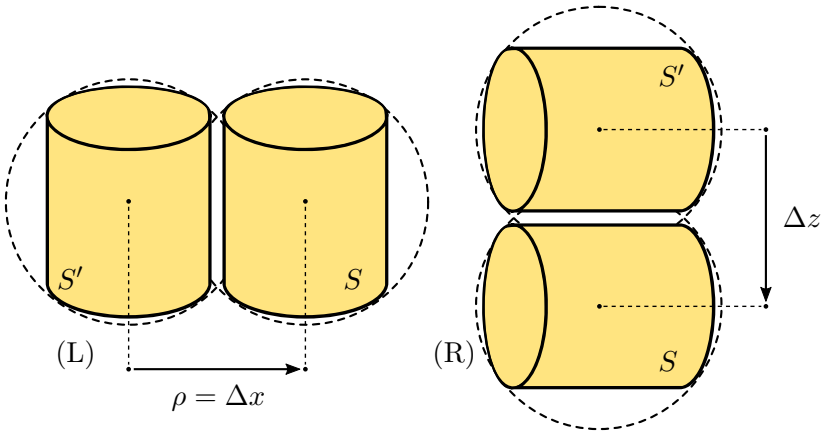

Figure 4.7: The lateral displacement $\rho = \Delta x$ in the laboratory coordinate system (L) of two cylinders in close vicinity translates into a vertical displacement Δz in the rotated coordinate system (R).

4.4.3 Radial lookup

For particle arrangements distributed along a horizontal plane, the Sommerfeld integral becomes independent of the particles' vertical positions $z_S = z_{S'} = z$. As a result, only a one dimensional lookup needs to be applied, which strongly reduces memory allocation and allows for a one dimensional interpolation scheme. Besides these advantages, the planar scattering layer allows to integrate the coordinate system rotation already within the lookup table. For flat particle arrangements, such a rotation is strictly necessary to ensure the horizontal plane of separation that enables the formalism (cf. section 4.2.1).
Any lateral displacement $\rho = |\mathbf{r_S} - \mathbf{r_{S'}}|$ can be interpreted as a one dimensional displacement along x. Then, a coordinate system rotation by Euler angles $(\alpha, \beta, \gamma) = (0, -\pi/2, 0)$ translates the lateral displacement into a strictly vertical displacement Δz (cf. figure 4.7). Hence, one has to evaluate the Sommerfeld integral

$$\tilde{I}_{jnn'}\left(\rho_{SS'}, z_S, z_{S'}\right) = \tilde{I}^{\pm}_{jnn'}\left(\rho_{SS'}\right) = \int_0^\infty d\kappa \frac{\kappa}{k_z k} J_{|m'-m|}(0) \tilde{f}^{\pm}_{jnn'}(\rho_{SS'}) \tag{4.23}$$

and then apply the rotations according to equation (4.13)

$$\mathbf{W}^{SS'} = \mathbf{D}^{\mathrm{T}}(0, -\frac{\pi}{2}, 0)\tilde{\mathbf{W}}^{SS'}\mathbf{D}^{\mathrm{T}}(0, \frac{\pi}{2}, 0). \tag{4.24}$$

4.5 A spheroidal particle cluster

To validate the implementation of the volumetric lookup table approach for PWC of nonspherical particles, I compare the DSCS of a dense cluster of 100 prolate spheroids between a reference FEM solution with T-matrix simulations relying on the conventional particle coupling scheme and the

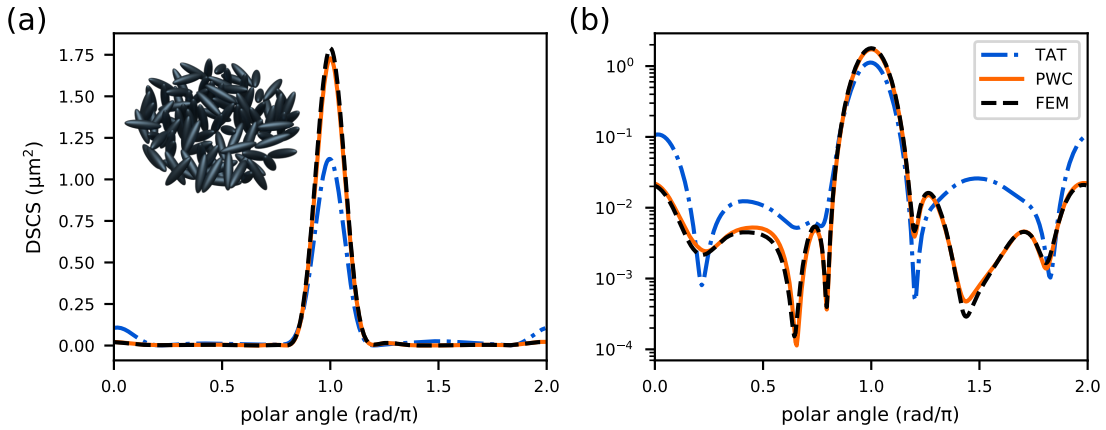

Figure 4.8: Comparison of the differential scattering cross sections along the xz-plane of a particle cluster, displayed on (a) linear and (b) logarithmic scale, between an FEM reference solution and T-matrix simulations based on the plane-wave coupling (PWC) procedure and the conventional translation addition theorem (TAT). Inset: Illustration of the particle cluster consisting of 100 prolate TiO_2 spheroids with semiminor axes of $a = b = 30\,\mathrm{nm}$ and a semimajor axis of $c = 120\,\mathrm{nm}$.

plane-wave-based approach.

The exemplary cluster is formed by identical prolate spheroids of semiminor axes of $a = b = 30\,\mathrm{nm}$ and a semimajor axis of $c = 120\,\mathrm{nm}$. Excited by a y-polarized plane wave propagating in negative z-direction at a vacuum wavelength of $\lambda_0 = 500\,\mathrm{nm}$, the in air embedded spheroids exhibit dimensionless size parameters of $ka = kb = 0.38$ and $kc = 1.51$. The particles' refractive index is set to $n_\mathrm{p} = 2.5$, which refers to titania nanoparticles in anatase phase [102]. An illustration of the particle cluster is shown as an inset of figure 4.8(a). With inter-particle distances down to $1\,\mathrm{nm}$ and a particle size parameter of 4, the example is chosen to pose an extreme challenge for the PWC scheme and the lookup table approach.

The comparison of the DSCS in figure 4.8 shows an excellent agreement between both the FEM reference solution (black, dashed) and the T-matrix results obtained via PWC (orange). Especially on a logarithmic scale (figure 4.8(b)) it becomes evident how well the T-matrix approach can resemble the reference result. The T-matrix simulations have been performed with a maximal multipole degree $l_\mathrm{max} = 10$ and a truncation of the in-plane wave vector at $n_\mathrm{eff,max} = 5$. These optimal values have been determined beforehand in the same way it is presented in section 4.3. The conventional T-matrix scheme based on the translation addition theorem (blue, dash-dotted) however, is not able to properly reproduce the cluster's scattering cross section.

4.6 Near-field of nonspherical particles

Besides the evaluation of direct particle coupling, a transformation into plane waves along a bounding plane of a nonspherical particle allows to derive near-field information from regions inside a scatterer's circumscribing sphere, where the spherical wave expansion of the particle's

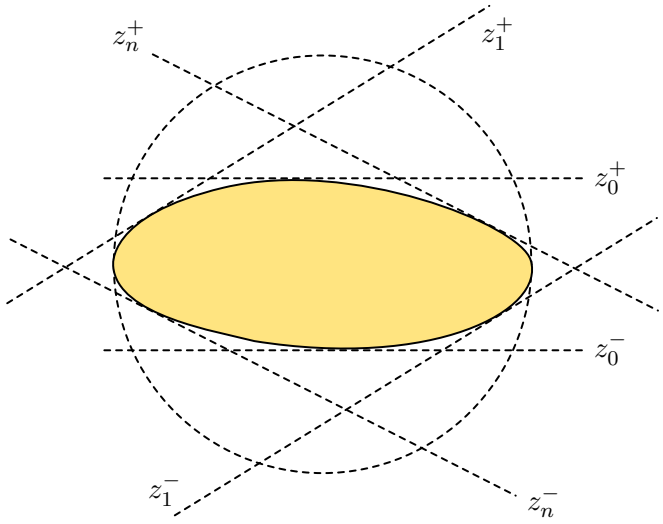

Figure 4.9: Inside the circumscribing sphere, the near-field of a nonspherical particle can be obtained piece wise by means of plane-wave expansions. To do so, a set of n rotations ensures that the particle's upper and lower bounding plane are parallel to the xy-plane of the respective rotated coordinate system.

scattered field diverges.

To obtain the near-field everywhere inside a particle's circumscribing sphere however, a number of n successive rotations is required to utilize the spherical-to-plane-wave transformation (2.40) along a set of upper and lower bounding planes $z_i^{\pm}$ that are parallel to the xy-plane of their rotated coordinate systems, respectively (cf. figure 4.9). How many rotations are necessary strongly depends on the actual shape of the scatterer and more importantly, on the point pattern for which the near-field data is demanded. Once the near-field is obtained for each position of the point pattern it can be *"stitched"* together, forming the full picture.

To investigate the potential of expanding a nonspherical particle's near-field in terms of plane waves, I compare the scattered field of an oblate spheroid with a reference FEM solution and the spherical-wave expansion that arises from the T-matrix method. The exemplary spheroid of semiminor axes $a = b = 100\,\mathrm{nm}$ and a semimajor axis of $c = 25\,\mathrm{nm}$ is excited by an x-polarized plane wave, propagating in negative z-direction. The spheroid orientation is given by Euler angles $(\alpha = 0, \beta = \pi/4, \gamma = 0)$ and its refractive index measures $n_\mathrm{p} = 2.4$, which refers to titania nanoparticles in anatase phase at a vacuum wavelength of $\lambda_0 = 550\,\mathrm{nm}$ [102]. The spheroids dimensionless size parameters measure $ka = kb = 1.14$ and $kc = 0.29$ in a homogeneous air environment $(n_\mathrm{amb} = 1)$.

In figure 4.10 the real part of the y-component of the spheroid's scattered field of all three solutions, as well as the relative deviation between the two different field expansions, compared to the FEM solution, is displayed. As expected, the scattered field's spherical wave expansion resembles the correct field everywhere outside the particle's circumscribing sphere, but strongly diverges from the reference solution for locations inside. On the contrary, the plane-wave expansion that is originating from the spherical wave expansion is able to match the FEM solution even at positions close to the

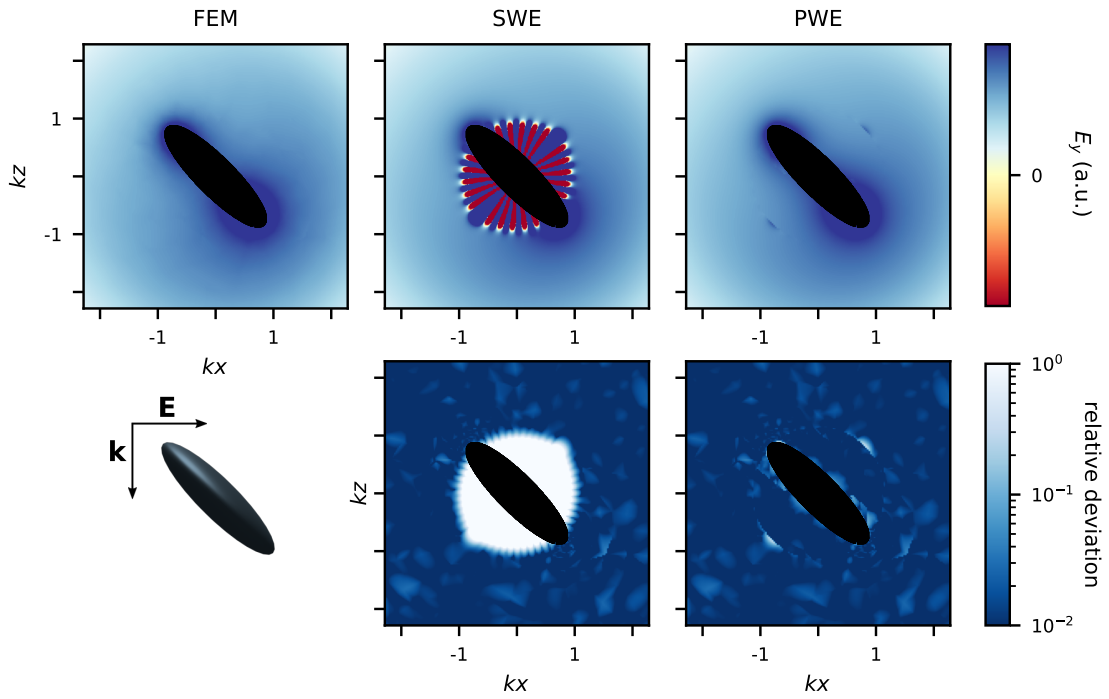

Figure 4.10: Top: Real part of the electric field's y-component in the xz-plane of an oblate spheroid for a reference FEM solution as well as the spherical-wave expansion (SWE) and plane-wave expansion (PWE) of the spheroid's scattered field. Bottom: Relative deviation between the field expansions and the reference solution.

particle surface. In this example, the maximal multipole degree was set to the rather large value of $l_{\mathrm{max}} = 25$. Hereby, the erroneous terms in the spherical wave expansion are pushed into strongly decaying evanescent waves. As a result, it is possible to evaluate the plane-wave spectrum up to an effective refractive index of $n_{\mathrm{eff,max}} = 9.2$ without deviating from the correct solution.

To highlight that the plane-wave representation can benefit both, the particle coupling as well as the near-field evaluation, I come back to the example of two oblate Ag spheroids from section 4.3. Figure 4.11 shows the comparison of the x-component of the dimer's electric near-field for $l_{\mathrm{max}} = 20$ and $n_{\mathrm{eff,max}} = 4$. In contrast to the previous example of a single particle, the near-field resulting from a T-matrix simulation is not only limited by the domain in which the spherical-wave expansions are valid, but also by the interaction between both scatterers. Therefore, it is no surprise that the near-field of the conventional T-matrix approach does not only differ from the FEM solution inside the particles' circumscribing spheres, but also outside. Utilizing plane waves for both, the particle coupling and the field representation, enables results that are in good agreement with the reference.

Despite all benefits, the results visualize one drawback of the "field stitching approach". Wherever a transition of different field representations takes place, be it from spherical waves to plane waves at the circumscribing sphere boundaries or from plane waves to plane waves resulting from a

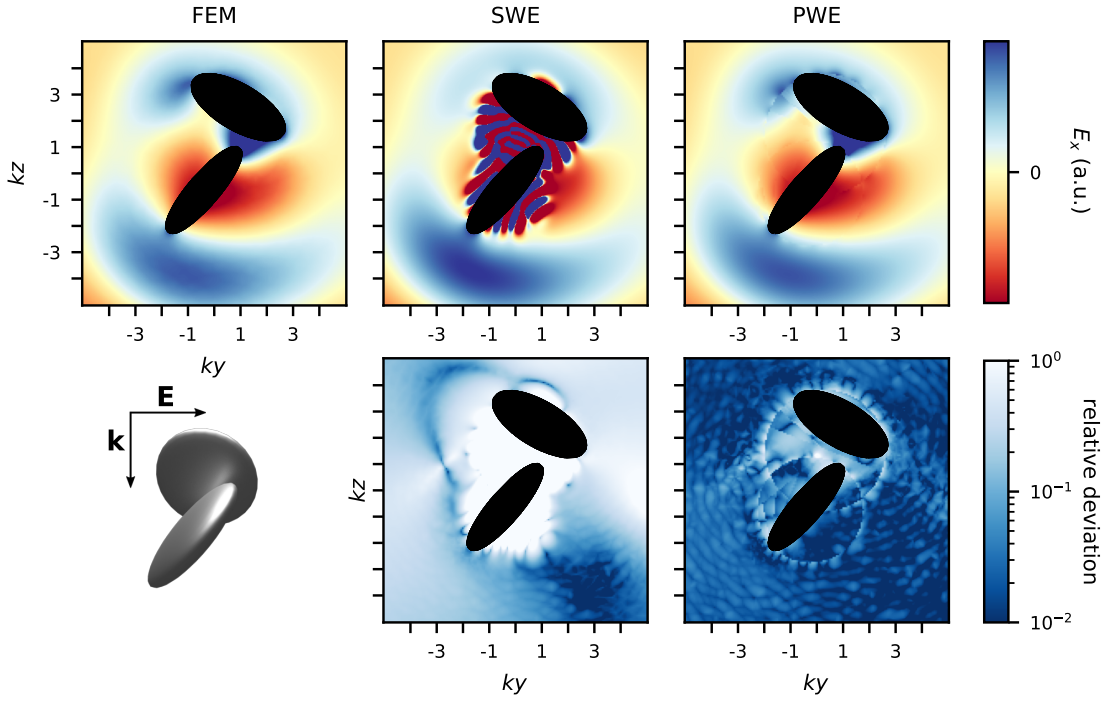

Figure 4.11: Top: Real part of the electric field's x-component in the yz-plane of two oblate Ag spheroids for an reference FEM solution as well as the spherical-wave expansion (SWE) and plane-wave expansion (PWE) of the spheroids' scattered field. Bottom: Relative deviation between the field expansions and the reference solution.

differently rotated coordinate system inside the circumscribing sphere, small artifacts can arise. This is especially the case for low multipole degrees where the truncation of the Sommerfeld integral prohibits to account for necessary parts of a particle's evanescent near-field spectrum.

4.7 Related work and recent developments

Although the Rayleigh hypothesis and the therewith accompanying issue that no single field representation is able to resemble the complete near-field of nonspherical particles is a long standing problem, a surprisingly large number of different approaches to overcome this limitation have been discussed within recent years.
To close this chapter, I would like to point the reader to some of these works that compete with the here presented plane-wave coupling formalism and could be advantageous in terms of applicability or precision.

- Rather than applying particle coupling in plane waves, the SVWFs can be transformed into the more complicated spheroidal vector wave functions. It is likely that in the special case of spheroidal scatterers, these spheroidal waves form a superior basis for the particle interaction.

Following the work of Asano and Yamamoto [57] on light scattering by spheroidal particles, Schulz *et al.* [103] derive the T-matrix of spheroidal particles directly in spheroidal waves, which could make a transformation-translation-transformation scheme obsolete, as long as only spheroidal particles are involved.

- In their work on highly accurate T-matrix calculations for spheroidal scatterers Somerville *et al.* [91, 104–106] identify and prevent the cause of a severe loss in precision, enabling numerical T-matrix calculations of quadruple-precision. Driven by highest precision, Auguie *et al.* [107] investigate the extend of the Rayleigh hypothesis for spheroidal scatterers with and without closeby particles [108]. Obtaining surprisingly accurate near-field and far-field properties for two-particle configurations, the authors emphasize that a special treatment for T-matrix simulations of nonspherical particles might not be necessary.

- To overcome the non-overlap restriction of nonspherical particles' circumscribing spheres, Torleif Martin [109] applies a translation of a particle's SVWFs. Hereby, the position and size of each circumscribing sphere is changed, preventing their intersection. This way, the combined T-matrix of two scatterers can be derived even for scatterers in close proximity. Successively combining the T-matrices of two scatterers, it is proposed that the T-matrix of a particle cluster could be formed.

- Introducing the *Global polarizability matrix*, Bertrand *et al.* [110] distribute a set of *numerical dipoles* throughout an arbitrary scatterer to construct its scattered near-field. In contrast to ordinary electric and magnetic dipoles that can be described by a local polarizability, the numerical dipoles are induced by the excitation field not only at their own position, but also by the field at all other dipole positions. Resulting from this spatial non-locality, the numerical dipoles provide a significantly larger amount of degrees of freedom per dipole compared to their classical pendant. As a result, a much lower number of dipoles is necessary to describe the scatterer compared to other distributed dipole approaches like, e.g., DDA. To obtain the global polarizability matrix of a specific particle, a learning set is used which comes from a secondary Maxwell solver. Therefore, a significant amount of computational effort is needed for each individual particle size, shape, or material combination. However, once obtained, the global polarizability matrix can be used for multiple scatterers located on a surface or in dense clusters. For complex scattering geometries, it remains open how the set of numerical dipoles has to be distributed within the scatterer.

- Questioning the ideal position of multiple distributed sources to resemble the scattered near-field of arbitrary scatterers at any point in space, Lamprianidis *et al.* [111] suggest a positioning of multipolar sources along the topological skeleton of a scatterer. Topological skeletons, well known, e.g., from biological shape recognition or computer animations, are the locus of all spheres that are tangent to the surface of an object in two or more points but do not intersect it. Impressive accuracy has been presented for light scattering by single, extremely complex objects.

To conclude, all mentioned approaches tackle the particle coupling between nonspherical particles in close vicinity. However, so far all of them lack evidence of their usability for large particle ensembles, in which we are here especially interested in. With the lookup table approach described in section 4.4, the PWC procedure does only add a minor additional work load to the conventional STMM and therefore thrives in the optical modeling of light scattering by large disordered particle arrangements. Recently, it has been picked up by different researchers and applied successfully to describe mutual coupling in dense antenna arrays on a substrate with strongly overlapping circumscribing spheres [112]. This example comes close to the optical modeling of dense surface structures that are utilized for light management in OLEDs.

5 Light extraction from OLEDs with dense, internal scattering structures

In this chapter, the application of the plane-wave coupling formalism (introduced in chapter 4) to account for light scattering in dense, nonspherical particle arrangements is illustrated by the example of organic light emitting diodes with compact internal scattering structures. After introducing the working principle of such devices, the trapped light problem and possible extraction strategies are reviewed in section 5.2. Section 5.3 focuses on planarized internal outcoupling layers of high and low refractive indices. The accuracy of the alternative coupling formalism for dense scatterers on a substrate is estimated in section 5.4. The modeling procedure is specified in section 5.5 and finally, results for different filling fractions and scatterer heights are presented in section 5.6.

Based on the separation of conduction and valence band of semiconductors, a light emitting diode (LED) transforms electrical energy into visible radiation by electroluminescence. Applying a voltage to the semiconductor, electrically excited electron-hole-pairs form bound states, so called excitions, that eventually decay to a state of lower energy and hereby emit photons.
Replacing the crystalline semiconductor with a carbon-based *organic semiconductor*, the organic light emitting diode (OLED) has a variety of properties that deviate from the classical LED and enable, e.g., homogeneous large area light emission.

5.1 Working principle of OLEDs

In contrast to the conduction and valence band of inorganic semiconductors, the molecular structure of organic semiconductors does not form a crystallinity in which charge carriers can move freely within the material compound, but rather discrete orbitals that belong to a distinct molecule or polymer. Hence, to move charge carriers through the material, the charges have to transition from one molecule to another called *hopping*, which results in much lower charge carriers mobilities and herewith a lower conductivity, compared to their inorganic counterparts. To cope with this limitation, OLEDs are typically fabricated as thin-film devices with an emitter material thickness typically between $10\,\mathrm{nm}$ and $100\,\mathrm{nm}$, but lateral dimensions often in the centimeter scale.

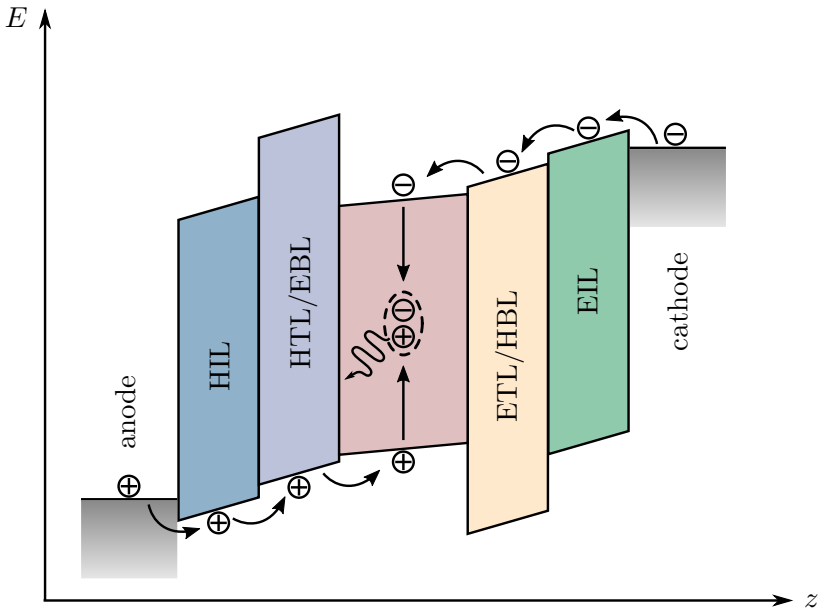

Figure 5.1: Typical energy diagram of an OLED stack consisting of an anode, a hole injection layer (HIL), a hole transport layer (HTL), an emitter, an electron transport layer (ETL), an electron injection layer (EIL) and a cathode. The HTL and ETL also function as an electron and a hole blocking layer (EBL and HBL) respectively. From the cathode, electrons are injected and transported through the materials' lowest unoccupied molecular orbitals (LUMO) and holes from the anode through the opposing layers' highest occupied molecular orbitals (HOMO) towards the emitter, where they form excitons that can recombine and emit a photon.

The fundamental processes necessary to generate light in an OLED can be explained by means of a energy diagram of the involved material layers. Such a typical energy diagram of a thin-film OLED stack is shown in figure 5.1, assuming no applied external voltage. In a first step, charge carriers need to be injected from the electrodes. Since the molecular orbitals of the emitter layer typically do not align with the work function of the two electrodes, injection layers are deposited on each electrode. On the anode's side, a hole injection layer (HIL) bridges the gap towards the emitter's highest occupied molecular orbital (HOMO), while on the cathode' side an electron injection layer (EIL) lowers the energy gap towards the emitter's lowest unoccupied molecular orbital (LUMO). Once injected, the charge carriers have to be transported to the emitter material. For this purpose, hole and electron transport layers (HTL/ETL) can be applied that exhibit much larger charge carrier mobilities. To prevent charge carriers to reach the opposing electrode and to increase the probability of an exciton formation, an electron blocking layer (EBL) and a hole blocking layer (HBL) provide a strong mismatch between the their HOMO/LUMO and the respective orbitals of the emitter. Finally, the bound electron-hole-pairs can recombine upon emission of light.
To simplify schematic 5.1, the transport and blocking layers are summarized in a single layer, which in practice can be achieved by a careful choice of materials and doping concentration that combine both functionalities.

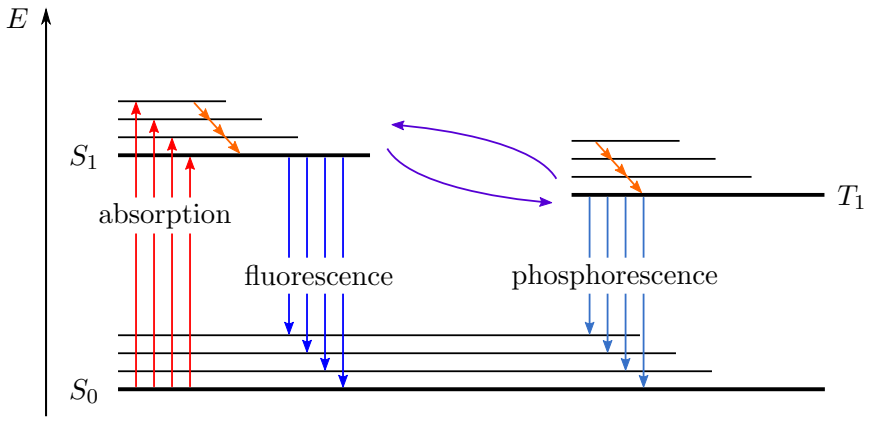

Figure 5.2: Jablonski diagram of optical transitions between the ground state S_0 and the first exited singlet and triplet states S_1 and T_1.

5.1.1 Optical transitions

In order to emit light, electrons in the organic molecule have to be raised from their ground state into an energetically higher, excited state. Prior to excitation, the Pauli principle requires the two electrons possibly populating a single orbital to exhibit alternating spins $m_s \in \pm\frac{1}{2}$, which adds up to a total spin of zero [113]. Upon excitation, e.g. via absorption of a photon, the excited electron preserves its spin and is raised into the first excited *singlet state* S_1. With the remaining hole in the ground state, the excited electron can form a singlet exciton that emits a photon upon recombination, which is called *fluorescence*. In contrast to the singlet exciton with a total spin of zero, the excited electron can transfer into the energetic slightly favorable *triplet state* by switching its spin. The radiative recombination of triplet excitons with a total spin of one is called *phosphorescence*. These optical transitions are summarized in the Jablonski diagram [114] in figure 5.2. Besides the direct transitions between the discrete energies of the ground state and the single/triplet states, electrons can transition to slightly higher discrete levels, the so called vibronic states, that result from rotations and vibrations of atoms within the molecule. The life time of theses vibronic states however is short, leading to a rapid decay of electrons into the respective main state. Hereby, a shift in absorption and emission spectra of organic semiconductors can be observed.
Phosphorescence does require a switch in spin of the excited electron upon relaxation, leading to a much lower probability of the optical transition compared to the fluorescent decay. However, due to the three times lower multiplicity of singlet excitons compared to triplet excitons, an OLED that is solely based on fluorescence is limited to an internal quantum efficiency of $25\,\%$. Therefore, phosphorescent emitter materials have been developed based on heavy nuclei like platinum [115] or iridium [116] that lead to a strong spin-orbit interaction. Hereby, the probability of phosphorescence is strongly increased, which enables an internal quantum efficiency of up to one. Besides the highly efficient phosphorescent emitters, materials with an especially low energy difference between the singlet and triplet state promote the conversion of triplet states back into the singlet state under

room temperature, called *thermally activated delayed fluorescence* (TADF) [117, 118], allowing all excited electrons to contribute to the fluorescent decay.

5.2 Optical loss mechanisms and light extraction

Discussing the efficiency of an OLED, one usually refers to its internal and external quantum efficiencies η_{int} and η_{ext}. The former denotes the rate at which injected electrons N_{e}, induced by a current I, contribute to the generation of optical power $P_{\mathrm{ph,int}}$ in form of photons $N_{\mathrm{ph,int}}$

$$\eta_{\mathrm{int}} = \frac{N_{\mathrm{ph,int}}}{N_{\mathrm{e}}} = \frac{P_{\mathrm{ph,int}}/(h\nu)}{I/e}. \tag{5.1}$$

Depending on the emitter design, various loss mechanisms can diminish the internal quantum efficiency. As discussed in the previous section, OLEDs that for example do not harvest triplet excitons, a priori have to expect a decreased efficiency of only $25\,\%$. In addition, excitons may recombine via non-radiative loss channels. However, addressing each of these loss mechanisms by specific design rules [119, 120], devices with internal quantum efficiencies of up to 1 can be achieved.

Assuming such an ideal emitter, the external efficiency η_{ext} is essentially determined by the outcoupling efficiency η_{out}

$$\eta_{\mathrm{ext}} = \eta_{\mathrm{int}}\eta_{\mathrm{out}}. \tag{5.2}$$

As depicted in figure 5.1, the generation of light in an OLED takes place within a thin-film stack between two electrodes, at least one of which has to be transparent. In a bottom emitting OLED, the transparent electrode, typically a transparent conductive oxide (TCO) like indium doped tin oxide (ITO) or aluminum doped zinc oxide (AZO), is deposited on top of a transparent, mechanically stable substrate like glass or flexible substrates like polyethylene terephthalate (PET) with an additional barrier layer [121].

With a metal electrode on the top side, the organic layers of refractive index $n_{\mathrm{organics}} \sim 1.7$, the TCO ($n_{\mathrm{TCO}} \sim 1.9$) and the substrate of $n_{\mathrm{sub}} \sim 1.5$ inevitably form a thin-film wave guide. Hence, the formation of wave-guided modes is supported. Those are solely propagating in lateral direction, but cannot escape the thin-film structure. In figure 5.3 two types of wave-guided modes are illustrated; the transversal-electric modes (red) expanding over the thin-film stack and the transversal-magnetic modes (dark blue) excited at the dielectric-metal interface, called surface plasmon polariton (SPP). In addition to wave guiding, a substantial fraction of light exhibits total internal reflection due to the strong refractive index contrast between the substrate and air. Only light propagating within the escape cone, i.e., propagation angles smaller than the critical angle, has the chance to couple out into air. In case of a glass substrate ($n_{\mathrm{sub}} = 1.5$) the critical angle measures $41.8°$. For angles beyond the critical angle, light is confined within the device.

Although the ratio between light that can be coupled out and light that is confined in substrate

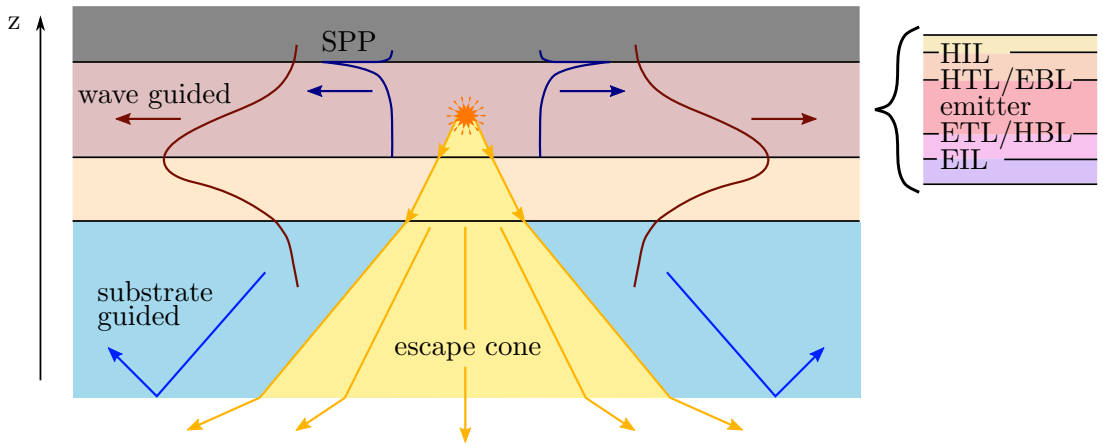

Figure 5.3: Optical loss channels in a planar OLED. Only light emitted within the escape cone, i.e., below the critical angle between substrate and air, contributes to the out-coupled light. Light propagating beyond the critical angle is lost due to the excitation of wave guided modes, surface plasmon polaritons (SPP) or substrate modes.

modes or wave-guided modes can vary depending on the specific choice of materials and layer thicknesses, the combined loss mechanisms typically lead to outcoupling efficiencies around $20\,\%$ [122]. The questions arises, to which extent each of the loss mechanisms hinder higher efficient OLEDs. A precise answer however, can only be given for a specific OLED design.

To visually exemplify the composition of different loss mechanisms I consider an OLED stack experimentally investigated in reference [5]. The planar OLED is summarized by the combined organic layers with total thickness of $d_{\mathrm{org}} = 97.8\,\mathrm{nm}$, sandwiched between an opaque aluminum (Al) cathode and an ITO anode ($d_{\mathrm{ITO}} = 135\,\mathrm{nm}$). Radiating around $\lambda_0 = 520\,\mathrm{nm}$, the effective refractive index of the organic layers reads $n_{\mathrm{org}} = 1.7$. The optical constant of aluminum has been taken from reference [123] and the refractive index of ITO ($n_{\mathrm{ITO}} = 2 + 0.01\mathrm{i}$) has been obtained via ellipsometry, performed by Adrian Mertens.

Assuming isotropic emission, the angular dependence of the dissipated power (shown in figure 5.4) allows to estimate the ratio of light contributing to the different loss mechanisms. Only light dissipated at an in-plane wave number smaller than the emitted light's wavenumber in air is capable to be coupled out ($n_{\mathrm{eff}} = \kappa/k \leq 1$). Light emitted under a larger effective refractive index will eventually exhibit total internal reflection at one or more layer interfaces, due to the constant in-plane wave vector of light that is propagating through a planar, layered environment. Depending on the refractive indices of the substrate, the transparent electrode and the organic layers, further intervals of the angular dependent power dissipation can be specified, contributing to either substrate modes, TE guided or TM guided modes.

The angular profile of a dipole emission depends on its specific layer environment, its position and orientation. Hence it is a good indicator of a device's performance. But it does not provide information of how much light will be lost due to parasitic absorption. Therefore, the angular dependence of dissipated power only provides an upper bound of the different optical loss channels

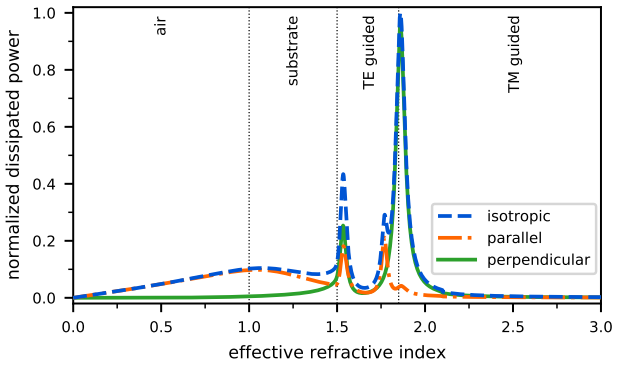

Figure 5.4: Dissipated power of an isotropic dipole emitter radiating from within a bottom emitting OLED as a function of its effective refractive index. Depending on its emission angle, light can be radiated into air modes, lost to substrate modes or electric and magnetic waveguide modes.

as well as the outcoupling efficiency.
In example 5.4, the isotropic emission has been estimated by an incoherent average of two parallel oriented dipoles with respect to the layer interfaces and a perpendicular dipole, which is common practice for planar OLED devices [124]. Especially in case of a perpendicular oscillating dipole, a large fraction of light is directly dissipated into SPPs.

5.2.1 Light extraction

To improve the external quantum efficiency of OLEDs, numerous approaches have been investigated that either focus on the extraction of substrate modes or the suppression of wave-guided modes. In the former case one often refers to *external*, in the latter to *internal outcoupling* techniques.
The following examples, addressing the OLED stack design, micro- and nanotextures as well as volumetric and planar scattering layers, only present an excerpt of the available literature. Comprehensive overviews of light extraction approaches can be found, e.g., in references [125–127].

Prior to any specific outcoupling structure the choice of materials and the careful tuning of layer thicknesses can strongly benefit the dissipation of light that already propagates within the escape cone and hence is directly eligible for the extraction into air.

- As illustrated in figure 5.4, the orientation of a point dipole source that is typically used to describe the molecular luminescence upon recombination of an exciton has a major influence on the possible outcoupling efficiency. Mainly radiating perpendicular to the dipole moment, a parallel orientation of the dipole transition strongly benefits the dissipation of light with a low effective refractive index. In contrast, perpendicular oriented dipoles strongly dissipate into wave-guided modes and surface plasmon polaritons. Different emitter

molecules generate a predominant **dipole moment orientation** [128, 129] and thus can be specifically designed to benefit light extraction.

- The choice of materials and their respective layer thicknesses influence the interference pattern within an OLED stack. Hereby, not only the exciton life time and hence the internal quantum efficiency is influenced, but also the angular emission profile is altered [130, 131]. A careful optimization of the weak **mircocavity**, formed between the metallic and the transparent electrode, ensures a favorable angular emission profile.
- In contrast to the microcavity approach, a **high index substrate** [132, 133] that matches the optical constant of the transparent electrode prevents the formation of TE-guide modes. The approach however worsens the refractive index mismatch at the substrate-air-interface and therefore requires its combination with a external outcoupling structure.

External outcoupling approaches that focus on the extraction of substrate guided modes lower the probability of TIR at the substrate-air-interface. Applied onto or within the substrate, the OLED design and fabrication remain largely unaffected. The large distance towards the active OLED stack however also prevents interaction with waveguide modes.

- Applying refractive-index-matched **microlens arrays** on top of the substrate [134, 135], light with arbitrary propagation angle can be extracted into air. Typically an external approach, their internal integration at the TCO-substrate-interface allows to couple waveguide modes into the substrate [136].
- While microlens arrays suppress reflections by a continuous curvature of the interface, **external scattering layers** can prevent TIR at the glass-air-interface upon random scattering events. Light propagating outside the escape cone receives a new chance to change direction any time it passes the scattering layer. To obtain the volumetric scattering layers, nanoparticles are dispersed in the polymer substrate [137] prior to its deposition. Alternatively, nanoparticle free porous networks can be introduced [138].

Internal outcoupling techniques focus on the extraction of waveguide modes by diffraction and scattering. To allow for a significant overlap with the mode profiles, the planar or volumetric textures have to be directly incorporated into the OLED stack or placed within close distance, resulting in more complex fabrication procedures.

- Typically deposited by a lithography process, **periodic, internal textures** based on one-dimensional gratings [18, 139] or two-dimensional photonic crystals [140, 141] allow to extract waveguide modes that would otherwise be confined to the organic layers or the transparent electrode. Angular color distortions arising from the periodicity can be suppressed with an additional external microlens diffusor [142].

- Bypassing the drawbacks of periodic structures, **disordered, internal textures** made of nanoholes/nanopillars or random nanowrinkles can be obtained, e.g., via phase separation of polymer blend [23, 143], UV treatment of imprinted gratings [144] or etching procedures [145, 146]. The nanotextures are often deposited between the substrate and the transparent electrode. To prevent corrugation of the neighboring OLED layers, the textures can be planarized. However, the textures' overlap with electric surface modes typically is weak.
- To create a strong scattering effect and to allow the disturbance of surface waves at the dielectric-metal electrode-interface, **corrugated OLED stacks** can be fabricated [147, 148]. With a corrugation traversing through the organic layers and the metal electrode, the OLED's electric properties are affected and special care has to be taken to circumvent electrical defects.
- Introducing a volumetric, **internal scattering layer** [37, 149–151] between the transparent electrode and the substrate, the propagation of light can be efficiently randomized. To allow for significant light scattering properties of the dispersed nanoparticles, their size has to be comparable to the emission wavelength, resulting in layer thickness of multiple micrometers. Hence, an overlap with wave-guided modes can only be ensured with a refractive index matrix comparable to the transparent electrode.

5.3 Internal outcoupling structures with low and high index planarization

In the following I will investigate light extraction from a green OLED with disordered, internal outcoupling structures that are planarized with either low or high index materials. The goal is to deduce differences in the extraction of both wave-guided and substrate modes, depending on the scattering layer materials, the particles' height and the influence of the nanotextures packing density. The investigated nanopillar structures, deposited between the glass substrate and the planar OLED stack, are inspired by the work of Yidenekachew Donie [5, 23, 152, 153] on phase separated nanostructures obtained via polymer blend lithography (PBL).

An experimental investigation of the considered green OLED with a TiO_2 nanostructure, planarized by a low index epoxy resin (SU-8), can be found in reference [5]. For the planar OLED stack, consisting of an aluminum cathode, the organic layers and an ITO anode, a maximal outcoupling efficiency of $25\,\%$ can be expected for an isotropic dipole emission that is radiating in proximity of the organic emitter layers' center (compare figure 5.5). This maximal outcoupling efficiency is approximately $3\,\%$ lower than the prediction based on the angular dissipation profile (see figure 5.4), which can be attributed to absorption within the ITO and the aluminum electrode.

To promote light extraction, a planarized scattering layer will be deposited on top of the glass substrate prior to the original OLED stack. The resulting layer sequence, the respective materials and the layer thicknesses are summarized in figure 5.6. In this study, I will consider two different

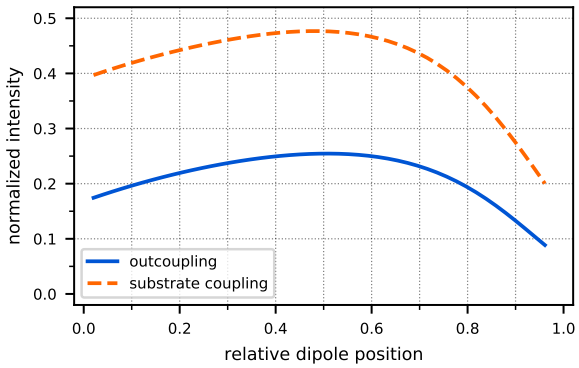

Figure 5.5: Substrate and outcoupling efficiency of the planar OLED stack as a function of the relative position of an isotropic dipole emission.

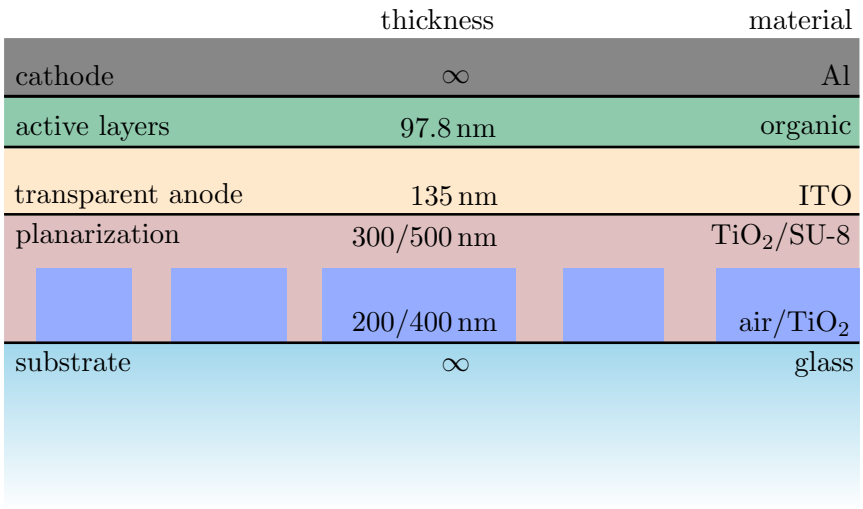

Figure 5.6: Investigated OLED stack with low or high index planarization of a disordered, internal nanotexture.

configurations of the scattering layer. First, a low index planarization of the transparent epoxy resin SU-8, covering TiO_2 nanopillars, which is identical to the configuration presented in reference [5]. Second, a high index planarization consisting of titania nanoparticles, enclosing nanopillar air voids.

These two opposing configurations raise the question whether one or the other is favorable to extract waveguide and/or substrate modes, as the additional planarization layer alters the OLED's microcavity and deforms the profile of wave-guided modes. In the former case of a low refractive index planarization, a good match with the optical constant of the glass substrate allows to bring the scattering configuration close to the waveguide that is centered around the transparent electrode. The resulting mode profiles of the fundamental electric and magnetic waveguide modes can be seen on the left of figure 5.7 for a planarization layer thickness of $300\,\mathrm{nm}$. Due to the low refractive index contrast between planarization and substrate, the mode profiles remain almost identical to

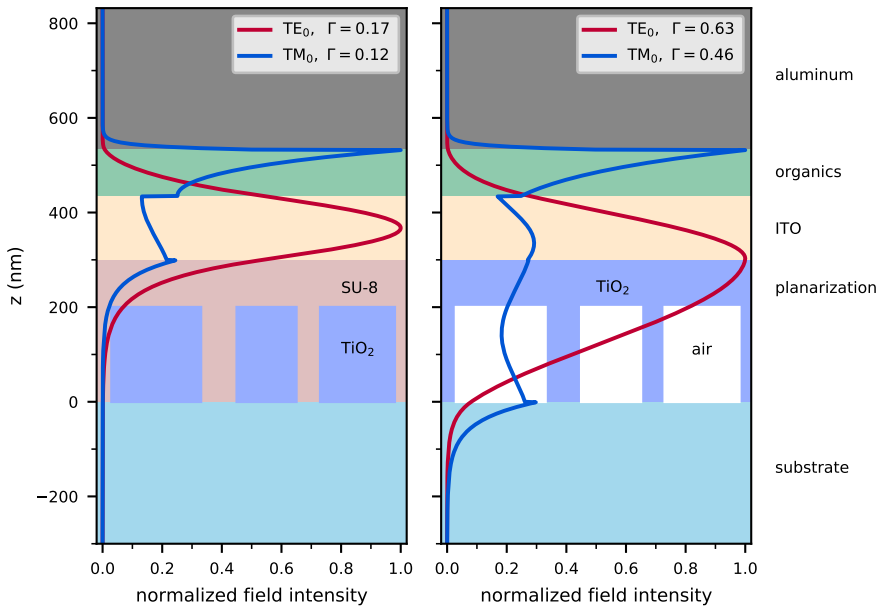

Figure 5.7: Illustration of the fundamental waveguide modes in OLEDs with low (left) and high index planarization layers (right). Nanopillars are solely displayed to emphasize the difference in mode overlap Γ between the respective waveguide modes and the planarization layer.

the planar OLED stack. In the second configuration however, the planarization material is chosen to match the refractive index of the transparent electrode. Hereby, the waveguide deforms into the planarization layer, allowing a much stronger overlap with possible scatterers (right hand side of figure 5.7).

5.3.1 Phase-separated nanotextures

The fabrication of the considered disordered nanotextures follows a procedure that is based on the self-assembly of two immiscible polymers [154, 155]. The necessary fabrication steps have been identified by Yidenekachew Donie, who also prepared all analyzed samples and scanning electron microscope (SEM) images.

To conduct the self-assembly, two polymers, typically polystyrene (PS) and poly(methyl methacrylate) (PMMA), are dissolved individually in a mutual solvent and are then mixed together. Deposited onto the glass substrate, e.g., via spin coating or inkjet printing [23], the two phases separate from each other as the solvent dissipates. Depending on the mass ratio between the two polymers, PS or PMMA pillars form within a host of the other. Selectively removing one or the other, nanoholes or nanopillars remain, which can be directly used as a scattering layer or be transferred into different materials.

The fabrication procedure of SU-8 planarized titania nanoparticles is described in detail in reference [5] and can be summarized in five steps: After deposition and self-assembly of the polymer

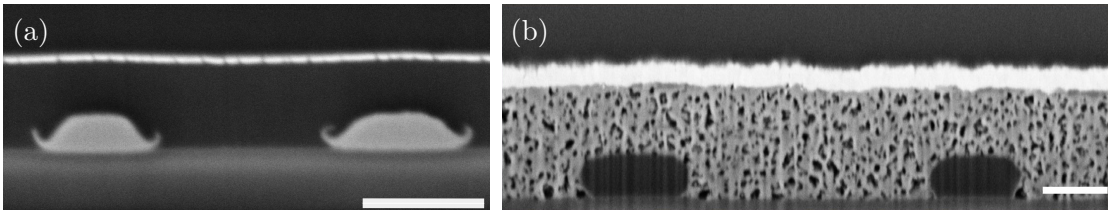

Figure 5.8: SEM images of focused ion beam cuts through the planarized scattering structures: (a) TiO_2 nanopillars on a glass substrate, covered by SU-8. The scale bar represents $350\,\mathrm{nm}$. (b) Air voids between a glass substrate and a nanoporous TiO_2 planarization layer. The scale bar represents $400\,\mathrm{nm}$. Images have been provided by Yidenekachew Donie.

blend (with a mass ratio of PMMA prevailing those of PS) the PS islands are selectively removed. Next, a TiO_2 layer is deposited via e-beam evaporation, covering up the nanoholes in the PMMA film. A lift-off of the PMMA structure results in TiO_2 nanopillars on a glass substrate. Finally, the texture can be planarized with SU-8 prior to the deposition of ITO, the organic layers and the aluminum electrode.
The second nanotexture of air voids, covered in TiO_2, follows a similar procedure. Instead of selectively removing the PS, the development of PMMA results in free standing PS nanopillars. After deposition of titania nanoparticles, with a particle size in the range of a few tens of nanometer, a baking step allows to vaporize the PS that escapes through the nanoporosity of the titania layer.

In figure 5.8 SEM images of focused ion beam (FIB)-cuts of both planarized scattering layers, deposited onto a glass substrate, are shown. The observed nanoporosity of the nanoparticle based TiO_2 planarization results in a decreased optical constant of $n_{TiO_2} \approx 1.93$ compared to the e-beam evaporated TiO_2 nanopillars of $n_{TiO_2} \approx 2.18$.[1] Depending on the fabrication parameters and deposition techniques, the morphology of the nanostructures can be varied, allowing a good control over resulting scattering properties. The lateral size distribution and surface coverage e.g., are affected by the rate of solvent evaporation [33], the polymer blend composition [5] or in case of spin-coating deposition, the angular velocity of the sample holder [152, 156]. Utilizing inkjet printing, the nanostructure height can be varied over a range of multiple hundred nanometer, largely without affecting the average surface coverage [23].

5.3.2 Particle distributions

To reconstruct particle distributions of the experimental, self-assembled nanopillar structures, three SEM images of samples with different fabrication parameters have been analyzed regarding the nanotexture's surface coverage and the particles' lateral size distributions. The results are displayed in figure 5.9. With an increasing filling fraction of nanopillars, an increase in the average particle diameter is observed. In case of the second sample, with a filling fraction of $35\,\%$, the radii of

[1] In-house measured ellipsometry data of optical constants for spin-coated and evaporated TiO_2 thin-films have been provided by Adrian Mertens.

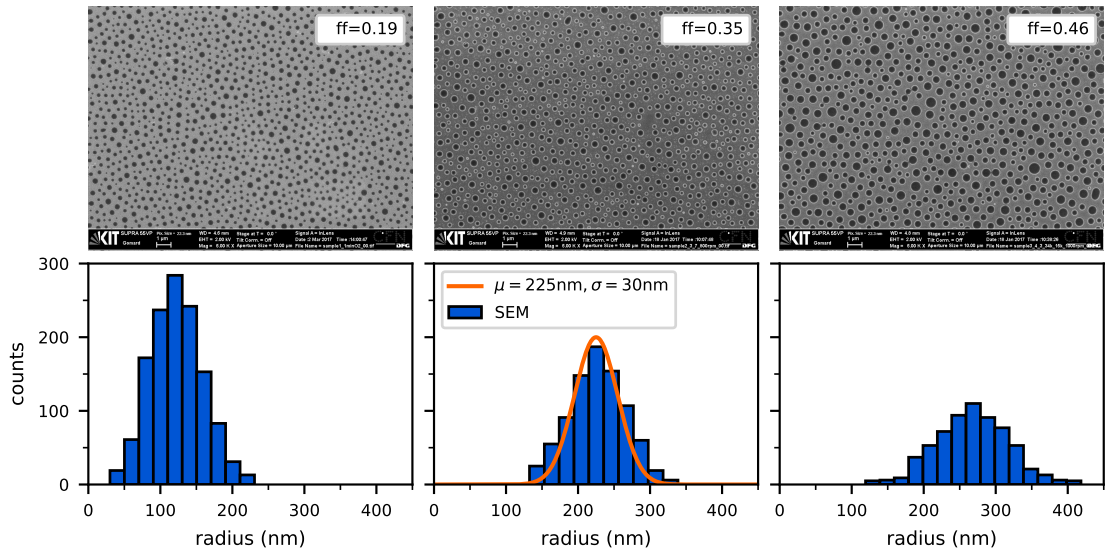

Figure 5.9: Top row: SEM images of disordered nanostructures of different filling fractions (ff), fabricated via polymer blend lithography. Bottom row: Respective particle size distributions.

the particle size distribution are in good agreement with a Gaussian distribution, centered around $\mu = 225\,\mathrm{nm}$ and a standard deviation of $\sigma = 30\,\mathrm{nm}$. To generate particle distributions of arbitrary size that are in good accordance with the experimental nanotextures, I have prepared random, two-dimensional, mono-disperse disc arrangements with filling fractions between $40\,\%$ - $80\,\%$, using a freely available code provided by Monica Skoge [157] that is based on the Lubachevsky-Stillinger algorithm. In a next step, the disc radii have been rescaled to match the filling fraction of the original sample and to mimic the Gaussian size distribution. However, to later simplify the use of the PWC formalism for nanopillars in close proximity, the Gaussian distribution has been discretized in five steps with radii $r_{\mathrm{disc},i} = \mu \pm x\sigma, x = 0, 1, 2$. The resulting disc patterns are displayed in figure 5.10, showing a constant filling fraction of $35\,\%$ and packing fractions between $40\,\%$ - $80\,\%$. Comparing to the original sample, the artificial disc arrangement with a packing fraction of $60\,\%$ is well suited to reconstruct the experimental long range disorder.

5.4 Cylindrical scatterers in close proximity

One goal of the present study is to compare light extraction from OLEDs with planar, internal extraction layers of different filling fractions, namely $20\,\%$, $30\,\%$ and $40\,\%$, and nanoparticle heights of $200\,\mathrm{nm}$ and $400\,\mathrm{nm}$. By increasing one of them, it is to be expected that more and more scatterers will be located in the vicinity of neighboring particles. To illustrate this, a top view of the six different artificial disc patterns with a constant packing fraction of $60\,\%$ is displayed in figure 5.11. The left column shows that for a filling fraction of $20\,\%$ no intersections of the particles' circumscribing spheres (black) with any neighboring particles are to be expected, independent of

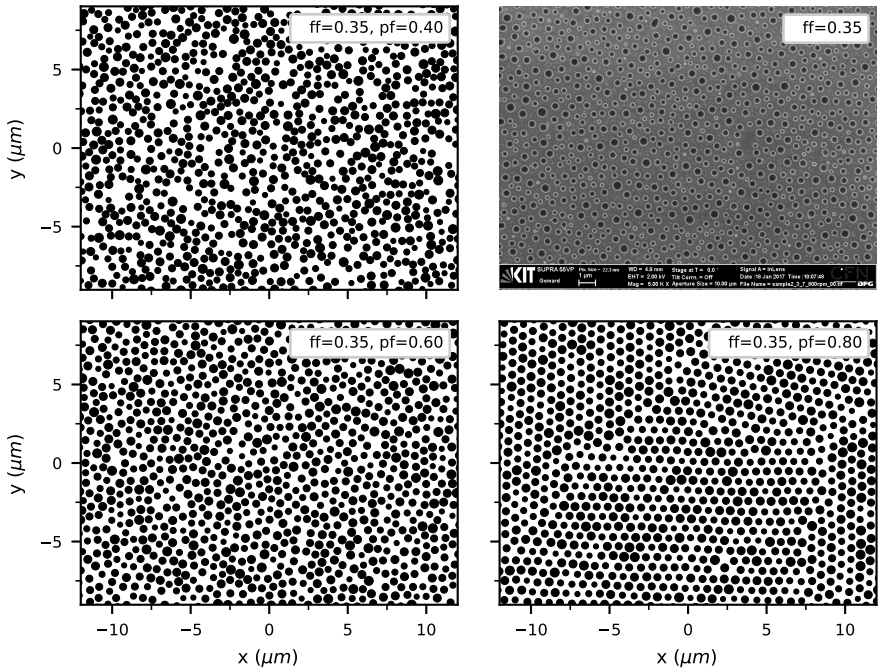

Figure 5.10: Artificial two-dimensional particle distributions of constant filling fractions (ff) but varying packing fractions (pf) in comparison to an experimental arrangement (SEM image).

the two particle heights. Considering a filling fraction of $40\,\%$ and a scatterer height of $400\,\mathrm{nm}$ however, almost all particles intersect with at least one neighbor's circumscribing sphere (red).

Considering optical simulations of dense scatterers on a substrate by means of the superposition T-matrix method is critical in two ways. On one side, all scatterers' circumscribing spheres intersect with the underlying glass substrate, which requires special care in the truncation of the Sommerfeld integrals that are evaluated for the particle-substrate interactions [7, 8]. On the other side, the intersections with neighboring particles are in general not correctly accounted for by the translation addition theorem for SVWFs and are in fact prohibited by the STMM. The in chapter 4 introduced alternative formulation of the translation addition theorem for SVWFs based on an intermediate plane-wave expansion however allows to account for direct particle interactions even if the particles' circumscribing spheres do intersect, and hence will be applied in all necessary cases.

5.4.1 Parameter selection

To obtain simulation results that meet a desirable accuracy without suffering from an inflated computation time, a number of simulation parameters have to be chosen that allow a balance between the two ambitions. These parameters mainly include quantities that influence the numerical evaluation of direct and indirect particle coupling between individual pairs of scatterers (cf. section 3.4.2). To simplify its usage, SMUTHI provides the user with several automated parameter selection

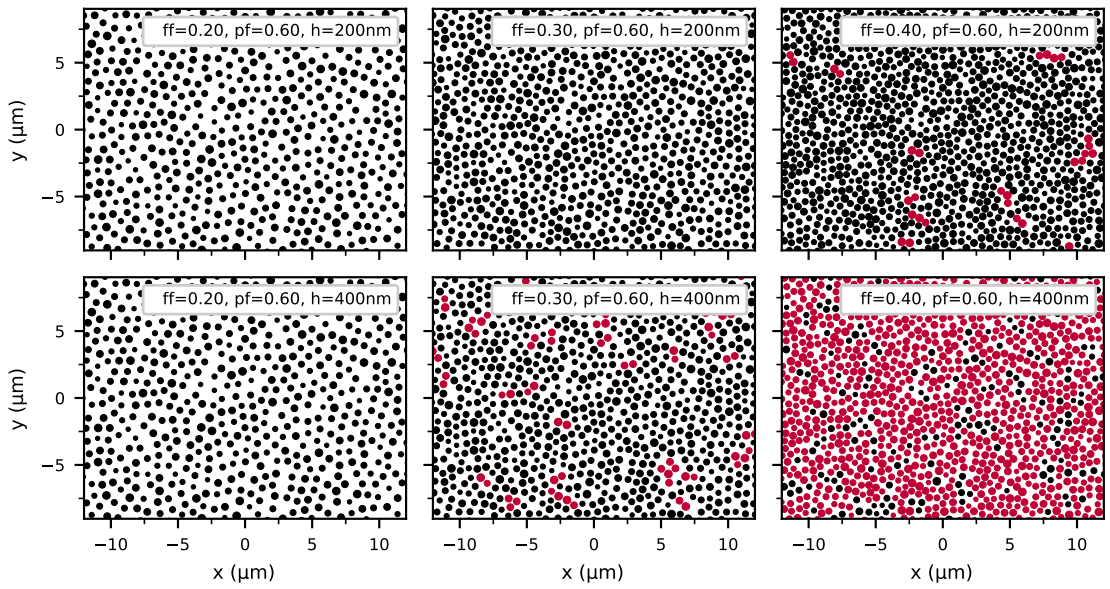

Figure 5.11: Top view of artificial, two-dimensional particle distributions of 20 % (left), 30 % (center) and 40 % (right) filling fraction and constant packing fraction of 60 % . The circumscribing spheres of nanopillars displayed in red intersect with neighboring scatterers, depending on the pillar height (top: $h_{\mathrm{cyl}} = 200\,\mathrm{nm}$, bottom: $h_{\mathrm{cyl}} = 400\,\mathrm{nm}$).

procedures and further a number of possible selection criteria have been suggested in reference [3]. Among all parameters, the number of multipoles (multipole order and degree) used to describe each particle's incoming and scattered field typically has the largest impact on both accuracy and time. Their automated selection can follow, e.g., the procedure presented in section 3.6.

Considering dense nanoparticles on a substrate, another important parameter is the maximal effective refractive index that determines the truncation of Sommerfeld integrals (see section 4.3) involved in the evaluation of particle-substrate interactions as well as the direct coupling between nonspherical particles in close vicinity. To distinguish between these two cases, I will from now on refer to $n_{\mathrm{eff,max}}^{\mathrm{R}}$ if particle-substrate interactions are considered and to $n_{\mathrm{eff,max}}$ in case of direct plane-wave coupling. In the former case of oblate scatterers on a substrate, an empirical formula was suggested [7] and its successful use for dense antenna arrays has been reported [112]. In the latter case however, an a priori criterion is missing so far.

In addition to a missing automated selection criterion, the present study considers dense particle size distributions, rather than particle aggregates of identical scatterers. It is to be expected, that the ideal truncation of the plane-wave spectra depends on the respective particle sizes involved. This however does not cope well with the interpolation of particle interactions from a single lookup table for the direct coupling and a single lookup for the indirect coupling (see section 4.4). To prevent that a preparation of multiple lookup tables for each coupling type become necessary, maximal effective refractive indices $n_{\mathrm{eff,max}}^{\mathrm{R}}$ and $n_{\mathrm{eff,max}}$ are sought that allow for accurate particle interactions for all involved scatterer sizes.

To do so, I will make use of reference solutions obtained with the freely available DDA software

Amsterdam DDA (ADDA) [53]. In comparison to the T-matrix method, the in DDA computations applied discretization of the scatterer domain remains within the physical picture of localized, excited dipoles that are responsible for a particle's scattered field. Thereby, DDA allows to yield accurate results for nonspherical scatterers on a substrate or multiple particles with overlapping circumscribing spheres. A systematic comparison of T-matrix results based on the PWC scheme and the reference solution allows to yield the optimal truncation criteria for both $n_{\mathrm{eff,max}}^{\mathrm{R}}$ and $n_{\mathrm{eff,max}}$. The procedure I follow can be summarized in five steps:

1. To select $n_{\mathrm{eff,max}}^{\mathrm{R}}$, T-matrix and reference simulations are performed, describing light scattering by a single scatterer on a glass substrate. Hereby, l_{max}, m_{max} and $n_{\mathrm{eff,max}}^{\mathrm{R}}$ are varied. This step is done for each considered cylinder radius and height.

2. By comparison of the particle's differential scattering cross section obtained from both simulation techniques, a maximal multipole degree and multipole order is determined for each particle size.

3. Given the chosen multipole order and multipole degree of each individual particle size, an average relative difference between both simulation techniques is determined as a function of the effective refractive index and the particles' height. The obtained average, relative difference functions as a decision criterion for $n_{\mathrm{eff,max}}^{\mathrm{R}}$.

4. To select the on average optimal $n_{\mathrm{eff,max}}$, a second particle scenario of two scatterers on a substrate with a lateral separation of $5\,\mathrm{nm}$ is considered for each particle size.

5. Taking the chosen l_{max}, m_{max} and $n_{\mathrm{eff,max}}^{\mathrm{R}}$ for an accurate particle substrate interaction into account, a comparison of the two-particle scenario between the PWC scheme and the reference solution allows to yield $n_{\mathrm{eff,max}}$.

The selection of the maximal multipole order l_{max} and the maximal multipole degree m_{max} (step 2) is summarized in table 5.1 for all considered particle sizes and the two respective configurations of $\mathrm{TiO_2}$ pillars embedded in the epoxy resin SU-8 and air voids embedded in $\mathrm{TiO_2}$.
With the multipole orders fixed, the average relative difference between ADDA reference solutions and T-matrix computations of one (step 3, left) and two $\mathrm{TiO_2}$ cylinders (step 5, right), embedded in SU-8 and directly located on a glass substrate, are displayed in figure 5.12 as a function of the maximal effective refractive index. The fine lines in the background refer to the individual cylinder radii between $165\,\mathrm{nm}$ and $285\,\mathrm{nm}$. The blue ($h_{\mathrm{cyl}} = 200\,\mathrm{nm}$) and orange arrows ($h_{\mathrm{cyl}} = 400\,\mathrm{nm}$) indicated a shift in relative difference that can be attributed to such a cylinder radius increase. From these results two clear trends can be observed. For flat cylindrical scatterers the particle's circumscribing sphere mainly overlaps with the substrate (cf. inset of figure 5.12) and hence a proper choice of $n_{\mathrm{eff,max}}^{\mathrm{R}}$ is more critical than the choice of $n_{\mathrm{eff,max}}$. As the aspect ratio between radius and height shifts towards larger radii, $n_{\mathrm{eff,max}}^{\mathrm{R}}$ gains further importance. In the opposing case of increasing cylinder heights, possible overlaps with neighboring particles become more pronounced and the proper selection of $n_{\mathrm{eff,max}}$ becomes significant.

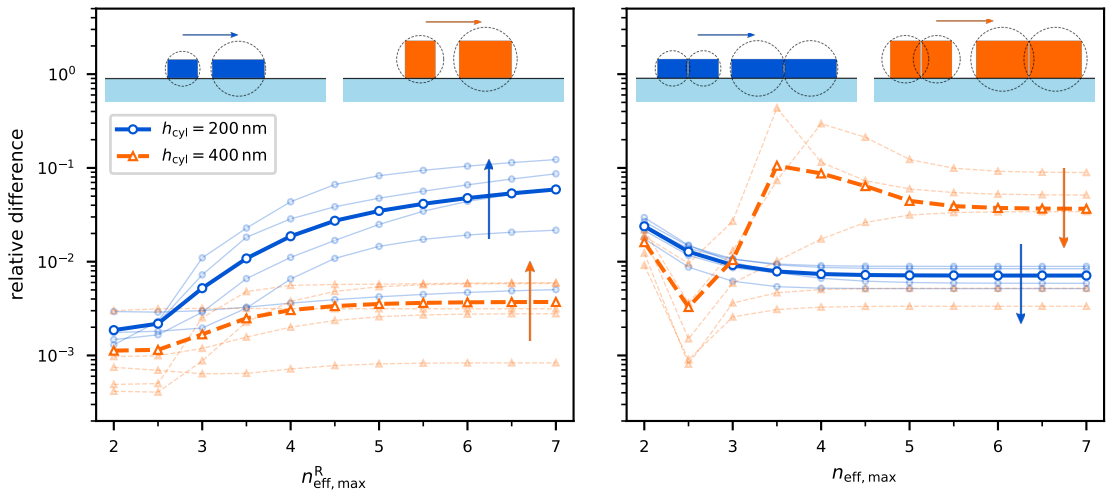

Figure 5.12: Light scattering by dielectric cylinders directly located on a substrate. Average relative difference between T-matrix simulations and a reference solution as a function of the maximal effective refractive indices $n^{\mathrm{R}}_{\mathrm{eff,max}}$ (particle-substrate interaction, left) and $n_{\mathrm{eff,max}}$ (particle-particle interaction, right). Arrows indicate a shift in relative difference when altering the cylinder radius from 165 nm to 285 nm.

Finally, I would like to note that the results also indicate the relative error that can be expected from the conventional T-matrix scheme for dense cylindrical particles on a substrate. This is due to the fact that results from the PWC scheme converge towards the result of the conventional scheme, as one increases $n_{\mathrm{eff,max}}$. For the here presented specific case, the conventional scheme would on average create a deviation of $4\,\%$ for each interaction of two cylinders in close vicinity ($h_{\mathrm{cyl}} = 400\,\mathrm{nm}$) compared to the reference solutions. This is about one magnitude larger than what can be achieved if the plane-wave spectrum is truncated at $n_{\mathrm{eff,max}} = 2.5$. In case of oblate cylinders however, no significant improvement in the direct particle coupling is to be expected.

		$l_{\max}$ / $m_{\max}$				
	r_{cyl} (nm)	165	195	225	255	285
	h_{cyl} (nm)					
TiO_2 in SU-8	200	7	7	8	9	10
	400	7	8	9	9	10
air in TiO_2	200	6	7	8	9	10
	400	7	8	10	12	12

Table 5.1: Selected maximal multipole degree and order, depending on the respecitve cylinder radius r_{cyl} and height h_{cyl}.

5.5 Modeling procedure

When modeling light extraction from an OLED, one inevitably has to deal with a multitude of length scales. While the generation of light originates within a thin-film layer environment characterized by dimensions in the nanometer range, the extraction takes place through a substrate in the micrometer range and possibly spreads over an area in the square centimeter or even square meter scale. As a result, neither a sole wave optics simulation, nor a ray optics scheme is able to map all involved mechanisms.

Here, I will follow an established modeling procedure presented in reference [158] that combines wave and ray optics simulations and is conducted in a three step process. At first, the angular dependent initial radiation pattern $X_j^{\mathrm{sub},0}(\lambda, \beta_{\mathrm{sub}})$ of light emitted into the optically thick substrate has to be determined. This initial substrate pattern can then be partially extracted into air (upon transmission through the substrate-air-interface) or be reflected back towards its origin. The same partial transmittance and reflectance takes place at the substrate-OLED-interface. This time however, scattering at the internal particle structure comprises the possibility of light being directed into different angles of propagation, presenting a new chance of its extraction. While the reflectance at the substrate-air-interface $R_j^{\mathrm{air}}(\lambda, \beta_{\mathrm{sub}})$ is simply determined by the Fresnel coefficients, its pendant at the substrate-OLED-interface $R_j^{\mathrm{oled}}(\lambda, \beta_{\mathrm{sub}})$ presents a *bidirectional reflectivity distribution function* (BRDF), which maps the directionality of incoming light to a probability distribution describing the direction of reflected light. Hence, a set of wave optics simulations becomes necessary that systematically draw the connection between light impinging onto the OLED stack and the angular distribution of its reflectance.

Knowing the initial substrate pattern, the reflectance at the substrate-air-interface and the OLED reflectivity, the substrate pattern

$$
\begin{aligned}
X_j^{\mathrm{sub}}(\lambda, \beta_{\mathrm{sub}}) &= \frac{1}{P_0(\lambda)} \frac{d}{d\beta_{\mathrm{sub}}} P_j^{\mathrm{sub}}(\lambda) \\
&= \begin{cases} R_j^{\mathrm{air}}(\lambda, \beta_{\mathrm{sub}}) X_j^{\mathrm{sub}}(\lambda, \pi - \beta_{\mathrm{sub}}) & \text{for } 0 \leq \beta_{\mathrm{sub}} \leq \pi/2 \\ R_j^{\mathrm{oled}}(\lambda, \beta_{\mathrm{sub}}) X_j^{\mathrm{sub}}(\lambda, \pi - \beta_{\mathrm{sub}}) + X_j^{\mathrm{sub},0}(\lambda, \beta_{\mathrm{sub}}) & \text{for } \pi/2 < \beta_{\mathrm{sub}} \leq \pi \end{cases}
\end{aligned}
\tag{5.3}
$$

functions as the starting point of a ray optics scheme that determines the extraction pattern

$$
\begin{aligned}
X_j^{\mathrm{air}}(\lambda, \beta_{\mathrm{air}}) &= \frac{1}{P_0(\lambda)} \frac{d}{d\beta_{\mathrm{air}}} P_j^{\mathrm{air}}(\lambda) \\
&= T_j^{\mathrm{air}}(\lambda, \beta_{\mathrm{sub}}) X_j^{\mathrm{sub}}(\lambda, \beta_{\mathrm{sub}}) \frac{d\beta_{\mathrm{sub}}}{d\beta_{\mathrm{air}}}.
\end{aligned}
\tag{5.4}
$$

In the above, $P_0(\lambda)$ denotes the emitted energy spectrum, $P_j^{\mathrm{sub}}(\lambda)$ the intensity of light with polarization j that propagates within the substrate, $P_j^{\mathrm{air}}(\lambda)$ the outcoupled intensity and $T_j^{\mathrm{air}}(\lambda, \beta_{\mathrm{sub}})$ the transmittance at the substrate air interface. In case of bottom-emitting OLEDs, the polar propagation angle β_{air} of light extracted into air only ranges between $\pi/2 \leq \beta_{\mathrm{air}} \leq \pi$, while the

substrate pattern consists of upwards and downwards propagating polar angles $0 \leq \beta_{\mathrm{air}} \leq \pi$.

5.5.1 Radiation into the substrate

A single simulation of a random dipole, dissipating power into a layer environment that incorporates a random scattering layer, only covers a single realization of an infinite set of possibilities. These realizations vary in the orientation of the dipole emitter and the arrangement of scatterers. To gain an estimate of the statistical behavior of such a system, a number of simulations need to be performed that allow for a sufficient averaging over all uncertainties. In this spirit, I perform a set of ten simulations, each with its own random realizations of the particle distributions and an incoherent set of 36 point dipoles. Hereby, the isotropic dipole emission is averaged over 360 dipole orientations, drawn from a uniform random distribution. To ensure the incoherence between the different dipole emitters in each simulation, the phase of each dipole oscillation is also drawn from a uniform random distribution. The average substrate coupling efficiency is then obtained from the individual simulations

$$\overline{\eta}_{\mathrm{sub}} = \frac{1}{N_{\mathrm{sim}}} \sum_i \eta_{\mathrm{sub},i}. \tag{5.5}$$

Since a single, random particle distribution already consists of a statistical distribution of possible particle positions and sizes, a low variance in the substrate efficiency that is caused by the distinct particle arrangements is to be expected and the relatively small number of simulations is sufficient to obtain a small standard deviation between the individual simulations [60].

Due to limited computational resources, each simulation can only consider a finite-sized particle arrangement. For light propagating within the wave guide this means that it only exhibits a relatively small lateral distance of propagation during which the chance of a scattering event is present. Once light has passed this *"soft"* simulation domain boundary, no further extraction of waveguide modes is possible. Compared to the distance light can travel in wave-guided modes before it is eventually lost to thermalization, the here considered finite particle arrangements are small. Hence, one systematically underestimates the fraction of light that can be coupled out of waveguide modes. To estimate the substrate coupling efficiency of an infinite particle distribution, an extrapolation according to

$$\eta_{\mathrm{sub}}(\rho) = \eta_{\mathrm{sub}} - \tilde{\eta} \exp(-\gamma\rho) \tag{5.6}$$

has been suggested [158, 159]. According to this formula, light is gradually scattered out of the waveguide while propagating in lateral direction, leading to an extinction γ. Thus, considering only finite sized particle arrangements of radius ρ, one underestimates the substrate coupling efficiency η_{sub} by $\tilde{\eta} \exp(-\gamma\rho)$.
In this study, I restrict myself to particle distributions with a lateral extend of $20\,\mu\mathrm{m}$. To provide

an estimate of an unbound simulation domain, I fit equation (5.6) to substrate coupling efficiencies obtained for various lateral dimensions between $10\,\mu\mathrm{m}$ and $20\,\mu\mathrm{m}$.

The here considered OLED stacks of low and high index planarization, the different particle filling fractions of 0.2, 0.3 and 0.4, the cylinder heights of $200\,\mathrm{nm}$ and $400\,\mathrm{nm}$ and the sample averaging over ten random particle configurations, each containing 36 random dipole emitters, results in a total number of $2 \times 3 \times 2 \times 10 = 120$ simulations for the evaluation of the substrate coupling efficiency.

5.5.2 OLED reflectivity

To obtain the OLED's BRDF $R^{oled}_{jj'}(\lambda, \beta, \beta')$ that maps the polar angle β of incident light with polarization j to the polar angle β' of light reflected with polarization j', the thin-film OLED stack is excited by a series of Gaussian beams with incident angles between $0°$ and $80°$ and transversal electric/magnetic polarization. By discretizing the polar angle of incident light into $10°$ steps, the number of simulations can be limited to $2 \times 3 \times 2 \times 9 \times 2 = 216$. Further reflectivity values have been obtained via linear interpolation. The beam waist of the Gaussian beams was set to $10\,\mu\mathrm{m}$. Hereby, a large number of scatterers is directly located within the beam of excitation, which is assumed to provide a sufficient averaging over possible particle configurations [60].

5.6 Results

With all simulations performed, finally one can compare the influence of the different parameters on the extraction of light from the thin-film OLED.
Figure 5.13(a) summarizes the substrate coupling efficiency of the different extraction layer designs, i.e. the fraction of light that can escape the thin-film layer stack and is coupled into the glass substrate. Comparing the light extraction layers with a low index planarization (LIP) and a high index planarization (HIP) shows that in case of HIP the stronger overlap of wave-guided modes with the scattering layer (cf. figure 5.7) allows to scatter more light into the substrate. Compared to the planar OLED stack (but with a planarization layer), the substrate coupling efficiency is increased on average by a factor of ≈ 1.27. In case of LIP only an average increase of ≈ 1.16 is observed. However, increasing the filling fraction of nanopillars covered by the HIP from $20\,\%$ to $30\,\%$ results only in a minor increase in substrate coupling efficiency. A further increase even seems to slightly harm the coupling of light into the substrate. These observations differ for the LIP, where an increase in filling fraction directly translates into an increased substrate coupling efficiency. Especially for larger nanopillars a stronger suppression of waveguide modes is observed.

OLEDs with an extraction layer of HIP scatter more light into the substrate and are hence set up to extract more light into air. However, the simulations show (summarized in figure 5.13(b)) that

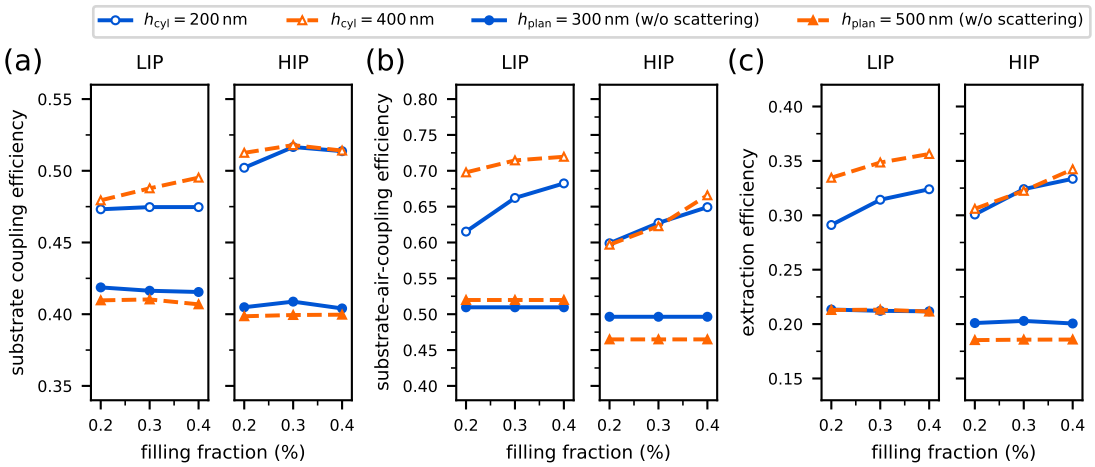

Figure 5.13: Light extraction from OLEDs with planar internal scattering layers, planarized by a low index material (LIP) and a high index material (HIP). (a) Fraction of light that is coupled into the substrate as a function of the cylinders' filling fraction and cylinder heights of 200 nm and 400 nm in comparison to the planar OLED stack without scattering, but the respective planarization layers of 300 nm and 500 nm height. (b) Fraction of light that can be coupled out of the substrate into air. (c) Extraction efficiency showing the fraction of light emitted into air.

OLEDs with a HIP exhibit a lower reflectivity for light impinging onto the device from within the substrate (compared to the LIP) and only allow to extract about 60 % to 65 % of light initially coupled into the substrate. For a LIP and high nanopillars more than 70 % hereof can be extracted. With these two trends counter-acting each other, comparable light extraction efficiencies, i.e., the fraction of light that can be coupled out into air, for both designs of low and a high index planarization are observed (see figure 5.13(c)). While the average increase for the LIP of ≈ 1.54 is lower than the factor of ≈ 1.66 for the HIP, the largest extraction efficiency of 35.6 % was obtained for large and dense scatterers, planarized with a material of low refractive index.

The simulation results summarized in figure 5.13 indicate that no major difference in extraction efficiency is to be expected from the two different designs of internal extraction layers made of high and low refractive index nanoparticles, planarized by materials of strongly deviating refractive indices. At first this might seem surprising, since the HIP is known to allow a strong leakage of waveguide modes into the scattering layer, due to a decent refractive index match with the transparent electrode. In addition, the refractive index contrast between the air voids and the surrounding nanoporous TiO_2 layer is even larger than in the opposite case of TiO_2 nanopillars embedded in SU-8.

To investigate whether or not the larger refractive index contrast directly translates into a stronger scattering of light into the glass substrate, single cylindrical scatterers made of TiO_2 and air are excited by a plane wave with a vacuum wavelength of $\lambda_0 = 520\,\mathrm{nm}$. The particles are embedded in SU-8 and TiO_2 respectively and located directly on a glass substrate. Figure 5.14 shows the nanopillar's scattering cross section as function of the polar angle θ for particles of various radii and heights. Excited under normal incidence (figures 5.14(a) and (b)) the cylindrical particles

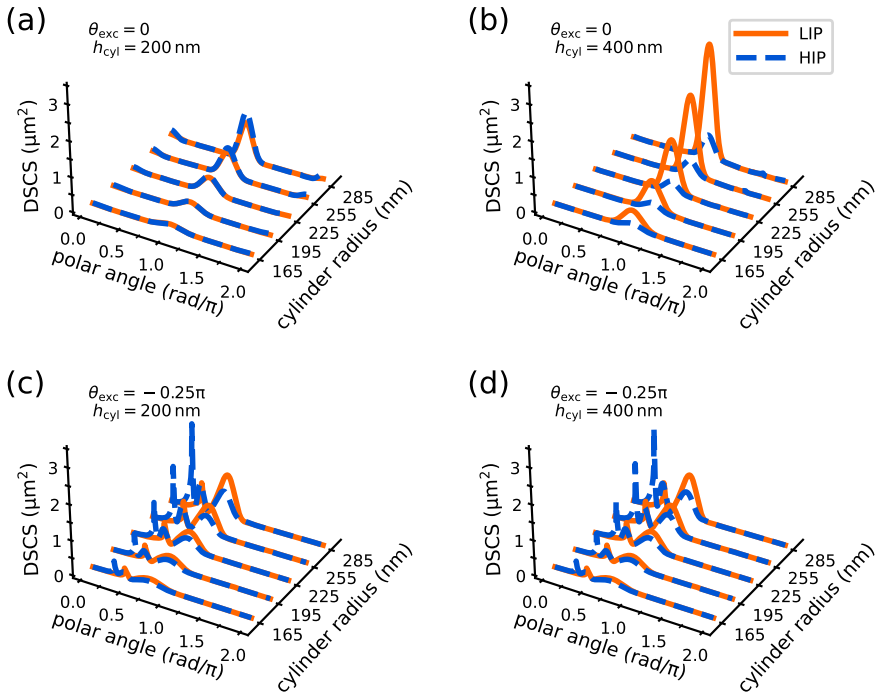

Figure 5.14: Differential scattering cross section (DSCS) of cylindrical scatterers on a glass substrate, excited by plane wave at $\lambda_0 = 520\,\mathrm{nm}$. Comparison between cylindrical TiO_2 scatterers embedded in a low index planarization of SU-8 (LIP) and air voids in a high index planarization of TiO_2 (HIP). (a) Cylinder heights of $200\,\mathrm{nm}$ and of (b) $400\,\mathrm{nm}$, excited under normal incidence. (c) Cylinder heights of $200\,\mathrm{nm}$ and of (d) $400\,\mathrm{nm}$, excited under a polar angle of $\theta_{exc} = -0.25\pi$.

mainly scatter light into the glass substrate, i.e., into polar angles of $0.5 < \theta < 1.5$. Especially in case of large scatterers, the TiO_2 nanopillars exhibit significantly larger scattering cross sections compared to the air voids in a HIP layer.
However, light propagating in waveguide modes will typically excite the scattering layer under oblique, rather than normal incidence. Figures 5.14(c) and (d) show the particles' DSCS for a polar excitation angle of $\theta_{exc} = -0.25\pi$. Again, the TiO_2 nanopillars scatter significantly more light into the glass substrate. In contrast, the air voids mainly show a specular reflection at $\theta = 0.25\pi$. These strong reflections can be attributed to the much lower critical angle of $\theta_{crit} \approx 0.28\pi$ compared to the LIP case with $\theta_{crit} \approx 0.4\pi$.

In summary, the results show that OLEDs with planarized scattering layer of a high index material do not necessarily outperform their counterparts of low index planarization. A HIP allows a good leakage of waveguide modes into the light extraction layer and hence a strong scattering of waveguided modes. However, the strong refractive index mismatch between the HIP and the substrate impairs a perfect coupling to the substrate. On the contrary, extraction layers with a LIP suffer from a comparably small overlap with the thin-film stack's waveguide modes. But they strongly benefit from larger scatterers and high particle filling fractions, which allows a decent suppression

of wave-guided light.
Once light is coupled into the substrate, OLEDs with a LIP extract more light into air than OLEDs with a HIP. Overall, comparable device efficiencies are observed for both extraction layer designs.

6 T-matrix simulations of periodic particle arrangements

This chapter introduces two-dimensional periodic boundary conditions on the basis of Ewald lattice sums to enable T-matrix simulations of periodic particle arrangements. Although concerned with aperiodic scattering ensembles, the boundary conditions allow to close the otherwise infinite simulation space and herewith limit the computational cost. After introducing the periodic superposition T-matrix formalism in section 6.2 and the Ewald lattice sums in section 6.3, near- and far-field properties of periodic scattered fields are summarized in section 6.4. Utilizing the plane-wave characteristics of periodic scattered fields, a plane-wave based approach to account for the direct and layer mediated interactions between infinite periodic grids is formulated in sections 6.5 and 6.6. Finally, the use of periodic boundaries to mimic disorder and numerical considerations for large unit cell dimensions are discussed.

The integration of Ewald lattice sums into the existing simulation framework has been realized in collaboration with Dominik Beutel. The influence of long range periodicities onto disordered particle arrangements has been investigated in the peer-reviewed journal article ***J. Quant. Spectrosc. Radiat. Transf. 272, 107802 (2021)*** *[2].*

6.1 Simulation domain boundaries

The optical modeling of optoelectronic devices often struggles with a disparity of the involved length scales. Being concerned with light matter interaction that can play a crucial role on a nanoscale does not cope well with device characteristics that often range from the centimeter- to the meter-scale. To comprise both, the local field interactions as well as the practically endless horizontal extend of light management structures in optoelectronic devices, the simulation model has to prevent edge effects.

The problem of a limited simulation domain is illustrated in figure 6.1(a). Due to limited computational resources and time, the seemingly endless extend of a scattering layer has to be limited to a finite domain. To prevent that any observable quantity is influenced by the domain boundaries, a variety of different strategies can be applied. In finite element or FDTD simulations, e.g., a popular approach to limit the simulation domain is to apply a perfectly matched layer (PML) [160] as an

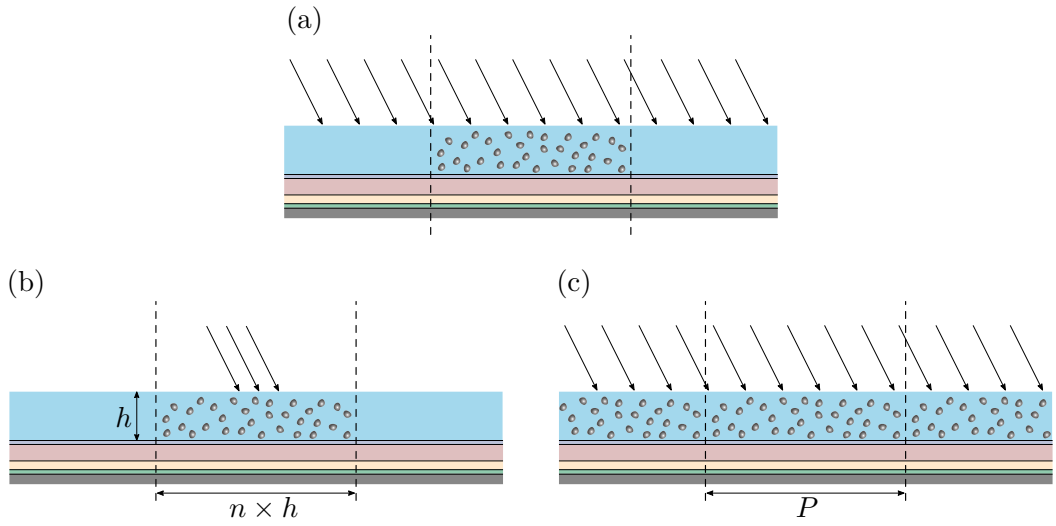

Figure 6.1: Illustration of a thin film solar cell with a volumetric scattering layer on top that is excited by a plane wave from afar. (a) The particle arrangement is limited to a certain simulation domain. To prevent edge effects: (b) the infinite extension of the excitation source is reduced to a local excitation; (c) periodic boundaries are applied to the simulation domain to mimic its virtually infinite extend.

artificial boundary condition. The goal of a PML is to absorb any electromagnetic wave that passes the domain boundaries while preventing its reflection back into the system.

In the here utilized T-matrix simulation framework, the layered environment's extend is in general infinite in lateral direction as well as semi-infinite in vertical direction of the outer layers. Hence, the simulation domain is unbounded in any direction. The particle arrangement however is limited in size, leading to a *"soft"* simulation domain boundary.

Up to this point, the here utilized strategy to prevent edge effects has been to excite the particle arrangement only locally in its lateral center (cf. figure 6.1(b)) rather than over its full extend. In this case it is sufficient to consider only a finite-sized particle arrangement, given that it is chosen large enough that only a negligible amount of light escapes at the arrangements vertical boundaries. How large the diameter of such a finite particle arrangement has to be chosen mainly depends on the system's height. Only for diameters that measure a multitude of its height, the probability of light leaving on the arrangement's lateral boundaries becomes insignificant. A sufficient factor between height and width however remains unknown, as it depends on the specific constellation at hand. As it is practically impossible to assess the exact, minimal domain dimensions that provide observable quantities independent of its size, one is forced to perform multiple simulations of various sizes and try to minimize the error by extrapolation [158, 159].

The strategy of locally excited, finite-sized particle arrangements inevitably runs into challenges regarding computational resources and time. This is especially the case for thick scattering layers, where the rapidly growing particle count renders it impossible to preserve a sufficiently large radius of the entire configuration. The same holds true, if the scattering layer is incorporated in a thick, layered environment, in which light might propagate tens of micrometer in lateral direction in

between interactions with the scattering sample.
Another popular strategy to deal with virtually infinite systems is to apply periodic boundary conditions (PBCs) where a finite-sized *unit cell* and its infinite periodic repetitions are regarded to cover all phenomena of interest. In general applicable for all kinds of lattice configurations in one or more dimensions, I will only consider two-dimensional, infinite cubic lattices of periodicity P that close the scattering layer in lateral direction (illustrated in figure 6.1(c)). The general perception I am following herewith is that the random nature of the particle arrangements can be preserved by a close-range disorder within one unit cell, while the detrimental influence of the artificial periodicity is kept low by applying *super cells* that comprise a large number of scatterers. Besides closing the simulation domain, PBCs are one tool to drastically reduce the computational load of a single simulation as they enable solution strategies to Maxwell's equations that specifically exploit the periodicity. Hereby, it becomes feasible to model and derive spectral information about wave-optical phenomena from thick, volumetric scattering layers that would otherwise be out of reach [2].

6.2 Periodic particle arrangements

In this section, I will specify the here considered periodic particle arrangements and the therewith associated notations that are necessary to reformulate the multiple scattering problem (introduced in section 3) to account for its periodicity.

Two-dimensional Bravais lattice

To mimic light propagation in large, volumetric, disordered particle arrangements, I will from now on consider particles that are periodically arranged in a two-dimensional Bravais lattice. To distinguish between each individual particle, i.e., particles in one unit cell, but also their periodic repetitions in every other unit cell, I introduce the q-th particle S_{pq} within unit cell p. Besides these individual particles, a particle collection S_q comprises all q-th particles that hence form a two-dimensional grid. Any displacement between two particles S_{pq} and $S_{p'q}$ that belong to the same collection

$$\mathbf{r}_{S_{p'q}} - \mathbf{r}_{S_{pq}} = n_1\mathbf{a}_1 + n_2\mathbf{a}_2 = \mathbf{R}_{p'} \tag{6.1}$$

can be displayed by a linear combination of two-dimensional lattice vectors $\mathbf{a}_1$ and $\mathbf{a}_2$ (illustrated in figure 6.2(a)). Here, n_1 and $n_2 \in \mathbb{Z}$ specify unit cell $(n_1, n_2) \rightarrow p'$ of lattice point $\mathbf{R}_{p'}$.
Besides the real space lattice vectors, I will make use of the reciprocal lattice vectors $\mathbf{b}_1$ and $\mathbf{b}_2$ that specify the reciprocal lattice points

$$\mathbf{G}_{\tilde{p}'} = \tilde{n}_1\mathbf{b}_1 + \tilde{n}_2\mathbf{b}_2, \tag{6.2}$$

with $\tilde{n}_1, \tilde{n}_2 \in \mathbb{Z}$ denoting the reciprocal space unit cell $(\tilde{n}_1, \tilde{n}_2) \rightarrow \tilde{p}'$.
The reciprocal lattice vectors can be generated from the real space lattice vectors via

$$\mathbf{b}_1 = \frac{2\pi R_{\pi/2}\mathbf{a}_2}{\mathbf{a}_1 \cdot R_{\pi/2}\mathbf{a}_2}, \qquad \mathbf{b}_2 = \frac{2\pi R_{\pi/2}\mathbf{a}_1}{\mathbf{a}_2 \cdot R_{\pi/2}\mathbf{a}_1}, \tag{6.3}$$

where rotation matrix $R_{\pi/2}$ denotes an anti-clockwise rotation of $90°$. Note that these lattice vectors fulfill $\mathbf{a}_i \cdot \mathbf{b}_j = 2\pi\delta_{ij}$ and $\mathbf{R}_{p'} \cdot \mathbf{G}_{\tilde{p}'} = 2\pi N$ for some integer N.

Periodic solutions of the multiple scattering problem

To assess the multiple scattering problem in periodic particle arrangements, let us for now assume the absence of any indirect particle coupling. Then, the multiple scattering problem formulated in section 3.5 reads

$$b_n^S - \sum_{n'} T_{nn'}^S \sum_{S'} \sum_{n''} W_{n'n''}^{SS'} b_{n''}^{S'} = \sum_{n'} T_{nn'}^S a_{n'}^{S,\mathrm{init}}. \tag{6.4}$$

Exciting the periodic arrangement by a plane wave, the initial incoming field at each particle within collection S_q resembles one another, but undergoes a phase shift that is based on the particle displacement and the in-plane wave vector $\mathbf{k}_{\mathrm{in}\parallel}$ of the initial field

$$a_n^{S_{p'q},\mathrm{init}} = \mathrm{e}^{\mathrm{i}\mathbf{k}_{\mathrm{in}\parallel}(\mathbf{r}_{S_{p'q}} - \mathbf{r}_{S_{0q}})} a_n^{S_{0q},\mathrm{init}} = \mathrm{e}^{\mathrm{i}\mathbf{k}_{\mathrm{in}\parallel}\mathbf{R}_{p'}} a_n^{S_{0q},\mathrm{init}}. \tag{6.5}$$

With the quasi-periodicity of the right-hand side of equation (6.5), the Bloch theorem [61, 161] demands for the same quasi-periodicity in the solution of equation (6.4), which thus satisfies

$$b_n^{S_{p'q}} = \mathrm{e}^{\mathrm{i}\mathbf{k}_{\mathrm{in}\parallel}\mathbf{R}_{p'}} b_n^{S_{0q}}. \tag{6.6}$$

Hence, the scattered field of particle collection S_q is fully described by the field coefficients $b_n^{S_{0q}}$ of the q-th particle in the arbitrary central unit cell ($p = 0$). Consequently, it is sufficient to only derive the field amplitudes of particles within one single unit cell.
Replacing S and S' with S_{0q} and $S_{p'q}$ and inserting equation (6.6) one can formulate the linear set of equations (6.4) for the arbitrary central unit cell

$$b_n^{S_{0q}} - \sum_{n'} T_{nn'}^{S_{0q}} \sum_{p'} \sum_{q'} \sum_{n''} W_{n'n''}^{S_{0q}S_{p'q'}} b_{n''}^{S_{p'q'}} = \sum_{n'} T_{nn'}^{S_{0q}} a_{n'}^{S_{0q},\mathrm{init}}. \tag{6.7}$$

Although the number of unknowns in equation (6.7) is massively reduced compared to the linear system of a non-periodic structure (cf. equation (3.53)), one now has to deal with an infinite number of particle-particle interactions between each particle collection

$$\sum_{p'} W_{nn'}^{S_{0q}S_{p'q'}} b_{n'}^{S_{p'q'}} = \sum_{p'} W_{nn'}^{S_{0q}S_{p'q'}} \mathrm{e}^{\mathrm{i}\mathbf{k}_{\mathrm{in}\parallel}\mathbf{R}_{p'}} b_{n'}^{S_{0q'}}. \tag{6.8}$$

As a result, we have to shift our focus from the explicit particle-particle interaction to the question of how particle collections couple to each other and how a collection couples with itself. Applying the definition of the translation addition operator (equations (2.35) and (2.36)) to the interaction between particles within collection S_q, the infinite sum takes the form

$$\begin{aligned}
&\sum_{p'} W_{nn'}^{S_{0q}S_{p'q}} \mathrm{e}^{\mathrm{i}\mathbf{k}_{\mathrm{in}\parallel}\mathbf{R}_{p'}} \qquad (6.9)\\
&\quad = \sum_{p'\neq 0} A_{n'n}(-\mathbf{R}_{p'}) \mathrm{e}^{\mathrm{i}\mathbf{k}_{\mathrm{in}\parallel}\mathbf{R}_{p'}}\\
&\quad = \sum_{L=|l-l'|}^{|l+l'|} \begin{cases} a_5(l',m'|l,m|L) & \\ b_5(l',m'|l,m|L) & \end{cases} \sum_{p'\neq 0} h_L^{(1)}(k|\mathbf{R}_{p'}|) Y_{LM}(-\mathbf{R}_{p'}) \mathrm{e}^{\mathrm{i}\mathbf{k}_{\mathrm{in}\parallel}\mathbf{R}_{p'}} \begin{array}{ll} \tau = \tau' \\ \tau \neq \tau', \end{array}
\end{aligned}$$

with $M = m' - m$.

While the direct numerical evaluation of equation (6.9) can be successful in some cases, it can be extremely time consuming due to a slow convergence of its inner sum over all unit cells. This sum however, is identical to the quantity D_{LM} that is used to derive a lattice's *structure constants* [162, 163] in low energy electron diffraction theory [164]

$$D_{LM}(\mathbf{R}_{p'}) = \sum_{p'\neq 0} h_L^{(1)}(k|\mathbf{R}_{p'}|) Y_{LM}(-\mathbf{R}_{p'}) \mathrm{e}^{\mathrm{i}\mathbf{k}_{\mathrm{in}\parallel}\mathbf{R}_{p'}}. \tag{6.10}$$

6.3 Ewald summation

To evaluate the particulate lattice sum (6.10), I will here make use of solutions provided by the Ewald summation technique. Originally applied to describe long-range optical and electrostatic interactions in crystal lattices [165], Ewald's method became a widely used technique to apply PBCs not only in strictly periodic crystals but also in large molecular structures [166] and dynamic fluids [167].

The basic concept of the Ewald summation is to separate a semi-convergent series into a rapid and a slowly converging part. Transforming the latter into reciprocal space by means of the Possion

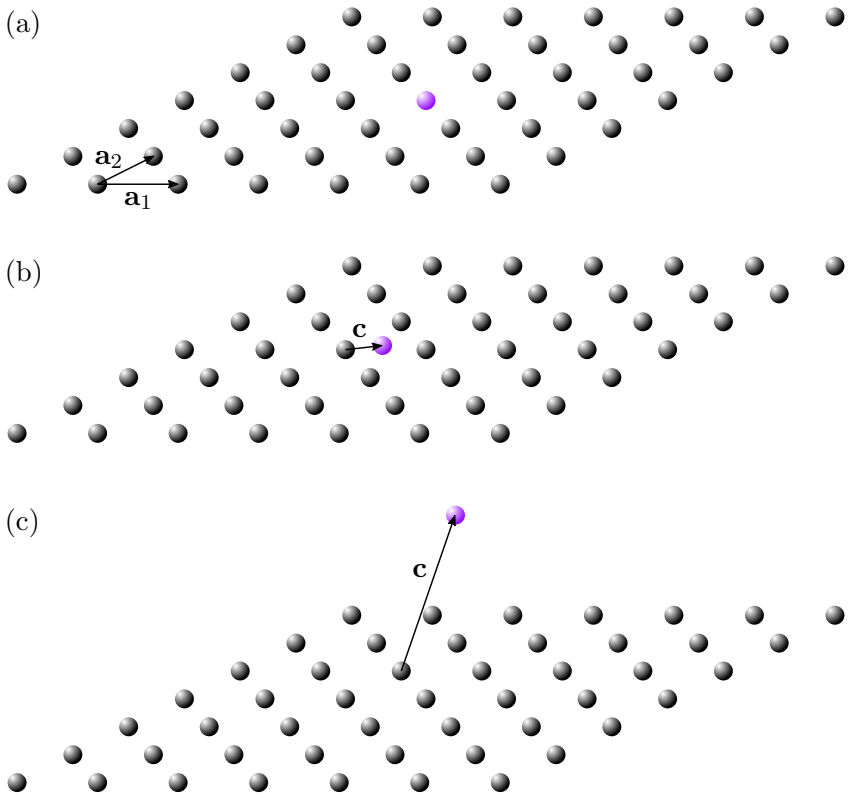

Figure 6.2: Three types of particulate lattice sums have to be evaluated: coupling between (a) particles within their own grid ($|\mathbf{c}| = 0$), (b) a particle grid and a particle of another displaced grid within the same horizontal plane ($c_z = 0$), (c) a particle grid and a particle from another particle collection at a different height ($c_z \neq 0$).

summation formula, one obtains a second, fast converging sum [168]. Following this idea, the Ewald type lattice sums are commonly written as

$$D^*_{LM} = D^{(1)}_{LM} + D^{(2)}_{LM} + \delta_{L0}\delta_{M0}D^{(3)}_{00}, \tag{6.11}$$

with $D^{(1)}_{LM}$ denoting the long range interactions evaluated in reciprocal space and $D^{(2)}_{LM}$ the short range contributions obtained from a real space sum. In addition, a correction term $D^{(3)}_{00}$ is added that only takes effect in the special case of coupling within a single particle collection and $L = M = 0$. For two-dimensional lattices the Ewald sum of periodic scattered fields in form of SVWFs has been derived by Kambe [169, 170]. Hereby providing an Ewald sum formulation that is directly applicable to the T-matrix formalism. Modeling the optical response of two-dimensional periodic particle arrays, T-matrix simulations in conjunction with an Ewald sum approach have been applied by Stefanou *et al.* [171, 172] and recently by Beutel *et al.* [173] as well as in three-dimensional arrays by Nečada *et al.* [174].

To build complex three-dimensional unit cells of a two-dimensional periodicity, I will need to determine the Ewald sum for three different kinds of lattice configurations (depicted in figure 6.2). Their explicit formulas can be traced back to Kambe [169, 170]. Here, I will stick to the

nomenclature presented in the supplementary material of reference [173], as my implementation of the lattice sums was realized in collaboration with Dominik Beutel. However, it is necessary to apply a normalization factor N_M to satisfy the normalization conventions of the SVWFs that are used throughout this work

$$D_{LM} = N_M D^*_{LM} = \sqrt{2\pi} \begin{cases} (-1)^{-M} \; D^*_{LM} & M > 0 \\ 1 & M \leq 0. \end{cases} \tag{6.12}$$

A short derivation of N_M can be found in Appendix C.

Coupling within one particle collection To account for the interaction between particles within the same particle collection S_q (illustrated in figure 6.2(a)), the long range contribution of lattice sum (6.10) reads

$$\begin{aligned} D^{(1)}_{LM} = \frac{\mathrm{i}^M}{(2k)^L} \frac{\sqrt{(2L+1)(L-M)!(L+M)!}}{Ak} \sum_{\tilde{p}} \mathrm{e}^{\mathrm{i}M\varphi_{\mathbf{k}_{\mathrm{in}\parallel}+\mathbf{G}_{\tilde{p}}}} \\ \times \sum_{\lambda=0}^{\frac{L-|M|}{2}} \frac{(\Gamma_{\mathbf{k}_{\mathrm{in}\parallel}+\mathbf{G}_{\tilde{p}}})^{2\lambda-1} |\mathbf{k}_{\mathrm{in}\parallel}+\mathbf{G}_{\tilde{p}}|^{L-2\lambda}}{\lambda!(\frac{L+M}{2}-\lambda)!(\frac{L-M}{2}-\lambda)!} \Gamma\left(\frac{1}{2}-\lambda, -\frac{\Gamma^2_{\mathbf{k}_{\mathrm{in}\parallel}+\mathbf{G}_{\tilde{p}}}}{4\eta^2}\right), \end{aligned} \tag{6.13}$$

with the azimuthal angle $\varphi_{\mathbf{k}_{\mathrm{in}\parallel}+\mathbf{G}_{\tilde{p}}}$ of the linear combination of the initial field's in-plane wave vector $\mathbf{k}_{\mathrm{in}\parallel}$ and the reciprocal lattice vector $\mathbf{G}_{\tilde{p}}$, the positive complex square root of

$$\Gamma_{\mathbf{k}_{\mathrm{in}\parallel}+\mathbf{G}_{\tilde{p}}} = \sqrt{k^2 - |\mathbf{k}_{\mathrm{in}\parallel}+\mathbf{G}_{\tilde{p}}|^2} \tag{6.14}$$

and the upper incomplete Gamma function

$$\Gamma(s,x) = \int_x^\infty t^{s-1}\mathrm{e}^{-t} dt. \tag{6.15}$$

A recursion formula for the evaluation of upper incomplete Gamma functions of negative half integers has been provided by Kambe [169].
The separation parameter η splits the lattice sum into its long range contribution and the short range summand

$$\begin{aligned} D^{(2)}_{LM} = (-\mathrm{i})(-1)^{\frac{L+M}{2}} \frac{\sqrt{(2L+1)(L-M)!(L+M)!}}{2^{L+1}\pi(\frac{L-M}{2})!(\frac{L+M}{2})!} \\ \times \sum_{p'\neq 0} \mathrm{e}^{\mathrm{i}\mathbf{k}_{\mathrm{in}\parallel}\mathbf{R}_{p'}} \mathrm{e}^{\mathrm{i}M\varphi_{-R_{p'}}} \frac{1}{k} \left(\frac{2|\mathbf{R}_{p'}|}{k}\right)^L \int_{\eta^2}^\infty u^{L-\frac{1}{2}} \mathrm{e}^{-|\mathbf{R}_{p'}|^2 u + \frac{k^2}{4u}} du. \end{aligned} \tag{6.16}$$

As mentioned above, for $L = M = 0$ a central particle correction is necessary to prevent that the particle couples with itself

$$D_{00}^{(3)} = \frac{1}{4\pi}\Gamma\left(-\frac{1}{2}, -\frac{k^2}{4\eta^2}\right). \tag{6.17}$$

Please note that for $L + M$ odd, the entire Ewald sum cancels itself and therefore vanishes completely [169].

Coupling between different particle collections If a unit cell is populated with more than one particle, one has to account for the interaction between different particle collections S_q and $S_{q'}$. Then, equation (6.9) that accounts for the contribution of collection $S_{q'}$'s scattered field to the incoming field of particles in collection S_q reads

$$\begin{aligned}\sum_{p'} W_{nn'}^{S_{0q}S_{p'q'}} \mathrm{e}^{\mathrm{i}\mathbf{k}_{\mathrm{in}\parallel}\mathbf{R}_{p'}} &= \sum_{p'\neq 0} A_{n'n}(-\mathbf{R}_{p'} - \mathbf{c}_{qq'})\mathrm{e}^{\mathrm{i}\mathbf{k}_{\mathrm{in}\parallel}\mathbf{R}_{p'}} \\ &= \sum_{L=|l-l'|}^{|l+l'|} \begin{cases} a_5(l',m'|l,m|L) & \tau = \tau' \\ b_5(l',m'|l,m|L) & \tau \neq \tau'. \end{cases} D_{LM}(\mathbf{R}_{p'} + \mathbf{c}_{qq'})\end{aligned} \tag{6.18}$$

In the above, a displacement vector $\mathbf{c}_{qq'} = \mathbf{r}_{0q} - \mathbf{r}_{0q'}$ was introduced that connects particles within one unit cell. The lattice sum then becomes

$$D_{LM}(\mathbf{R}_{p'} + \mathbf{c}_{qq'}) = \sum_{p'\neq 0} h_L^{(1)}(k|\mathbf{R}_{p'} + \mathbf{c}_{qq'}|)Y_{LM}(-\mathbf{R}_{p'} - \mathbf{c}_{qq'})\mathrm{e}^{\mathrm{i}\mathbf{k}_{\mathrm{in}\parallel}\mathbf{R}_{p'}}. \tag{6.19}$$

For its evaluation one has to distinguish between two cases. First, two particle collections that are located within the same plane of periodicity (cf. figure 6.2(b)), and secondly, two particle collections spanning over different planes (figure 6.2(c)).
In the former case ($c_z = 0$), the long range contribution can be evaluated via

$$\begin{aligned}D_{LM}^{(1)} = \frac{i^M}{(2k)^L}\frac{\sqrt{(2L+1)(L-M)!(L+M)!}}{Ak} \sum_{\tilde{p}} \mathrm{e}^{-\mathrm{i}(\mathbf{k}_{\mathrm{in}\parallel}+\mathbf{G}_{\tilde{p}})\mathbf{c}} \mathrm{e}^{\mathrm{i}M\varphi_{\mathbf{k}_{\mathrm{in}\parallel}+\mathbf{G}_{\tilde{p}}}} \\ \times \sum_{\lambda=0}^{\frac{L-|M|}{2}} \frac{(\Gamma_{\mathbf{k}_{\mathrm{in}\parallel}+\mathbf{G}_{\tilde{p}}})^{2\lambda-1}|\mathbf{k}_{\mathrm{in}\parallel} + \mathbf{G}_{\tilde{p}}|^{L-2\lambda}}{\lambda!(\frac{L+M}{2}-\lambda)!(\frac{L-M}{2}-\lambda)!}\Gamma\left(\frac{1}{2}-\lambda, -\frac{\Gamma^2_{\mathbf{k}_{\mathrm{in}\parallel}+\mathbf{G}_{\tilde{p}}}}{4\eta^2}\right)\end{aligned} \tag{6.20}$$

and in the latter ($c_z \neq 0$) via,

$$D_{LM}^{(1)} = \frac{(-i)^M}{(-2)^L} \frac{\sqrt{(2L+1)(L-M)!(L+M)!}}{Ak^2} \sum_{\tilde{p}} \mathrm{e}^{-\mathrm{i}(\mathbf{k}_{\mathrm{in}\parallel}+\mathbf{G}_{\tilde{p}})\mathbf{c}} \mathrm{e}^{\mathrm{i}M\varphi_{\mathbf{k}_{\mathrm{in}\parallel}+\mathbf{G}_{\tilde{p}}}} \times \sum_{n=0}^{L-|M|} \left(\frac{\Gamma_{\mathbf{k}_{\mathrm{in}\parallel}+\mathbf{G}_{\tilde{p}}}}{k}\right)^{2n-1} \Delta_n \sum_{s=n}^{\min(L-|M|,2n)} \frac{(-kc_z)^{2n-s} \left(\frac{|\mathbf{k}_{\mathrm{in}\parallel}+\mathbf{G}_{\tilde{p}}|}{k}\right)^{L-s}}{(2n-s)!(s-n)! \left(\frac{L+|M|-s}{2}\right)! \left(\frac{L-|M|-s}{2}\right)!}. \tag{6.21}$$

Independent of the particle displacement, the short range contribution reads

$$D_{LM}^{(2)} = -i\sqrt{\frac{2}{\pi}} \sum_{p'} \mathrm{e}^{\mathrm{i}\mathbf{k}_{\mathrm{in}\parallel}\mathbf{R}_{p'}} (k|\mathbf{R}_{p'}+\mathbf{c}|)^L \frac{Y_{LM}(-\mathbf{R}_{p'}-\mathbf{c})}{N_M} \times \int_{\eta^2}^{\infty} u^{2L} \mathrm{e}^{-\frac{(k|\mathbf{R}_{p'}+\mathbf{c}|)^2u^2}{2}+\frac{1}{2u^2}} du. \tag{6.22}$$

Besides the upper incomplete Gamma function, Kambe also provides recursion formulas for the evaluation of integral Δ_n and the integrals in equations (6.16) and (6.22) [169, 170].
With the above defined lattice sums, I now have all the tools available to build and solve light scattering in complex three-dimensional periodic particle arrangements of two dimensional periodicity. But before doing so, we shall first consider how to evaluate the scattered near- and far-field properties of periodic particle arrangements and incorporate the periodic structures into a planar, layered environment.

6.4 Periodic scattered fields

In contrast to non-periodic particle arrangements where the scattered field can be evaluated by superposition of each individual particle's scattered field, the scattered field of periodic particle arrangements is composed of an infinite number of source terms, rendering its direct evaluation challenging. However, any arrangement consists of a finite number of particle collections that each form a perfect lattice. Hence, the infinite periodic collections only scatter light into a finite number of discrete propagating waves and an infinite number of discrete evanescent waves [175], favoring a field representation in plane waves.

6.4.1 Scattered near-field

To obtain the scattered near-field of particle collection S_q, I start with the spherical-wave expansion of its individual particles

$$\begin{aligned}\mathbf{E}_{S_q}(\mathbf{r}) &= \sum_p \sum_n b_n^{S_{pq}} \mathbf{M}_n^{(3)}\left(\mathbf{r} - \mathbf{r}_{S_{pq}}\right) \\ &= \sum_{p'} \sum_n b_n^{S_{0q}} \mathrm{e}^{\mathrm{i}\mathbf{k}_{\mathrm{in}\parallel}\mathbf{R}_{p'}} \mathbf{M}_n^{(3)}(\mathbf{r} - \mathbf{r}_{S_{0q}} - \mathbf{R}_{p'}).\end{aligned} \tag{6.23}$$

Transforming equation (6.23) into plane waves (cf. equation (2.40)), the infinite sum reads

$$\begin{aligned}\mathbf{E}_{S_q}(\mathbf{r}) =& \frac{1}{2\pi} \sum_{p'} \sum_n b_n^{S_{0q}} \sum_{j=1}^{2} \int \frac{d^2\mathbf{k}_\parallel}{k_z k} \mathrm{e}^{\mathrm{i}m\alpha} \\ &\times B_{nj}\left(\pm\frac{k_z}{k}\right) \mathrm{e}^{\mathrm{i}\mathbf{k}^\pm(\mathbf{r}-\mathbf{r}_{S_{0q}})} \mathrm{e}^{\mathrm{i}(\mathbf{k}_{\mathrm{in}\parallel}-\mathbf{k}^\pm)\mathbf{R}_{p'}} \hat{\mathbf{e}}_j^\pm, \qquad \text{for } z \gtrless z_{S_{0q}}.\end{aligned} \tag{6.24}$$

Whether upwards or downwards propagating plane waves are taken into account depends on the relative position of $\mathbf{r}$ with respect to the particle collection S_q.
Splitting

$$\mathrm{e}^{\mathrm{i}(\mathbf{k}_{\mathrm{in}\parallel}-\mathbf{k}^\pm)\mathbf{R}_{p'}} = \mathrm{e}^{\pm\mathrm{i}k_z\mathbf{R}_{p'}} \mathrm{e}^{\mathrm{i}(\mathbf{k}_{\mathrm{in}\parallel}-\mathbf{k}_\parallel)\mathbf{R}_{p'}} \tag{6.25}$$

into its in-plane and z-component allows us to use the Poisson summation formula

$$\sum_{p'} \mathrm{e}^{\mathrm{i}(\mathbf{k}_{\mathrm{in}\parallel}-\mathbf{k}_\parallel)\mathbf{R}_{p'}} = \frac{(2\pi)^2}{A_{\mathrm{uc}}} \sum_{\tilde{p}} \delta(\mathbf{k}_\parallel - \mathbf{k}_{\mathrm{in}\parallel} + \mathbf{G}_{\tilde{p}}), \tag{6.26}$$

to "reduce" the infinite sum of plane-wave integral representations into an infinite sum of discrete plane waves $\mathbf{\Phi}_j^\pm$

$$\mathbf{E}_{S_q}(\mathbf{r}) = \sum_{j=1}^{2} \sum_{\tilde{p}} g_{S_{0q},j}^\pm(\kappa,\alpha) \mathbf{\Phi}_j^\pm(\kappa,\alpha;\mathbf{r}-\mathbf{r}_{S_{0q}}) \delta(\mathbf{k}_\parallel - \mathbf{k}_{\mathrm{in}\parallel} + \mathbf{G}_{\tilde{p}}). \tag{6.27}$$

The amplitudes of each plane wave read

$$g_{S_{0q},j}^\pm(\kappa,\alpha) = \frac{2\pi}{A_{\mathrm{uc}}} \sum_n \frac{b_n^{S_{0q}}}{k_z k} \mathrm{e}^{\mathrm{i}m\alpha} B_{nj}\left(\pm\frac{k_z}{k}\right), \tag{6.28}$$

where A_{uc} specifies the base area of one unit cell.
The obtained formula shows that the infinite periodic lattice only scatters into an infinite number of discrete angles, for which the in-plane wave vector $\mathbf{k}_\parallel$ coincides with the sum of the initial field's in-plane wave vector $\mathbf{k}_{\mathrm{in}\parallel}$ and the reciprocal lattice points $\mathbf{G}_{\tilde{p}}$. In practice, the infinite sum (6.27) needs to be truncated at the finite order of unit cells $\tilde{p} < \tilde{p}_{\max}$ that add a meaningful

contribute to the collection's near-field. For positions $\mathbf{r}$ in great distance to the particle collection, it can be sufficient to account for propagating waves only, i.e., in-plane wave vectors $\mathbf{k}_{\parallel}$ for which $|\mathbf{k}_{\mathrm{in}\parallel} - \mathbf{G}_{\tilde{p}}| < k$.

6.4.2 Scattered far-field

The plane-wave expansion (6.27) does not only contain information about the scattered near-field of a periodic particle collection but also about far-field properties. Removing all evanescent waves from the discrete plane-wave spectrum, the angle dependent transmittance and reflectance can be determined.
The power flow of a plane wave into vertical direction per area

$$I_A^{\pm} = \frac{dP}{dA} = \frac{k}{2\omega\mu_0} \cos\beta^{\pm} \, |g^{\pm}(\kappa, \alpha)|^2, \tag{6.29}$$

depends on its polar angle of propagation β, with $\beta^{+} = \arcsin(\kappa/k)$ and $\beta^{-} = \pi - \arcsin(\kappa/k)$. To obtain the total transmitted and reflected power of a periodic arrangement, the sum over all scattered, propagating waves yields

$$I^{\pm} = \frac{k}{2\omega\mu_0} \sum_{q} \sum_{j=1}^{2} \sum_{\tilde{p}} \cos\beta \, |g^{\pm}_{S_{0q},j}(\kappa, \alpha)|^2 \delta(\mathbf{k}_{\parallel} - \mathbf{k}_{\mathrm{in}\parallel} + \mathbf{G}_{\tilde{p}}), \qquad \kappa \leq k. \tag{6.30}$$

Independent of the complexity of a unit cell, each particle collection scatters into the identical discrete plane waves resulting from the one periodicity all particle collections have in common. Hence, the scattered far-field of a periodic system does not exhibit a continuous angular field distribution [176], which is in clear contrast to a finite, disordered particle arrangement. However, the length of reciprocal lattice vectors decreases for larger unit cell sizes, allowing an increasing number of propagating diffraction orders. In the limit of an infinite unit cell size, the periodic system merges into an aperiodic system, causing the angular far-field distribution to become continuous.
To illustrate the discrete directionality of periodic scattered fields, the polar distribution of a simple cubic lattice with a single particle per unit cell is displayed in figure 6.3(a). The period P of the lattice measures two times the length of the excitation's wavelength, allowing the scattered field to propagate only under 0°, 30° and 45°. For comparison, the polar distributions of the scattered far-field for various finite grid sizes are shown. As expected, the finite sized grids show side maxima that diminish with increasing lattice size. Increasing the period-wavelength-ratio P/λ, more and more propagating waves populate the angular distribution, leading to a typical far-field pattern of a periodic particle arrangement with a large unit cell of $P/\lambda = 7.5$ (figure 6.3(b)). To mimic the diffusive character of transmittance and reflectance by disordered media, the size of a unit cell thus plays an important role in any periodic modeling approach.

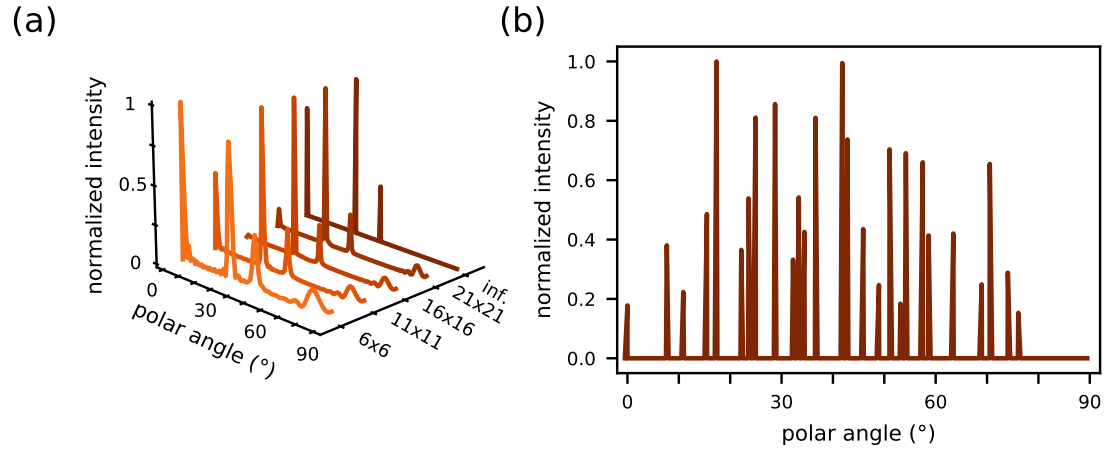

Figure 6.3: Scattered far-field polar distribution of a two-dimensional, periodic particle arrangement (a) for an infinite grid and different finite grid sizes between 6 by 6 and 21 by 21 unit cells with a cubic period-wavelength-ratio P/λ of 2. (b) Typical far-field distribution for an infinite periodic particle arrangement with a cubic unit cell of $P/\lambda = 7.5$.

6.5 Periodic plane-wave coupling

Chapter 4 deals with a direct plane-wave coupling formalism to account for interactions between particles with overlapping circumscribing spheres. For the periodic particle arrangements I do not consider such dense, nonspherical particle collections. Nevertheless, it can be beneficial to account for the direct coupling between periodic particle collections by means of a plane-wave expansion. In the previous section, the scattered field of a periodic particle collection has been expressed by a discrete set of plane waves (cf. equation (6.27)) that is valid everywhere above or below the particle grid. Given that a vertical plane of separation between particle collections S_q and $S_{q'}$ can be found

$$z_{S_{0q}} - z_{S_{0q'}} = \Delta z_{S_q S_{q'}} > r_{S_{0q}} - r_{S_{0q'}}, \tag{6.31}$$

the plane-wave expansion can be used to account for the direct coupling between the two-dimensional lattices.

I start with the scattered field of particle collection $S_{q'}$ and translate it to the center of S_q

$$\begin{aligned}\mathbf{E}_{S_{q'}}(\mathbf{r}) = \frac{2\pi}{A_{\mathrm{uc}}} \sum_{j=1}^{2} \sum_{\tilde{p}} \sum_{n'} \frac{b_{n'}^{S_{0q'}}}{k_z k} \mathrm{e}^{\mathrm{i}m'\alpha} B_{n'j}\left(\pm\frac{k_z}{k}\right) \\ \times \mathbf{\Phi}_j^{\pm}(\kappa, \alpha; \mathbf{r} - \mathbf{r}_{S_{0q'}}) \delta(\mathbf{k}_{\parallel} - \mathbf{k}_{\mathrm{in}\parallel} + \mathbf{G}_{\tilde{p}}) \\ = \frac{2\pi}{A_{\mathrm{uc}}} \sum_{j=1}^{2} \sum_{\tilde{p}} \sum_{n'} \frac{b_{n'}^{S_{0q'}}}{k_z k} \mathrm{e}^{\mathrm{i}m'\alpha} B_{n'j}\left(\pm\frac{k_z}{k}\right) \mathrm{e}^{\mathrm{i}\mathbf{k}^{\pm}(\mathbf{r}_{S_{0q}} - \mathbf{r}_{S_{0q'}})} \\ \times \mathbf{\Phi}_j^{\pm}(\kappa, \alpha; \mathbf{r} - \mathbf{r}_{S_{0q}}) \delta(\mathbf{k}_{\parallel} - \mathbf{k}_{\mathrm{in}\parallel} + \mathbf{G}_{\tilde{p}}).\end{aligned} \tag{6.32}$$

With the retransformation into regular SVWFs (cf. equation (2.39))

$$\mathbf{E}_{S_{q'}}(\mathbf{r}) = \frac{8\pi}{A_{\mathrm{uc}}} \sum_{n} \sum_{j=1}^{2} \sum_{\tilde{p}} \sum_{n'} \frac{b_{n'}^{S_{0q'}}}{k_z k} \mathrm{e}^{\mathrm{i}(m'-m)\alpha} B_{n'j}\left(\pm\frac{k_z}{k}\right) B_{nj}^{\dagger}\left(\pm\frac{k_z}{k}\right) \times \mathrm{e}^{\mathrm{i}\mathbf{k}^{\pm}(\mathbf{r}_{S_{0q}}-\mathbf{r}_{S_{0q'}})} \mathbf{M}_{n}^{(1)}(\mathbf{r}-\mathbf{r}_{S_{0q}}) \delta(\mathbf{k}_{\parallel}-\mathbf{k}_{\mathrm{in}\parallel}+\mathbf{G}_{\tilde{p}}), \tag{6.33}$$

one obtains the incoming field at particle S_{0q} that directly originates from the scattered field of particle collection $S_{q'}$. The spherical-wave amplitudes then read

$$a_{n}^{S_{0q}S_{q'}} = \frac{8\pi}{A_{\mathrm{uc}}} \sum_{j=1}^{2} \sum_{\tilde{p}} \sum_{n'} \frac{b_{n'}^{S_{0q'}}}{k_z k} \mathrm{e}^{\mathrm{i}(m'-m)\alpha} B_{n'j}\left(\pm\frac{k_z}{k}\right) B_{nj}^{\dagger}\left(\pm\frac{k_z}{k}\right) \times \mathrm{e}^{\mathrm{i}\mathbf{k}^{\pm}(\mathbf{r}_{S_{0q}}-\mathbf{r}_{S_{0q'}})} \delta(\mathbf{k}_{\parallel}-\mathbf{k}_{\mathrm{in}\parallel}+\mathbf{G}_{\tilde{p}}). \tag{6.34}$$

$$\tag{6.35}$$

Compared with the definition of the coupling matrix (3.36)

$$a_{n}^{S_{0q}S_{q'}} = \sum_{n'} W_{nn'}^{S_{0q}S_{q'}} b_{n'}^{S_{0q'}}, \tag{6.36}$$

I find

$$W_{nn'}^{S_{0q}S_{q'}} = \frac{8\pi}{A_{\mathrm{uc}}} \sum_{j=1}^{2} \sum_{\tilde{p}} \frac{1}{k_z k} \mathrm{e}^{\mathrm{i}(m'-m)\alpha} B_{n'j}\left(\pm\frac{k_z}{k}\right) B_{nj}^{\dagger}\left(\pm\frac{k_z}{k}\right) \times \mathrm{e}^{\mathrm{i}\mathbf{k}^{\pm}(\mathbf{r}_{S_{0q}}-\mathbf{r}_{S_{0q'}})} \delta(\mathbf{k}_{\parallel}-\mathbf{k}_{\mathrm{in}\parallel}+\mathbf{G}_{\tilde{p}}). \tag{6.37}$$

With this coupling operator, it is possible to evaluate the lattice sum (6.18) and to avoid the much more complicated Ewald summation. However, the plane-wave formalism is in general only valid if an infinite number of scattered wave vectors $\mathbf{k}^{\pm}$ are taken into account for which $\mathbf{k}_{\parallel} = \mathbf{k}_{\mathrm{in}\parallel} + \mathbf{G}_{\tilde{p}}$. In comparison to the Ewald summation, the greatest reduction in computation time can be achieved if $\Delta z_{S_q S_{q'}} \gg r_{S_{0q}} + r_{S_{0q'}}$, for which only propagating plane waves add a meaningful contribution to the particle coupling.

In the simulation examples of chapter 7 thick scattering layers are treated. For these, I will often make use of the alternative coupling operator, since most interactions between particle collections have to bridge a large vertical displacement, ensuring a strong damping of evanescent contributions.

6.6 Layer mediated coupling

In section 6.2 I have excluded periodic particle arrangements that are located in a planar, layered environment to simplify the introduction of the lattice sums and herewith the periodic solutions

of the multiple scattering problem. Later, we have seen that the scattered field of a periodic particle collection can be described by a discrete set of plane waves. These plane waves can now be utilized to describe the indirect particle coupling between periodic particle collections in a layered environment, following the transformation-translation-transformation scheme for the indirect coupling between individual particles, presented in section 3.4.2.2.
Again, the formalism starts with the scattered field of particle collection $S_{q'}$ and its transformation into plane waves (cf. equation (6.24))

$$\begin{aligned}\mathbf{E}_{S_{q'}}(\mathbf{r}) &= \sum_p \sum_{n'} b_{n'}^{S_{pq'}} \mathbf{M}_{n'}^{(3)}\left(\mathbf{r}-\mathbf{r}_{S_{pq'}}\right) \\ &= \frac{2\pi}{A_{\mathrm{uc}}} \sum_{j=1}^{2} \sum_{\tilde{p}} \sum_{n'} \frac{b_{n'}^{S_{0q'}}}{k_{z,i_{S_{q'}}} k_{i_{S_{q'}}}} \mathrm{e}^{\mathrm{i}m'\alpha} B_{n'j}\left(\pm\frac{k_{z,i_{S_{q'}}}}{k_{i_{S_{q'}}}}\right) \\ &\qquad \times \mathbf{\Phi}_j^{\pm}(\kappa,\alpha;\mathbf{r}-\mathbf{r}_{S_{0q'}})\delta(\mathbf{k}_{\parallel}-\mathbf{k}_{\mathrm{in}\parallel}+\mathbf{G}_{\tilde{p}}).\end{aligned} \tag{6.38}$$

A translation to the layer anchor point $\mathbf{r}_{i_{S_{q'}}}$ yields the plane-wave expansion

$$\begin{aligned}\mathbf{E}_{S_{q'}}(\mathbf{r}) &= \frac{2\pi}{A_{\mathrm{uc}}} \sum_{j=1}^{2} \sum_{\tilde{p}} \sum_{n'} \frac{b_{n'}^{S_{0q'}}}{k_{z,i_{S_{q'}}} k_{i_{S_{q'}}}} \mathrm{e}^{\mathrm{i}m'\alpha} B_{n'j}\left(\pm\frac{k_{z,i_{S_{q'}}}}{k_{i_{S_{q'}}}}\right) \mathrm{e}^{\mathrm{i}\mathbf{k}^{\pm}(\mathbf{r}_{i_{S_{q'}}}-\mathbf{r}_{S_{0q'}})} \\ &\qquad \times \mathbf{\Phi}_j^{\pm}(\kappa,\alpha;\mathbf{r}-\mathbf{r}_{i_{S_{q'}}})\delta(\mathbf{k}_{\parallel}-\mathbf{k}_{\mathrm{in}\parallel}+\mathbf{G}_{\tilde{p}}) \\ &= \sum_{j=1}^{2} \sum_{\tilde{p}} g^{\pm}_{S_{0q'},i_{S_{q'}},j}(\kappa,\alpha)\mathbf{\Phi}_j^{\pm}(\kappa,\alpha;\mathbf{r}-\mathbf{r}_{i_{S_{q'}}})\delta(\mathbf{k}_{\parallel}-\mathbf{k}_{\mathrm{in}\parallel}+\mathbf{G}_{\tilde{p}}),\end{aligned} \tag{6.39}$$

with amplitudes

$$g^{\pm}_{S_{0q'},i_{S_{q'}},j}(\kappa,\alpha) = \frac{2\pi}{A_{\mathrm{uc}}} \frac{\mathrm{e}^{-\mathrm{i}\mathbf{k}_{\parallel}\mathbf{r}_{S_{0q',\parallel}}}}{k_{z,i_{S_{q'}}} k_{i_{S_{q'}}}} \sum_{n'} b_{n'}^{S_{0q'}} \mathrm{e}^{\mathrm{i}m'\alpha} \beta^{\pm}_{S_{0q'},n',j}(\kappa). \tag{6.40}$$

To match the formalism for individual particles, I have included $\beta^{\pm}(\kappa)$ (cf. equation 3.42) that only contains the lateral translation between particle $S_{0q'}$ and its layer anchor point.
In analogy to equations (3.21) and (3.22), the layer system response in layer i_{S_q}, in which collection S_q is located, takes the form of

$$\begin{aligned}\mathbf{E}^{\mathrm{R}}_{S_{q'}}(\mathbf{r}) = \sum_{j=1}^{2} \sum_{\tilde{p}} &\left[\mathbf{\Phi}_j^{+}(\kappa,\alpha;\mathbf{r}-\mathbf{r}_{i_{S_q}}), \mathbf{\Phi}_j^{-}(\kappa,\alpha;\mathbf{r}-\mathbf{r}_{i_{S_q}})\right] \begin{bmatrix} g^{\mathrm{R}+}_{S_{0q'},i_{S_q},j}(\kappa,\alpha) \\ g^{\mathrm{R}-}_{S_{0q'},i_{S_q},j}(\kappa,\alpha)\end{bmatrix} \\ &\times \delta(\mathbf{k}_{\parallel}-\mathbf{k}_{\mathrm{in}\parallel}+\mathbf{G}_{\tilde{p}})\end{aligned} \tag{6.41}$$

with the plane wave amplitudes

$$\begin{bmatrix} g^{\mathrm{R}+}_{S_{0q'},i_{S_q},j}(\kappa,\alpha) \\ g^{\mathrm{R}-}_{S_{0q'},i_{S_q},j}(\kappa,\alpha) \end{bmatrix} = \frac{2\pi}{A_{\mathrm{uc}}} \frac{\mathrm{e}^{-\mathrm{i}\mathbf{k}_\parallel \mathbf{r}_{S_{q',\parallel}}}}{k_{z,i_{S_{q'}}} k_{i_{S_{q'}}}} \sum_{n'} b^{S_{0q'}}_{n'} \mathrm{e}^{\mathrm{i}m'\alpha} L_j^{i_{S_q},i_{S_{q'}}}(\kappa) \begin{bmatrix} \beta^{+}_{S_{0q'},n',j}(\kappa) \\ \beta^{-}_{S_{0q'},n',j}(\kappa) \end{bmatrix}. \tag{6.42}$$

Translating the layer system response from the layer anchor point $\mathrm{r}_{i_{S_q}}$ to the central particle of collection S_q and retransforming the plane-wave expansion into regular SVWFs (cf. equation (2.39)) I find

$$\mathbf{E}^{\mathrm{R}}_{S_{q'}}(\mathbf{r}) = \sum_n a_n^{S_q,\mathrm{R},S_{q'}} \mathbf{M}^{(1)}_n(\mathbf{r} - \mathbf{r}_{S_q}) \tag{6.43}$$

with the spherical wave amplitudes

$$\begin{aligned} a_n^{S_q,\mathrm{R},S_{q'}} &= 4 \sum_{j=1}^{2} \sum_{\tilde{p}} \mathrm{e}^{-\mathrm{i}m\alpha} \mathrm{e}^{\mathrm{i}\mathbf{k}_\parallel \mathbf{r}_{S_{0q},\parallel}} \\ &\quad \times \left[\beta^{+,\dagger}_{S_{0q},n,j}(\kappa), \beta^{-,\dagger}_{S_{0q},n,j}(\kappa) \right] \begin{bmatrix} g^{\mathrm{R}+}_{S_{0q'},i_{S_q},j}(\kappa,\alpha) \\ g^{\mathrm{R}-}_{S_{0q'},i_{S_q},j}(\kappa,\alpha) \end{bmatrix} \delta(\mathbf{k}_\parallel - \mathbf{k}_{\mathrm{in}\parallel} + \mathbf{G}_{\tilde{p}}) \\ &= \sum_{n'} W^{S_q,\mathrm{R},S_{q'}}_{nn'} b^{S_{0q'}}_{n'}. \end{aligned} \tag{6.44}$$

Inserting equation (6.42), one obtains the elements of the layer system response coupling matrix

$$\begin{aligned} W^{S_q,\mathrm{R},S_{q'}}_{nn'} =& \frac{8\pi}{A_{\mathrm{uc}}} \sum_{j=1}^{2} \sum_{\tilde{p}} \frac{\mathrm{e}^{\mathrm{i}\mathbf{k}_\parallel (\mathbf{r}_{S_q,\parallel} - \mathbf{r}_{S_{q'},\parallel})}}{k_{z,i_{S_{q'}}} k_{i_{S_{q'}}}} \mathrm{e}^{\mathrm{i}(m'-m)\alpha} \\ &\times \left[\beta^{+,\dagger}_{S_{0q},n,j}(\kappa), \beta^{-,\dagger}_{S_{0q},n,j}(\kappa) \right] L_j^{i_{S_q},i_{S_{q'}}}(\kappa) \begin{bmatrix} \beta^{+}_{S_{0q'},n',j}(\kappa) \\ \beta^{-}_{S_{0q'},n',j}(\kappa) \end{bmatrix} \delta(\mathbf{k}_\parallel - \mathbf{k}_{\mathrm{in}\parallel} + \mathbf{G}_{\tilde{p}}) \end{aligned} \tag{6.45}$$

that describes how the scattered field of particle collection $S_{q'}$ acts on the incoming field of collection S_q mediated by the planar, layered environment.

6.7 Validation

To validate the implementation of the periodic T-matrix formalism and Ewald's method to account for infinite lattice sums, the transmittance of plane waves through periodic particle arrangements is compared to a FEM reference solution.

In the here studied exemplary configuration, one cubic unit cell with a period of $P = |\mathbf{a}_1| = |\mathbf{a}_2| = 1\,\mu\mathrm{m}$ is randomly populated with 15 spheres of various sizes. Figure 6.4 shows the transmittance for polar angles of excitation between $0°$ and $90°$. Hereby, the downwards propagating, linear

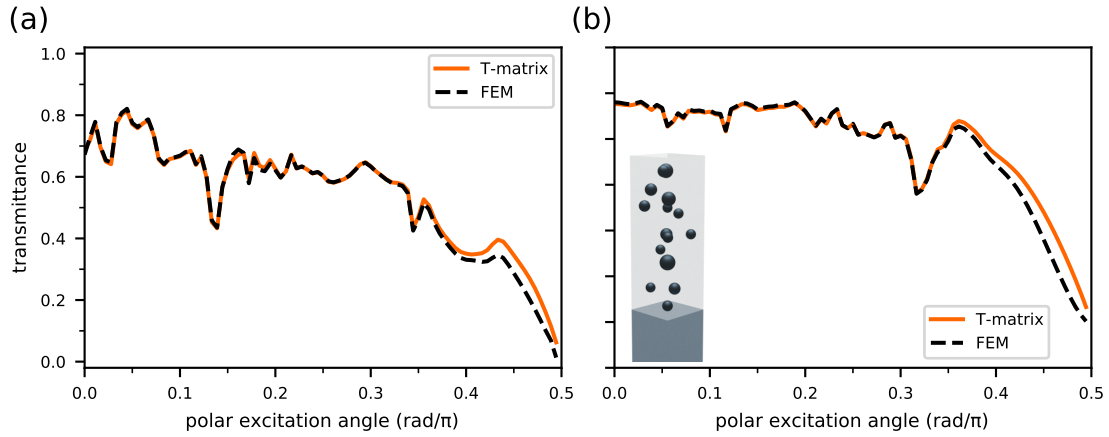

Figure 6.4: Transmittance of a plane wave through a periodic particle arrangement of 15 spheres per unit cell, for polar angles of excitation between 0 and 0.5π, turning the x-polarized plane wave into z-polarization. Comparison to an FEM reference solution for (a) particles embedded in a homogeneous air environment, (b) particles embedded in a low refractive index material between a glass substrate and air.

polarized plane wave ($\lambda_0 = 500\,\mathrm{nm}$) is varied from x-polarization ($\beta = 0$) to z-polarization ($\beta = \pi/2$). Figure 6.4 (a) draws the comparison between the T-matrix solution (orange) and the FEM reference (black, dashed) for particles in a homogeneous air environment. In figure 6.4 (b) the particles of refractive index $n_\mathrm{p} = 2$ are embedded in an ambient material of $n_\mathrm{amb} = 1.3$ that is surrounded by a glass substrate and air. An illustration of the configuration can be found as an inset of figure 6.4 (b).

The two scenarios are chosen in a way that all previously introduced lattice sums for particle configurations in and out of plane, the direct plane-wave coupling as well as the indirect layer mediated coupling are applied. For both configurations, the T-matrix and FEM simulations show excellent agreement, validating the implementation of the periodic T-matrix approach. However, for highly oblique angles of excitation, a slight deviation between both techniques can be observed. Its cause remains open, as I suspect numerical difficulties for both techniques under highly oblique incidence. In case of finite element simulations, PMLs are known to reflect a considerable amount of light back into the simulation domain for highly oblique incidence [177]. To improve their performance, a variety of specialized techniques have been discussed [178], which are beyond the scope of this work. In my example, I have applied a simple coordinate stretching within the PML that adjusts the wavenumber $k_\mathrm{PML} = k\cos(\beta)$ by the polar angle of excitation. Without this adjustment I have obtained non-physical results for $\beta > \pi/4$. In the other case, the evaluation of the Ewald type lattice sums is numerically challenging once the second argument of the upper incomplete Gamma function

$$\Gamma\left(\frac{1}{2}-\lambda, -\frac{\Gamma^2_{\mathbf{k}_{\mathrm{in}\parallel}+\mathbf{G}_{\tilde{p}}}}{4\eta^2}\right) = \Gamma\left(\frac{1}{2}-\lambda, -\frac{k^2-|\mathbf{k}_{\mathrm{in}\parallel}+\mathbf{G}_{\tilde{p}}|^2}{4\eta^2}\right) \tag{6.46}$$

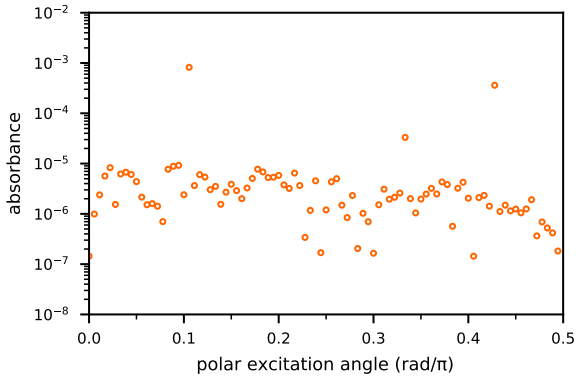

Figure 6.5: Absorbance of a plane wave exciting a periodic particle arrangement embedded in a waveguide, between a glass substrate and air. The infinite particle extend prevents the formation of wave-guided modes.

approaches zero. For highly oblique incidence ($|\mathbf{k}_{\mathrm{in}\parallel}| \approx k$), the exponential growth in the upper incomplete Gamma function can thus lead to numerical overflow [179, 180].

Besides the comparison with external software, a test of energy conservation can verify the consistency of a simulation result and therefore is a powerful tool to rule out errors in complex software. For this purpose, the far-field balance of any lossless, exemplary configuration can be reviewed. The absence of loss, i.e., only non-absorbing material and a layer structure that does not support wave guiding, is required to prevent a mismatch in the far-field balance.
The example discussed in figure 6.4 meets both these conditions and therefore would be a suitable exemplary configuration. However, I would like to emphasize that for infinite periodic particle arrangements incorporated into a wave guide structure, the formation of wave guided modes can be prevented and hence, also allows to test the conservation of energy.
To illustrate the suppression of waveguide modes in a wave guide structure with an infinite periodic particle arrangement, the exemplary configuration from figure 6.4 is altered, by replacing the particles' low refractive index ambient by a refractive index of $n_{\mathrm{amb}} = 1.7$. In case of a finite particle arrangement, light exciting this system, would in part be scattered into the waveguide, leading to a mismatch in the far-field energy balance. In case of infinite periodic systems however, the almost negligible absorbance of a plane wave ($\lambda_0 = 650\,\mathrm{nm}$) exciting the structure under various incident angles, shown in figure 6.5, confirms the suppression of waveguide modes and the conservation of energy.

6.8 Mimicking disorder

As indicated at the beginning of this chapter, I have applied periodic boundary conditions to the superposition T-matrix approach to mimic light scattering in large, disordered particle arrangements. In doing so, I expect to reduce the computational effort to an acceptable level that allows

to investigate light management structures in optoelectronic devices not only for a few distinct wavelengths, but to derive a continuous wavelength dependency.
Applying artificial periodicities to disordered nanostructures has been widely practiced in the past. In commonly applied effective medium approximations e.g., light scattering is taken into account by a periodic, average scattering response of a heterogeneous medium's sub-domain [181, 182]. Based on these coherent potential approximations [183], the medium's disorder is packaged in a cubic periodicity, allowing to utilize many of the available tools for crystalline band structures [162, 163].
Aside from various effective medium approximations, many approaches to solve Maxwell's equations have capitalized on artificial periodicities. With the possibility to comprise a particle ensemble's multiple scattering response in a single, collective T-matrix, the spherical-wave-based formalism can be applied to approximate disorder in form of a two-dimensional lattice of an average unit cell [184–186]. Comparable to this multipole approach, the optical response of heterogeneous media was also investigated [176, 187] on the basis of the periodic DDA [188, 189].
Independent of the method of choice, the goal of mimicking disorder raises two central questions:

To what extent does an artificial periodicity influence any observable quantity?

How does one minimize any detrimental effect of an artificial periodicity?

Considering a single simulation, these questions might be hard to assess as it is unclear how an exact reference solution could be obtained. Therefore, it is in general necessary to perform a sample averaging to rule out fluctuations in the scattering response of discrete particle arrangements.

Averaging the transmittance of plane waves impinging onto infinite, periodic porous polymer layers, it has been shown that fluctuations between individual random realizations cannot explain the severe wavelength dependency that was observed [2]. More likely, one can attribute the strong wavelength dependency to lattice resonances that can be excited even if the periodicity measures a multitude of the wavelength of interest. To visualize such lattice resonances, figure 6.6(a) shows the L^2-norm of the direct coupling operator between a particle and its own infinite periodic extent (cf. equation (6.9)) as a function of periodicity and period-wavelength-ratio, for a lattice excited under normal incidence. With an increasing particle separation, an exponential decay in the coupling strength between individual particles is to be expected. Overall, such a decay can be observed for two-particle configurations (black, dashed), as well as for finite (orange) and infinite grids (blue). For distinct period-wavelength-ratios however, strong resonances in the particle coupling arise, when the linear combination of the excitation's in-plane wave vector and the reciprocal lattice vector coincide with the wavenumber of excitation. Hereby, the radicand of the positive square root

$$\Gamma_{\mathbf{k}_{\mathrm{in}||}+\mathbf{G}_{\tilde{p}}} = \sqrt{k^2 - |\mathbf{k}_{\mathrm{in}||} + \mathbf{G}_{\tilde{p}}|^2} \tag{6.47}$$

causes singularities in the Ewald lattice sums. The formation of lattice resonances can also be observed in finite particle grids (in this case 21 x 21 unit cells), for which the particle coupling is computed as the direct sum of the translation addition operator, indicating that the singularities do

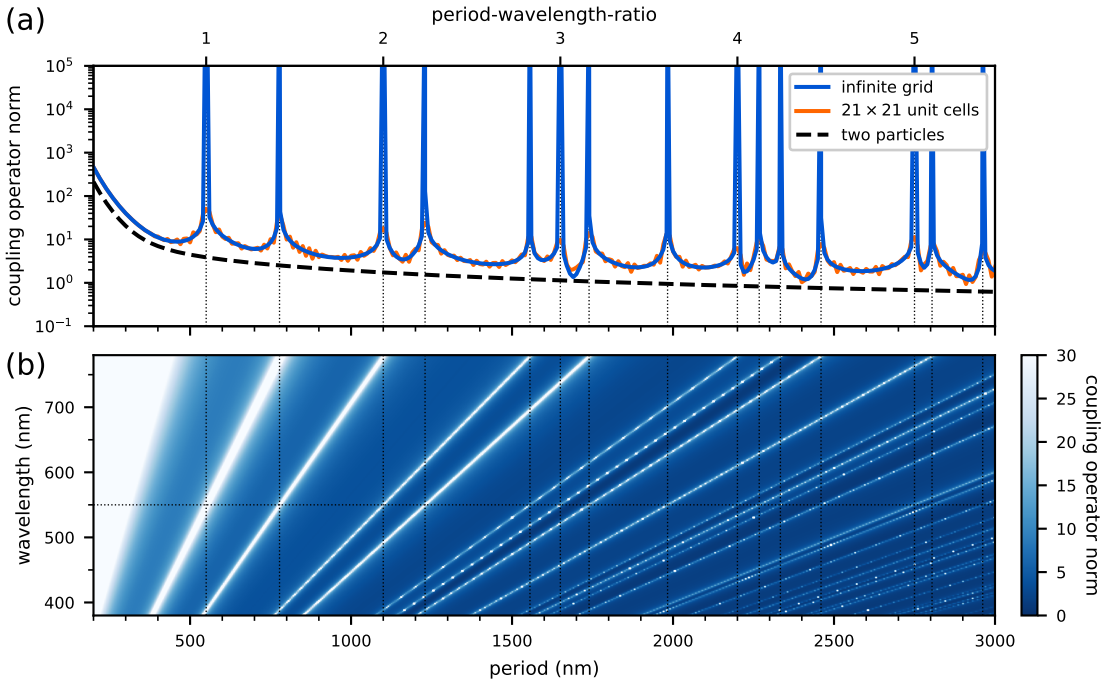

Figure 6.6: (a) Comparison of the L^2-norm of the coupling operator between particles within an infinite lattice, a finite lattice of 21 times 21 unit cells and two distinct scatterers as a function of the particle displacement. Embedded in vacuum, the particles ($n_\mathrm{p} = 2$) have been excited by a perpendicular propagating plane wave ($\lambda_0 = 550\,\mathrm{nm}$) with respect to the particle displacement. Adapted from reference [2]. (b) Resonances in the lattice coupling operator norm linearly shift with the wavelength of excitation.

not arise from a mathematical misfeature in the Ewald sum.

For a given angle of incidence, the linear relationship between wavenumber k and in-plane wavenumber $\kappa = |\mathbf{k}_{\mathrm{in}||}|$ causes the lattice resonances to shift linearly with the wavelength of excitation (see figure 6.6(b)). This opens up the possibility to fully circumvent the excitation of lattice resonances throughout a wavelength sweep by linearly shifting the unit cell size with the wavelength of excitation.

The effect of a constant period-wavelength-ratio P/λ on the average transmittance of plane waves by a $2\,\mu\mathrm{m}$ thick, periodic particle slab is shown in figure 6.7(a). The example compares a constant period of $2\,\mu\mathrm{m}$ with a constant period-wavelength-ratio of 9.65 and is taken from reference [2]. Varying the unit cell size to preserve P/λ clearly removes any strong variations in the measured transmittance. The explicit ratio of P/λ has been chosen somewhat arbitrary but in clear distance to the neighboring resonances at $P/\lambda = 9.49$ and 9.85. A comparison between wavelength sweeps of different period-wavelength-ratios that are free of lattice resonances can be seen in figure 6.7(b). Preserving the period-wavelength-ratio throughout a wavelength sweep requires to change the simulation model for each excitation wavelength. To ensure that the particle arrangements change only slightly between the different wavelengths, I prepare the particle configuration only for the largest unit cell needed. For different wavelengths of excitation only a sub-domain of this original unit cell is considered. This process inevitably leads to small variations in particle density. To

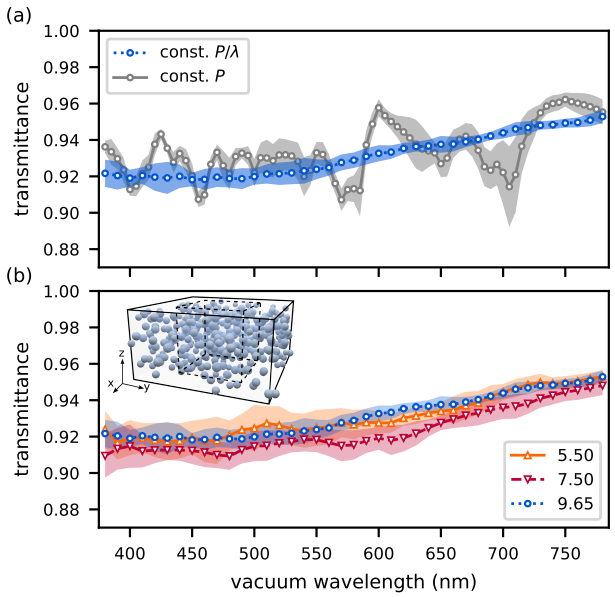

Figure 6.7: (a) Average transmittance of plane waves, impinging onto $2\,\mu\mathrm{m}$ thick, periodic particle arrangements of a constant period and a constant period-wavelength-ratio. (b) Comparison between various period-wavelength-ratios. This figure was published in reference [2], © Elsevier.

minimize these, I randomly confirm or remove particles from the boundaries of the unit cell in each simulation. The inset of figure 6.7(b) illustrates the largest and smallest wavelength-dependent unit cell size of the exemplary simulation for $P/\lambda = 7.5$.

Angular dependence Besides the wavelength dependency, one is often interested in the scattering response under various excitation angles. As the initial field's polar angle of incidence influences the square root (6.47) that allows us to detect lattice resonances, the questions arises, whether their excitation can be avoided in a continuous angle sweep.
In the here discussed two-dimensional lattices, resonances arise for all possible linear combinations of reciprocal lattice vectors $\mathbf{G}_{\tilde{p}}$ that close the gap between the initial field's wavenumber and its in-plane wave vector. In a cubic lattice under normal incidence, this applies for every lattice point (cf. equation (6.1)) for which

$$\frac{P}{\lambda} = \sqrt{n_1^2 + n_2^2} \qquad \text{for } n_1, n_2 \in \mathbb{Z}. \tag{6.48}$$

Altering the angle of incidence however, resonances of different lattice points intermix, leading to a complex resonance pattern.

To illustrate the above, figure 6.8 shows the angular dependence of the coupling operator between a particle and its own infinite periodic grid. The complex resonance pattern prevents the performance of continuous angle sweeps that are free of lattice resonances, without making substantial and more importantly uncontinuous modifications to the model's periodicity between each polar angle of excitation. However, for any period-wavelength-ratio a set of discrete polar angles can be found for

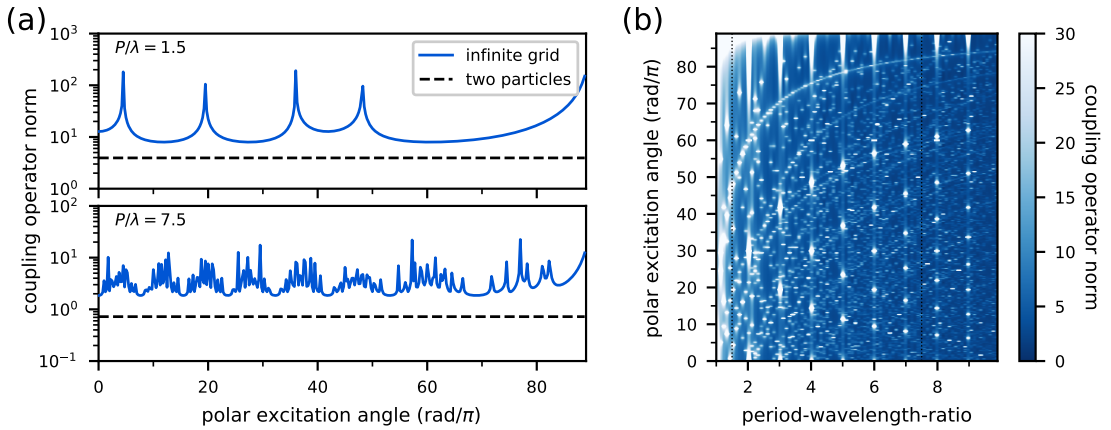

Figure 6.8: (a) Comparison of the L^2-norm of the coupling operator between particles within an infinite lattice and two distinct scatterers as a function of the polar angle of excitation for period-wavelength-ratios of 1.5 and 7.5. Embedded in vacuum, the particles ($n_\mathrm{p} = 2$) have been excited by a plane wave ($\lambda_0 = 550\,\mathrm{nm}$). (b) Dependence of the coupling operator norm over the polar angle of excitation and the period-wavelength-ratio.

which no resonances are excited. Hereby it can be possible to mimic light scattering by disordered system for different angles of incidence via interpolation.

6.9 Numerical considerations

Choice of the separation parameter The separation parameter η splits the evaluation of the infinite lattice sum into the short range particle interactions and the long range contributions, evaluated in real and reciprocal space respectively. Its choice mainly determines the rate of convergence of both sums, with low values favoring the evaluation of short range interactions and vice versa. For two-dimensional lattices with unit cell sizes comparable to the wavelength of excitation, the optimal choice for the convergence of both sums is $\eta = \sqrt{\pi/A_\mathrm{uc}}$ [190, 191]. For large unit cells however, the reciprocal lattice vectors decrease in size, leading to a negative real part in the second argument of the upper incomplete Gamma function

$$\Gamma\left(\frac{1}{2} - \lambda, \frac{|\mathbf{k}_{\mathrm{in}||} + \mathbf{G}_{\tilde{p}}|^2 - k^2}{4\eta^2}\right) \tag{6.49}$$

that is applied in the long range lattice sums (6.13) and (6.20). The exponential growth of the upper incomplete Gamma function with respect to a negative second argument rapidly causes a numerical overflow. To prevent such, only a different choice of the separation parameter can limit

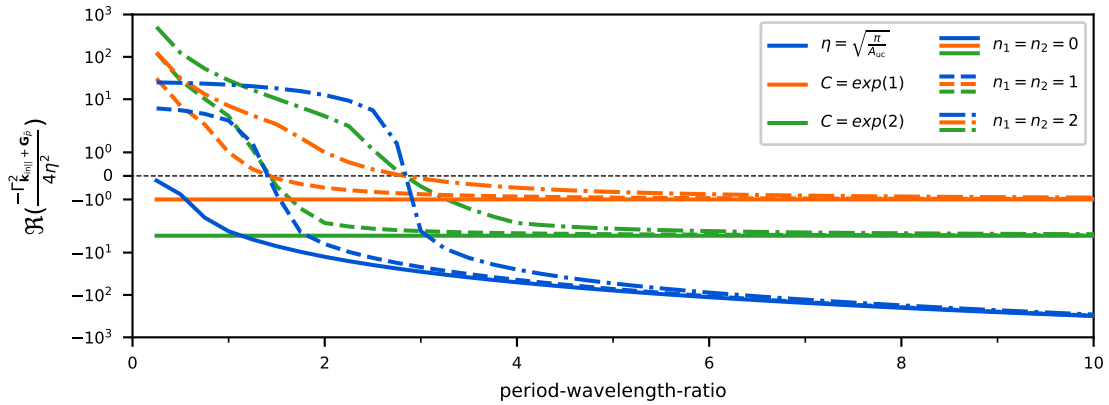

Figure 6.9: Real part of the second argument of the upper incomplete gamma function for three different choices of the separation parameter η as a function of the period-wavelength-ratio. The optimal choice of $\eta = \sqrt{\pi/A_{\mathrm{uc}}}$ causes an exponential decay leading to numerical overflow in the upper incomplete Gamma function. Regularized by a different choice, the argument can be limited by a lower bound. The effect is displayed for three different unit cells of the infinite lattice sums.

the second argument's absolute value.
For large unit cells, I will here apply a separation parameter of

$$\eta = \sqrt{\frac{k^2 - |\mathbf{k}_{\mathrm{in}||} + \mathbf{G}_{\tilde{p}}|^2}{2 \log C}} \tag{6.50}$$

that was suggested by Nečada *et al.* [174]. Proposed for high frequencies, which is in fact identical to large unit cells, the constant C creates a lower bound for the second argument of the Gamma function of $(\log C)^2$. The effect on the second argument for two choices of C in comparison to the conventional optimal choice of the separation parameter is displayed in figure 6.9 for the contribution of three different unit cells. With an increasing constant C, the convergence rate of the long range lattice sums decays, but ensures an accurate evaluation.
For large angles of excitation however, the effect of a large unit cell is counteracted, yielding a regularization of the Gamma function's second argument unnecessary.

Numba implementation The simulation framework SMUTHI is a Python software package that in case of large particle arrangements relies on CUDA-acceleration for an efficient, iterative solving of the linear system of equations. For the solution of periodic particle arrangements no solver scheme for a graphical processing unit (GPU) is available so far.
For now, the need of an iterative solver scheme does not strictly arise, since in comparison to the non-periodic scattering ensembles only particle counts of multiple hundreds to thousands per unit cell have been considered. The number of multipoles to describe such particle arrangements of "moderate" size is in the range of what can be stored in the currently available main memories of common working stations.
To still provide a time efficient solver scheme for the use case of periodic particle arrangements, a

parallelization of the time-consuming Ewald summation on the central processing unit (CPU) that is based on the Python library *Numba* has been implemented. Numba is a just-in-time CPython compiler that allows to remain within Python instead of switching to low-level languages for a better performance [192].

7 Diffuse, white reflectance from solar cells

This chapter illustrates the application of periodic boundary conditions in superposition T-matrix simulations, introduced in chapter 6, to model light propagation in thick, volumetric scattering layers. The presented example covers the wavelength and angular dependent reflection and absorption of a thin-film lead halide Perovskite solar cell. At first, the working principle of solar cells and the arsing optical loss mechanisms are summarized. Addressing such, an overview of typical light management tools for an improved energy conversion is given. Aside efficiency, light management can also serve different objectives. This is illustrated by applying a porous polymer film to the Perovskite solar cell to shape its visual appearance and to facilitate the building integration of photovoltaics. In addition to the diffuse, white cover layer, a pigment based approach that facilitates wavelength dependent scattering is emphasized to compensate for the intrinsic color appearance of the planar solar cell.

To proceed with an increasing independence of fossil fuels and to retain hope in limiting global warming, solar energy has to cover a substantial share of the renewable energy mix. The success of photovoltaics has been and remains largely driven by a reduction in cost and increased efficiencies. However, further aspects like visual appearance gain importance as the technology's integration in existing urban landscapes becomes pivotal.
To emphasize the use of light management in photovoltaics, I will start with its working principle and the accompanying optical loss mechanisms. For this purpose, I refer to the comprehensive description of various solar cell technologies and the involved physics that can be found in reference [193].

7.1 Working principle of solar cells

Solar cells convert light directly into electrical power utilizing the internal photoelectric effect. In this process, an incoming photon of energy E_{ph} that exceeds the band gap E_{g} of a semiconductor is absorbed. Photons that cannot insert enough energy to overcome the band gap are not absorbed and hence, are transmitted through the absorber. In case of absorption, a bound electron-hole pair is formed, called exciton. Before the bound electron-hole pair recombines, it needs to be

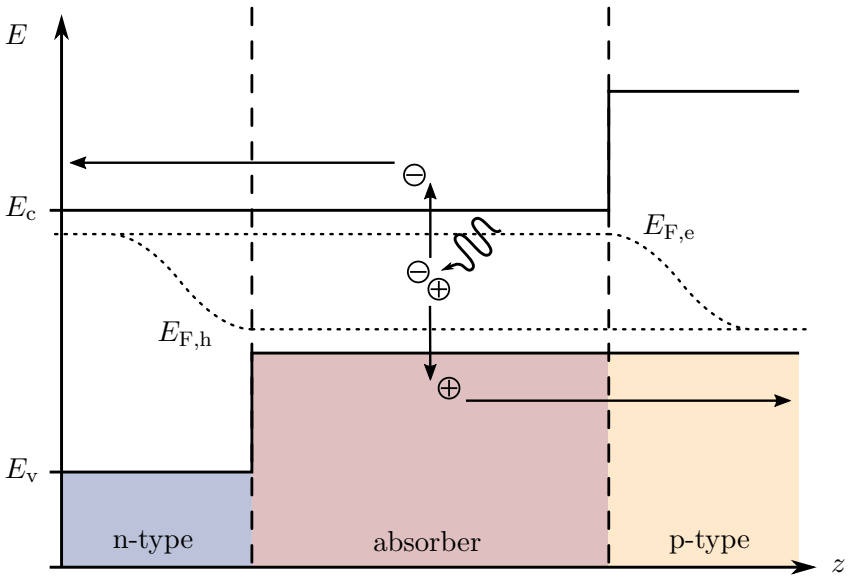

Figure 7.1: Band diagram of a p-i-n junction in contact, close to open circuit conditions. Illuminated through the hole transport layer, the splitting of quasi Fermi levels drives the separation of charges. Different band gaps of the transport and absorber layers block the collection of minority charge carriers at the respective electrodes.

separated which allows the collection of charge carriers. To promote the separation of charges, the basic active layers of a solar cell usually consist of a p-n homojunction, where two layers of the same intrinsic semiconductor are doped with donator and acceptor atoms respectively. The n-type material is overloaded with electrons, raising its Fermi energy E_F towards the energy level of the conduction band E_c. In contrast, a lack of electrons in the p-type material decreases the Fermi level, moving it closer to the energy level of its valence band E_v.

In contact, the two materials form a space charge region with an electric field counteracting the diffusion of majority carriers in the p- and n-type material towards the opposing side. As a result, an equilibrium state is reached with a constant Fermi energy throughout the p-n junction.

Under illumination, the large number of generated negative charges requires the Fermi level to be close to the conduction band. Simultaneously, the large number of generated positive charges enforces a Fermi level close to the valence band. As a result, the Fermi level splits into quasi Fermi levels for electrons $E_{\mathrm{F,e}}$ and holes $E_{\mathrm{F,h}}$, driving the separation of charge carriers into the conduction band and valence band that now can be collected at the respective electrodes. Once separated, all absorbed energy that exceeds the absorber's band gap is rapidly lost to thermalization.

Besides the basic p-n junction, p-i-n heterojunctions are commonly applied that prevent charge carriers to flow towards the wrong electrodes. This is achieved by an intrinsic absorber that is surrounded by an n-type electron transport layer (ETL) and a p-type hole transport layer (HTL) (cf. figure 7.1). Due to a difference in band gap between the absorber and the charge transport layers, p-n like membranes are formed on both sides of the absorber, blocking the minority charge carriers [193].

A typical model to describe the electric characteristics of a solar cell is a two-diode model (figure

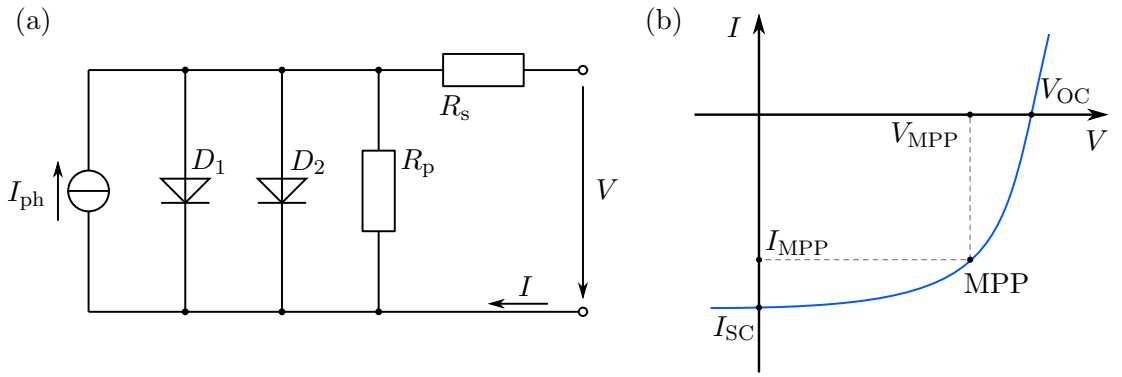

Figure 7.2: (a) Two-diode model of a solar cell. The generated photo current I_{ph} flowing into a load is limited by internal recombination, material defects and ohmic losses. (b) Typical IV-characteristic of a solar cell under illumination.

7.2(a)). Connecting the solar cell to an external load, the net current I resulting from the generated photo current I_{ph} is limited by internal recombination due to defects in the crystal lattice or dopants as well as leakage currents caused by shunts in the solar cell stack and ohmic losses within the solar cell and its connection with the load. Taking all these losses into account, the IV-characteristics can be written as [193]

$$I = I_{\mathrm{ph}} + I_{\mathrm{S1}}\left(\mathrm{e}^{\frac{q(V-IR_{\mathrm{s}})}{k_{\mathrm{B}}T}} - 1\right) + I_{\mathrm{S2}}\left(\mathrm{e}^{\frac{q(V-IR_{\mathrm{s}})}{2k_{\mathrm{B}}T}} - 1\right) + \frac{V - IR_{\mathrm{s}}}{R_{\mathrm{p}}}. \tag{7.1}$$

Here, I_{S1} and I_{S2} denote the saturation currents in diodes D_1 and D_2, q the elementary charge of an electron, k_{B} the Boltzmann constant and T the temperature. A typical solar cell IV-curve is shown in figure 7.2(b). Under illumination, the diode-like behavior of a solar cell is shifted towards negative photo currents. The shift results in a negative short circuit current I_{SC} and a positive open circuit voltage V_{OC} and thus the maximum power point (MPP) of a solar cell is located in the fourth quadrant of the IV-plot. At this working point, the maximal output power P_{max} is generated with a power conversion efficiency (PCE) of

$$\mathrm{PCE} = \frac{P_{\mathrm{max}}}{P_{\mathrm{in}}} = \frac{V_{\mathrm{MPP}}\, I_{\mathrm{MPP}}}{P_{\mathrm{in}}}. \tag{7.2}$$

With its MPP deviating from the ideal I_{SC} and V_{OC}, the efficiency of power conversion of a specific solar cell is limited to a fraction of the incoming power. To maximize the photo current, thicker absorber layers can yield larger short circuit currents until the diffusion length of the charge carriers is reached, but limit the open circuit voltage. In addition, the choice of material, and herewith its band gap, poses an upper limit of the spectrum that can be absorbed but determines the electric potential between electrons and holes that can be harnessed. Assuming infinite mobility of charge carriers and hereby a lossless extraction, the upper limit of a single-junction solar cell as a function of the absorber band gap has been derived by Shockley and Queisser [194].

7.2 Optical loss mechanisms and light management

Besides the aforementioned electrical loss mechanisms and the intrinsic limit linked to the absorber band gap, a significant amount of incoming light is not harvested in the absorber layer due to different optical loss mechanisms.
The largest share of optical loss can be attributed to reflections that occur at any layer interface within the solar cell stack, but most importantly at the glass-air-interface between the cell and its environment. Under normal incidence, the Fresnel coefficients (cf. equations (3.3) and (3.5)) yield a reflectance of $4\,\%$ at the outer interface for $n_{\mathrm{air}} = 1$ and $n_{\mathrm{glass}} = 1.5$. With increasing incident angle these reflection losses drastically increase. Under realistic conditions, solar panels have to be operated under a wide range of incident angels, yielding a reduction of reflection losses detrimental. Aside reflection losses, parasitic absorption can take place in the transport layers and electrodes which does not contribute to the power generation. While parasitic absorption mainly depends on the choice of materials and cannot be fully prevented, a proper choice of layer thicknesses ensures that the center of the absorption profile coincides with the center of the absorber layer [195].

To prevent optical losses, a variety of different light management techniques and structures have been applied, taking the special needs into account that arise from the different available single- and multi-junction solar cells based on silicon, as well as thin-film technologies like CIGS, organic solar cells or Perovskites. A comprehensive overview can be found, e.g., in reference [196]. Here, I would like to point the reader only to a few examples addressing antireflection coatings, external micro- and nanotextures, as well as internal diffraction gratings and scattering layers.

- To suppress reflections at the air-substrate-interface, a layer with an optical thickness of one quarter wavelength can be coated on top of the substrate. If the refractive index of the **antireflection coating** matches

$$n_{\mathrm{ARC}} = \sqrt{n_{\mathrm{air}}\, n_{\mathrm{sub}}}, \tag{7.3}$$

  zero reflection is enabled by destructive interference. Due to a lack of materials that match the necessary refractive index around 1.23, with respect to most common substrates, the deposition of nanoporous layers can decrease the effective refractive index. Applying a porous layer of magnesium fluoride ($\mathrm{MgF_2}$) onto a silica ($\mathrm{SiO_2}$) substrate, a reflectance of $1\,\%$ was achieved between $500\,\mathrm{nm}$ and $800\,\mathrm{nm}$ under normal incidence [197].

- Inspired by nocturnal insects, arrays of tapered sub-wavelength pillars, as they are found in moth eyes, have been replicated [198] to obtain an effective medium with a continuous refractive index gradient between substrate and air. The **optical impedance matching** allows to suppress reflections over a broad visible range and up to highly oblique incident angles [199].

- Besides the suppression of reflection losses, light management **micro-textures** can also increase the average optical path length within the active layers, promoting absorption. For this purpose, the substrate surface is textured with micrometer-sized pyramidal [200] or conical structures [27] that change the direction of propagation of incident light. In addition, the retro-reflective properties of these structures trap light within the solar cell, which is the case due to an increase in propagation angle upon transmission into the substrate.
- Adapting the growth conditions or by chemical etching, the transparent conductive oxides, e.g., doped zinc oxide (ZnO), functioning as a top electrode, can be textured with a random nanostructure to scatter light into wave guided modes of thin-film solar cells [201]. To prevent the modification of the actual solar cell stack, the random **nanotextures** can also be replicated onto the glass substrate [202].
- In combination with antireflection coatings, the optical path length within silicon thin-film solar cells can be strongly increased by **internal diffraction gratings** [203] as well as **photonic crystals** [204] that are directly imprinted into one of the transport layers. In contrast to the previous examples, the active layer stack is directly modified, requiring special layer designs.
- In organic solar cells, metallic and dielectric **scattering particles** have been incorporated into the absorber as well as the transport layers and transparent electrodes. While metallic particles can enhance the absorption by both a strong field enhancement due to the excitation of surface plasmons [205] and an average optical path enhancement due to strong scattering [206], dielectric nanoparticles do not introduce additional parasitic absorption [207].

All here mentioned light management techniques have in common that an increase in optical performance is achieved by a reduced reflection at the outer cell interface, and/or by a randomization of the optical path upon diffraction or scattering. The focus on improved absorption comes with no surprise, as the upper most prominent concern of photovoltaics is the economic efficiency of renewable power generation and herewith its competitiveness.
In the following however, I will shift my focus towards white and colorful solar cells, where light management introduces additional loss in order to provide a tailored appearance, rather than an optimized power conversion.

7.3 Building integrated photovoltaics

To utilize the enormous surfaces of roofs, glazings and building facades of inhabited and urban areas for the solar power generation, not only the power conversion efficiency, but also architectural desires and safety concerns play a crucial role. Building integrated photovoltaic (BIPV) is meant to replace the conventional building envelope, which presents the potential to significantly contribute to the renewable power generation without dissipating additional space.

With its integration in roof tops, facades and semi-transparent glazings, also a number of different challenges arise concerning environmental stability, durability and public acceptance [208]. From an architectural perspective, some prefer a clear visual recognition of the photovoltaic system, while others have a strong demand for a discreet hiding of the solar modules [209]. To meet these desires, photovoltaic modules have to mimic the conventional look of building materials, which requires a large flexibility in visual appearance. In that sense, BIPV has to cover three key aspects: the tunable color, its angular stability, and the suppression of strong, specular reflection.

7.3.1 White and colored solar cells

To customize its visual appearance and hereby addressing one of the key purchase criterions for solar modules [210], its spectral dependent reflectance typically has to be altered. This means, that the incident radiation is on purpose reflected in part and therefore is not available for absorption. To introduce such a customized loss channel, various concepts exist. One way is to alter the multi-layered antireflection coatings in order to obtain control over the wavelength dependent transmittance [211]. The thin-film interference in such a distributed Bragg reflector allow a precise control of the band pass transmittance. However, it influences the underlying solar cell stack and requires customized optimization of the solar cell designs. Similarly, colored solar cells relying on photonic crystals [212, 213] and diffraction gratings [214] have been applied but cannot preserve color appearance for a wide range of incident and observant angles. Contrary to such approaches, the color of a solar cell can also be influenced by color conversion materials that downshift UV radiation into the visible [215]. Hereby, no additional reflection losses are introduced and the power conversion can even benefit partly from the converted emission.
The most prominent and desired color for building facades is white in all its variants. However, its realization requires a broad reflection over the full visible spectrum which is counter-intuitive to the working principle of solar cells [216]. Hence, a careful balance between reflectance and transmittance of the visible spectrum is necessary to preserve any meaningful absorbance, unless the solar cell absorption is shifted towards infrared irradiance [217].

In the following, I will investigate the potential of attaching an external porous polymer film on top of a solar cell to provide a tunable, broadband white reflectance, without altering the underlying solar cell stack. To investigate the solar cell performance over the full visible spectrum and various incident angles, I will apply periodic boundary conditions (introduced in chapter 6) to the multiple micrometer thick porous networks, which are mimicked by a random distribution of spherical air voids in a polymer host. The exemplary simulations serve as an illustration for the improved performance of T-matrix simulations that rely on periodic boundaries. With a strong decrease in individual simulation time, the method's scope is strongly broadened, enabling thick, volumetric scattering layers as well as the investigation of their spectral and angular dependence.

7.4 Perovskite solar cell

To investigate the potential of light scattering by porous polymer films as a light management layer for white solar cells, I start with a planar Perovskite solar cell stack, depicted in figure 7.3. The shown n-i-p structure is similar to the wide-bandgap, double-cation Perovskite solar cells fabricated in our group [218]. The layer sequence and the respective layer thicknesses (summarized in figure 7.3) have been provided by Raphael Schmager. To utilize the available refractive index data that is provided in reference [219], I have replaced the Perovskite composition with the similar Perovskite $Cs_{0.17}FA_{0.83}Pb(Br_{0.17}I_{0.83})_3$. Further refractive index data of the ITO electrode can be found in reference [220], for the tin oxid (SnO_2) ETL and the spiro-OMeTAD HTL in [221] and the gold electrode in [222].
In what follows throughout this chapter, I will only consider light impinging onto the thin-film solar cell stack that is already propagating within the poly(methyl methacrylate) (PMMA) substrate, which will later function as the polymer host of the porous network. Hereby, one neglects any reflections at the air-substrate-interface that in practice would anyhow be treated by one of the antireflection strategies summarized in section 7.2. This simplification also circumvents the necessity to treat the optically thick substrate by means of geometrical optics that would split each simulation into a two-step process in which the thin-film stack's BRDF would be required for each wavelength. I consider this to be justified in order to focus onto the spectral dependent absorbance and reflectance by the thin-film solar cell stack in combination with light scattering by thick, porous networks, rather than to comprise the system in all its complexity at once.

	thickness	material
substrate	∞	PMMA
cathode	130 nm	ITO
ETL	10 nm	SnO_2
absorber	470 nm	$Cs_{0.17}FA_{0.83}Pb(Br_{0.17}I_{0.83})_3$
HTL	220 nm	spiro-OMeTAD
anode	80 nm	Au
	∞	air

Figure 7.3: Investigated n-i-p Perovskite solar cell architecture.

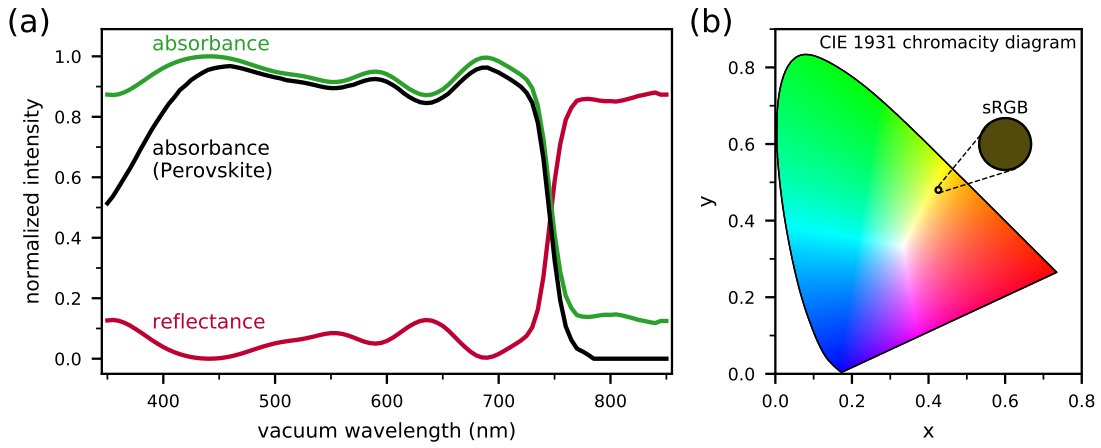

Figure 7.4: (a) Spectral dependent absorbance and reflectance of the planar Perovskite solar cell under normal incidence. (b) Color appearance of the planar Perovskite solar cell illuminated by the standard illuminant D65 in x, y color coordinates of the CIE 1931 chromacity diagram and in sRGB.

7.4.1 Visual appearance

The spectral dependent absorbance (green) and reflectance (red) of the planar Perovskite solar cell under normal incidence is shown in figure 7.4(a). Subtracting any parasitic absorption in the electrodes and transport layers that does not contribute to the power generation, the absorbance within the Perovskite layer is depicted in black. Below the Perovskite's band gap of $1.62\,\mathrm{eV}$ [219] most light is reflected, while irradiation below a wavelength of $765\,\mathrm{nm}$ is strongly absorbed, leading to the typical dark appearance of the solar cell.

To characterize the color appearance of the investigated solar cells, I weight the visible reflectance spectra with the spectrum of the CIE standard illuminant D65 [223] and the color matching functions $\overline{x}(\lambda)$, $\overline{y}(\lambda)$, $\overline{z}(\lambda)$ [224] to obtain the tristimulus

$$X = \frac{1}{N}\int_{380\,\mathrm{nm}}^{780\,\mathrm{nm}} R(\lambda)\, S_{\mathrm{D65}}(\lambda)\, \overline{x}(\lambda) d\lambda, \tag{7.4}$$

$$Y = \frac{1}{N}\int_{380\,\mathrm{nm}}^{780\,\mathrm{nm}} R(\lambda)\, S_{\mathrm{D65}}(\lambda)\, \overline{y}(\lambda) d\lambda, \tag{7.5}$$

$$Z = \frac{1}{N}\int_{380\,\mathrm{nm}}^{780\,\mathrm{nm}} R(\lambda)\, S_{\mathrm{D65}}(\lambda)\, \overline{z}(\lambda) d\lambda, \tag{7.6}$$

with the normalization factor

$$N = \int_{380\,\mathrm{nm}}^{780\,\mathrm{nm}} S_{\mathrm{D65}}(\lambda)\, \overline{y}(\lambda) d\lambda. \tag{7.7}$$

Then, the color coordinates of the CIE 1931 chromacity diagram read

$$x = \frac{X}{X+Y+Z}, \qquad y = \frac{Y}{X+Y+Z}. \tag{7.8}$$

For the yellow reflectance of the planar Perovskite solar cell the color coordinates measure $(x, y) = (0.4258, 0.4800)$, as depicted in figure 7.4(b). However, the reduction of the three-dimensional color space into a two-dimensional diagram removes the information about the color's lightness, rendering it impossible to mimic our visual perception of the measured reflectance. To obtain a visual impression of the theoretical color appearance, the reflectance is also displayed in sRGB color coordinates. The conversion between the CIE XYZ coordinates and sRGB has been performed according to reference [225].
For the later comparison of different broadband, "white" reflections with only small variations in XYZ and RGB color coordinates, I will also make use of the CIE LAB color space. Originally introduced to obtain a uniform color space, in which a change in color perception is represented in a comparable shift in color coordinates, the quantity L^* represents the color's lightness between 0 (black) and 1 (white), a^* the relative ratio between green and red contributions (negative values indicate a green surplus) and b^* corresponding to the ratio between blue and yellow (positive values represent a blue depletion). The respective conversion between color spaces is specified in reference [226].
In case of the planar solar cell the coordinates measure $(L^*, a^*, b^*) = (31.69, -4.68, 35.79)$, indicating a relatively dark appearance with a decent balance between green and red and clear surplus of yellow compared to blue.

7.5 Porous polymer films

To obtain a white, diffuse and in the ideal case excitation angle independent reflectance, I will investigate light scattering by porous polymer films that are directly attached to the planar Perovskite solar cell stack.
Such porous films consist of a polymer host medium that is riddled by a random network of nano- and micro-sized air bubbles. In recent years, polymer matrices have received a lot of attention as a possible substitute of conventional white pigments. Due to its strong light scattering, low cost fabrication and chemical and thermal stability, the most prominent white pigment, namely titanium dioxide (TiO_2) nanoparticles, has replaced almost every other industrial relevant pigment for the production of white plastic packaging, coatings, paints, cosmetics and even toothpaste [227]. Nonetheless, the use of TiO_2 raises an increasing number of concerns, as the eco-friendliness of its energy intensive production and the therewith arising by-products is in question [228] and has been related to health issues [229].
Providing a similar white appearance, pigment-free polymer foams are regarded as an inexpensive and easily recyclable alternative. Mechanically stable, yet flexible, such polymer foams could

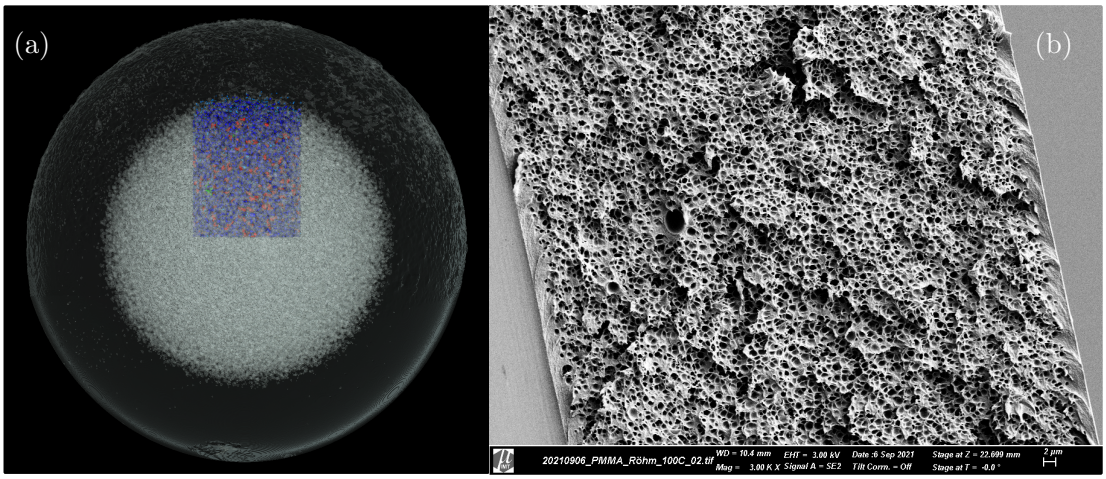

Figure 7.5: (a) Micro-CT reconstruction of a porous network enclosed within a PMMA sphere of a 30 µm radius. The particle size distribution has been analyzed over the blue volume that has been mapped with high resolution. (b) SEM image of a porous polymer film.

replace TiO_2 in plastic packaging and cosmetics [230], but also in optoelectronic devices like solar cells, where diffuse white back reflectors can be used for light management purposes [20, 231].
One strategy to obtain porous polymer films is supercritical carbon dioxide (CO_2) foaming. In a first step, the polymer is saturated with CO_2 under constant pressure and temperature. While the CO_2 concentration increases, the glass transition temperature of the polymer decreases; the polymer becomes viscous. By a rapid pressure drop and due to the comparatively slow decaying CO_2 concentration a supersaturation of the polymer host is caused and nucleation occurs. Not soluble in the polymer host anymore, the CO_2 escapes into the nuclei, which grow into pores. As the CO_2 concentration decreases, the glass transition temperature of the polymer host rises again and hence solidifies [232]. A precise control of pressure and temperature throughout the foaming process allows to control size and density of the porous network [38], which hence can be tailored to match the desired optical properties.
Within our group, supercritical CO_2 foaming has been utilized, e.g., to obtain porous polymer networks that support the color conversion of QD films [233] or as a semi-transparent reflector to improve the energy conversion of organic solar cells [234].
Besides the described supercritical foaming procedure, porous polymer films can also be fabricated by phase separation [28, 230] or via electrospinning [235], each providing porous disorder but varying topologies.

For the modeling of light scattering by porous polymer films, I recall on pore size distributions and densities that have been obtained via micro-CT measurements performed by Cristine Santos de Oliveira on porous networks enclosed within PMMA spheres. A three-dimensional micro-CT reconstruction of such a pore distribution is displayed in figure 7.5(a). All investigated samples have been fabricated by Luisa Borgmann, who also provided the SEM image of a porous polymer film shown in figure 7.5(b). Depending on the fabrication parameters, namely pressure and temperature,

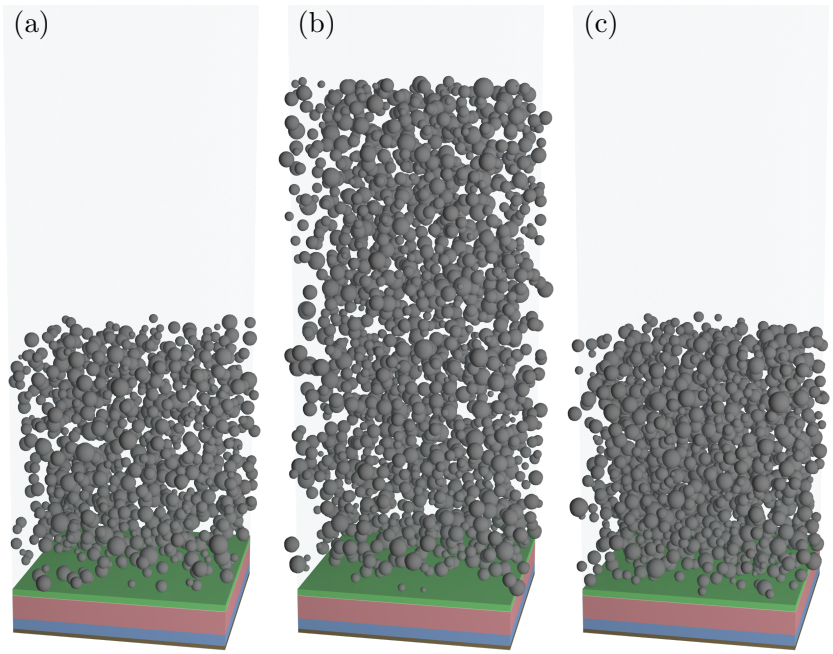

Figure 7.6: Graphical illustration of one unit cell of the Perovskite solar cell and a porous polymer film on top. The pore radii follow a Gaussian distribution around 120 nm with a standard deviation of 30 nm. (a) Film thickness of $h = 5\,\mu\mathrm{m}$ and a pore density of $\rho = 10\,\%\,(\mathrm{v/v})$, (b) $h = 10\,\mu\mathrm{m}$, $\rho = 10\,\%\,(\mathrm{v/v})$, (c) $h = 5\,\mu\mathrm{m}$, $\rho = 15\,\%\,(\mathrm{v/v})$.

pore densities between $3\,\%\,(\mathrm{v/v})$ and $15\,\%\,(\mathrm{v/v})$ and size distributions with average pore radii between $90\,\mathrm{nm}$ and $150\,\mathrm{nm}$ and standard deviations between $30\,\mathrm{nm}$ and $45\,\mathrm{nm}$ have been reported. For the here presented simulations, I restrict myself to pore sizes that follow a Gaussian distribution around $120\,\mathrm{nm}$ with a standard deviation of $30\,\mathrm{nm}$ and different film thicknesses h and pore densities ρ. A graphical illustration of three exemplary porous networks can be found in figure 7.6. Shown is a single unit cell with a period of $P = 4250\,\mathrm{nm}$ that correspond to an excitation vacuum wavelength of $\lambda_0 = 850\,\mathrm{nm}$ in a non-dispersive polymer host of $n_{\mathrm{amb}} = 1.5$ and a period-wavelength-ratio of $P/\lambda = 7.5$. The importance of the period-wavelength-ratio on the optical mimicking of disordered structures by artificial periodicities is described in section 6.8. To cope with such unit cell size, the separation parameter η that splits the lattice sums into its short- and long-range contributions has been chosen according to equation (6.50) with constant $C = \mathrm{e}^3$.
Each particle configuration has been generated by random sequential addition of particles to the target volume until the desired volume filling fraction is reached. This procedure however has only been done for the largest investigated unit cells. For smaller wavelengths of excitation, the fixed period-wavelength ratio results in a decreased period size. In this case, only a subdomain of the largest unit cell has been considered. Inevitably, this procedure leads to small fluctuations in the particle density between simulations of different excitation wavelengths. To minimize such, particles that intersect the unit cell boundaries have been verified or removed from the simulation model in random order. As a result, the simulation model of the identical parameter set but slightly varying excitation wavelengths only exhibit small variations, which already allows for consistent

simulation results without performing sample averaging over multiple particle configurations. Although these unit cells contain more than 2000 individual particles, small deviations between individual configurations are to be expected. Each simulation result will be averaged over 6 random configurations, half of which are excited by either a TE- or a TM-polarized plane wave.

7.6 White reflectance

The simulated wavelength dependent reflectance and absorbance of light impinging onto the Perovskite solar cell under normal incidence are summarized in figure 7.7 for three different parameter sets of thickness h and pore density ρ of the porous polymer substrates (illustrated in figure 7.6)

- (1) $\rho = 10\,\%\,(\mathrm{v/v})$, $h = 5\,\mu\mathrm{m}$,
- (2) $\rho = 10\,\%\,(\mathrm{v/v})$, $h = 10\,\mu\mathrm{m}$,
- (3) $\rho = 15\,\%\,(\mathrm{v/v})$, $h = 5\,\mu\mathrm{m}$.

The solar cell's average reflectance as a function of excitation wavelength under normal incidence is shown in figure 7.7(a). With increasing wavelength, the pores' scattering cross-section continuously decreases, leading to a slow, approximately linear decrease in reflectance over the visible spectrum. This trend is in line with measured data from comparable porous films [38]. Slightly varying between each individual random realization of the porous network, the results' standard deviations are denoted by red corridors. As expected, both an increase in film thickness or pore density increases the observed reflectance, which in principle allows to continuously vary the film's transparency towards opaqueness. For all three scattering samples, the reflectance of the underlying, planar device does not overlay the measured reflectance spectra, indicating a disguise of the solar cell.
The absorbance in the Perovskite absorber layer is shown in figure 7.7(b) in black. Only slightly decreased from the total absorbance (green), the results show that light scattering does not favor any parasitic absorption in the electrodes or transport layers. The introduction of additional reflection loss and the herewith reduced possible energy conversion is hence fully utilized for the solar cells' color appearance. I would like to note that the simulations indicated an absorbance in the Perovskite layer even above bandgap ($\lambda_0 > 765\,\mathrm{nm}$) of about $12\,\%$ for solar cells with a porous substrate. This measured absorbance can be attributed to light, scattered into the waveguide, that is formed by the Perovskite layer and the surrounding $\mathrm{SnO_2}$ and spiro-OMeTAD of lower refractive indices. Infinitely propagating within the waveguide, the scattered light is missing in the energy balance between light entering and dissipating on both sides of the absorber film and hence is attributed to its absorbance. For the planar reference this is not the case, since it is impossible to couple light into a waveguide by refraction.

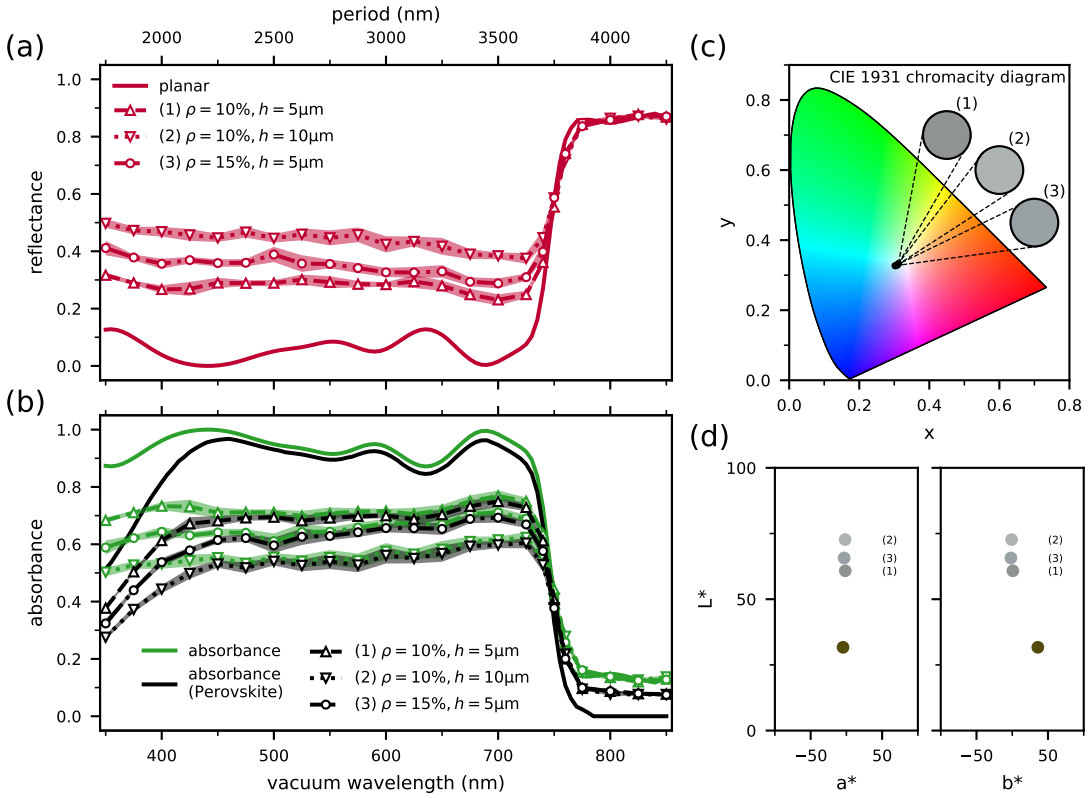

Figure 7.7: Wavelength dependent reflectance (a) and absorbance (b) of a Perovskite solar cell attached to porous polymer substrates of different pore densities ρ and foamed film thicknesses h, in comparison to the planar reference device. (c) Color appearance of the solar cells illuminated by the standard illuminant D65 in x, y color coordinates of the CIE 1931 chromacity diagram and in sRGB. (d) Comparison of lightness and color appearance in the CIE LAB color space.

ρ (%(v/v))	h (µm)	Y	x	y	L^*	a^*	b^*
planar Perovskite solar cell		0.0695	0.4258	0.4800	31.69	−4.68	35.79
White porous polymer							
(1) 10	5	0.2904	0.3119	0.3329	60.83	−1.57	0.89
(2) 10	10	0.4469	0.3078	0.3284	72.69	−1.78	−0.88
(3) 15	5	0.3494	0.3027	0.3270	65.70	−3.12	−1.85
SiO_2 - ZnS core-shell nanoparticles							
(4) 5	5	0.0947	0.3092	0.3315	36.88	−1.43	0.142
(5) 10	10	0.1669	0.2383	0.2604	47.87	−3.45	−23.03

Table 7.1: Color coordinates of the CIE XYZ and CIE LAB color space of measured reflectance spectra, weighted by the spectrum of the standard illuminant D65 for the planar Perovskite solar cell and attached to porous polymer substrates or scattering layers containing SiO_2 - ZnS core-shell nanoparticles.

In figure 7.7(c) the color appearance of the reflected spectra stemming from the Perovskite solar cell attached to the three different porous films under illumination with the standard illuminant D65 is illustrated in x, y-coordinates of the CIE 1931 chromacity diagram and in sRGB. To distinguish between the different lightness of the reflectance spectra, CIE LAB color coordinates are displayed in figure 7.7(d). The respective values are summarized in table 7.1. With the x, y-color coordinates only slightly varying from the white point $(Y_\mathrm{w}, x_\mathrm{w}, y_\mathrm{w}) = (1, 0.33, 0.33)$, all three samples provide a white reflectance, but exhibit a slight blue shift. Dependent on the ratio between absorbance and reflectance, the samples exhibit different lightness, creating varying shades of white. The here presented theoretical color coordinates of reflectance spectra, arising from a Perovskite solar cell with a porous polymer film, are in good accordance with experimental data of Perovskite solar cells with an inkjet-printed, particle based white cover layer [236]. A white reflectance with a lightness of $L^* \approx 65$ was found to fully disguise the underlying Perovskite solar cell and was further utilized as an intermediate layer to achieve other vivid colors.

7.6.1 White reflectance via blue scattering

Besides a broadband white reflectance from a porous polymer film or conventional white pigments, a neutral color appearance of the Perovskite solar cell can also be achieved by balancing out the reflectance spectra of the planar device. The here discussed exemplary device exhibits a yellowish appearance due to a lack of blue contributions in the reflectance spectrum (see section 7.4). Similar to white light emission, obtained from a blue LED in combination with a yellow phosphor, the yellow reflectance of the Perovskite solar cell can be complemented by an additional blue reflection. For this purpose, I replace the porous network in the PMMA substrate with silica ($\mathrm{SiO_2}$[1]) - zinc sulfide (ZnS) core-shell nanoparticles. Due to its relatively high, almost constant refractive index (cf. figure 7.8(a)) throughout the visible spectrum, ZnS is known as a typical white pigment [237] that exhibits almost negligible absorption between $400\,\mathrm{nm}$ and $650\,\mathrm{nm}$. Today, ZnS has been mostly replaced as a white pigment by $\mathrm{TiO_2}$ [238]. Coated onto $\mathrm{SiO_2}$ nanoparticles however, the $\mathrm{SiO_2}$ - ZnS core-shell particles exhibit the here desired blue scattering properties. A good size control during the fabrication process has been demonstrated for a wide range of core sizes and shell thicknesses [239], which makes $\mathrm{SiO_2}$ - ZnS an ideal candidate for a tailored scattering response by possibly varying both, core and shell radii. Figure 7.8(b) shows the spectral dependency of the normalized scattering efficiency of $\mathrm{SiO_2}$ - ZnS core-shell particles of $120\,\mathrm{nm}$ radius embedded in homogeneous host environment of $n_\mathrm{amb} = 1.5$. With decreasing shell thickness d_s, the particle's scattering efficiency exhibits a blue shift. To illustrate the particles dominant blue light scattering, its scattering efficiency is displayed in the respective sRGB color for an excitation with the standard illuminant D65. With increasing shell thickness, the blue scattering slowly shifts towards the whitish response of solid ZnS nanoparticles.

[1] The in-house measured refractive index data of thin film $\mathrm{SiO_2}$ have been provided by Adrian Mertens.

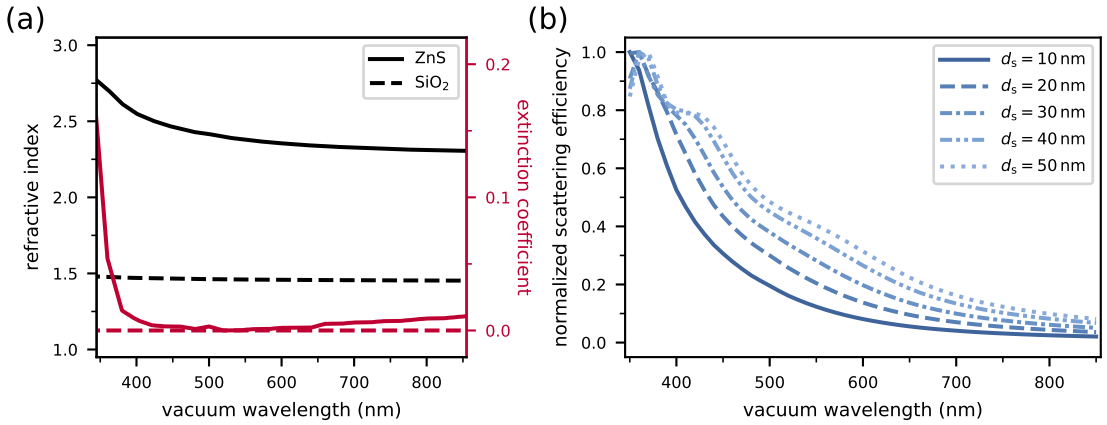

Figure 7.8: (a) Real valued refractive index and extinction coefficient of ZnS [240] and SiO_2. (b) Normalized scattering efficiency of SiO_2 - ZnS core-shell nanoparticles embedded in an ambient medium of $n_{amb} = 1.5$ with a radius of 120 nm and varying ZnS shell thicknesses d_s between 10 nm and 50 nm.

Figures 7.9(a) and (b) display the reflectance and absorbance spectra of the Perovskite solar cell attached to scattering layers of SiO_2 - ZnS core-shell nanoparticles embedded in a PMMA substrate. To compensate for the lack of blue reflection by the planar Perovskite cell, a particle density of 5 %(v/v) randomly dispersed in a 5 µm thick film is sufficient. Compared to the planar device, only a slight decrease in absorbance below 550 nm has to be sacrificed for a strong shift in color appearance towards white (see figure 7.9(c)). Above 550 nm negligible light scattering is observed and the device behaves similar to its planar pendant. Due to a small increase in total reflectance its lightness only slightly increases, resulting in a dark gray appearance (figure 7.9(d)). The respective color coordinates are summarized in table 7.1.
Further promoting scattering by a thicker or denser scattering layer shifts the device appearance into the blue. Hereby, a significant increase in parasitic absorption within the scattering layer can be observed, which hence is not utilized for the solar cell's power conversion, nor for its visual appearance.
While the approach is suitable to compensate for the intrinsic color of the planar device, one cannot achieve a bright white reflectance. This renders the approach only suitable to achieve a neutral color appearance, while preserving a good absorption efficiency.

Another drawback of the color-neutral reflectance obtained via blue light scattering is shown in figure 7.10. While the broad white reflectance of the porous polymer film preserves a strong reflection haze throughout the visible spectrum, the negligible light scattering of the core-shell particles towards green and red excitation results in a strong specular reflection of the underlying planar device. For building integration however, a suppression of specular reflection is highly demanded to prevent interfering with traffic and an uncomfortable blinding of people.
The reflection haze has been derived as the fraction of diffuse reflectance outside a $\pm 5°$ cone of the specular reflection, with respect to the total reflectance, as illustrated in the inset of figure 7.10.

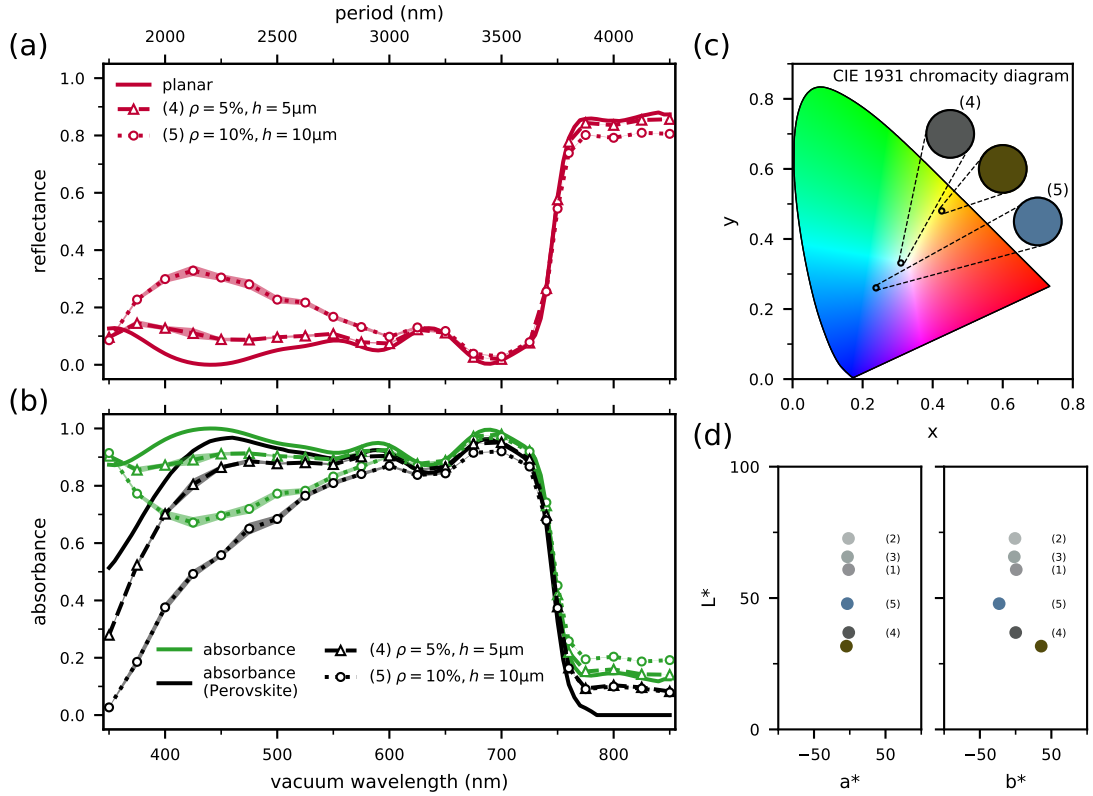

Figure 7.9: Wavelength dependent reflectance (a) and absorbance (b) of a Perovskite solar cell attached to polymer substrates doped with SiO_2 - ZnS core-shell nanoparticles of different densities ρ and film thicknesses h, in comparison to the planar reference device. (c) Color appearance of the solar cells illuminated by the standard illuminant D65 in x, y color coordinates of the CIE 1931 chromacity diagram and in sRGB. (d) Comparison of lightness and color appearance in the CIE LAB color space.

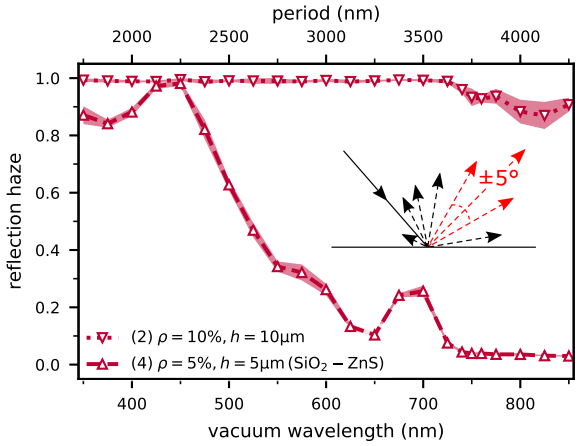

Figure 7.10: Reflection haze of white solar cells based on a porous polymer film (sample (2)) and SiO_2 - ZnS core-shell nanoparticles (sample (4)). Inset: The reflectance within a $\pm 5°$ cone is attributed to the specular reflection.

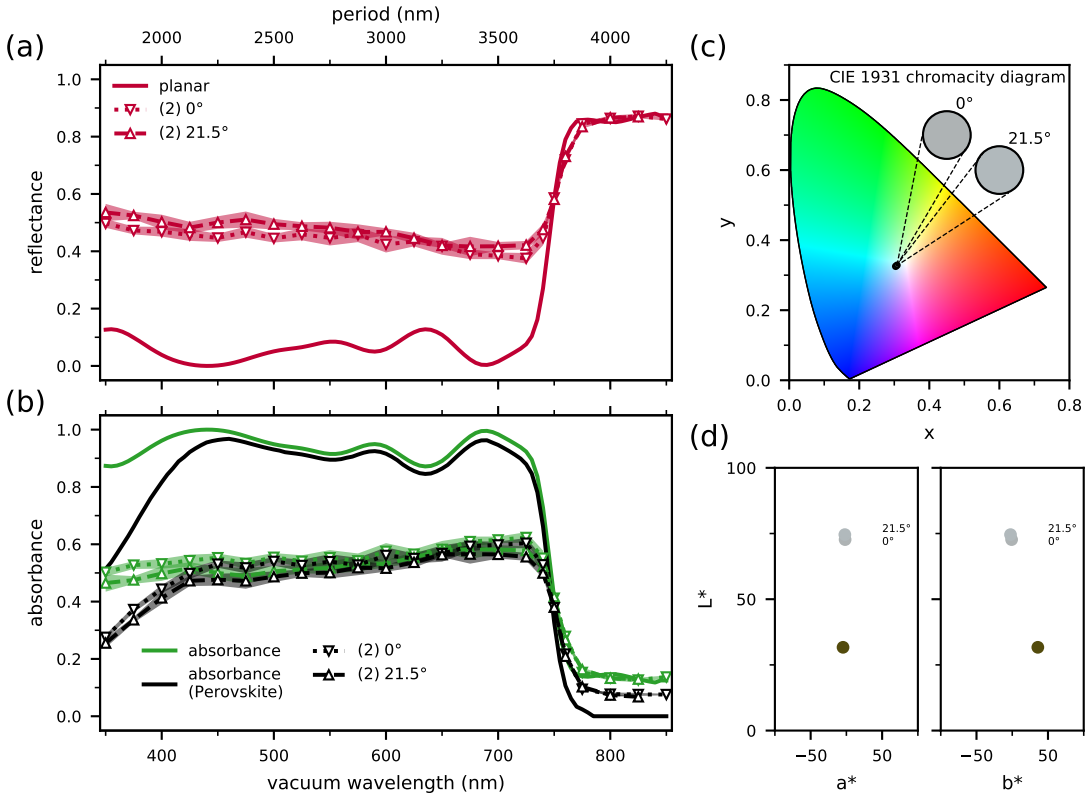

Figure 7.11: Wavelength dependent reflectance (a) and absorbance (b) of a Perovskite solar cell attached to porous polymer substrates of $\rho = 10\,\%(\mathrm{v/v})$ and foamed film thicknesses $h = 10\,\mu\mathrm{m}$ (sample (2)), excited at a polar angle of 0° and 21.5°. (c) Color appearance of the solar cells illuminated by the standard illuminant D65 in x, y color coordinates of the CIE 1931 chromacity diagram and in sRGB. (d) Comparison of lightness and color appearance in the CIE LAB color space.

7.6.2 Angular color stability

Besides the desired white reflectance, building integrated photovoltaics demands for the angular stability of the solar cell appearance. As shown above, the porous polymer films provide a strong reflection haze and therefore ensure that a moving observer does not witness strong shifts in the device appearance.

Next, we have to ask ourselves how the solar cell's visual appearance shifts over the course of a day, while the relative position of the sun moves across the sky. To answer this question, I alter the polar angle of excitation of the Perovskite solar cell that is attached to a porous polymer film with a pore density of $\rho = 10\,\%(\mathrm{v/v})$ and foamed film thicknesses of $h = 10\,\mu\mathrm{m}$ (identical to sample (2), discussed in figure 7.7).

Figure 7.11 summarizes a minor increase of the reflectance for a polar angle of excitation of $\theta = 21.5°$. This increase can be attributed to an increased average optical path length within the porous film compared to normal incidence. The increase in optical path length is almost independent of the wavelength of excitation and hence, the overall spectral dependence of reflectance

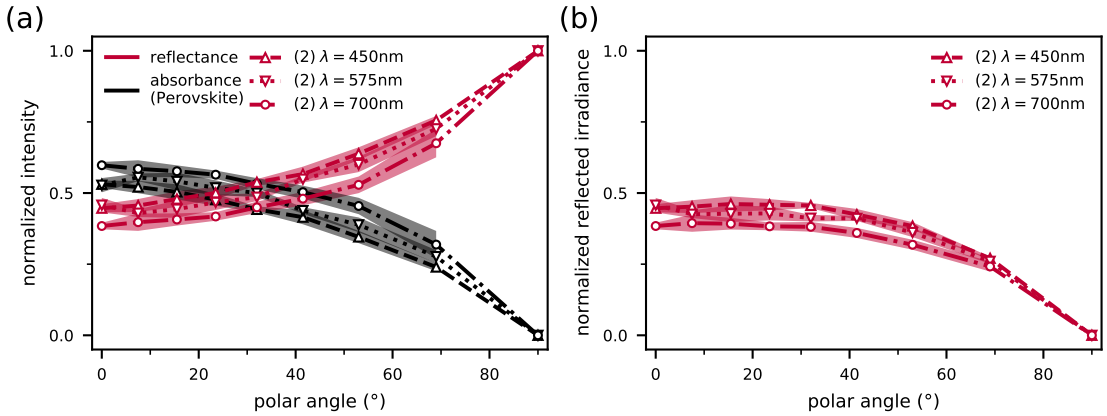

Figure 7.12: Polar incident angle dependence of (a) the reflectance and absorbance, and (b) the normalized reflected irradiance of a Perovskite solar cell, attached to porous polymer substrate (sample (2)) at three different wavelengths

remains unchanged. Therefore, only a small increase in lightness can be observed but no significant color shift.

To further investigate the dependence of the angle of incidence on the solar cell reflectance, I will restrict myself to three wavelengths of excitation, namely $450\,\mathrm{nm}$ (blue), $575\,\mathrm{nm}$ (green) and $700\,\mathrm{nm}$ (red). This is sufficient, as no major difference in the scattering response of air voids in a non-dispersive medium have to be expected throughout the visible spectrum. Figure 7.12(a) shows a continuous decrease in absorbance within the Perovskite layer that results from an increased reflectance of the porous film with growing angle of incidence. As expected, the porous network behaves similarly for all three considered wavelengths of excitation. From this I suspect without proof that the white reflectance remains largely intact for all angles of incidence and that only the sample's lightness might change. To find out whether this is the case, one has to take the incoming irradiance E_e into account that is the fraction of incoming radiant flux Φ_e per area, which scales with the cosine of the polar angle of incidence. Figure 7.12(b) shows the normalized reflected irradiance, which has been obtained as the reflectance, weighted with the cosine of the polar angle. Although the fraction of reflected light increases with the polar angle of incidence, the irradiance decreases, which leads to a somewhat stable amount of light that is reflected per area of the solar cell for angles up to $\approx 40°$. With a further increase of θ, the solid angle under which the solar cell is illuminated strongly diminishes and eventually overtakes the increase in reflectance. As a result, a solar cell attached to a porous polymer film is expected to show only small changes in visual appearance throughout the day unless it is illuminated under highly oblique incidence.

I would like to note that the non-equidistant discretization of polar angles in figure 7.12 is the result of the applied periodic boundary conditions, the choice of period-wavelength-ratio and the necessity to avoid lattice resonances. For more information please see section 6.8. Moreover, the data point at $\theta = 90°$ has not been calculated but was added for completeness, as it is given a priori. Further, the considerations regarding incoming irradiance are not rigorous in a sense that I

have not considered a change in the incoming irradiance spectra due the sun's movement and the therewith varying air mass coefficients. Nevertheless, I consider this to be justified, as it does not further simplify the outer most constraint I have formulated in section 7.4, which states that only light is considered which is already propagating within the substrate. This assumption of a perfect antireflection coating already removed any angular intensity dependence of the incoming light and was necessary to reduce this study to a bearable cost.

8 Conclusions and outlook

The central objective of this work has been to strengthen the applicability of a superposition T-matrix scheme for the optical modeling of disordered light management structures in optoelectronic devices. Following this goal, I have modeled light extraction from OLEDs and light harvesting in solar cells, but I have also worked on quantum dot light conversion [4] and particle-based wavelength selective filter designs [1]. All these different applications in mind, the challenge has been to adapt the existing framework to the variety of prevailing circumstances.

In this work, new insights have been gained in regard to:

Superposition T-matrix method for dense, nonspherical particle aggregates An alternative formulation of the translation addition operator for SVWFs, based on an intermediate transformation into plane waves, allows to separate the propagating field contributions from the evanescent plane-wave spectrum. Hereby, erroneous terms in the evanescent near-field can be removed from the direct particle interactions. Doing so, the particle separation restriction of the superposition T-matrix method can be neglected. High accuracy of the approach has been demonstrated for both, volumetric aggregates of spheroidal scatterers and dense pillar structures on a substrate.

Nearfield of nonspherical scatterers Switching into a plane-wave representation of scattered fields, not only the direct interactions between nonspherical particles in close vicinity can be accurately described. Also the particle's direct nearfield becomes accessible with good accuracy down to the particle surface. Hereby, the series expansion approach becomes interesting for the description of dipole emitters in direct vicinity of nonspherical scatterers and the design of surface-enhanced Raman spectroscopy textures.

Low vs. high index planarized scattering layers The effect of low and high index planarization on the extraction of light from a green OLED has been investigated for various filling fractions and two different aspect ratios of scatterers. The results show that the high index planarization does not necessarily outperform extraction layers with a low index planarization, even if a material combination is found that allows for a strong refractive index mismatch between the scatterer and the planarization layer. For oblique incidence, the high index scatterers show a broader scattering response compared to their low index counterparts, especially promoting the extraction of substrate modes.

Periodic boundary conditions in T-matrix computations Ewald-type lattice sums to account for particle interactions between planar, periodic particle grids distributed in three dimensions have been integrated into the existing superposition T-matrix framework. With the introduction of periodic boundary conditions, the open simulation domain boundaries can be closed, preventing edge effects of the otherwise finite particle arrangements. A parallelized evaluation of the Ewald lattice sums in conjunction with a grid-to-grid interaction scheme based on plane waves for periodic distributions with a large vertical displacement enable the efficient modeling of light scattering in very large three-dimensional unit cells that host thousands of arbitrary particles.

Mimicking disorder in periodic particle arrangements The effect of introducing an artificial periodicity into an otherwise random particle arrangement has been investigated. Even for periodicities much larger than the wavelength of interest, strong lattice resonances can be observed for aligning combinations of periodicity, excitation's wavenumber and incident angle. Avoiding those resonances by a systematic adjustment of the artificial periodicity in accordance to a change of excitation allows for the prediction of spectral and angular behavior of random, volumetric scattering layers.

White solar cells for building integration The potential of porous polymer films to obtain diffuse, white reflectance from solar cells has been investigated for their use in building integrated photovoltaics. A precise control of the porous network morphology in terms of pore size and density allows to gradually shift the reflectance spectra from dark gray to white. Attaching a porous network onto the optimized solar cell does not promote parasitic absorption. As a result, all incident light can either contribute to the power conversion or the device's visual appearance.

SMUTHI The in this work described optical modeling techniques for dense nonspherical particles and periodic particle arrangements are integrated into the existing framework and will be released for free use in the publicly available software package SMUTHI [3].

8.1 Outlook

Besides questions that have been answered, some remain open and new ones have been raised. Along these lines, I see the following opportunities for a continuation of this work:

Automated truncation criterion for plane-wave coupling The alternative formulation of the translation addition operator for SVWFs based on an intermediate plane-wave expansion enables superposition T-matrix simulations of large and dense aggregates of nonspherical particles. However, an accurate evaluation of the direct particle interactions can only be ensured, if a precise truncation of the evanescent plane-wave spectrum is performed. So far, an automated truncation criterion based on a phenomenological formula is only available for individual scatterers that are directly located on a substrate. It will be crucial to also derive such an automated criterion for arbitrary pairs of particles so that the formalism can be widely adopted.

Comparison of new techniques Besides the plane-wave coupling formalism, a number of different techniques (reviewed in section 4.7) are currently in development that allow to deal with nonspherical scatterers in close vicinity. It would be interesting to perform an in-depth comparison between the different approaches for various, typical application scenarios to identify the advantages and disadvantages of each technique, which would allow an appropriate choice depending on the task at hand. Thus, it might become apparent that in case of highly nonspherical particles, one of the multi-source methods, such as the global polarizability matrix [110] or the multipole distribution along a particle's topological skeleton [111], are necessary. For less complex particles, but possibly larger systems, the plane-wave coupling formalism (cf. chapter 4) or the multipole translation scheme [109] could be sufficient but faster.

Periodic boundary conditions and internal excitation Periodic boundary conditions do not only imply an infinite periodic extent of the particle arrangement, but also a periodicity in excitation. This makes them particularly interesting for applications that are excited by an external plane wave. However, also internal excitation by means of a periodic repetition of dipole emitters could be realized by a decomposition of the periodic emission into upwards and downwards propagating, discrete plane waves. Alternatively to the periodic dipole excitation it could also be possible to consider only a single dipole and to enforce the periodicity by a Floquet transform [241]. For this, one would first need to answer how this technique would translate to the here applied series approach.

Iterative solver scheme The periodic particle arrangements considered in this work consist of up to a few thousand scatterers. While already quite large, it is still possible to store the system of linear equations in the main memory of common work stations, which allows for a direct evaluation. However, the somewhat limited ratio between excitation wavelength and periodicity results in a discrete angular distribution of the scattered far-field. To mimic the continuous far-field pattern of disordered particle arrangements, significantly larger period sizes are required, which further increases the number of unknowns. A lookup table, similar to the solution strategy for non-periodic particle arrangements, would allow to interpolate the Ewald lattice sums from a discrete set of precalculated grid displacements and enables an iterative solver scheme. Hereby, the use of a graphical processing unit becomes feasible, which could significantly speed up the computations.

Appendix

A Wigner D-functions

To relate spherical vector wave functions in a rotated coordinate system (R) to those in the laboratory coordinate system (L) of identical origin, the Wigner D-functions are applied (cf. equation (2.37)). With the Euler angles α, β and γ successively rotating the laboratory coordinate system into the rotated coordinate system via the z, y', z'-convention (cf. figure 2.4), the Wigner D-functions read [63]

$$D^l_{mm'}(\alpha,\beta,\gamma) = (-1)^{m+m'} \mathrm{e}^{\mathrm{i}m\alpha} \Delta_{mm'} d^l_{mm'}(\beta) \mathrm{e}^{\mathrm{i}m'\gamma}, \tag{A.1}$$

with

$$\Delta_{mm'} = \begin{cases} 1, & m \geq 0, \quad m' \geq 0 \\ (-1)^{m'}, & m \geq 0, \quad m' < 0 \\ (-1)^{m}, & m < 0, \quad m' \geq 0 \\ (-1)^{m+m'}, & m < 0, \quad m' < 0. \end{cases} \tag{A.2}$$

For their construction, I make use of an iterative scheme of the Wigner d-functions presented in Appendix B of reference [56]. The Wigner d-functions are defined by

$$\begin{aligned} d^l_{mm'}(\beta) = {} & \sqrt{(l+m)!(l-m)!(l+m')!(l-m')!} \\ & \times \sum_s (-1)^s \frac{(\cos\frac{\beta}{2})^{2l-2s+m-m'} (\sin\frac{\beta}{2})^{2s-m+m'}}{s!(l+m-s)!(l-m'-s)!(m'-m+s)!}, \end{aligned} \tag{A.3}$$

where the sum is performed over all integer s that lead to non-negative faculties and $\beta \in [0, \pi]$. Their construction follows a recursion, with

$$\begin{aligned} d^{l+1}_{mm'}(\beta) = {} & \frac{1}{l\sqrt{(l+1)^2 - m^2}\sqrt{(l+1)^2 - m'^2}} \\ & \times \Big((2l+1) \left[l(l+1)\cos\beta - mm' \right] d^l_{mm'}(\beta) \\ & \qquad - (l+1)\sqrt{l^2 - m^2}\sqrt{l^2 - m'^2}\, d^{l-1}_{mm'}(\beta) \Big) \end{aligned} \tag{A.4}$$

and the starting points

$$d_{mm'}^{l_{\min}-1}(\beta) = 0, \tag{A.5}$$

$$d_{mm'}^{l_{\min}}(\beta) = \frac{\xi_{mm'}}{2^{-l_{\min}}} \left[\frac{(2l_{\min})!}{(|m-m'|)!(|m+m'|)!} \right]^{\frac{1}{2}} (1-\cos\beta)^{\frac{m-m'}{2}} (1+\cos\beta)^{\frac{m+m'}{2}}, \tag{A.6}$$

with $l_{\min} = \max(|m|, |m'|)$ and

$$\xi_{mm'} = \begin{cases} 1, & \text{for } m' \geq m \\ (-1)^{m-m'}, & \text{for } m' < m. \end{cases} \tag{A.7}$$

In the special case of $m = m' = 0$, the Wigner d-function can be obtained from the Legendre Polynomials

$$d_{00}^{l}(\beta) = P_l(\cos\beta). \tag{A.8}$$

B Plane of separation for spheroidal particles

In section 4.2.1 I have introduced a formalism of a direct coupling operator for nonspherical particles in close vicinity that is based on an intermediate plane-wave representation of the outgoing spherical wave expansion. For a pair of particles that cannot be separated by a plane that is parallel to the xy-plane of the laboratory coordinate system (cf. figure 4.3) the formalism demands to rotate the particles into a coordinate system in which a horizontal plane of separation exists.
One strategy to find a plane of separation between particles with a convex surface shape is to determine the points $\mathbf{p}$ and $\mathbf{p}'$ on the surfaces of scatterers S and S' that are closest to each other. With these, the vector $\overline{\mathbf{p}'\mathbf{p}}$ is normal to the separation plane. Hence, one faces the problem of finding $\mathbf{p}$ and $\mathbf{p}'$, for which

$$\boldsymbol{\Delta}^2 = \left(\mathbf{p}-\mathbf{p}'\right)^{\mathrm{T}}\left(\mathbf{p}-\mathbf{p}'\right) \quad \text{with} \quad \boldsymbol{\Delta} = |\overline{\mathbf{p}'\mathbf{p}}| \tag{B.1}$$

becomes minimal.

Here, I will present one possible procedure to determine these points for two spheroidal particles, following the ideas presented in reference [242].
Let $\hat{\mathbf{A}}_{S'}$ be the quadric of spheroid S'

$$\hat{\mathbf{A}}_{S'} = \begin{bmatrix} a^{-2} & 0 & 0 \\ 0 & a^{-2} & 0 \\ 0 & 0 & c^{-2} \end{bmatrix} \tag{B.2}$$

with the eigenvalues being the inverse square of the spheroid's semi-half axes a and c that are aligned along the x-, y- and z-axes of a Cartesian coordinate system. Then, a spheroid of arbitrary orientation (rotated by Euler angles (α, β, γ) with respect to the aligned spheroid) is defined by

$$\left(\mathbf{r}-\mathbf{r}_{S'}\right)^{\mathrm{T}}\mathbf{A}_{S'}\left(\mathbf{r}-\mathbf{r}_{S'}\right) = 1, \tag{B.3}$$

with the quadric of the rotated spheroid

$$\mathbf{A}_{S'} = \mathbf{R}^{\mathrm{T}}_{\alpha,\beta,\gamma}\hat{\mathbf{A}}_{S'}\mathbf{R}_{\alpha,\beta,\gamma} \tag{B.4}$$

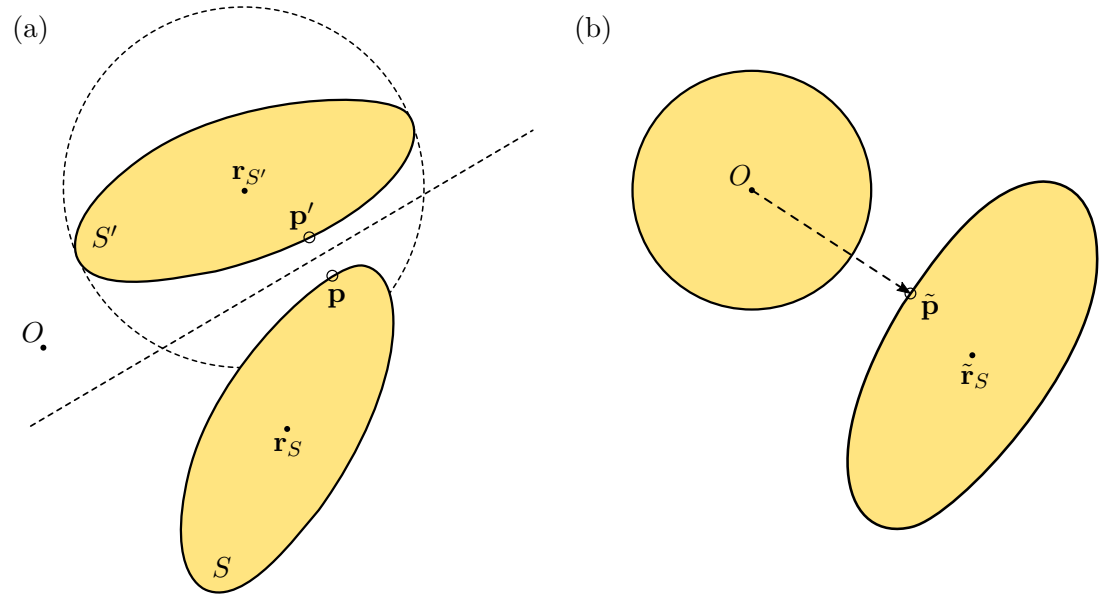

Figure B.1: (a) To determine a plane of separation between two spheroidal scatterers, the surface points $\mathbf{p}$ and $\mathbf{p}'$ are sought-for. (b) To simplify the three-dimensional minimization problem, a coordinate transformation converts scatterer S' into the unit sphere, centered at origin.

and $\mathbf{R}_{\alpha,\beta,\gamma}$ being the rotation matrix of successive rotations according to the $zy'z'$-convention (cf. figure 2.4).

The now presented formalism is based on the idea that in a transformed coordinate system, in which one of the two spheroids can be represented by the unit sphere centered at origin, the problem of finding $\mathbf{p}$ and $\mathbf{p}'$ simultaneously reduces into finding a single point on the other spheroids surface that is closest to the center of the coordinate system (illustrated in figure B.1).
I start with the Cholesky decompose of the spheroid's quadric

$$\mathbf{L}_{S'}\mathbf{L}_{S'}^{\mathrm{T}} = \mathbf{A}_{S'} \tag{B.5}$$

to perform the coordinate transformation of

$$\tilde{\mathbf{r}} = \mathbf{L}_{S'}\left(\mathbf{r} - \mathbf{r}_{S'}\right) \tag{B.6}$$

that converts spheroid S' into the unit sphere centered at origin

$$\left(\mathbf{r} - \mathbf{r}_{S'}\right)^{\mathrm{T}} \mathbf{A}_{S'} \left(\mathbf{r} - \mathbf{r}_{S'}\right) = 1 \quad \rightarrow \quad \tilde{\mathbf{r}}^{\mathrm{T}}\tilde{\mathbf{r}} = 1. \tag{B.7}$$

Under the same transformation, the quadric representation of spheroid S takes the form

$$\left(\tilde{\mathbf{r}} - \tilde{\mathbf{r}}_S\right)^{\mathrm{T}} \tilde{\mathbf{A}}_S \left(\tilde{\mathbf{r}} - \tilde{\mathbf{r}}_S\right) = 1, \tag{B.8}$$

with

$$\tilde{\mathbf{A}}_S = \mathbf{L}_{S'}^{-\mathrm{T}} \mathbf{A}_S \mathbf{L}_{S'}^{-1} \tag{B.9}$$

and

$$\tilde{\mathbf{r}}_S = \mathbf{L}_{S'} \left(\mathbf{r}_S - \mathbf{r}_{S'} \right). \tag{B.10}$$

Looking for a point $\tilde{\mathbf{p}}$ on the transformed spheroid of S, I rewrite equation (B.8) into

$$\begin{aligned} 1 &= \left(\tilde{\mathbf{p}} - \tilde{\mathbf{r}}_S \right)^{\mathrm{T}} \tilde{\mathbf{A}}_S \left(\tilde{\mathbf{p}} - \tilde{\mathbf{r}}_S \right) \\ &= \left(\tilde{\mathbf{p}} - \tilde{\mathbf{r}}_S \right)^{\mathrm{T}} \tilde{\mathbf{L}}_S \tilde{\mathbf{L}}_S^{\mathrm{T}} \left(\tilde{\mathbf{p}} - \tilde{\mathbf{r}}_S \right) \\ &= \mathbf{y}^{\mathrm{T}} \mathbf{y}, \end{aligned} \tag{B.11}$$

where I have introduced $\tilde{\mathbf{A}}_S = \tilde{\mathbf{L}}_S \tilde{\mathbf{L}}_S^{\mathrm{T}}$ and

$$\begin{aligned} \mathbf{y} &= \tilde{\mathbf{L}}_S^{\mathrm{T}} \left(\tilde{\mathbf{p}} - \tilde{\mathbf{r}}_S \right), \\ \tilde{\mathbf{p}} &= \tilde{\mathbf{L}}_S^{-\mathrm{T}} \mathbf{y} + \tilde{\mathbf{r}}_S. \end{aligned} \tag{B.12}$$

Now, one can rewrite the minimization problem (B.1) in the transformed coordinate system and utilize the properties of the unit sphere to find

$$\begin{aligned} \tilde{\boldsymbol{\Delta}}^2 &= \left(\tilde{\mathbf{p}} - \tilde{\mathbf{p}}' \right)^{\mathrm{T}} \left(\tilde{\mathbf{p}} - \tilde{\mathbf{p}}' \right) \\ &= \tilde{\mathbf{p}}^{\mathrm{T}} \tilde{\mathbf{p}}. \end{aligned} \tag{B.13}$$

Inserting equation (B.12) into (B.13) one obtains

$$\begin{aligned} \tilde{\boldsymbol{\Delta}}^2 &= \left(\tilde{\mathbf{L}}_S^{-\mathrm{T}} \mathbf{y} + \tilde{\mathbf{r}}_S \right)^{\mathrm{T}} \left(\tilde{\mathbf{L}}_S^{-\mathrm{T}} \mathbf{y} + \tilde{\mathbf{r}}_S \right) \\ &= \left(\mathbf{y}^{\mathrm{T}} \tilde{\mathbf{L}}_S^{-1} + \tilde{\mathbf{r}}_S^{\mathrm{T}} \right) \left(\tilde{\mathbf{L}}_S^{-\mathrm{T}} \mathbf{y} + \tilde{\mathbf{r}}_S \right) \\ &= \mathbf{y}^{\mathrm{T}} \tilde{\mathbf{L}}_S^{-1} \tilde{\mathbf{L}}_S^{-\mathrm{T}} \mathbf{y} + 2 \tilde{\mathbf{r}}_S^{\mathrm{T}} \tilde{\mathbf{L}}_S^{-\mathrm{T}} \mathbf{y} + \tilde{\mathbf{r}}_S^{\mathrm{T}} \tilde{\mathbf{r}}_S, \end{aligned} \tag{B.14}$$

which can be minimized, e.g., with a sequential least square algorithm to find $\mathbf{y}$. Finally the retransformation yields

$$\mathbf{p} = \mathbf{L}_{S'} \tilde{\mathbf{p}} + \mathrm{r}_{S'} \tag{B.15}$$

on the surface of spheroid S that is closest to spheroid S'.
Once $\mathbf{p}$ is found it can be inserted into equation (B.1), which then has the form of (B.13) and hence $\mathbf{p}'$ can be determined with the same minimization procedure.
With this, one has found a plane of separation that can be used for the plane-wave coupling formalism.

C Normalization factor for Ewald sums

The in section 6.3 specified lattice sums have been derived by Kambe for the case of SVWFs in two-dimensional periodic lattices. In literature one can find various formulations that also compensate a minor error in Kambe's derivation. Due to their complexity, I have decided to not add another notation that would explicitly fit to the here used normalization conventions. I rather stick to the notation I was provided by Dominik Beutel and add a normalization factor N_m.
To find N_m I have compared all relevant definitions related to the spherical vector wave functions used in this work that are based on reference [63] with the respective definitions in [173] based on reference [243]. All differences in the normalizations can be traced back to the spherical harmonics and the therein applied associated Legendre functions. Rewriting equations (2.27) - (2.29), I have applied the spherical harmonics

$$Y_{lm}(\theta,\varphi) = \sqrt{\frac{2l+1}{2}\frac{(l-|m|)!}{(l+|m|)!}}\tilde{P}_l^{|m|}(\cos\theta)\,\mathrm{e}^{\mathrm{i}m\varphi}, \tag{C.1}$$

with

$$\tilde{P}_l^m(x) = \left(1-x^2\right)^{m/2}\frac{d^m P_l(x)}{dx^m}. \tag{C.2}$$

Comparing equation (C.1) to the spherical harmonics specified in reference [173]

$$Y^*_{lm}(\theta,\varphi) = \sqrt{\frac{2l+1}{4\pi}\frac{(l-m)!}{(l+m)!}}(-1)^m\tilde{P}_l^m(\cos\theta)e^{im\phi}, \tag{C.3}$$

one has to distinguish between positive and negative indices m.

$\mathbf{m \geq 0}$:

$$Y_{lm}(\theta,\varphi) = \sqrt{2\pi}(-1)^{-m}Y^*_{lm}(\theta,\varphi) \tag{C.4}$$

$\mathbf{m < 0}$:
For negative m, I utilize that

$$\bar{P}_l^m(x) = (-1)^m\tilde{P}_l^m(x) \tag{C.5}$$

can be construct from positive indices [243]

$$\bar{P}_l^m(x) = (-1)^{|m|} \frac{(l-|m|)!}{(l+|m|)!} \bar{P}_l^{|m|}(x). \tag{C.6}$$

Inserting equation (C.5) into (C.1) and equation (C.6) into (C.3) I find by comparison

$$Y_{lm}(\theta,\varphi) = \sqrt{2\pi}(-1)^{-2|m|} \sqrt{\frac{(l+m)!}{(l-m)!}} \sqrt{\frac{(l+|m|)!}{(l-|m|)!}} Y_{lm}^*(\theta,\varphi) \tag{C.7}$$

$$= \sqrt{2\pi} Y_{lm}^*(\theta,\varphi). \tag{C.8}$$

The normalization factor then reads

$$Y_{lm}(\theta,\varphi) = N_m Y_{lm}^*(\theta,\varphi) = \sqrt{2\pi} \begin{cases} (-1)^{-m} \; Y_{lm}^*(\theta,\varphi) & m > 0 \\ 1 & m \leq 0, \end{cases} \tag{C.9}$$

which can directly be applied to the lattice sum (6.10).

For the SVWFs in both notations (cf. equation (2.25) and reference [173]) the normalization difference in spherical harmonics translates into

$$\mathbf{M}_{lm\tau}^{(\nu)}(\mathbf{r}) = \mathrm{i}\sqrt{\pi} \begin{cases} (-1)^{-m} \; \mathbf{M}_{lm\tau}^{*(\nu)}(\mathbf{r}) & m > 0 \\ 1 & m \leq 0. \end{cases} \tag{C.10}$$

List of Figures

List of Tables

List of publications

Peer-reviewed journal articles

[1] Junchi Chen, Dominik Theobald, Abdullah Bin Shams, Qihao Jin, Adrian Mertens, Guillaume Gomard, and Uli Lemmer. Silver-Nanoparticle-Based Metallodielectric Wavelength-Selective Reflectors for Quantum-Dot-Enhanced White-Light-Emitting Diodes. *ACS Appl. Nano Mater.*, 2021.

[2] Dominik Theobald, Dominik Beutel, Luisa Borgmann, Henning Mescher, Guillaume Gomard, Carsten Rockstuhl, and Uli Lemmer. Simulation of light scattering in large, disordered nanostructures using a periodic T-matrix method. *J. Quant. Spectrosc. Radiat. Transf.*, 272:107802, 2021.

[3] Amos Egel, Krzysztof M. Czajkowski, Dominik Theobald, Konstantin Ladutenko, Alexey S. Kuznetsov, and Lorenzo Pattelli. SMUTHI: A python package for the simulation of light scattering by multiple particles near or between planar interfaces. *J. Quant. Spectrosc. Radiat. Transf.*, 273:107846, 2021.

[4] Dominik Theobald, Shudong Yu, Guillaume Gomard, and Uli Lemmer. Design of Selective Reflectors Utilizing Multiple Scattering by Core-Shell Nanoparticles for Color Conversion Films. *ACS Photonics*, 7(6):1452–1460, 2020.

[5] Yidenekachew J. Donie, Dominik Theobald, Somayeh Moghadamzadeh, Adrian Mertens, Ihteaz M. Hossain, Ulrich W. Paetzold, Uli Lemmer, and Guillaume Gomard. Planarized and Compact Light Scattering Layers Based on Disordered Titania Nanopillars for Light Extraction in Organic Light Emitting Diodes. *Adv. Opt. Mater.*, page 2001610, 2020.

[6] Dominik Theobald, Amos Egel, Guillaume Gomard, and Uli Lemmer. Plane-wave coupling formalism for T-matrix simulations of light scattering by nonspherical particles. *Phys. Rev. A*, 96(3):033822, 2017.

[7] Amos Egel, Yuri Eremin, Thomas Wriedt, Dominik Theobald, Uli Lemmer, and Guillaume Gomard. Extending the applicability of the T-matrix method to light scattering by flat particles on a substrate via truncation of sommerfeld integrals. *J. Quant. Spectrosc. Radiat. Transf.*, 202:279–285, 2017.

[8] Amos Egel, Dominik Theobald, Yidenekachew Donie, Uli Lemmer, and Guillaume Gomard. Light scattering by oblate particles near planar interfaces: on the validity of the T-matrix approach. *Opt. Express*, 24(22):25154, 2016.

Conference contributions

[9] Dominik Theobald, Guillaume Gomard, and Uli Lemmer. Design of light scattering nanoparticles for improved photon management in light-emitting devices. In Sven Burger, editor, *Work. Theor. Numer. Tools Nanophotonics*. Zuse Institut Berlin, 2020.

[10] Shudong Yu, Benjamin Fritz, Dominik Theobald, Siegbert Johnsen, Dmitry Busko, Bryce S. Richards, Marc Hippler, Gabriele Wiegand, Yong Tang, Zongtao Li, Uli Lemmer, Hendrik Hölscher, and Guillaume Gomard. Foamed polymer/quantum dots composite films with enhanced photoluminescence efficiency. In *OSA Adv. Photonics Congr. 2019 (IPR, Networks, NOMA, SPPCom, PVLED)*, page PT2C.4. OSA, 2019.

[11] Shudong Yu, Benjamin Fritz, Dominik Theobald, Kejian Wu, Siegbert Johnsen, Dmitry Busko, Bryce S. Richards, Gabriele Wiegand, Yong Tang, Zongtao Li, Uli Lemmer, Hendrik Holscher, and Guillaume Gomard. Enhanced color conversion of quantum dots - polymer hybrid films in light emitting diodes. In *2019 20th Int. Conf. Electron. Packag. Technol.*, pages 1–4. IEEE, 2019.

[12] Dominik Theobald, Amos Egel, Guillaume Gomard, and Uli Lemmer. Simulation of light scattering in clusters of nonspherical nanoparticles: an adapted T-matrix approach. In *Nanophotonics VII*, page 82. SPIE, 2018.

[13] Dominik Theobald, Amos Egel, Guillaume Gomard, and Uli Lemmer. T-matrix simulations of light scattering by densely packed nonspherical particles. In Nadia Zakharova, editor, *Seventeenth Conf. Electromagn. Light Scatt.*, College Station, 2018. NASA.

[14] Dominik Theobald, Amos Egel, Guillaume Gomard, and Uli Lemmer. Improved accuracy of T-matrix simulations for nearfield coupling of scattered electromagnetic waves at spheroids. In Thomas Wriedt, editor, *Bremen Work. Light Scatt. 2017*, 2017.

[15] Amos Egel, Dominik Theobald, Yidenekachew J. Donie, Jan B. Preinfalk, Guillaume Gomard, and Uli Lemmer. Accurate Modeling of Outcoupling from OLEDs: Volumetric versus Flat Internal Scattering Layers. In *Light. Energy Environ.*, page SSW2D.3. OSA, 2016.

Supervised thesis projects

[16] Mohamed Mobarak. *Simulative study of the optical properties of an aerogel-based photo catalyst support system*. Master thesis, Karlsruhe Institute of Technology, 2020.

[17] Abdullah Bin Shams. *Simulation of Spectrum Selective Metasurface for Enhanced Light Outcoupling in Quantum Dot LED using Core-Shell Nanoparticles*. Master thesis, Karlsruhe Institute of Technology, 2019.

Bibliography

[18] Christian Kluge, Michael Rädler, Arfat Pradana, Matthias Bremer, Peter-Jürgen Jakobs, Nicole Barié, Markus Guttmann, and Martina Gerken. Extraction of guided modes from organic emission layers by compound binary gratings. *Opt. Lett.*, 37(13):2646, 2012.

[19] Kevin Vynck, Matteo Burresi, Francesco Riboli, and Diederik S. Wiersma. Photon management in two-dimensional disordered media. *Nat. Mater.*, 11(12):1017–1022, 2012.

[20] Benjamin G. Lee, Paul Stradins, David L. Young, Kirstin Alberi, Ta-Ko Chuang, J. Gregory Couillard, and Howard M. Branz. Light trapping by a dielectric nanoparticle back reflector in film silicon solar cells. *Appl. Phys. Lett.*, 99(6):064101, 2011.

[21] Filippo Pratesi, Matteo Burresi, Francesco Riboli, Kevin Vynck, and Diederik S. Wiersma. Disordered photonic structures for light harvesting in solar cells. *Opt. Express*, 21(S3):A460, 2013.

[22] Qing-Dong Ou, Lei Zhou, Yan-Qing Li, Su Shen, Jing-De Chen, Chi Li, Qian-Kun Wang, Shuit-Tong Lee, and Jian-Xin Tang. Extremely Efficient White Organic Light-Emitting Diodes for General Lighting. *Adv. Funct. Mater.*, 24(46):7249–7256, 2014.

[23] Yidenekachew J. Donie, Stefan Schlisske, Radwanul H. Siddique, Adrian Mertens, Vinayak Narasimhan, Fabian Schackmar, Manuel Pietsch, Ihteaz M. Hossain, Gerardo Hernandez-Sosa, Uli Lemmer, and Guillaume Gomard. Phase-Separated Nanophotonic Structures by Inkjet Printing. *ACS Nano*, 15(4):7305–7317, 2021.

[24] Pete Vukusic, Benny Hallam, and Joe Noyes. Brilliant Whiteness in Ultrathin Beetle Scales. *Science*, 315(5810):348–348, 2007.

[25] Serge Berthier. *Iridescences: The Physical Colors of Insects*. Springer, New York, 2007.

[26] Silvia Vignolini, Edwige Moyroud, Beverley J. Glover, and Ullrich Steiner. Analysing photonic structures in plants. *J. R. Soc. Interface*, 10(87):20130394, 2013.

[27] Raphael Schmager, Benjamin Fritz, Ruben Hünig, Kaining Ding, Uli Lemmer, Bryce S. Richards, Guillaume Gomard, and Ulrich W. Paetzold. Texture of the Viola Flower for Light Harvesting in Photovoltaics. *ACS Photonics*, 4(11):2687–2692, 2017.

[28] Weizhi Zou, Lorenzo Pattelli, Jing Guo, Shijia Yang, Meng Yang, Ning Zhao, Jian Xu, and Diederik S. Wiersma. Biomimetic Polymer Film with Brilliant Brightness Using a One-Step Water Vapor–Induced Phase Separation Method. *Adv. Funct. Mater.*, 29(23):1808885, 2019.

[29] Matteo Burresi, Lorenzo Cortese, Lorenzo Pattelli, Mathias Kolle, Peter Vukusic, Diederik S. Wiersma, Ullrich Steiner, and Silvia Vignolini. Bright-White Beetle Scales Optimise Multiple Scattering of Light. *Sci. Rep.*, 4(1):6075, 2014.

[30] Benjamin Fritz, Ruben Hünig, Raphael Schmager, Michael Hetterich, Uli Lemmer, and Guillaume Gomard. Assessing the influence of structural disorder on the plant epidermal cells' optical properties: a numerical analysis. *Bioinspir. Biomim.*, 12(3):036011, 2017.

[31] Ardavan Oskooi, Pedro A. Favuzzi, Yoshinori Tanaka, Hiroaki Shigeta, Yoichi Kawakami, and Susumu Noda. Partially disordered photonic-crystal thin films for enhanced and robust photovoltaics. *Appl. Phys. Lett.*, 100(18):181110, 2012.

[32] Peter M. Piechulla, Lutz Muehlenbein, Ralf B. Wehrspohn, Stefan Nanz, Aimi Abass, Carsten Rockstuhl, and Alexander Sprafke. Fabrication of Nearly-Hyperuniform Substrates by Tailored Disorder for Photonic Applications. *Adv. Opt. Mater.*, 6(7):1701272, 2018.

[33] Cheng Huang, Markus Moosmann, Jiehong Jin, Tobias Heiler, Stefan Walheim, and Thomas Schimmel. Polymer blend lithography: A versatile method to fabricate nanopatterned self-assembled monolayers. *Beilstein J. Nanotechnol.*, 3(1):620–628, 2012.

[34] Zelio Fusco, Renheng Bo, Yuling Wang, Nunzio Motta, Hongjun Chen, and Antonio Tricoli. Self-assembly of Au nano-islands with tuneable organized disorder for highly sensitive SERS. *J. Mater. Chem. C*, 7(21):6308–6316, 2019.

[35] A. Rahimzadegan, D. Arslan, R. N. S. Suryadharma, S. Fasold, M. Falkner, T. Pertsch, I. Staude, and C. Rockstuhl. Disorder-Induced Phase Transitions in the Transmission of Dielectric Metasurfaces. *Phys. Rev. Lett.*, 122(1):015702, 2019.

[36] Peter M. Piechulla, Bodo Fuhrmann, Evgeniia Slivina, Carsten Rockstuhl, Ralf B. Wehrspohn, and Alexander N. Sprafke. Tailored Light Scattering through Hyperuniform Disorder in Self-Organized Arrays of High-Index Nanodisks. *Adv. Opt. Mater.*, 9(17):2100186, 2021.

[37] Jan B. Preinfalk, Thomas Eiselt, Thomas Wehlus, Valentina Rohnacher, Thomas Hanemann, Guillaume Gomard, and Uli Lemmer. Large-Area Screen-Printed Internal Extraction Layers for Organic Light-Emitting Diodes. *ACS Photonics*, 4(4):928–933, 2017.

[38] Julia Syurik, Radwanul Hasan Siddique, Antje Dollmann, Guillaume Gomard, Marc Schneider, Matthias Worgull, Gabriele Wiegand, and Hendrik Hölscher. Bio-inspired, large scale, highly-scattering films for nanoparticle-alternative white surfaces. *Sci. Rep.*, 7(1):46637, 2017.

[39] Akira Ishimaru. *Wave Propagation and Scattering in Random Media*. Academic Press, New York, 1978.

[40] Michael I. Mishchenko. Vector radiative transfer equation for arbitrarily shaped and arbitrarily oriented particles: a microphysical derivation from statistical electromagnetics. *Appl. Opt.*, 41(33):7114, 2002.

[41] Michael I. Mishchenko. Poynting–Stokes tensor and radiative transfer in discrete random media: the microphysical paradigm. *Opt. Express*, 18(19):19770, 2010.

[42] R. Bathelt, D. Buchhauser, C. Gärditz, R. Paetzold, and P. Wellmann. Light extraction from OLEDs for lighting applications through light scattering. *Org. Electron.*, 8(4):293–299, 2007.

[43] Bahareh Ramezan pour and Daniel W. Mackowski. Radiative transfer equation and direct simulation prediction of reflection and absorption by particle deposits. *J. Quant. Spectrosc. Radiat. Transf.*, 189:361–368, 2017.

[44] R.H.T. Bates. Analytic Constraints on Electromagnetic Field Computations. *IEEE Trans. Microw. Theory Tech.*, 23(8):605–623, 1975.

[45] Kane Yee. Numerical solution of initial boundary value problems involving maxwell's equations in isotropic media. *IEEE Trans. Antennas Propag.*, 14(3):302–307, may 1966.

[46] Thomas Wriedt. A Review of Elastic Light Scattering Theories. *Part. Part. Syst. Charact.*, 15(2):67–74, 1998.

[47] J. L. Volakis, A. Chatterjee, and L. C. Kempel. Review of the finite-element method for three-dimensional electromagnetic scattering. *J. Opt. Soc. Am. A*, 11(4):1422, 1994.

[48] Thomas Wriedt. Light scattering theories and computer codes. *J. Quant. Spectrosc. Radiat. Transf.*, 110(11):833–843, 2009.

[49] Bruce T. Draine and Piotr J. Flatau. Discrete-Dipole Approximation For Scattering Calculations. *J. Opt. Soc. Am. A*, 11(4):1491, 1994.

[50] Pasi Yla-Oijala, Johannes Markkanen, Seppo Jarvenpaa, and Sami P. Kiminki. Surface and Volume Integral Equation Methods for Time-Harmonic Solutions of Maxwell's Equations. *Prog. Electromagn. Res.*, 149(July):15–44, 2014.

[51] Diego M. Solís, José M. Taboada, Fernando Obelleiro, Luis M. Liz-Marzán, and F. Javier García de Abajo. Toward Ultimate Nanoplasmonics Modeling. *ACS Nano*, 8(8):7559–7570, 2014.

[52] D. M. Solis, M. G. Araujo, L. Landesa, S. Garcia, J. M. Taboada, and F. Obelleiro. MLFMA-MoM for Solving the Scattering of Densely Packed Plasmonic Nanoparticle Assemblies. *IEEE Photonics J.*, 7(3):1–9, 2015.

[53] Maxim A. Yurkin and Alfons G. Hoekstra. The discrete-dipole-approximation code ADDA: Capabilities and known limitations. *J. Quant. Spectrosc. Radiat. Transf.*, 112(13):2234–2247, 2011.

[54] M G Moharam and T K Gaylord. Rigorous coupled-wave analysis of planar-grating diffraction. *J. Opt. Soc. Am.*, 71(7):811, 1981.

[55] P. C. Waterman. Matrix Formulation of Electromagnetic Scattering. *Proc. IEEE*, 53(8):805 – 812, 1965.

[56] Michael I Mishchenko, Larry D Travis, and Andrew A Lacis. *Scattering, Absorption, and Emission of Light by Small Particles*. Cambridge University Press, 2002.

[57] Shoji Asano and Giichi Yamamoto. Light Scattering by a Spheroidal Particle. *Appl. Opt.*, 14(1):29, 1975.

[58] Amos Egel, Lorenzo Pattelli, Giacomo Mazzamuto, Diederik S. Wiersma, and Uli Lemmer. CELES: CUDA-accelerated simulation of electromagnetic scattering by large ensembles of spheres. *J. Quant. Spectrosc. Radiat. Transf.*, 199:103–110, 2017.

[59] Johannes Markkanen and Alex J. Yuffa. Fast superposition T-matrix solution for clusters with arbitrarily-shaped constituent particles. *J. Quant. Spectrosc. Radiat. Transf.*, 189:181–188, 2017.

[60] Amos Egel. Accurate optical simulation of disordered scattering layers for light extraction from organic light emitting diodes. *Thesis*, 2018.

[61] Lukas Novotny and Bert Hecht. *Principles of Nano-Optics*. Cambridge University Press, Cambridge, 2006.

[62] Thorkild B. Hansen and Arthur D. Yaghjian. *Plane-Wave Theory of Time-Domain Fields*. IEEE, 1999.

[63] Adrian Doicu, Thomas Wriedt, and Yuri A. Eremin. *Light Scattering by Systems of Particles*, volume 124 of *Springer Series in OPTICAL SCIENCES*. Springer Berlin Heidelberg, Berlin, Heidelberg, 2006.

[64] O R Cruzan. Translational addition theorems for spherical vector wave functions. *Q. Appl. Math.*, 20(1):33–40, 1962.

[65] Daniel A. Mackowski. Analysis of Radiative Scattering for Multiple Sphere Configurations. *Proc. Math. Phys. Sci.*, 433(1889):599–614, 1991.

[66] Seymour Stein. Addition Theorems for Spherical Wave Functions. *Q. Appl. Math.*, 19(1):15–24, 1961.

[67] A. Boström, G. Kristensson, and S. Ström. Transformation Properties of Plane, Spherical and Cylindrical Scalar and Vector Wave Functions. In *F. Represent. Introd. to Scatt.*, pages 165–210. Elsevier Science Publishers B.V., 1991.

[68] John Lekner and Michael C. Dorf. Matrix methods for the calculation of reflection amplitudes. *J. Opt. Soc. Am. A*, 4(11):2092, 1987.

[69] Charalambos C. Katsidis and Dimitrios I. Siapkas. General transfer-matrix method for optical multilayer systems with coherent, partially coherent, and incoherent interference. *Appl. Opt.*, 41(19):3978, 2002.

[70] D. Y. K. Ko and J. R. Sambles. Scattering matrix method for propagation of radiation in stratified media: attenuated total reflection studies of liquid crystals. *J. Opt. Soc. Am. A*, 5(11):1863, 1988.

[71] Amos Egel and Uli Lemmer. Dipole emission in stratified media with multiple spherical scatterers: Enhanced outcoupling from OLEDs. *J. Quant. Spectrosc. Radiat. Transf.*, 148:165–176, 2014.

[72] Michael I. Mishchenko, Gorden Videen, Victor A. Babenko, Nikolai G. Khlebtsov, and Thomas Wriedt. T-matrix theory of electromagnetic scattering by particles and its applications: A comprehensive reference database. *J. Quant. Spectrosc. Radiat. Transf.*, 88:357–406, 2004.

[73] Michael I. Mishchenko, Gorden Videen, Victor A. Babenko, Nikolai G. Khlebtsov, and Thomas Wriedt. Comprehensive T-matrix reference database: A 2004-06 update. *J. Quant. Spectrosc. Radiat. Transf.*, 106(1-3):304–324, 2007.

[74] Michael I. Mishchenko, Gorden Videen, Nikolai G. Khlebtsov, Thomas Wriedt, and Nadia T. Zakharova. Comprehensive T-matrix reference database: A 2006-07 update. *J. Quant. Spectrosc. Radiat. Transf.*, 109(8):1447–1460, 2008.

[75] Michael I. Mishchenko, Nadia T. Zakharova, Gorden Videen, Nikolai G. Khlebtsov, and Thomas Wriedt. Comprehensive T-matrix reference database: A 2007-2009 update. *J. Quant. Spectrosc. Radiat. Transf.*, 111(4):650–658, 2010.

[76] Nadezhda T. Zakharova, Gorden Videen, and Nikolai G. Khlebtsov. Comprehensive T-matrix reference database: A 2009-2011 update. *J. Quant. Spectrosc. Radiat. Transf.*, 113(14):1844–1852, 2012.

[77] Michael I. Mishchenko, Gorden Videen, Nikolai G. Khlebtsov, and Thomas Wriedt. Comprehensive T-matrix reference database: A 2012-2013 update. *J. Quant. Spectrosc. Radiat. Transf.*, 123:145–152, 2013.

[78] Michael I. Mishchenko, Nadezhda T. Zakharova, Nikolai G. Khlebtsov, Thomas Wriedt, and Gorden Videen. Comprehensive thematic T-matrix reference database: A 2013-2014 update. *J. Quant. Spectrosc. Radiat. Transf.*, 146:349–354, 2014.

[79] Michael I. Mishchenko, Nadezhda T. Zakharova, Nikolai G. Khlebtsov, Gorden Videen, and Thomas Wriedt. Comprehensive thematic T-matrix reference database: A 2014-2015 update. *J. Quant. Spectrosc. Radiat. Transf.*, 178:276–283, 2016.

[80] Michael I. Mishchenko, Nadezhda T. Zakharova, Nikolai G. Khlebtsov, Gorden Videen, and Thomas Wriedt. Comprehensive thematic T-matrix reference database: A 2015–2017 update. *J. Quant. Spectrosc. Radiat. Transf.*, 202:240–246, 2017.

[81] M. I. Mishchenko and P. A. Martin. Peter Waterman and T-matrix methods. *J. Quant. Spectrosc. Radiat. Transf.*, 123:2–7, 2013.

[82] R H T Bates. Modal expansions for electromagnetic scattering from perfectly conducting cylinders of arbitrary cross-section. *Proc. IEEE*, 115(10):1443–1445, 1968.

[83] Gustav Mie. Beiträge zur Optik trüber Medien, speziell kolloidaler Metallösungen. *Ann. Phys.*, 330(3):277–445, 1908.

[84] A. Doicu and T. Wriedt. Extended boundary condition method with multipole sources located in the complex plane. *Opt. Commun.*, 139(1-3):85–91, 1997.

[85] Daniel W. Mackowski. Discrete dipole moment method for calculation of the T matrix for nonspherical particles. *J. Opt. Soc. Am. A*, 19(5):881, 2002.

[86] Martin Fruhnert, Ivan Fernandez-Corbaton, Vassilios Yannopapas, and Carsten Rockstuhl. Computing the T-matrix of a scattering object with multiple plane wave illuminations. *Beilstein J. Nanotechnol.*, 8(1):614–626, 2017.

[87] M.A. Morgan, C.H. Chen, S.C. Hill, and P.W. Barber. Finite element-boundary integral formulation for electromagnetic scattering. *Wave Motion*, 6(1):91–103, 1984.

[88] J. V. Dave. Scattering of Electromagnetic Radiation by a Large, Absorbing Sphere. *IBM J. Res. Dev.*, 13(3):302–313, 1969.

[89] W J Wiscombe. Improved Mie scattering algorithms. *Appl. Opt.*, 19(9):1505, 1980.

[90] Antonio Alvaro Ranha Neves and Dario Pisignano. Effect of finite terms on the truncation error of Mie series. *Opt. Lett.*, 37(12):2418, 2012.

[91] W.R.C. Somerville, B. Auguié, and E.C. Le Ru. Accurate and convergent T-matrix calculations of light scattering by spheroids. *J. Quant. Spectrosc. Radiat. Transf.*, 160:29–35, 2015.

[92] Lord Rayleigh. On the Dynamical Theory of Gratings. *Proc. R. Soc. London. Ser. A, Contain. Pap. a Math. Phys. Character*, 79(532):399–416, 1907.

[93] P. van den Berg and J. Fokkema. The Rayleigh hypothesis in the theory of diffraction by a cylindrical obstacle. *IEEE Trans. Antennas Propag.*, 27(5):577–583, 1979.

[94] M.L. Burrows. Equivalence of the Rayleigh solution and the extended-boundary-condition solution for scattering problems. *Electron. Lett.*, 5(12):277, 1969.

[95] R.H.T. Bates. Rayleigh hypothesis, the extended-boundary condition and point matching. *Electron. Lett.*, 5(25):654, 1969.

[96] R.F. Millar. Rayleigh hypothesis in scattering problems. *Electron. Lett.*, 5(17):416, 1969.

[97] Thomas Wriedt, Roman Schuh, and Adrian Doicu. Scattering by Aggregated Fibres Using a Multiple Scattering T-Matrix Approach. *Part. Part. Syst. Charact.*, 25(1):74–83, apr 2008.

[98] a. Doicu, Yu.A. Eremin, and T. Wriedt. Convergence of the T-matrix method for light scattering from a particle on or near a surface. *Opt. Commun.*, 159(4-6):266–277, 1999.

[99] Julius Adams Stratton. *Electromagnetic Theory*. McGraw-Hill Book Company, New York and London, 1941.

[100] Edward D. Palik. *Handbook of Optical Constants of Solids*. Academic Press, San Diego, 1997.

[101] COMSOL, Comsol Multiphysics, www.comsol.com, 2021.

[102] Juho Pertti Jalava, Veli Matti Taavitsainen, Ralf Johan Lamminmäki, Minna Lindholm, Sami Auvinen, Matti Alatalo, Erik Vartiainen, and Heikki Haario. Modeling TiO2's refractive index function from bulk to nanoparticles. *J. Quant. Spectrosc. Radiat. Transf.*, 167:105–118, 2015.

[103] F. Michael Schulz, Knut Stamnes, and Jakob J. Stamnes. Scattering of electromagnetic waves by spheroidal particles: a novel approach exploiting the T matrix computed in spheroidal coordinates. *Appl. Opt.*, 37(33):7875, 1998.

[104] W.R.C. Somerville, B. Auguié, and E.C. Le Ru. Severe loss of precision in calculations of T-matrix integrals. *J. Quant. Spectrosc. Radiat. Transf.*, 113(7):524–535, 2012.

[105] W.R.C. Somerville, B. Auguié, and E.C. Le Ru. A new numerically stable implementation of the T-matrix method for electromagnetic scattering by spheroidal particles. *J. Quant. Spectrosc. Radiat. Transf.*, 123:153–168, 2013.

[106] W.R.C. Somerville, B. Auguié, and E.C. Le Ru. smarties: User-friendly codes for fast and accurate calculations of light scattering by spheroids. *J. Quant. Spectrosc. Radiat. Transf.*, 174:39–55, 2016.

[107] Baptiste Auguié, Walter R C Somerville, Stanley Roache, and Eric C Le Ru. Numerical investigation of the Rayleigh hypothesis for electromagnetic scattering by a particle. *J. Opt.*, 18(7):075007, 2016.

[108] D. Schebarchov, E. C. Le Ru, J. Grand, and B. Auguié. Mind the gap: testing the Rayleigh hypothesis in T-matrix calculations with adjacent spheroids. *Opt. Express*, 27(24):35750, 2019.

[109] Torleif Martin. T-matrix method for closely adjacent obstacles. *J. Quant. Spectrosc. Radiat. Transf.*, 234:40–46, 2019.

[110] Maxime Bertrand, Alexis Devilez, Jean-Paul Hugonin, Philippe Lalanne, and Kevin Vynck. Global polarizability matrix method for efficient modeling of light scattering by dense ensembles of non-spherical particles in stratified media. *J. Opt. Soc. Am. A*, 37(1):70, 2020.

[111] Aristeidis Lamprianidis, Carsten Rockstuhl, and Ivan Fernandez-Corbaton. Overcoming the Rayleigh Hypothesis with sources distributed on the topological skeleton of the scatterer: a numerical demonstration of the method. In Thomas Wriedt, editor, *Bremen Work. Light Scatt. 2021*, 2021.

[112] Jesus Rubio and Rafael Gomez-Alcala. Mutual Coupling of Antennas With Overlapping Minimum Spheres Based on the Transformation Between Spherical and Plane Vector Waves. *IEEE Trans. Antennas Propag.*, 69(4):2103–2111, 2021.

[113] Anna Köhler and Heinz Bässler, editors. *Electronic Processes in Organic Semiconductors An Introduction*. Wiley-VCH Verlag GmbH & Co KGaA, Weinheim, 2015.

[114] Aleksander Jablonski. Efficiency of Anti-Stokes Fluorescence in Dyes. *Nature*, 131:839–840, 1933.

[115] M A Baldo, D. F. O'Brien, Y. You, A Shoustikov, S Sibley, M E Thompson, and S R Forrest. Highly efficient phosphorescent emission from organic electroluminescent devices. *Nature*, 395(6698):151–154, 1998.

[116] Chihaya Adachi, Marc A. Baldo, Mark E. Thompson, and Stephen R. Forrest. Nearly 100% internal phosphorescence efficiency in an organic light-emitting device. *J. Appl. Phys.*, 90(10):5048–5051, 2001.

[117] Ayataka Endo, Keigo Sato, Kazuaki Yoshimura, Takahiro Kai, Atsushi Kawada, Hiroshi Miyazaki, and Chihaya Adachi. Efficient up-conversion of triplet excitons into a singlet state and its application for organic light emitting diodes. *Appl. Phys. Lett.*, 98(8):083302, 2011.

[118] Qisheng Zhang, Bo Li, Shuping Huang, Hiroko Nomura, Hiroyuki Tanaka, and Chihaya Adachi. Efficient blue organic light-emitting diodes employing thermally activated delayed fluorescence. *Nat. Photonics*, 8(4):326–332, 2014.

[119] Klaus Müllen and Ullrich Scherf, editors. *Organic Light Emitting Devices. Synthesis, Properties and Applications*. Wiley-VCH Verlag GmbH & Co KGaA, Weinheim, 2006.

[120] Wolfgang Brütting, Jörg Frischeisen, Tobias D. Schmidt, Bert J. Scholz, and Christian Mayr. Device efficiency of organic light-emitting diodes: Progress by improved light outcoupling. *Phys. status solidi*, 210(1):44–65, 2013.

[121] Tobias Bocksrocker, Neele Hülsmann, Carsten Eschenbaum, Andreas Pargner, Stefan Höfle, Florian Maier-Flaig, and Uli Lemmer. Highly efficient fully flexible indium tin oxide free organic light emitting diodes fabricated directly on barrier-foil. *Thin Solid Films*, 542:306–309, 2013.

[122] Sebastian Reineke, Michael Thomschke, Björn Lüssem, and Karl Leo. White organic light-emitting diodes: Status and perspective. *Rev. Mod. Phys.*, 85(3):1245–1293, 2013.

[123] Kevin M. McPeak, Sriharsha V. Jayanti, Stephan J. P. Kress, Stefan Meyer, Stelio Iotti, Aurelio Rossinelli, and David J. Norris. Plasmonic Films Can Easily Be Better: Rules and Recipes. *ACS Photonics*, 2(3):326–333, 2015.

[124] Stefan Nowy, Benjamin C. Krummacher, Jörg Frischeisen, Nils A. Reinke, and Wolfgang Brütting. Light extraction and optical loss mechanisms in organic light-emitting diodes: Influence of the emitter quantum efficiency. *J. Appl. Phys.*, 104(12):123109, 2008.

[125] Kanchan Saxena, V.K. Jain, and Dalip Singh Mehta. A review on the light extraction techniques in organic electroluminescent devices. *Opt. Mater. (Amst).*, 32(1):221–233, 2009.

[126] Kihyon Hong and Jong-Lam Lee. Review paper: Recent developments in light extraction technologies of organic light emitting diodes. *Electron. Mater. Lett.*, 7(2):77–91, 2011.

[127] Amin Salehi, Xiangyu Fu, Dong-Hun Shin, and Franky So. Recent Advances in OLED Optical Design. *Adv. Funct. Mater.*, 29(15):1808803, 2019.

[128] Michael Flämmich, Jörg Frischeisen, Daniel S. Setz, Dirk Michaelis, Benjamin C. Krummacher, Tobias D. Schmidt, Wolfgang Brütting, and Norbert Danz. Oriented phosphorescent emitters boost OLED efficiency. *Org. Electron.*, 12(10):1663–1668, 2011.

[129] A. Graf, P. Liehm, C. Murawski, S. Hofmann, K. Leo, and M. C. Gather. Correlating the transition dipole moment orientation of phosphorescent emitter molecules in OLEDs with basic material properties. *J. Mater. Chem. C*, 2(48):10298–10304, 2014.

[130] V. Bulović, V. B. Khalfin, G. Gu, P. E. Burrows, D. Z. Garbuzov, and S. R. Forrest. Weak microcavity effects in organic light-emitting devices. *Phys. Rev. B*, 58(7):3730–3740, 1998.

[131] Shizuo Tokito, Tetsuo Tsutsui, and Yasunori Taga. Microcavity organic light-emitting diodes for strongly directed pure red, green, and blue emissions. *J. Appl. Phys.*, 86(5):2407–2411, 1999.

[132] Georg Gaertner and Horst Greiner. Light extraction from OLEDS with (high) index matched glass substrates. In *Org. Optoelectron. Photonics III*, volume 6999, page 69992T, 2008.

[133] Saso Mladenovski, Kristiaan Neyts, Domagoj Pavicic, Ansgar Werner, and Carsten Rothe. Exceptionally efficient organic light emitting devices using high refractive index substrates. *Opt. Express*, 17(9):7562, 2009.

[134] S. Möller and S. R. Forrest. Improved light out-coupling in organic light emitting diodes employing ordered microlens arrays. *J. Appl. Phys.*, 91(5):3324–3327, 2002.

[135] Sang-Hyun Eom, Edward Wrzesniewski, and Jiangeng Xue. Close-packed hemispherical microlens arrays for light extraction enhancement in organic light-emitting devices. *Org. Electron.*, 12(3):472–476, 2011.

[136] Yue Qu, Jongchan Kim, Caleb Coburn, and Stephen R. Forrest. Efficient, Nonintrusive Outcoupling in Organic Light Emitting Devices Using Embedded Microlens Arrays. *ACS Photonics*, 5(6):2453–2458, 2018.

[137] J. J. Shiang, T. J. Faircloth, and Anil R. Duggal. Experimental demonstration of increased organic light emitting device output via volumetric light scattering. *J. Appl. Phys.*, 95(5):2889–2895, 2004.

[138] Kyung Min Lee, Romain Fardel, Lianfeng Zhao, Craig B. Arnold, and Barry P. Rand. Enhanced outcoupling in flexible organic light-emitting diodes on scattering polyimide substrates. *Org. Electron.*, 51(July):471–476, 2017.

[139] B. J. Matterson, John M Lupton, Alexei F Safonov, Martin G Salt, William L Barnes, and Ifor D W Samuel. Increased Efficiency and Controlled Light Output from a Microstructured Light-Emitting Diode. *Adv. Mater.*, 13(2):123–127, 2001.

[140] Young Rag Do, Yoon-Chang Kim, Young-Woo Song, and Yong-Hee Lee. Enhanced light extraction efficiency from organic light emitting diodes by insertion of a two-dimensional photonic crystal structure. *J. Appl. Phys.*, 96(12):7629–7636, 2004.

[141] M. Fujita, T. Ueno, T. Asano, S. Noda, H. Ohhata, T. Tsuji, H. Nakada, and N. Shimoji. Organic light-emitting diode with ITO/organic photonic crystal. *Electron. Lett.*, 39(24):1750, 2003.

[142] Tobias Bocksrocker, Jan Benedikt Preinfalk, Julian Asche-Tauscher, Andreas Pargner, Carsten Eschenbaum, Florian Maier-Flaig, and Uli Lemme. White organic light emitting

diodes with enhanced internal and external outcoupling for ultra-efficient light extraction and Lambertian emission. *Opt. Express*, 20(S6):A932, 2012.

[143] Cholho Lee and Jang-Joo Kim. Enhanced Light Out-Coupling of OLEDs with Low Haze by Inserting Randomly Dispersed Nanopillar Arrays Formed by Lateral Phase Separation of Polymer Blends. *Small*, 9(22):3858–3863, 2013.

[144] Won Hoe Koo, Samyul Boo, Soon Moon Jeong, Suzushi Nishimura, Fumito Araoka, Ken Ishikawa, Takehiro Toyooka, and Hideo Takezoe. Controlling bucking structure by UV/ozone treatment for light extraction from organic light emitting diodes. *Org. Electron.*, 12(7):1177–1183, 2011.

[145] Ji-Hyang Jang and Min-Cheol Oh. Outcoupling Enhancement of OLEDs With a Randomly Distributed ITO Pattern Fabricated by Maskless Wet Etching Method. *J. Disp. Technol.*, 9(11):900–903, 2013.

[146] Yungui Li, Milan Kovacic, Jasper Westphalen, Steffen Oswald, Zaifei Ma, Christian Hänisch, Paul-Anton Will, Lihui Jiang, Manuela Junghaehnel, Reinhard Scholz, Simone Lenk, and Sebastian Reineke. Tailor-made nanostructures bridging chaos and order for highly efficient white organic light-emitting diodes. *Nat. Commun.*, 10(1):2972, 2019.

[147] Ali Ozhan Altun, Sohee Jeon, Jongyoup Shim, Jun-Ho Jeong, Dae-Geun Choi, Ki-Don Kim, Jun-Hyuk Choi, Soon-Won Lee, Eung-Sug Lee, Hyung-Dol Park, Jae R. Youn, Jang-Joo Kim, Yong-Hee Lee, and Jae-Wook Kang. Corrugated organic light emitting diodes for enhanced light extraction. *Org. Electron.*, 11(5):711–716, 2010.

[148] Yue-Feng Liu, Ming-Hui An, Xu-Lin Zhang, Yan-Gang Bi, Da Yin, Yi-Fan Zhang, Jing Feng, and Hong-Bo Sun. Enhanced efficiency of organic light-emitting devices with corrugated nanostructures based on soft nano-imprinting lithography. *Appl. Phys. Lett.*, 109(19):193301, 2016.

[149] Helmut Bechtel, Wolfgang Busselt, and Joachim Opitz. Subwavelength particle layers for improved light outcoupling of OLEDs. In Zakya H. Kafafi and Paul A. Lane, editors, *Org. Light. Mater. Devices VIII*, volume 5519, page 194, 2004.

[150] Boris Riedel, Yuxin Shen, Julian Hauss, Markus Aichholz, Xiaochen Tang, Uli Lemmer, and Martina Gerken. Tailored Highly Transparent Composite Hole-Injection Layer Consisting of Pedot:PSS and SiO2 Nanoparticles for Efficient Polymer Light-Emitting Diodes. *Adv. Mater.*, 23(6):740–745, 2011.

[151] Chur-Hyun Shin, Eul Yong Shin, Min-Hoi Kim, Jae-Hyun Lee, and Yoonseuk Choi. Nanoparticle scattering layer for improving light extraction efficiency of organic light emitting diodes. *Opt. Express*, 23(3):A133, 2015.

[152] Yidenekachew J. Donie, Michael Smeets, Vladimir Smirnov, Jan B. Preinfalk, Amos Egel, Uli Lemmer, Karsten Bittkau, and Guillaume Gomard. Light Management in Thin Film Solar Cells using Internal Scattering layers made by Polymer Blend Lithography. In *Light. Energy Environ.*, page PTh2A.6, Washington, D.C., 2016. OSA.

[153] Yidenekachew J. Donie, Michael Smeets, Amos Egel, Florian Lentz, Jan B. Preinfalk, Adrian Mertens, Vladimir Smirnov, Uli Lemmer, Karsten Bittkau, and Guillaume Gomard. Light trapping in thin film silicon solar cells via phase separated disordered nanopillars. *Nanoscale*, 10(14):6651–6659, 2018.

[154] S. Reich and Y. Cohen. Phase separation of polymer blends in thin films. *J. Polym. Sci. Polym. Phys. Ed.*, 19(8):1255–1267, 1981.

[155] A. Karim, T. M. Slawecki, S. K. Kumar, J. F. Douglas, S. K. Satija, C. C. Han, T. P. Russell, Y. Liu, R. Overney, J. Sokolov, and M. H. Rafailovich. Phase-Separation-Induced Surface Patterns in Thin Polymer Blend Films. *Macromolecules*, 31(3):857–862, 1998.

[156] Yang Li, Kai Hu, Xiao Han, Qinyu Yang, Yifeng Xiong, Yuhang Bai, Xu Guo, Yushuang Cui, Changsheng Yuan, Haixiong Ge, and Yanfeng Chen. Phase Separation of Silicon-Containing Polymer/Polystyrene Blends in Spin-Coated Films. *Langmuir*, 32(15):3670–3678, 2016.

[157] Monica Skoge, Aleksandar Donev, Frank H. Stillinger, and Salvatore Torquato. Packing hyperspheres in high-dimensional Euclidean spaces. *Phys. Rev. E*, 74(4):041127, 2006.

[158] Amos Egel, Guillaume Gomard, Siegfried W. Kettlitz, and Uli Lemmer. Accurate optical simulation of nano-particle based internal scattering layers for light outcoupling from organic light emitting diodes. *J. Opt.*, 19(2):025605, 2017.

[159] Christopher Wiesmann. *Nano-structured LEDs - Light extraction mechanisms and applications*. Universitätsverlag Regensburg, 2010.

[160] Jean-Pierre Berenger. A perfectly matched layer for the absorption of electromagnetic waves. *J. Comput. Phys.*, 114(2):185–200, 1994.

[161] Felix Bloch. Ueber die Quantenmechanik der Elektronen in Kristallgittern. *Zeitschrift fuer Phys.*, 52(7-8):555–600, 1929.

[162] J Korringa. On the calculation of the energy of a Bloch wave in a metal. *Physica*, 13(6-7):392–400, aug 1947.

[163] W. Kohn and N. Rostoker. Solution of the Schrödinger Equation in Periodic Lattices with an Application to Metallic Lithium. *Phys. Rev.*, 94(5):1111–1120, 1954.

[164] John B. Pendry. *Low energy electron diffraction : the theory and its application to determination of surface structure*. Academic Press, 1974.

[165] P. P. Ewald. Die Berechnung optischer und elektrostatischer Gitterpotentiale. *Ann. Phys.*, 369(3):253–287, 1921.

[166] Tom Darden, Lalith Perera, Leping Li, and Lee Pedersen. New tricks for modelers from the crystallography toolkit: the particle mesh Ewald algorithm and its use in nucleic acid simulations. *Structure*, 7(3):R55–R60, 1999.

[167] Mahfoud Belhadj, Howard E. Alper, and Ronald M. Levy. Molecular dynamics simulations of water with Ewald summation for the long range electrostatic interactions. *Chem. Phys. Lett.*, 179(1-2):13–20, 1991.

[168] Brian Stout. Spherical harmonic Lattice Sums for Gratings. In Evgeny Popov, editor, *Gratings Theory Numer. Appl.*, pages 6.1 – 6.41. Institut Fresnel, 2 edition, 2013.

[169] Kyozaburo Kambe. Theory of Low-Energy Electron diffraction: I. Application of the Cellular Method to Monatomic Layers. *Zeitschrift fuer Naturforsch.*, 22 a:322–330, 1967.

[170] Kyozaburo Kambe. Theory of Low-Energy Electron Diffraction: II. Cellular Method for Complex Monolayers and Multilayers. *Zeitschrift fuer Naturforsch.*, 23 a:1280–1294, 1968.

[171] N. Stefanou, V. Yannopapas, and A. Modinos. Heterostructures of photonic crystals: frequency bands and transmission coefficients. *Comput. Phys. Commun.*, 113(1):49–77, 1998.

[172] N. Stefanou, V. Yannopapas, and A. Modinos. MULTEM 2: A new version of the program for transmission and band-structure calculations of photonic crystals. *Comput. Phys. Commun.*, 132(1-2):189–196, 2000.

[173] Dominik Beutel, Achim Groner, Carsten Rockstuhl, and Ivan Fernandez-Corbaton. Efficient simulation of biperiodic, layered structures based on the T-matrix method. *J. Opt. Soc. Am. B*, 38(6):1782, 2021.

[174] Marek Nečada and Päivi Törmä. Multiple-Scattering T-Matrix Simulations for Nanophotonics: Symmetries and Periodic Lattices. *Commun. Comput. Phys.*, 30(2):357–395, 2021.

[175] Prof W H Bragg and W L Bragg. The reflection of X-rays by crystals. *Proc. R. Soc. London. Ser. A, Contain. Pap. a Math. Phys. Character*, 88(605):428–438, 1913.

[176] S. Sukhov, D. Haefner, and A. Dogariu. Coupled dipole method for modeling optical properties of large-scale random media. *Phys. Rev. E*, 77(6):066709, 2008.

[177] Hadrien Bériot and Axel Modave. An automatic perfectly matched layer for acoustic finite element simulations in convex domains of general shape. *Int. J. Numer. Methods Eng.*, 122(5):nme.6560, 2020.

[178] Jonathan Viquerat, Nikolai Schmitt, and Claire Scheid. Simulating 3D periodic structures at oblique incidences with discontinuous Galerkin time-domain methods: theoretical and practical considerations. *SMAI J. Comput. Math.*, 5:131–159, 2019.

[179] Amparo Gil, Javier Segura, and Nico M Temme. Efficient and Accurate Algorithms for the Computation and Inversion of the Incomplete Gamma Function Ratios. *SIAM J. Sci. Comput.*, 34(6):A2965–A2981, 2012.

[180] Rémy Abergel, Lionel Moisan, Rémy Abergel, and Lionel Moisan Fast. Fast and accurate evaluation of a generalized incomplete gamma function. *hal-01329669v2*, 2019.

[181] W. Lamb, D. M. Wood, and N. W. Ashcroft. Long-wavelength electromagnetic propagation in heterogeneous media. *Phys. Rev. B*, 21(6):2248–2266, 1980.

[182] A Liebsch and B N J Persson. Optical properties of small metallic particles in a continuous dielectric medium. *J. Phys. C Solid State Phys.*, 16(27):5375–5391, 1983.

[183] Fumiko Yonezawa and Kazuo Morigaki. Coherent Potential Approximation. *Prog. Theor. Phys. Suppl.*, 53:1–76, 1973.

[184] A. Modinos. Scattering of electromagnetic waves by a plane of spheres-formalism. *Phys. A Stat. Mech. its Appl.*, 141(2-3):575–588, 1987.

[185] N. Stefanou and A. Modinos. Scattering of light from a two-dimensional array of spherical particles on a substrate. *J. Phys. Condens. Matter*, 3(41):8135–8148, 1991.

[186] N. Stefanou and A. Modinos. Scattering of electromagnetic waves by a disordered two-dimensional array of spheres. *J. Phys. Condens. Matter*, 5(47):8859–8868, 1993.

[187] Daniel Mackowski and Bahareh Ramezanpour. A plane wave model for direct simulation of reflection and transmission by discretely inhomogeneous plane parallel media. *J. Quant. Spectrosc. Radiat. Transf.*, 213:95–106, 2018.

[188] Bruce T. Draine and Piotr J. Flatau. Discrete-dipole approximation for periodic targets: theory and tests. *J. Opt. Soc. Am. A*, 25(11):2693, 2008.

[189] Daniel Mackowski. Van de Hulst Essay: The DDA, the RTE, and the computation of scattering by plane parallel layers of particles. *J. Quant. Spectrosc. Radiat. Transf.*, 189:43–59, 2017.

[190] Kirk E. Jordan, Gerard R. Richter, and Ping Sheng. An efficient numerical evaluation of the Green's function for the Helmholtz operator on periodic structures. *J. Comput. Phys.*, 63(1):222–235, 1986.

[191] C. M. Linton. Lattice Sums for the Helmholtz Equation. *SIAM Rev.*, 52(4):630–674, 2010.

[192] Siu Kwan Lam, Antoine Pitrou, and Stanley Seibert. Numba: a LLVM-based Python JIT compiler. In *Proc. Second Work. LLVM Compil. Infrastruct. HPC - LLVM '15*, pages 1–6, New York, New York, USA, 2015. ACM Press.

[193] Peter Würfel and Uli Würfel. *Physics of Solar Cells: From Basic Principles to Advanced Concepts*. Wiley, 3 edition, 2016.

[194] William Shockley and Hans J. Queisser. Detailed Balance Limit of Efficiency of p-n Junction Solar Cells. *J. Appl. Phys.*, 32(3):510–519, 1961.

[195] Jan Mescher, Nico Christ, Siegfried Kettlitz, Alexander Colsmann, and Uli Lemmer. Influence of the spatial photocarrier generation profile on the performance of organic solar cells. *Appl. Phys. Lett.*, 101(7):073301, 2012.

[196] Francesco Enrichi and Giancarlo C. Righini. *Solar Cells and Light Management*. Elsevier, 2020.

[197] Denis Bernsmeier, Jörg Polte, Erik Ortel, Thoralf Krahl, Erhard Kemnitz, and Ralph Kraehnert. Antireflective Coatings with Adjustable Refractive Index and Porosity Synthesized by Micelle-Templated Deposition of MgF 2 Sol Particles. *ACS Appl. Mater. Interfaces*, 6(22):19559–19565, 2014.

[198] P. B. CLAPHAM and M. C. HUTLEY. Reduction of Lens Reflexion by the "Moth Eye" Principle. *Nature*, 244(5414):281–282, 1973.

[199] Karen Forberich, Gilles Dennler, Markus C. Scharber, Kurt Hingerl, Thomas Fromherz, and Christoph J. Brabec. Performance improvement of organic solar cells with moth eye anti-reflection coating. *Thin Solid Films*, 516(20):7167–7170, 2008.

[200] Patrick Campbell and Martin A. Green. Light trapping properties of pyramidally textured surfaces. *J. Appl. Phys.*, 62(1):243–249, 1987.

[201] C. Rockstuhl, S. Fahr, K. Bittkau, T. Beckers, R. Carius, F.-J. Haug, T. Söderström, C. Ballif, and F. Lederer. Comparison and optimization of randomly textured surfaces in thin-film solar cells. *Opt. Express*, 18(S3):A335, 2010.

[202] Corsin Battaglia, Karin Söderström, Jordi Escarré, Franz-Josef Haug, Didier Dominé, Peter Cuony, Mathieu Boccard, Grégory Bugnon, Céline Denizot, Matthieu Despeisse, Andrea Feltrin, and Christophe Ballif. Efficient light management scheme for thin film silicon solar cells via transparent random nanostructures fabricated by nanoimprinting. *Appl. Phys. Lett.*, 96(21):213504, 2010.

[203] Rahul Dewan and Dietmar Knipp. Light trapping in thin-film silicon solar cells with integrated diffraction grating. *J. Appl. Phys.*, 106(7):074901, 2009.

[204] Dayu Zhou and Rana Biswas. Photonic crystal enhanced light-trapping in thin film solar cells. *J. Appl. Phys.*, 103(9):093102, 2008.

[205] Seok-Soon Kim, Seok-In Na, Jang Jo, Dong-Yu Kim, and Yoon-Chae Nah. Plasmon enhanced performance of organic solar cells using electrodeposited Ag nanoparticles. *Appl. Phys. Lett.*, 93(7):073307, 2008.

[206] Se-Woong Baek, Jonghyeon Noh, Chun-Ho Lee, Bongsoo Kim, Min-Kyo Seo, and Jung-Yong Lee. Plasmonic Forward Scattering Effect in Organic Solar Cells: A Powerful Optical Engineering Method. *Sci. Rep.*, 3(1):1726, 2013.

[207] Zheng Tang, Anders Elfwing, Jonas Bergqvist, Wolfgang Tress, and Olle Inganäs. Light Trapping with Dielectric Scatterers in Single- and Tandem-Junction Organic Solar Cells. *Adv. Energy Mater.*, 3(12):1606–1613, 2013.

[208] M. Tripathy, P.K. Sadhu, and S.K. Panda. A critical review on building integrated photovoltaic products and their applications. *Renew. Sustain. Energy Rev.*, 61:451–465, 2016.

[209] Bjørn Petter Jelle, Christer Breivik, and Hilde Drolsum Røkenes. Building integrated photovoltaic products: A state-of-the-art review and future research opportunities. *Sol. Energy Mater. Sol. Cells*, 100(7465):69–96, 2012.

[210] Heidi Q. Chen, Tomonori Honda, and Maria C. Yang. Approaches for Identifying Consumer Preferences for the Design of Technology Products: A Case Study of Residential Solar Panels. *J. Mech. Des.*, 135(6), 2013.

[211] J.H. Selj, T.T. Mongstad, R. Søndenå, and E.S. Marstein. Reduction of optical losses in colored solar cells with multilayer antireflection coatings. *Sol. Energy Mater. Sol. Cells*, 95(9):2576–2582, 2011.

[212] Wei Zhang, Miguel Anaya, Gabriel Lozano, Mauricio E. Calvo, Michael B. Johnston, Hernán Míguez, and Henry J. Snaith. Highly Efficient Perovskite Solar Cells with Tunable Structural Color. *Nano Lett.*, 15(3):1698–1702, 2015.

[213] Anishkumar Soman and Aldrin Antony. Tuneable and spectrally selective broadband reflector – Modulated photonic crystals and its application in solar cells. *Sol. Energy*, 162(September 2017):525–532, 2018.

[214] Dae-Hyung Cho, Sung-Hoon Hong, Woo-Jung Lee, Joo Yeon Kim, and Yong-Duck Chung. Colorful solar cells utilizing off-axis light diffraction via transparent nanograting structures. *Nano Energy*, 80:105550, 2021.

[215] Stefan Schlisske, Florian Mathies, Dmitry Busko, Noah Strobel, Tobias Rödlmeier, Bryce S. Richards, Uli Lemmer, Ulrich W. Paetzold, Gerardo Hernandez-Sosa, and Efthymios Klampaftis. Design and Color Flexibility for Inkjet-Printed Perovskite Photovoltaics. *ACS Appl. Energy Mater.*, 2(1):764–769, 2019.

[216] Anishkumar Soman and Aldrin Antony. Colored solar cells with spectrally selective photonic crystal reflectors for application in building integrated photovoltaics. *Sol. Energy*, 181:1–8, 2019.

[217] J. Escarre, H.-Y Li, L. Sansonnens, F. Galliano, G. Cattaneo, P. Heinstein, S. Nicolay, J. Bailat, S. Eberhard, C. Ballif, and L.-E Perret-Aebi. When PV modules are becoming real building elements: White solar module, a revolution for BIPV. In *2015 IEEE 42nd Photovolt. Spec. Conf.*, pages 1–2. IEEE, 2015.

[218] Saba Gharibzadeh, Bahram Abdollahi Nejand, Marius Jakoby, Tobias Abzieher, Dirk Hauschild, Somayeh Moghadamzadeh, Jonas A. Schwenzer, Philipp Brenner, Raphael Schmager, Amir Abbas Haghighirad, Lothar Weinhardt, Uli Lemmer, Bryce S. Richards, Ian A. Howard, and Ulrich W. Paetzold. Record Open-Circuit Voltage Wide-Bandgap Perovskite Solar Cells Utilizing 2D/3D Perovskite Heterostructure. *Adv. Energy Mater.*, 9(21):1803699, 2019.

[219] Salman Manzoor, Jakob Häusele, Kevin A. Bush, Axel F. Palmstrom, Joe Carpenter, Zhengshan J. Yu, Stacey F. Bent, Michael D. Mcgehee, and Zachary C. Holman. Optical modeling of wide-bandgap perovskite and perovskite/silicon tandem solar cells using complex refractive indices for arbitrary-bandgap perovskite absorbers. *Opt. Express*, 26(21):27441, 2018.

[220] Zachary C. Holman, Miha Filipič, Antoine Descoeudres, Stefaan De Wolf, Franc Smole, Marko Topič, and Christophe Ballif. Infrared light management in high-efficiency silicon heterojunction and rear-passivated solar cells. *J. Appl. Phys.*, 113(1):013107, 2013.

[221] E. Raoult, R. Bodeux, S. Jutteau, S. Rives, A. Yaiche, D. Coutancier, J. Rousset, and S. Collin. Optical characterizations and modelling of semitransparent perovskite solar cells for tandem applications. In *36th Eur. Photovolt. Sol. Energy Conf. Exhib.*, pages 757–763, 2019.

[222] P. B. Johnson and R. W. Christy. Optical Constants of the Noble Metals. *Phys. Rev. B*, 6(12):4370–4379, 1972.

[223] DIN 5033-7:2014-10, Colorimetry - Part 7: Measuring conditions for object colours (German Version).

[224] DIN EN ISO 11664-1:2011, Colorimetry - Part 1: CIE standard colorimetric observers (German Version).

[225] DIN EN 61966-2-1:2003-09, Multimedia systems and equipment - Colour measurement and management - Part 2-1: Colour management - Default RGB colour space - sRGB (German Version).

[226] DIN EN ISO 11664-4:2011-06, Colorimetry - Part 4: CIE 1976 L*a*b* Colour space (German Version).

[227] Juergen H. Braun, Andrejs Baidins, and Robert E. Marganski. TiO2 pigment technology: a review. *Prog. Org. Coatings*, 20(2):105–138, 1992.

[228] M. J. A. Ruszala, N. A. Rowson, L. M. Grover, and R. A. Choudhery. Low Carbon Footprint TiO2 Substitutes in Paint: A Review. *Int. J. Chem. Eng. Appl.*, 6(5):331–340, 2015.

[229] Pierre Pichat. A Brief Survey of the Potential Health Risks of TiO2 Particles and TiO2- Containing Photocatalytic or Non-Photocatalytic Materials. *J. Adv. Oxid. Technol.*, 13(3):238–246, 2010.

[230] Julia Syurik, Gianni Jacucci, Olimpia D. Onelli, Hendrik Hölscher, and Silvia Vignolini. Bio-inspired Highly Scattering Networks via Polymer Phase Separation. *Adv. Funct. Mater.*, 28(24):1706901, 2018.

[231] Zheng Tang, Anders Elfwing, Jonas Bergqvist, Wolfgang Tress, and Olle Inganäs. Light Trapping with Dielectric Scatterers in Single- and Tandem-Junction Organic Solar Cells. *Adv. Energy Mater.*, 3(12):1606–1613, 2013.

[232] Stéphane Costeux. CO 2 -blown nanocellular foams. *J. Appl. Polym. Sci.*, 131(23):41293, 2014.

[233] Shudong Yu, Benjamin Fritz, Siegbert Johnsen, Dmitry Busko, Bryce S. Richards, Marc Hippler, Gabriele Wiegand, Yong Tang, Zongtao Li, Uli Lemmer, Hendrik Hölscher, and Guillaume Gomard. Enhanced Photoluminescence in Quantum Dots-Porous Polymer Hybrid Films Fabricated by Microcellular Foaming. *Adv. Opt. Mater.*, 7(12):1900223, 2019.

[234] Shudong Yu, Bing Guo, Siegbert Johnsen, Gabriele Wiegand, Uli Lemmer, Xia Guo, Maojie Zhang, Yongfang Li, Christian Sprau, Hendrik Hölscher, Alexander Colsmann, and Guillaume Gomard. Nanoporous Polymer Reflectors for Organic Solar Cells. *Energy Technol.*, page 2100676, 2021.

[235] Shudong Yu, Junchi Chen, Guanwei Liang, Xinrui Ding, Yong Tang, and Zongtao Li. White hairy layer on the Boehmeria nivea leaf—inspiration for reflective coatings. *Bioinspir. Biomim.*, 15(1):016003, 2019.

[236] Helge Eggers, Saba Gharibzadeh, Stefan Koch, Fabian Schackmar, David Ritzer, Tobias Abzieher, Bryce S. Richards, Christof Erban, and Ulrich W. Paetzold. Perovskite Solar Cells with Vivid, Angle-invariant and Customizable Inkjet-printed Colorization for Building-Integrated Photovoltaics. *Solar RRL*, 2021.

[237] Franz Hund. Inorganic Pigments: Bases for Colored, Uncolored, and Transparent Products. *Angew. Chemie Int. Ed. English*, 20(9):723–730, 1981.

[238] Gunter Buxbaum and Gerhard Pfaff, editors. *Industrial Inorganic Pigments*. Wiley-VCH Verlag GmbH & Co KGaA, Weinheim, 3 edition, 2005.

[239] Krassimir P. Velikov and Alfons van Blaaderen. Synthesis and Characterization of Monodisperse Core-Shell Colloidal Spheres of Zinc Sulfide and Silica. *Langmuir*, 17(16):4779–4786, 2001.

[240] Marvin Querry. Optical Constants of Minerals and Other Materials from the Millimeter to the Ultraviolet, Contractor Report CRDEC-CR-88009. Technical report, 1987.

[241] Lin Zschiedrich, Horst J. Greiner, Sven Burger, and Frank Schmidt. Numerical analysis of nanostructures for enhanced light extraction from OLEDs. In *Light. Diodes Mater. Devices, Appl. Solid State Light. XVII*, volume 8641, page 86410B, 2013.

[242] Stephen B. Pope. Algorithms for Ellipsoids. *Cornell Univ. Rep. FDA 08-01*, 2008.

[243] L. Tsang, J. A. Kong, and R. T. Shin. *Theory of Microwave Remote Sensing (Wiley Series in Remote Sensing and Image Processing)*. Wiley-Interscience, 1985.

Acknowledgements

The encounters I have had over the past years at the Light Technology Institute have been among the most fortunate, inspiring and challenging experiences of my life.
First of all, I would like to thank Prof. Dr. Uli Lemmer for the confidence he has put into me that made this thesis project possible in the first place. The freedom that I was given allowed me to develop myself not only scientifically, but also encouraged responsibility. I am sincerely grateful to Dr. Guillaume Gomard for the vision and guidance he provided me with, the enthusiasm he spread within our group and the intense dedication he put into our work. Furthermore, I would like to thank Prof. Dr. Carsten Rockstuhl for supporting the collaboration between our groups and for acting as a second referee.

I would like to thank Dr. Amos Egel, not only for his scientific guidance during my early work, but especially for his motivation to continuously develop SMUTHI and for the scientific discussions during his spare time. Without him, I would not have found my way into this community. Also, I would like to thank Dr. Lorenzo Pattelli. I am still amazed by his willingness to write comprehensive answers to any questions I have raised. Both of them are characteristic for the willingness to help each other within the nanophotonics community that I have experienced time and time again.

I would like to thank the Karlsruhe School of Optics and Photonics (KSOP) and 3D Matter Made to Order (3DMM2O) for providing graduate programs that connected me with many young scientists of various disciplines.

Over the years, I had the pleasure to share collaborative work with many colleagues. Among those, special thanks go to Dr. Yidenekachew Donie, Dr. Adrian Mertens, Isabel Allegro, Luisa Borgmann, Junchi Chen, Dr. Shudong Yu, Dominik Beutel and Paul Kant. These and many other colleagues have lightened my every day work.
I am especially grateful to Henning Mescher and Robert Huber for the friendship that I have found in them.

Schlussendlich möchte ich meinen Eltern Arno und Brigitte danken, die mir ein sorgenfreies Studium ermöglicht und mich hierher gebracht haben. Meinen Schwestern Isabelle und Vivienne danke ich für den Eifer, den sie in mir wecken. Meinem Großvater Adolf für das Glück, ihn noch immer bei uns zu wissen. Meiner Freundin Luisa danke ich für das Ersticken jedes Selbstzweifels und den Rückhalt, den ich immer bei mir weiß.